

**On the Lithographic Fabrication of Fe and Co  
Nanostructures via Focused Electron/Photon  
Beam Induced Processing:  
*Properties and Applications of the Structures***

---

Lithographische Herstellung von Fe und Co Nanostrukturen über  
Fokussierte Elektronen-/Photonenstrahl Induzierte Verarbeitung:  
Eigenschaften und Anwendungen der Strukturen

---

Der Naturwissenschaftlichen Fakultät der  
Friedrich-Alexander-Universität Erlangen-Nürnberg

zur Erlangung des Doktorgrades Dr. rer. nat.

vorgelegt von

**Fan Tu**

Jiangxi, China

Als Dissertation genehmigt

von der Naturwissenschaftlichen Fakultät

der Friedrich-Alexander-Universität Erlangen-Nürnberg

Tag der mündlichen Prüfung: 12.12.2017

Vorsitzender des Promotionsorgans: Prof. Dr. Georg Kreimer

Gutachter: PD. Dr. Hubertus Marbach

Prof. Dr. Rainer Fink

*This work is dedicated to my parents and family.  
Diese Arbeit ist meinen Eltern und Familie gewidmet.*



# Table of contents

<b>1 Introduction .....</b>	<b>1</b>
<b>2 Literature review .....</b>	<b>5</b>
2.1 FEBIP and AG .....	6
2.2 Oxidation of iron nanoparticles .....	9
2.3 Magnetic properties of EBID deposits .....	10
2.4 CVD growth of CNTs.....	13
2.5 X-ray lithography.....	16
<b>3 Techniques.....</b>	<b>17</b>
3.1 Scanning electron microscopy .....	17
3.2 Auger electron spectroscopy.....	20
3.3 Scanning tunneling microscopy (STM).....	22
3.4 Transmission electron microscopy (TEM) .....	23
3.5 Scanning transmission X-ray microscopy (STXM) .....	25
3.6 Other techniques .....	26
<b>4 Experimental details.....</b>	<b>29</b>
4.1 The UHV instrument .....	29
4.1.1 The preparation chamber .....	29
4.1.2 The analysis chamber .....	30
4.2 Sample holders.....	33
4.3 Ingredients.....	35
4.3.1 The precursors .....	35
4.3.2 The substrates .....	36
4.3.3 Other gases .....	37
4.4 Experimental details .....	37
4.4.1 Nanostructure fabrication and in-situ characterization with UHV-SEM .....	37

4.4.2 Characterization with TEM .....	38
4.4.3 Characterization and nanofabrication with STXM.....	39
4.4.4 CVD-CNTs growth.....	43
4.4.5 MgO thin film growth.....	44
<b>5 TEM investigation of Fe nanocrystal growth.....</b>	<b>47</b>
5.1 Introduction.....	47
5.2 Results and discussion .....	48
5.2.1 Fabrication of iron nanostructures.....	48
5.2.2 AG growth model .....	51
5.2.3 Chemical composition analysis .....	52
5.3 Conclusions.....	53
<b>6 On the magnetization properties of iron nanostructures via EBID plus AG .....</b>	<b>55</b>
6.1 Introduction.....	55
6.2 Results and discussion .....	56
6.2.1 Iron nanostructures fabricated via EBID .....	56
6.2.2 Magnetic properties of EBID iron nanostructures.....	62
6.3 Conclusions.....	68
<b>7 Secondary CNT growth on EBID-deposits.....</b>	<b>71</b>
7.1 Introduction.....	71
7.2 Results and discussion .....	72
7.2.1 CNT growth on EBID-Fe deposits .....	72
7.2.2 Optimization of Fe deposits fabrication .....	74
7.2.3 Fabrication of CNT forests on Al <sub>2</sub> O <sub>3</sub> support layer .....	79
7.2.4 Co containing EBID deposits as catalyst for CNT growth.....	84
7.3 Conclusions.....	85
<b>8 A novel nano-fabrication technique: FXBID .....</b>	<b>87</b>
8.1 Introduction.....	87

8.2 Results and discussion .....	89
8.2.1 Cobalt nanostructures fabricated via FXBID .....	89
8.2.2 Mn nanostructures fabricated via FXBID .....	95
8.2.3 Growth mode of Mn and Co precursors .....	98
8.3 Conclusions.....	99
<b>9 EBID and EBISA on MgO(100)/Ag(100).....</b>	<b>101</b>
9.1 Introduction.....	101
9.2 Results and discussion .....	102
9.2.1 Nanostructure fabrication .....	102
9.2.2 Activation mechanism .....	104
9.3 Conclusions.....	106
<b>10 Binary Fe/Co alloy fabrication.....</b>	<b>107</b>
10.1 Introduction.....	107
10.2 Results and discussion .....	108
10.2.1 Precursors .....	108
10.2.2 Fe-Co binary nanostructures fabricated via EBID .....	110
10.3 Conclusions.....	114
<b>11 Summary .....</b>	<b>117</b>
<b>12 Zusammenfassung.....</b>	<b>121</b>
<b>13 Appendix .....</b>	<b>125</b>
13.1 Chapter 4.4.3 Characterization and nanofabrication with STXM.....	125
13.2 Chapter 7.2.2 Optimization of Fe deposits fabrication.....	126
13.3 Chapter 10.2.1 Precursors.....	128
<b>14 References .....</b>	<b>131</b>
<b>Acknowledgement .....</b>	<b>150</b>
<b>Publication list .....</b>	<b>152</b>



## List of abbreviations

<b>AES</b>	Auger Electron Spectroscopy	<b>QMS</b>	Quadrupole Mass Spectrometer
<b>AG</b>	Autocatalytic Growth	<b>SE</b>	Secondary Electron
<b>AL</b>	Attenuation Length	<b>SEM</b>	Scanning Electron Microscopy
<b>BSE</b>	Backscattered Electron	<b>SR-CVD</b>	Synchrotron Radiation induced Chemical Vapor Deposition
<b>CNT</b>	Carbon Nanotube	<b>STEM</b>	Scanning Transmission Electron Microscopy
<b>CVD</b>	Chemical Vapor Deposition	<b>STM</b>	Scanning Tunneling Microscopy
<b>EBL</b>	Electron Beam Lithography	<b>STXM</b>	Scanning Transmission X-ray Microscopy
<b>EBID</b>	Electron Beam Induced Deposition	<b>SWNT</b>	Single-Walled Carbon Nanotube
<b>EBISA</b>	Electron Beam Induced Surface Activation	<b>TEM</b>	Transmission Electron Microscopy
<b>EDX</b>	Energy Dispersive X-ray	<b>2D</b>	Two Dimensional
<b>EELS</b>	Electron Energy Loss Spectroscopy	<b>3D</b>	Three Dimensional
<b>FEBIP</b>	Focused Electron Beam Induced Processing	<b>UHV</b>	Ultra-High Vacuum
<b>FSE</b>	Forward Scattered Electron	<b>XAS</b>	X-ray Absorption Spectroscopy
<b>FXBID</b>	Focused X-ray Beam Induced Deposition	<b>XMCD</b>	X-ray Magnetic Circular Dichroism
<b>HV</b>	High Vacuum	<b>XRL</b>	X-ray Lithography
<b>IMFP</b>	Inelastic Mean Free Path		
<b>LEED</b>	Low Energy Electron Diffraction		
<b>MFM</b>	Magnetic Force Microscopy		
<b>MOKE</b>	Magneto-Optical Kerr Effect		
<b>MWNT</b>	Multi-walled carbon nanotube		
<b>NEXAFS</b>	Near-Edge X-ray Absorption Fine Structure		
<b>PE</b>	Primary Electron		
<b>PVD</b>	Physical Vapor Deposition		
<b>QCM</b>	Quartz Crystal Microbalance		



# 1 Introduction

Nanoscience and nanotechnology are nowadays abundant in several applications, like computer technology, which are part in people's daily life not to speak of their importance in all relevant scientific and technical areas. The basic ideas and concepts of nanoscience and nanotechnology were already introduced on December 29th 1959 with a talk entitled "There's Plenty of Room at the Bottom" by the physicist Richard Feynman at the annual meeting of the American Physical Society at the California Institute of Technology (CalTech) [1]. In this famous talk, he emphasized the possibility of manipulating and controlling things on a very small scale, where the physical and chemical properties of materials might drastically change.

Semiconductor industry drives and also benefits a lot from the development of nanotechnology. As predicted by Moore's law [2], the number of individual nano-components such as transistors on a chip is still rising, increasing the density of functional entities and thus improving the computational power. Concerning the fabrication of nanostructures on substrates, there are two main distinguished concepts: bottom-up and top-down approach. A bottom-up approach basically relies on the (self-) assembly of small building blocks (i.e., atoms and molecules) to form more complex systems, while in a top-down approach, small devices are produced from larger components via various structuring techniques. A top-down approach is realized with classical UV-lithography as used in semiconductor industry, including sequences of processing steps as follows: substrate preparation, photoresist spin coat, exposure to the photon source through mask, development of the resist and pattern transfer [3].

One powerful method for the controlled fabrication on the nanometer scale is focused electron beam induced processing (FEBIP) [4-6]. Therein, a focused electron beam is used to locally modify the properties of a substrate, enabling the fabrication of nanostructures with arbitrary shape and controlled chemical composition. The most frequently applied and prominent FEBIP technique is electron beam induced deposition (EBID) [4, 5, 7-9], in which certain precursor molecules are locally dissociated by the impact of the electron beam, leading to the deposition of the nonvolatile fragments of the precursors. In 2010, electron beam induced surface activation (EBISA), as a novel process in FEBIP, has been developed by using electron beam to directly change the properties of the substrate itself, leading to the catalytic and eventually subsequent autocatalytic decomposition of certain precursor molecules, yielding demanded

## 1 Introduction

deposits [10-12]. Furthermore, under ultra-high vacuum (UHV) condition, autocatalytic growth (AG) processes can be observed even at room temperature when using suitable precursors, i.e., precursor molecules autocatalytically dissociate on pre-formed deposits fabricated by either EBID or EBISA, resulting in enlarged nanostructures with desirable properties, such as high purity [13, 14]. In this respect, massive deposits can be grown via AG process without further electron exposed and thus proximity effects can be diminished [13, 15, 16]. Therefore, at the beginning of the thesis at hand, AG of Fe nanocrystals by using iron pentacarbonyl ( $\text{Fe}(\text{CO})_5$ ) as precursor was investigated via scanning electron microscopy (SEM) and transmission electron microscopy (TEM). Electron diffraction and electron energy loss spectroscopy (EELS) were employed to monitor the crystalline and chemical composition of fabricated Fe nanocrystals (Chapter 5).

It has been proved that the EBID technique can be used to lithographically write Fe magnetic logic circuits with further applications in magnetic logic devices [17]. Chapter 6 deals with the characterization of magnetic properties on the fabricated Fe nanostructures via EBID combined with AG process. Synchrotron based scanning transmission X-ray microscopy (STXM) was applied as a powerful tool for not only microscopic but also microspectroscopic characterization. Through near-edge X-ray absorption fine structure (NEXAFS) spectra, oxidation states and chemical composition of Fe deposits can be identified. Combining with X-ray magnetic circular dichroism (XMCD) contrast in STXM images, magnetic domains were observed and further magnetic properties such as the coercivity values for systematically varied Fe deposits were determined.

Another attractive property for Fe and Co nanostructures is their catalytic activity towards the growth of carbon nanotubes (CNTs) via chemical vapor deposition (CVD) techniques. The combination of EBID with CVD-CNT was explored and investigated in the frame of the thesis at hand with the goal to produce CNTs at predefined positions with nanoscale accuracy. Chapter 7 discusses the influence of the parameters in catalyst fabrication via EBID and the following CVD process systematically. The morphology of produced CNT was characterized via SEM and chemical analysis was realized by energy dispersive X-ray (EDX).

Chapter 8 reports on the exploration of a novel nanofabrication technique to be referred to as focused X-ray beam induced deposition (FXBID), in which the stimulation source changes

## 1 Introduction

from electron beam to focused soft X-ray. A significant selectivity of the deposition process (with respect to the incident photon energy) was proposed and could be verified. This effect is attributed to the enhanced X-ray absorption cross section of the precursor molecules for near-threshold excitation. Two precursors were employed: cobalt tricarbonyl nitrosyl ( $\text{Co}(\text{CO})_3\text{NO}$ ) and methylenecyclopentadienyl manganese tricarbonyl ( $\text{MnCpMn}(\text{CO})_3$ ). Energy dependent dissociation was investigated for the  $L_{2,3}$ -edges of the respective metal centers as well as the N and O  $K$ -edges of the respective ligands.

Furthermore EBID and EBISA were expanded for the first time to MgO (100) thin films on Ag(100) with  $\text{Fe}(\text{CO})_5$  as precursor, as discussed in Chapter 9. MgO thin films were prepared by physical vapor deposition (PVD) to epitaxially grow on the Ag(100) single crystal. The quality of MgO was monitored via standard surface science techniques, such as quartz crystal microbalance (QCM), Auger electron spectroscopy (AES), low energy electron diffraction (LEED), SEM and scanning tunneling microscopy (STM).

Finally, the fabrication of Fe/Co binary alloy nanostructure using mixture gas of  $\text{Fe}(\text{CO})_5$  and  $\text{Co}(\text{CO})_3\text{NO}$  was addressed in Chapter 10. Influence of the precursor's ratio in the mixture gas was discussed and the chemical composition of produced Fe/Co alloy can be adjusted by the AG process, according to different autocatalytic property of each precursor.



## 2 Literature review

FEBIP is a powerful method for the controlled fabrication of structures on the nanometer scale [4, 5, 10, 18-20]. Thereby a focused electron beam of a SEM or a STEM can be used to locally modify the properties of the irradiated substrate itself or of adsorbed precursor molecules. One of the most frequently applied and prominent FEBIP techniques is EBID. In the last decades, substantial efforts have been taken to understand the surface chemistry process during the EBID process on a fundamental level [5, 7, 9, 12, 16, 20-22]. Another novel nanofabrication technique in FEBIP family is EBISA, with which large massive production of nanostructures can be realized [10]. In this respect, this chapter is organized in the following way:

A short description of the EBID and EBISA including the subsequent AG process shall be firstly discussed, giving an overview of the experimental data and theoretical background, with a specific focus on the fabrication of Fe nanostructures.

It is well known that Fe will be oxidized when exposed to ambient, i.e., air. It is important to understand the oxidation process of Fe nanoparticles (or nanocrystals here), which plays an important role in the further applications, such as functionalized magnetic logic circuit, data storage, and catalysis. Some important results of investigation of Fe oxidation process via TEM will be introduced.

In the third part of this chapter, magnetic properties of EBID deposits will be discussed, including Fe and Co deposits fabricated via EBID with various strategies, from 2D to 3D magnetic nanostructures.

Another attractive application of EBID-deposits is to act as catalyst for the localized growth of CNTs. Thereby, an introduction to CVD and some previous results of EBID-deposits as catalyst for CNTs growth will be presented.

Finally, a brief overview on the state of the art of X-ray lithography will be summarized, as X-ray beam presents some interesting peculiarities. Based on these reviews, a novel nanofabrication technique has been developed and results are presented in latter chapters.

## 2.1 FEBIP and AG

Fabrication of arbitrary structures with controllable chemical composition on the nanoscale drives the development of nanotechnology. One powerful technique in this respect is EBID, which is a mask-less, “direct-writing” method [4-6, 8, 19, 20]. In EBID, a focused electron beam is employed to induce the local dissociation of surface adsorbed metal organic precursor molecules supplied from the gas phase. The non-volatile dissociation products remain as a deposit on the surface while the volatile ones are pumped off by the vacuum system (Figure 2-1).

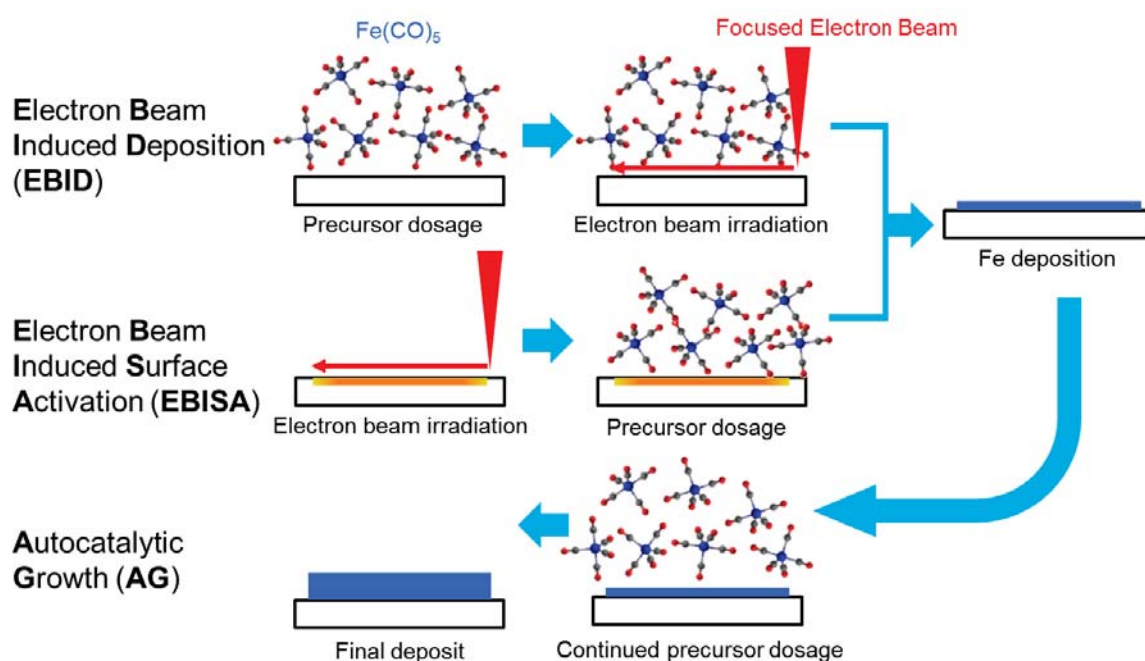


**Figure 2-1:** Principle of EBID technique with the precursor  $\text{Fe}(\text{CO})_5$ . **EBID:** local dissociation of adsorbed  $\text{Fe}(\text{CO})_5$  molecules by the impact of primary electrons (PE) from the focused electron beam and/or emitted backscattered and secondary electrons (generated within the orange cone). Dissociation of  $\text{Fe}(\text{CO})_5$  into volatile  $\text{CO}$  and non-volatile  $\text{Fe}$  fragments, and desorption of intact  $\text{CO}$  resulting in a clean  $\text{Fe}$  deposit. **EBISA:** Local irradiation of a suitable surface (e.g.,  $\text{SiO}_x$  and  $\text{TiO}_2$ ) with the focused electron beam. Successive dosage and dissociation of  $\text{Fe}(\text{CO})_5$  at the electron-modified surface sites leads to the deposition of pure  $\text{Fe}$ . **Autocatalytic growth (AG):** additional gas dosage after EBID and EBISA leads to an enlarged  $\text{Fe}$  deposit due to autocatalytic dissociation of  $\text{Fe}(\text{CO})_5$  at the initial  $\text{Fe}$  nuclei at room temperature in UHV.

## 2 Literature review

EBISA has been introduced into the FEBIP family in 2010, in which the electron beam is used to locally change the properties of the substrate such that the irradiated areas become chemically active towards the decomposition of certain precursors, resulting in desired deposits [12]. Most recently, EBISA has been expanded to  $\text{SiO}_x$ ,  $\text{TiO}_2$  and molecular layers, such as 2H-tetraphenylporphyrins on  $\text{TiO}_2(110)$  and  $\text{Ag}(111)$ . The mechanism for oxide surface is quite simple: oxygen vacancies generated from electron stimulated desorption of oxygen act as the active sites for the dissociation of certain precursor molecules (i.e.,  $\text{Fe}(\text{CO})_5$ ) under UHV condition. This mechanism has been proved by AES investigations of the  $\text{SiO}_x$  sample with electron beam irradiation [23]. However, in the case of molecular layer (i.e., 2H-tetraphenylporphyrins on  $\text{Ag}(111)$ ) [24], the chemical nature of the active species formed during electron beam irradiation is still unclear and needs further investigations.

Both EBID and EBISA deposits might continue to grow autocatalytically (AG) upon additional precursor dosage as depicted in Figure 2-1. Enlarged Fe deposit was produced due to autocatalytic decomposition of  $\text{Fe}(\text{CO})_5$  at the initial Fe nuclei at room temperature in the UHV chamber, as long as the precursor was supplied [13]. Xu investigated the decomposition of  $\text{Fe}(\text{CO})_5$ ,  $\text{Cr}(\text{CO})_6$ ,  $\text{Mo}(\text{CO})_6$  and  $\text{W}(\text{CO})_6$  on clean and well-prepared  $\text{Ni}(100)$  surface in UHV chamber [25]. It was observed that all carbonyls decomposed on the surface below room temperature. The corresponding mechanism was ascribed to the change of molecular geometry upon adsorption, in which the surface becomes a sixth ligand for the central iron metal. Except  $\text{Fe}(\text{CO})_5$ , other precursors such as  $\text{Co}(\text{CO})_3\text{NO}$  and  $\text{Co}_2(\text{CO})_8$  was also reported to exhibit autocatalytic growth under certain conditions [26, 27].

During EBID process, three important interactions can be categorized in more details: substrate-precursor molecule interaction, electron-substrate interaction and electron-precursor molecule interaction [4]. At the beginning, the precursor molecules are dosed through a needle close to the substrate where the electron beam hits the surface. The dynamics of the precursor molecules on the substrate can be divided into diffusion, adsorption, and desorption. As the EBID process proceeds, the pristine surface will change to the deposit interface. The electron beam is focused onto the substrate, interacting with the surface (substrate and deposit), resulting in secondary electrons (SEs) and backscattered electrons (BSEs) due to scattering process of the primary electron (PE) beam [7, 21]. The focused electron beam will, of course, also interact with the pre-absorbed precursor molecules, leading to dissociation which is the basic step in EBID

## 2 Literature review

process. From the description above, many factors have been involved in the deposition process. The residence time of the precursor molecules and the energy of the primary beam contribute to the final resolution, chemical composition and physical properties of the EBID-deposits. The state of the art of EBID, especially the interaction of electrons with precursor molecules, has been reviewed in numerous articles, summarizing the experimental data and introducing theoretical aspects in more details [4, 5, 8, 10, 18-20].

Concerning EBISA, electron beam is also utilized to activate the surface. Thereby, many concepts derived from EBID can be applied, especially the aspects of electron-substrate interaction. Since no deposits is formed during the electron irradiation, EBISA allows to visualize and thus to investigate fundamental aspects of electron backscattering [10, 11, 16]. However, there are many drawbacks: the high demands for the cleanliness of the environment to perform EBISA, precursors are limited to several metal carbonyls ( $\text{Fe}(\text{CO})_5$  and  $\text{Co}(\text{CO})_3\text{NO}$ ), and less effective compared with EBID process [24]. Discussions in details about EBISA can be found in a review article [10].

There are important applications of EBID based on its various and promising features, i.e., every combination of deposit materials and substrates can be targeted in EBID as there is a large variety of precursor molecules and nearly no restrictions in regard to the substrate. Examples are functionalized tips for scanning probe microscopy [28, 29], spintronic devices [30, 31], catalysts for nanotube growth [32-34], and an important tool in semiconductor industry the masks repair for high resolution EUV-lithography [35]. However, two main challenges are identified in EBID: firstly, the unintended co-deposition of materials/contaminations (either from the residual gas or the precursor itself) will hamper the fabrication of deposits with well-defined chemical composition. Secondly, the so-called electron proximity effects will broaden the fabricated structures due to electron scattering either in the substrate (BSEs) [11, 16, 36] or in the already formed deposit (forward scattered electrons, FSE) [37, 38]. Considering the purity issue, many efforts have been devoted to the development of purification methods [20, 39-44], even though rare exceptions have also been demonstrated, i.e., near-bulk cobalt resistivity without post-processing can be achieved [45] and single-crystal tungsten nanowires are grown from  $\text{WF}_6$  without additional treatment [46]. A common strategy to diminish the BSE proximity effect in EBID is to reduce the electron interaction volume by simply using thin membranes. With this approach and by applying low electron doses, extremely small deposits below 10 nm could be

## 2 Literature review

realized [18, 47-49]. However, Waltz et al. [11, 16] also discovered a new type proximity effects due to the positive charging of the  $\text{Si}_3\text{N}_4$  membrane, which broadened the deposits significantly. This suggests that we should also consider the change of chemical properties on  $\text{Si}_3\text{N}_4$  membrane even in the regions exceed the primary electron beam diameter and the area where electrons are backscattered. Electron proximity effects can also be significantly reduced by using EBISA, since for the deposition of additional materials, one can solely rely on increased precursor dosage without further electron dose.

### 2.2 Oxidation of iron nanoparticles

Fe nanoparticles are considered promising candidates for a variety of key applications such as high-density data storage [48], catalysts to carbon nanotube growth [33, 50] and water treatment [51], target drug delivery [52] and cancer therapy [53]. It is important to fundamentally understand the oxidation process of Fe on the nanoscale, such as oxide form by exposure to ambient. A core-shell structure is typical for the initially oxidized metal nanoparticles [54, 55] and is well understood based on a generally accepted theory of metal oxidation [56]. The iron core consists of a body-centered cubic structure while the oxide shell is composed of an inverse spinel structure of  $\text{Fe}_3\text{O}_4$ ,  $\gamma\text{-Fe}_2\text{O}_3$ , or an intermediate phase [57]. Figure 2-2 depicts the evolution of the Fe/Fe oxide core-shell structures with increasing the exposure time to ambient [57]. The metal/oxide interface continues to progress towards the particle interior with an oxidation front. A fully oxidized particle is shown after approximately two years reacting with air (Figure 2-2c), showing an approximately spherical shape. A reduced intensity is observed in the center of the fully oxidized particle, indicating the presence of a void which can be attributed to the imbalance in the relative rates for the inward diffusion of O and outward diffusion of Fe [58, 59].

As described previously, Fe nanocrystals with high purity (>95 at.%) can be fabricated via EBID, using  $\text{Fe}(\text{CO})_5$  as precursors at room temperature under UHV condition [12, 22, 23, 48]. The formed Fe cubic nanocrystal was identified as bcc  $\alpha\text{-Fe}$  by indexing the electron diffraction pattern [48]. They will be natively oxidized once exposed to air. A heating treatment was employed to reduce the Fe oxide, leading to various phases:  $\alpha\text{-Fe}$ ,  $\text{Fe}_5\text{C}_2$ ,  $\text{Fe}_7\text{C}_3$  and  $\text{Fe}_2\text{C}$ , which are all magnetic with Curie temperatures about 473 K [48].

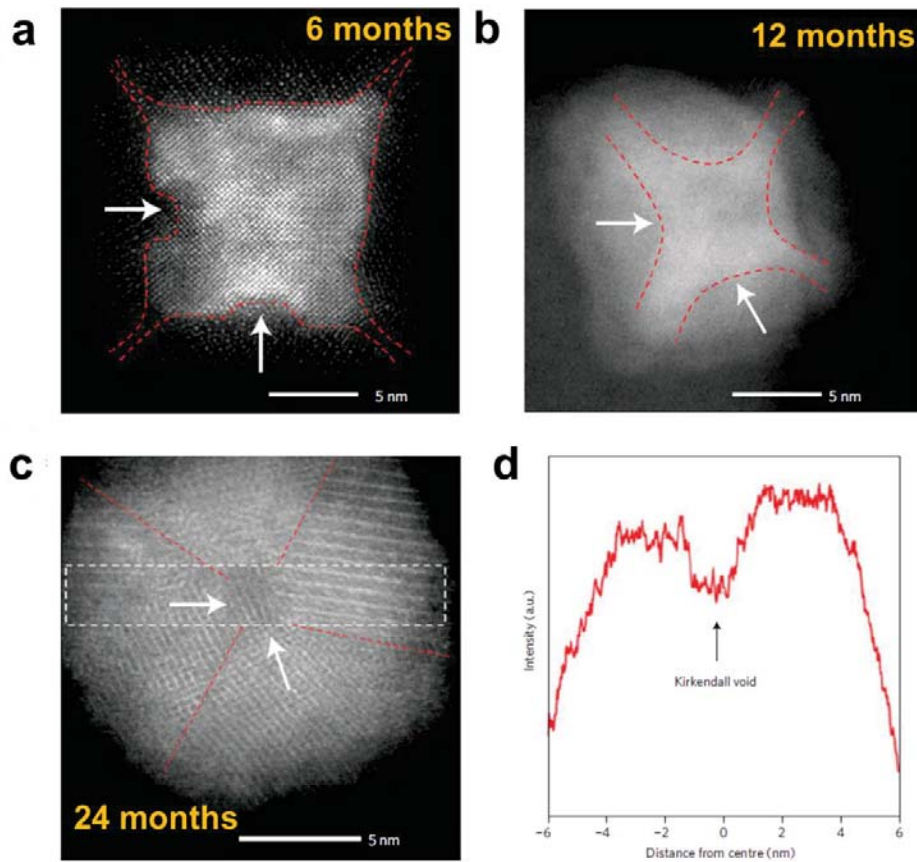


**Figure 2-2:** Shape evolution of oxidized Fe nanoparticle with increasing exposure time to ambient. (a)-(c) Fe nanoparticles at different stages of oxidation after 6, 12 and 24 months, respectively. Red dashed lines indicated the oxidation front. The Fe core is fully oxidized with four distinct oxide domains. (d) A line profile of the dashed region highlighted in (c). The presence of a void in the center of the fully oxidized nanoparticle can be revealed. The spherical shape of the fully oxidized nanoparticles can be explained by the strain induced morphological change [57]. Reprinted and adjusted from A. Pratt et al [57].

### 2.3 Magnetic properties of EBID deposits

As a mask-less, direct-writing nanofabrication technique, EBID has several advantages compared to other corresponding techniques, such as EBL, indicating the ability to produce extremely small structures ( $< 10$  nm) [18], precise position control during fabrication, the realization of arbitrary shapes and a large variety of applicable precursors. In this context, EBID

## 2 Literature review

is a promising route for the direct growth of magnetic nanostructures in a single step [60-65]. There are various precursors used so far for magnetic deposits, which has been reviewed carefully in reference [62, 65]. The most common magnetic deposits in EBID are Co [45, 60, 66], Fe [13, 67, 68], and FeCo alloy [69], even though there are also some reports about Ni [64], and CoPt alloy [63].

In the case of cobalt, there is magnetic switching behavior of Co structures by EBID based on the metallic concentration. Deposits with high Co content (>90 at.%) show metallic and ferromagnetic behavior [70, 71], whereas deposits with low Co content (<80 at.%) present semiconducting and paramagnetic or super-paramagnetic property [72]. Co deposits with high content consist of polycrystalline Co with a small (5~7 nm) grain size and the magnetocrystalline anisotropy is averaged to zero, resulting in the shape anisotropy governed magnetic reversal behavior. This gives rise to the tunable coercive field through modification of the dimensions of the Co nanostructures [71]. On the other hand, deposits with low Co content are usually formed by small isolated grains within a non-magnetic carbonaceous matrix, leading to a super-paramagnetic behavior and application in Hall sensors with high sensitivity [72].

Considering the magnetic properties of Fe-based nanostructures fabricated by EBID, ferromagnetic character has been demonstrated via Kerr effect and magnetoresistance measurements on the deposits fabricated using a mixture of H<sub>2</sub>O and Fe<sub>2</sub>(CO)<sub>9</sub> [68]. Further Hall-effect measurements on those samples revealed that the saturation magnetization value scales with the deposited Fe content, indicating 70 % of Fe bulk saturation magnetization for deposit with 70 at.% Fe content. A careful investigation of the shape influence has been carried out via Magnetic Force Microscopy (MFM) by Gavagnin et al [17]. They found that the coercive field was different for three different thicknesses. The shape anisotropy was proved to be the main anisotropy source for the nanomagnets of Fe fabricated via EBID. Rodríguez et al [73] reported that H<sub>C</sub> systematically varies with thickness and width of the Fe nanowires. H<sub>C</sub> decreased unexpectedly as thickness (10~45 nm) of the EBID-Fe elongated “nanowire” deposit is increased. The corresponding hysteresis loops were determined by magneto-optical Kerr effect (MOKE) experiments, i.e., without the possibility to image the magnetic domains in the experiment. The coercive field decreased with increasing width and thickness.

## 2 Literature review

The growth of Co and Fe alloys by EBID can be achieved by using either simultaneously two precursors or a single bimetallic precursor [62]. The former one is usually followed by subsequent annealing procedures to obtain desired chemical composition. In the case of single bimetallic precursor, i.e.,  $\text{HFeCo}_3(\text{CO})_{12}$ , a composition of CoFeCO (6:2:1:1) can be realized without any post-treatment [69]. This deposit consisted of a bcc Co-Fe phase mixed with a  $\text{FeCo}_2\text{O}_4$  spinel oxide phase with nanograins about 5 nm. The lowest room-temperature resistivity is found to be  $43 \mu \Omega \text{ cm}$  and the maximum magnetic induction is around 1.6 T.

One of the key challenges for future electronic memory and logic devices is to construct truly 3D devices, allowing many-fold increase in performance [74, 75]. The racetrack memory [74] and the vertical soliton shift register [75] have been proved as promising concepts towards the creation of 3D microchips for memory and logic applications. In the racetrack memory, magnetic domains are used to store information in sufficiently narrow ( $< 100\text{nm}$ ) magnetic columns which are necessary for the spin momentum transfer interaction of the current with the domain wall to dominate over the self-field of the current. Concerning the vertical soliton shift register, functional thin magnetic layers are fabricated and sharp magnetic kink solitons can be shifted from one magnetic layer to another by carefully controlling the thickness of each layer. For the realization and further progress of both approaches, non-conventional nanolithography techniques as well as advanced characterization methods are strongly required, with high resolution and the ability to investigate the chemical, mechanical and magnetic properties of real 3D nanostructures. In this respect, EBID presents promising features for complex 3D nanostructure fabrication. Most recently, a fully 3D hybrid Monte Carlo-continuum simulation tool has been developed to predict the growth of 3D objects via EBID and an excellent agreement between experiments and simulations has been realized [76]. With this simulation tool, complex 3D nanostructures can be grown in a controlled manner. It has been reported that a magnetic gas precursor ( $\text{Co}_2(\text{CO})_8$ ) was firstly employed to fabricate high aspect-ratio 3D nanowires via EBID, presenting high metallic content, low roughness and functional magnetic properties (Figure 2-3) [77].

More details about the magnetic properties of the EBID-nanostructure have been reviewed by several articles [4, 5, 62, 65], discussing the parameters of fabrication, the magnetic characterization and the important applications.

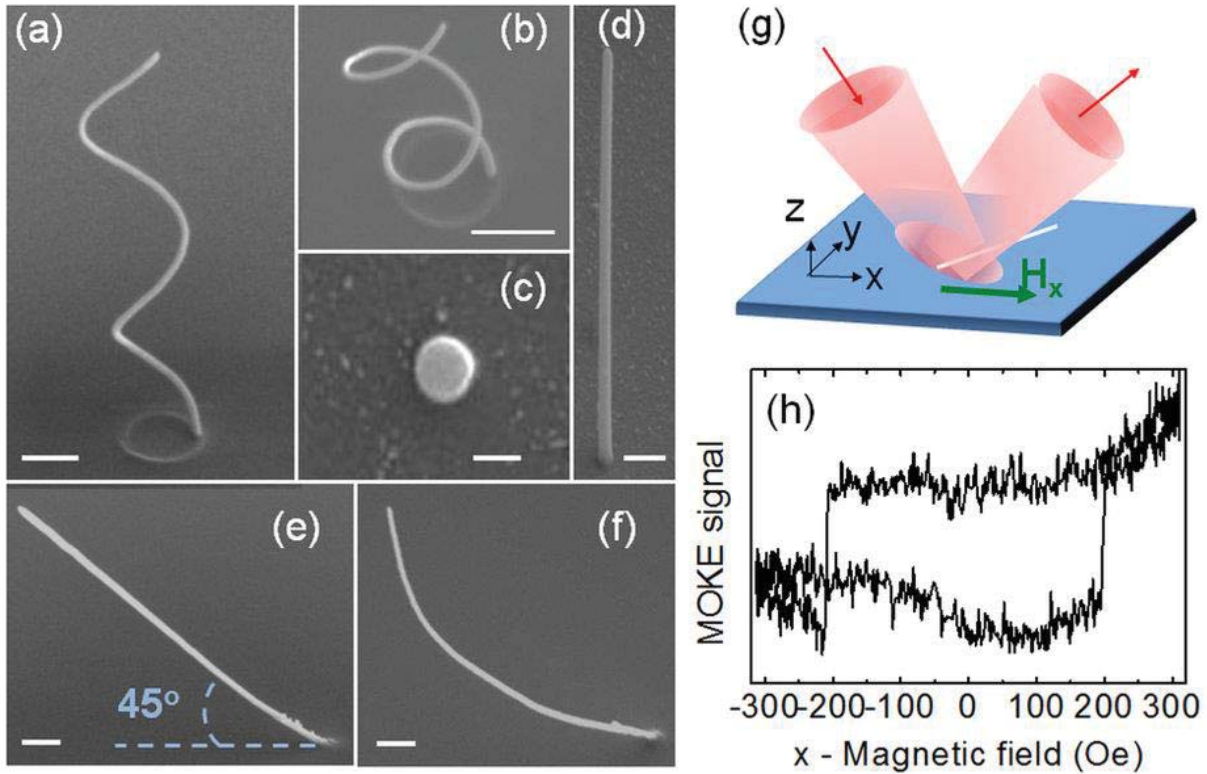


**Figure 2-3:** 3D magnetic Co nanostructures grown by EBID. (a) and (b) are different views of a double-loop nano-spiral. (c) Top-view of a straight nanowire. (d) and (e) are lateral view of nanowire grown at 0 and 45 degrees, respectively, to the substrate plane. (f) Curved nanowire after MOKE measurements. The scale bar is 500 nm in all images, except in (c), where it is 100 nm. (g) Sketch of the experimental configuration used to obtain MOKE hysteresis loops of 3D-nanowires at 45 degrees. (h) MOKE hysteresis loop of a 3D wire. Reprinted from A. Fernández-Pacheco et al [77].

## 2.4 CVD growth of CNTs

Due to the wide range of potential applications in molecular electronics, sensors and energy storage, CNTs have attracted enormous interest in the last decades [78-85]. Many efforts have been made towards producing CNTs with high yield and desired atomic structures [50, 78, 79, 86-89]. One of the most common synthesis method is catalytic chemical vapor deposition (CVD) [78, 80, 81], providing optimum control over the growth conditions and therefore purity and selectivity [32, 50, 90-95]. Mostly used catalysts in CVD are transitional metals, in particular

## 2 Literature review

iron [50, 92, 96], cobalt [97, 98], and nickel [99, 100], which can catalytically grow either single-walled (SWNTs) or multi-walled carbon nanotubes (MWNTs). In the CVD process, transition metals first restructure during a heating procedure, forming catalytically active islands. Then, carbon will dissolve into these islands as the carbon source is provided and CNTs start to grow under specific conditions (i.e., temperature, and gas flux rate) (Figure 2-4).

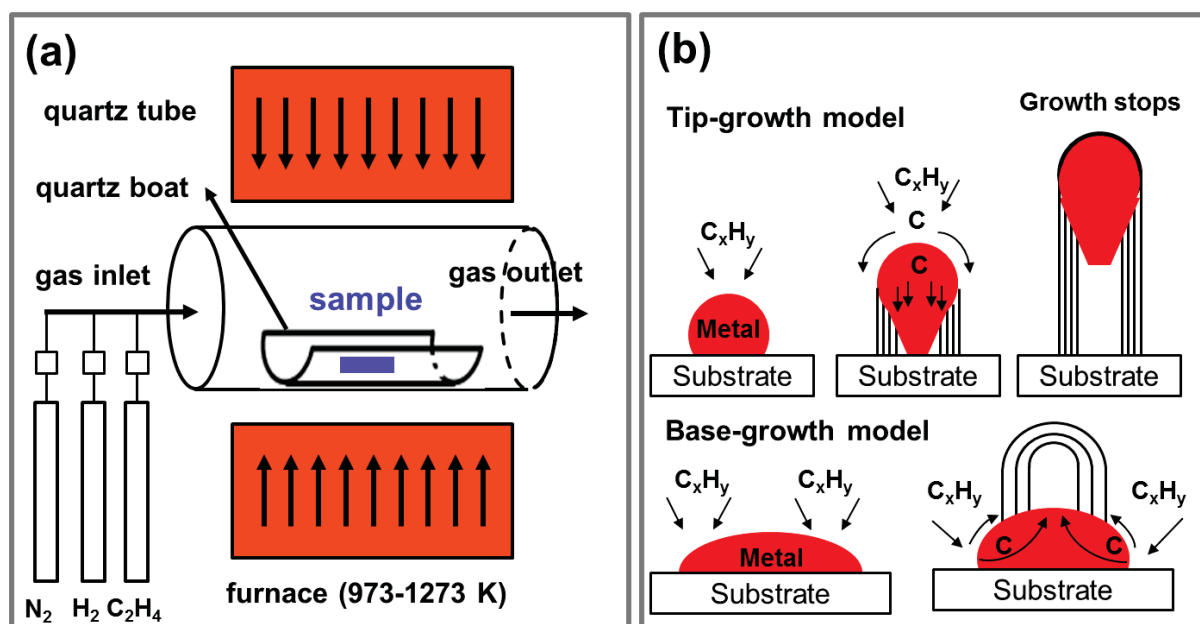


Figure 2-4: (a) Scheme of the catalytic CVD setup. The furnace temperature can range from 973 K to 1273 K, and the sample was placed horizontally on a movable quartz boat inside the quartz tube. The components of the gas source mixture can be controlled independently. (b) Scheme of tip-growth and base-growth mechanism of CNT growth. Reprinted and modified from Y.B. Yan et al [80].

Numerous works have been devoted to understand the growth mechanism of CNT, and two main growth models are discussed (Figure 2-4b) [50, 78, 80, 81, 86-88, 91]. During The CVD process, the metal particles may be rooted either at the tip (tip growth) or at the base of the CNT (base growth) [86]. Bulk diffusion is always related to the former while surface diffusion to the latter. In addition, metal-substrate interactions have influence on the growth model [86, 92, 101]. Usually, a strong metal-substrate interaction will result in the base-growth mechanism.

## 2 Literature review

It has long been recognized that the size and the surface structure of the catalyst influence the catalytic activity [102-108]. There are also many reports about the correlation between the size of the catalyst particles and the diameter of the resulting nanotubes [109-111]. In most cases, a direct correlation between the nanotube outer diameter and the largest diameter of the catalyst particle can be observed. Thereby, it is important to understand the evolution of catalyst particles during CVD process at a certain temperature (673 K~1273 K). Supported metal particles will coarsen either by diffusion of single metal atoms from small particles to large ones (Ostwald ripening) or by the migration and coalescence of whole particles (Smoluchowski ripening) [78, 112, 113]. The former process is driven by the fact that the corresponding vapor pressure varies inversely with particle size. It follows that metal atoms escape more quickly from small particles than from larger ones, resulting in a net flow of matter from the former to the latter [78, 113].

At higher temperatures, metal particles might form carbides when exposed to carbon-bearing molecules. Some metal carbides are reported as catalytic element for CNT growth in CVD [50]. In the case of Fe, it has been found that the main catalyst phase strongly depends on the  $\alpha/\gamma$ -Fe proportion from in situ TEM and XRD data [50]. Metallic Fe is the main active catalyst phase for  $\gamma$ -rich catalyst mixture while  $\text{Fe}_3\text{C}$  was the main catalyst phase in the case of  $\alpha$ -rich catalyst mixtures.

Additionally, metal particles also tend to diffuse into silicon, which is a standard substrate for nanotube growth, forming metal silicides with much lower surface reactivity. For instance, Fe will react with silicon to form silicide at temperature of 1073~1123 K [114, 115]. Oxide (i.e.,  $\text{Al}_2\text{O}_3$  and  $\text{SiO}_2$ ) as diffusion barriers are commonly employed to prevent the silicide forming [116-118]. Many factors determine the efficiency of this diffusion barrier, such as the thickness, structural quality, metal catalyst, and gas phase composition. Mattevi et al. [101] observed that the CNT yield increased almost two orders of magnitude by using  $\text{Al}_2\text{O}_3$  support layer between the Fe and  $\text{SiO}_2$  substrate. It was proposed that Fe nanoparticle mobility was restricted as the interaction of Fe with  $\text{Al}_2\text{O}_3$  is much stronger than with  $\text{SiO}_2$ . This resulted in much narrower Fe catalyst particle size distribution, leading to a higher CNT nucleation density.

### 2.5 X-ray lithography

Lithographic techniques based on the irradiation of materials (or mask) with photons or particles comprise a major class of methods for nanostructure fabrication [119-121]. The most common forms of lithographic nanofabrication operate subtractively, modifying the irradiated material radiochemically such that it can be removed (or removes itself spontaneously), e.g., by wet or dry-chemical processing and development steps. In this respect, X-ray lithography (XRL) employs X-ray beam to irradiate directly on the resist in a controlled manner, causing changes to its chemical properties [120, 121]. Depending on the chemical nature of the resist material, the X-ray exposed areas may cause cross linking (negative resist) or bond breaking (positive resist). The sample then undergoes a development procedure, utilizing the proper solvent [122, 123]. The exposed areas in a positive resist will dissolve, leaving behind unexposed areas. Alternatively, the exposed areas in a negative resist will not be affected while the unexposed areas will dissolve.

Another direct lithographic patterning technique has been reported, using a synchrotron based focused X-ray beam to locally stimulate CVD process on the surface. Metal-organic molecules (i.e.,  $\text{Fe}(\text{CO})_5$ ,  $\text{W}(\text{CO})_6$ , and  $\text{Cr}(\text{CO})_6$ ) have been employed as precursors in such technique, which are also common precursors in EBID [124-126]. This technique was referred to as synchrotron radiation induced chemical vapor deposition (SR-CVD) in 1990s. Various metal and semiconductor thin films with moderate purity have been produced. However, the investigation of energy-selective deposition was not possible due to the broad band second generation synchrotron source. Also the UV portion of the incident light might also contribute to the deposition process. The last and most important is that only large area thin films were deposited at that time.

Most recently, an STXM with 10 nm resolution has been developed [127-130], thanks to the modern fabrication techniques for X-ray optics. Sub-25 nm continuous, reproducible features with arbitrary geometry were created in a direct write (maskless) way, using focused X-ray beam from STXM, analogous to conventional electron beam lithography [122]. There are some potential advantages of using focused X-ray beams in direct write nanofabrication, including minimal scattering, less or no sample charging effects, and ability of chemically selective patterning by tuning energy related to the specimen composition.

## 3 Techniques

The following sections will give a brief introduction to the applied experimental techniques. The main instrument applied in the frame work of this thesis is focused electron beam for nanostructure fabrication and SEM characterization. Local Auger spectroscopy and scanning Auger microscopy was performed to analyze the chemical composition of nanostructures or the surface. Atomic level investigation of the surface was realized by STM, for example, characterization of the thin film MgO prepared on Ag(100). Investigations of the magnetic properties of metallic iron nanostructures were carried out in a synchrotron based STXM. Finally, other standard surface science techniques such as LEED, QMS, QCM, and PVD will be described shortly.

### 3.1 Scanning electron microscopy

In a scanning electron microscopy, a focused electron beam is used instead of visible light to provide improved magnification and depth of sharpness compared to a (conventional) optical microscopy. The focused electron beam is scanning over a surface pixel by pixel. Interaction of the incident electron beam with the sample results in emitted electrons, which can be utilized for image formation. In addition to that, it is possible to obtain chemical information by using specialized X-ray and electron energy analyzers. A detailed introduction to SEM including the physics of image formation and microanalysis can be found in reference [131].

Figure 3-1 depicts the interaction volume of the PE beam with the specimen. This interaction volume is defined as the volume of elastic and inelastic scattering of the primary electrons. Different signals can be used for image formation or chemical analysis of the specimen. Auger electrons are generated during the relaxation of inner shell electron vacancies caused by incident PEs. The hole is filled by an electron, while the gained energy is transferred to another electron, which is emitted as an Auger electron. SEs are defined as electrons having an energy ranging from 0 to 50 eV with the majority having energy of 2 to 5 eV [131]. Due to their low energy and therefore limited mean free path, they are only emitted from the top surface layer of the specimen with a mean escape depth of  $\sim 1-20$  nm. BSEs are inelastically scattered PEs and therefore exhibit a broad energy spectrum between 50 eV and the PE energy, with a maximum at  $\sim 3/4$  of the PE energy. The diameter of the BSE exit area and the depth depends on the PE

### 3 Techniques

energy and sample properties such as density and mean atomic number, and can be in the  $\mu\text{m}$  range. Besides the described generation of different types of electrons, also characteristic and continuous X-rays are generated. The characteristic X-rays are the complementary process to the generation of Auger electrons, as instead of emitting electrons, energy is released as photons. The characteristic X-rays are specific as Auger see above for the element in the specimen and is utilized for chemical analysis. As X-rays have a higher mean free path compared to electrons, chemical analysis using characteristic X-rays is more bulk sensitive compared to Auger electrons. In the case of K shell electrons, for lower atomic number elements ( $Z < 20$ ), the emission of Auger electrons is dominant, while the mission of characteristic X-rays is more pronounced at higher atomic numbers.

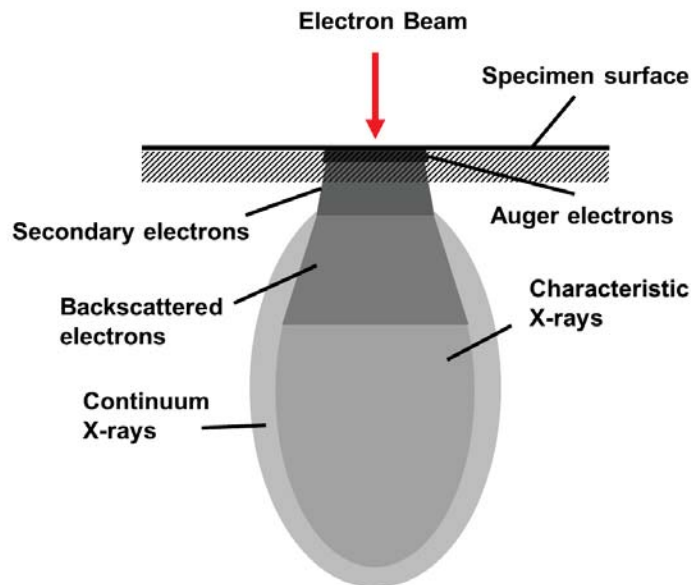


**Figure 3-1:** Schematic drawing of the teardrop-shaped interaction volume of the primary electrons with the specimen. A variety of different signals are generated and the typical relative escape depths are indicated.

The most common imaging mode in SEM is detection of SEs emitted from atoms excited by the PEs. The yield of SEs ( $\delta$ ) depends on many factors. At normal incidence of the PEs, the emission of SEs with respect to the surface normal follows the Lambert law (Equation (3-1)), with  $\xi$  being the emission angle relative to the surface normal and  $d\Omega$  being the respective solid angle [131]. The yield of SEs increases with energy of PEs, with a peak around a PE energy of

### 3 Techniques

several 100 eV. After this maximum the yield of SEs decreases. Generally, the yield increases with increasing atomic number  $Z$  of the specimen.

$$\frac{d\delta}{d\Omega} = \frac{\delta}{\pi} \cos(\xi) \quad (3-1)$$

The emission of the BSEs is analogous to the SEs and follows for normal incidence the Lambert law (Equation (3-1)). In general, the BSE yield increases with increasing energy of the PE. However, at energies higher than 10 kV the BSE yield is approximately constant. The yield also increases with increasing atomic number  $Z$  of the specimen.

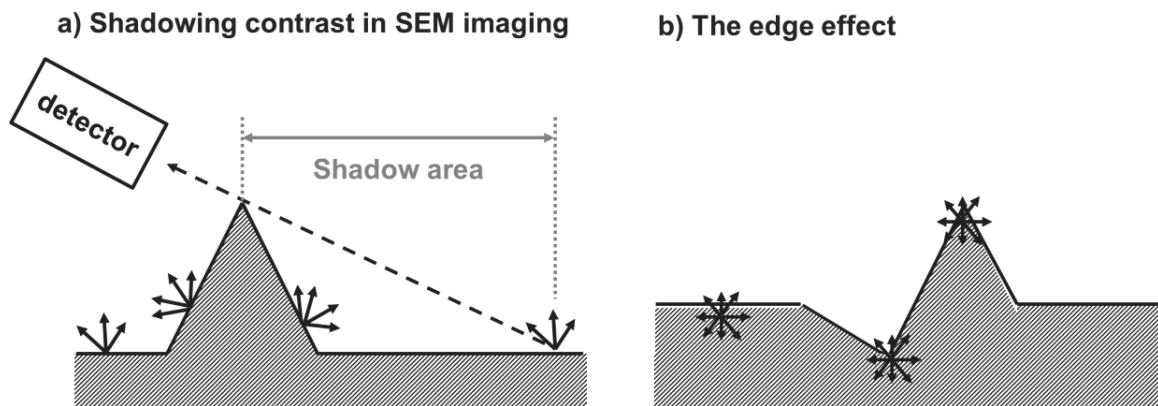


**Figure 3-2:** Schematic drawing of contributions to the topographic contrasts. (a) Shadowing contrast. Arrows indicate the electrons emitted from surface. (b) Edge effect. Edges appear brighter than surface sites which are surrounded by material.

There are many different contrast mechanisms for imaging in SEM, which depend on various parameters such as the detected signal, the applied primary electron energy, the tilting of the specimen, collected angular range and the detector configuration [131]. Two basic contrast mechanisms shall be described: topographic contrast and material based contrast. In the topographic contrast, a three-dimensional impression of the surface topography is formed in SEM and many points contribute to this effect: (i) surface-tilt contrast, (ii) shadowing contrast, (iii) edge effect, (iv) surface roughness contrast. It is obvious that the smaller the angle between the surface and the PE beam, the closer the interaction volume of the PE is to the surface, thus more SEs and BSEs are emitted, resulting in brighter contrast. The shadowing contrast is based on the position of the detector. The areas of the objects which are not directed toward the

### 3 Techniques

detector appear darker, while areas which are facing the detector appear brighter (Figure 3-2a). It is apparent that the emission signals from the edges are more intense than from other parts (Figure 3-2b), as less electrons are reabsorbed by surrounding material. The roughness contrast is a mixture of the contrast mechanisms mentioned above. Micro-rough surfaces appear brighter than flat surfaces of the same material.

The material based contrast depends on the physical and chemical properties of the investigated specimen, i.e., mean atomic number, crystal orientations, and electric potentials of the surface. As the number of emitted SEs also depends on the number of BSEs produced in the interaction volume, the material based contrast can also be detected with an SE detector.

### 3.2 Auger electron spectroscopy

Auger electron spectroscopy is one powerful technique in surface science for qualitative and quantitative chemical analysis. The basic mechanism behind AES is the Auger electron emission process which is depicted in Figure 3-3. Under an incident irradiation (electrons, photons or ions), a core hole (here in the  $K$  shell) is created and the atom becomes an ion, which is in an excited state and will relax back to the ground state. An electron from a higher level (e.g.,  $L_{2,3}$  level) drops down and fills the hole. The released energy during this process can be transferred to another electron (e.g., the same level  $L_{2,3}$ ), which is then ejected from the atom as an Auger electron. Alternatively, this energy can also be released as photons, i.e. X-ray fluorescence. The kinetic energy of the ejected electron depends only on the binding energies of the three involved electrons and is independent of the energy of the primary beam which would have sufficient energy for the initial ionization of the atom. The Auger electron emission process is always a three-electron process and the case presented above can be denoted as  $KL_{2,3}L_{2,3}$  Auger process (Figure 3-3). It is common to omit the subscripts when referring to the group of Auger emissions involving the same principle quantum numbers and  $KL_{2,3}L_{2,3}$  can be shorted as  $KLL$ .

The kinetic energy of a  $KL_{2,3}L_{2,3}$  Auger electron is approximately equal to the difference between the energy of the core hole ( $K$  level) and the energy levels of the two respective outer shell electrons ( $L_{2,3}$ ):

$$E_{KL_{2,3}L_{2,3}} \approx E_K - E_{L_{2,3}} - E_{L_{2,3}} \quad (3-2)$$

### 3 Techniques

This model is too simple as it does not account for the interaction energies between the core holes ( $K$  and  $L_{2,3}$ ) nor the relaxation energies resulted from the core screening. It is complex to calculate the real Auger electro energy and some empirical approximation methods can be applied according to references [132, 133].

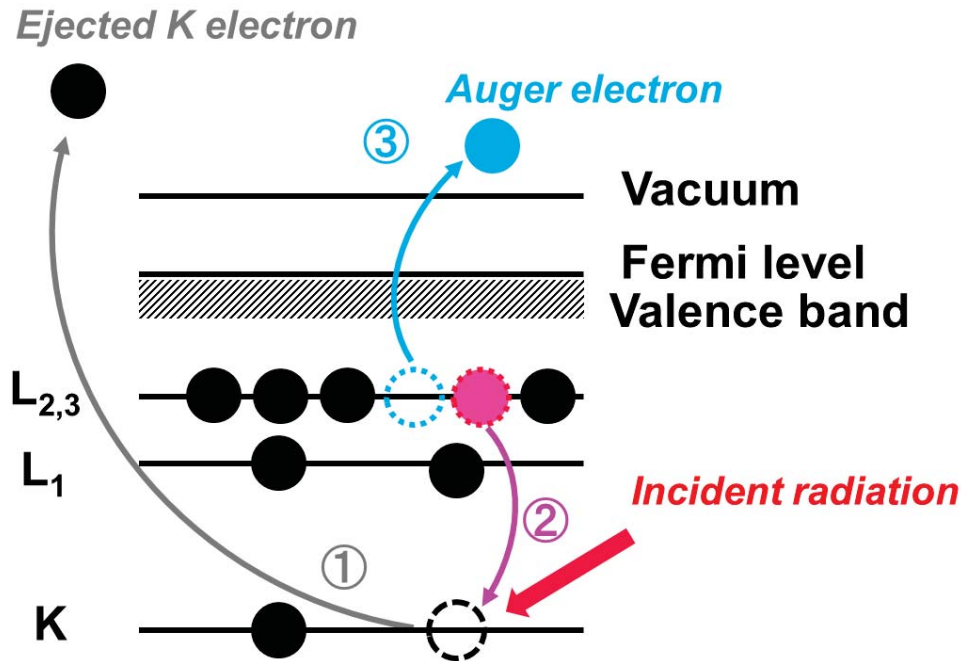


**Figure 3-3:** Schematic description of the Auger process. 1: A  $K$ -shell electron is ejected by the incident radiation, creating a vacancy. 2: An electron from an outer shell ( $L_{2,3}$ ) falls down to fill the hole, releasing energy. 3: The released energy is transferred to another electron ( $L_{2,3}$ ), which is then emitted as the Auger electron.

The inelastic mean free path (IMFP) of Auger electrons is in the range of 1~3 nm, depending on the kinetic energy of the electrons and the materials of the specimen. As more than 95 percent of the measured Auger signal originate from a depth less than 3 times the IMFP, AES is a surface sensitive characterization technique. In addition to obtaining chemical information of the specimen, one can also estimate the thickness of a possible overlayer. An “attenuation length” (AL) concept was suggested as “a value resulting from overlayer-film experiments on the basis of a model in which elastic electron scattering is assumed to be insignificant” [134]. With this the thickness of the deposited layer can be quantified by equations as following:

### 3 Techniques

$$I = I_0 \cdot \exp\left[-\frac{d}{\lambda_{AL} \cdot \cos \theta}\right] \quad (3-3)$$

$$\lambda_{AL} = 0.316a^{3/2} \left\{ \frac{E}{Z^{0.45}[\ln(E/27)+3]} + 4 \right\} \quad (3-4)$$

$$a = 10^8 \left( \frac{\mu}{\rho N_{Av}} \right)^{1/3} \quad (3-5)$$

Where  $I_0$  is the intensity of a clean substrate,  $I$  is the intensity of the substrate with the overlayer,  $\lambda_{AL}$  is the attenuation length which can be calculated via Equation (3-4),  $Z$  is the mean atomic number of the matrix,  $E$  is the energy of the emitted Auger electron,  $a$  is the overlayer lattice parameter which can be estimated via Equation (3-5),  $N_{Av}$  is the Avogadro constant ( $6.02 \times 10^{23} \text{ mol}^{-1}$ ),  $\mu$  is the average atomic mass of the matrix (in g), and  $\rho$  is the density of the matrix (in  $\text{kg/m}^3$ ).

### 3.3 Scanning tunneling microscopy (STM)

STM enables visualization of individual atoms in real space. In STM, a probe tip, usually made from tungsten or a platinum/iridium alloy, is attached to a piezo element which can be driven in all three directions (x, y and z). As the tip and the sample are brought to a distance of a few Å to each other, the quantum mechanics electron wave functions of tip and sample can overlap. Usually, a bias voltage is applied between the tip and the sample, and the electrical tunneling current flows either from the tip to the surface or vice versa, depending on the polarity.

The principle of the STM is based on the current mentioned above, which tunnels through a potential barrier between the tip and the surface. To simplify, this tunneling phenomenon can be illustrated as a particle in a one-dimensional box. The potential barrier is  $V_0$  and the total energy of the particle is smaller than the energy barrier. With classical mechanics, such particles approaching the potential barrier would be totally reflected as the energy is not sufficient to pass the barrier. However, according to quantum mechanics, there is a certain probability that the particle can tunnel through the barrier  $V_0$ . Based on a simplified, one-dimensional picture, the Schrödinger equation for an electron with energy smaller than barrier ( $V_0$ ) can be described as:

$$E\varphi(x) = \left[ \left( -\frac{\hbar^2}{2m} \right) \left( \frac{\partial}{\partial x} \right)^2 + V(x) \right] \varphi(x) \quad (3-6)$$

### 3 Techniques

with total energy of the electron  $E$ , the electron wave function  $\varphi(x)$ ,  $\hbar = \frac{h}{2\pi}$  and Planck's constant  $h$  as well as the mass of the electron  $m$ . Additional calculations can be found in references [135, 136] and the transmission coefficient  $T$  as the probability to penetrate the barrier is given in Equation (3-7). It is obvious that  $T$  is larger than zero even for electrons with  $E < V_0$ .

$$T \sim e^{-\frac{2d}{\hbar}\sqrt{2m(V_0-E)}} \quad (3-7)$$

The tunneling current  $I_T$  is directly proportional to the local density of states in the sample within the interval between the Fermi level  $E_F$  and  $E_F - eU_T$ , with the bias voltage  $U_T$ . It can be approximated by Equation (3-8), where  $\phi$  is the effective work function, which can be approximated as the mean work function of tip and sample. The tunneling current is thus decreasing exponentially with increasing distance between the sample and tip  $d$  as well as proportional to the bias voltage  $U_T$ .

$$I_T \sim U_T \cdot e^{-\frac{2d}{\hbar}\sqrt{2m\phi}} \quad (3-8)$$

STM can provide sub-nanometer lateral resolution, depending on the tip shape and electronic structure of the tip and the sample. From Equation (3-8), the tunneling current depends exponentially on the distance between the tip and the surface. Thereby, STM can achieve high resolution in the order of down to subatomic regime [137]. The STM can be used not only in UHV but also in air, water, and various other liquid or gas ambient, and at temperature ranging from a few K to hundred K above room temperature [135, 137]. For further discussion of the applications and other related STM techniques, interested readers are recommended to various sources, including books [135-137] and references [138-143].

### 3.4 Transmission electron microscopy (TEM)

TEM uses high energy electrons which are transmitted through a specimen to achieve a high resolution image. According to the de Broglie equation, the wavelength of electrons  $\lambda$  is related to the energy by

$$\lambda = \frac{h}{mv} = \frac{h}{\sqrt{2m_0eV(1+eV/2m_0c^2)}} \quad (3-9)$$

### 3 Techniques

where  $m_0$  is the stationary mass of electron,  $h$  is the Planck constant,  $c$  is the speed of the light and  $e$  is the electron charge. In this equation, the relativistic effect is considered as the speed of the electrons reaches 50~99% of the speed of light when acceleration voltages above 100 kV are applied. With this, it can be seen that in TEM, sub-picometer resolution is achieved with acceleration voltages of 100 kV following the classic Rayleigh criterion [144, 145]. However, it is not only the electron wavelength that restricts resolution, but also the lens aberrations, mainly spherical and chromatic aberration, as can be found discussed in more detail in various references [146-149].

A TEM consists of an electron emission source, electromagnetic lenses and an electron detector. The electron beam is produced, accelerated and then transmitted through a very thin specimen. There are two types of TEM used in this work: HRTEM and STEM. The setup of HRTEM and STEM is quite similar, but with different working principle. In HRTEM, the object lens is below the specimen and focuses the diffracted beam after the specimen, determining the final image/diffraction pattern. In STEM, electron beam is focused by a set of condenser lenses and the objective lens. Then the focused electron beam scans over the specimen and image is formed by collecting the transmitted signal. Atomic number contrast (Z-contrast) can be obtained by using a STEM and a high-angle annular detector.

Electron beams that interacted with very thin specimen, generated various signals which can be detected, such as direct transmitted electron beam. EDX spectra can be obtained from very small regions (few nm) of the specimen by detecting the characteristic X-rays, while EELS can provide elemental identification and even additional information about electronic structure or chemical bonds [150-152].

In TEM, electrons do not simply transmit through the specimen, but scatter mostly in the forward direction. This scattering leads to electron diffraction, which is a powerful technique in TEM and is frequently used to study the crystal structure of a solid [144, 153-155]. If the probed area is of macroscopic size, diffraction patterns of nanoparticles form a ring pattern as the nanoparticles are oriented isotropically in all directions. If a smaller area is selected (i.e. nanometer regime) by reducing the aperture size, diffraction patterns of nanoparticles tend to form a spot pattern with discrete spots arranged on rings.

### 3 Techniques

According to the Bragg diffraction, electron waves are diffracted from two atomic planes with a spacing  $d$  and a diffraction angle  $\theta_B$  (Bragg-angle). The total path difference between these waves is  $2d \sin\theta_B$  and the condition of constructive interference leads to Bragg's law:

$$n\lambda = 2d\sin\theta_B \quad (3-10)$$

with  $n$  being integer values. The small size of nanoparticles results in a broadening of the diffraction rings (size effect). This effect can be used to evaluate the mean nanoparticle size from selected area diffraction patterns by applying the Scherrer equation:

$$\Delta(2\theta) = \frac{K\lambda}{L\cos(\theta_B)} \quad (3-11)$$

Where  $K$  is the shape factor (0.89 for spheres and 0.94 for cubes),  $L$  is the nanoparticle size,  $\theta_B$  is the Bragg angle (in radians) which can be obtained from Equation (3-10), and  $\Delta(2\theta)$  is the broadening of the diffraction ring at FWHM (in radians).

### 3.5 Scanning transmission X-ray microscopy (STXM)

The term STXM is usually used for microscopes working in the soft X-ray range [156]. A thin specimen is raster-scanned across a focused X-ray beam. The transmitted X-ray intensity is recorded as a function of the sample position, generating microscopic images of the specimen. This technique falls into the category of "spectromicroscopy" as X-ray absorption spectra (XAS) can be obtained from microscopic features on the scanned sample, providing chemical information [157]. With the development of Fresnel zone plate, the best spatial resolution in STXM is currently 10 nm [129, 130].

XAS is a powerful method to characterize chemical states, especially of light elements like C, N, and O [158]. The near-edge structures of XAS spectra are often characteristic of specific chemical compounds and the total absorption above the edge provides quantitative information about the abundance of the element [156, 158]. The intensity of the transmitted X-ray flux can be expressed as:

$$I = I_0 \exp(-\sum(\mu_i \rho_i d_i)) \quad (3-12)$$

where  $I_0$  is the initial flux,  $\mu_i$  is the mass absorption coefficient,  $\rho_i$  is the density and  $d_i$  is the thickness for element  $i$ .

### 3 Techniques

STXM finds application not only to chemical and biological science, but also in the investigation of magnetisation dynamics in thin film magnetic nanostructures [159-161]. The X-ray magnetic circular dichroism (XMCD) absorption contrast is obtained from the difference spectrum of two X-ray absorption spectra taken in a magnetic field with different circularly polarized light (positive and negative, respectively). This contrast is employed in STXM to observe the magnetic domains. A time resolution of  $\sim 30 - 100$  ps can be also achieved in STXM depending on the width of the electron bunches in the synchrotron storage ring [156, 162].

#### 3.6 Other techniques

Besides the various microscopic techniques used, some standard UHV and surface science techniques have been employed within this work. There will be only brief descriptions of these techniques to understand the results in following chapters.

**LEED** is one of the most powerful techniques available for surface structure analysis. In LEED, a beam of low energy electrons illuminate the surface, and then diffracts in numerous directions depending on the surface crystallography. Diffracted electrons can be observed as spots on a fluorescent screen. This technique gives direct information about the symmetry, spacing of atoms, and dimensions of the unit cells in a surface [163, 164]. Investigation of the long-range order of self-assembled organic molecules on the surface is also possible, such as tetraphenylporphyrin (2HTPP) on  $\text{TiO}_2(100)$  [165]. In the work at hand, the fingerprint LEED patterns are sufficient for determining the quality of desired surface.

**QMS** can be found in most UHV systems, with the ability to analyze the residual gas within the vacuum chamber. Generally, molecules are ionized by low energetic electrons (typically 70~100 eV), and then accelerated by a voltage toward a quadrupole mass filter. This filter enables only ionic fragments with a specific mass-to-charge ratio ( $m/z$ ) to pass. At the end of the filter, the ions can be detected by a Faraday cup or a secondary electron multiplier [166-168]. In this thesis, QMS was applied to analyze the composition of the residual gas, the purity of applied precursor molecules in all experiments, and the purity of the gas for surface preparation (e.g., Ar,  $\text{O}_2$  and  $\text{H}_2$ ).

### 3 Techniques

**QCM** relies on the measuring the mass variation per unit area by the measuring the change in frequency of a quartz crystal, based on the Sauerbrey equation [169]:

$$\Delta f = -C_f \cdot \Delta m \quad (3-13)$$

where  $\Delta f$  is the observed frequency change in Hz,  $\Delta m$  is the change in mass per unit area ( $\text{g}/\text{cm}^2$ ) and  $C_f$  is the sensitivity factor of the crystal. QCM is especially useful for monitoring the rate of deposition of thin films under vacuum condition. It has also been used to measure the amount of deposited organic molecules. In this work, QCM was employed to monitor the deposition rate of MgO on Ag(100), and the recorded value was compared with the one evaluated via AES.



# 4 Experimental details

Nanostructure fabrication in the work at hand (except for the secondary CNT growth) was performed in a UHV instrument (Multiscan Lab, Scienta Omicron GmbH, Germany). This UHV system consists of two main chambers: preparation chamber and analysis chamber, operating at the base pressure in the range of  $10^{-10}$  mbar. The whole vacuum system, including the equipment for sample preparation, surface science analysis tools, and other functional attachments such as a self-constructed gas dosing system, has been described in detail previously [166, 167, 170]. Therefore, only a short overview of the instrument is given in Chapter 4.1.

In Chapter 4.2, the various sample holders are introduced, which were used to performing different types of sample preparation and characterization. The applied materials including precursor gases, reactive gases and substrates will be presented in Chapter 4.3. Finally, the experimental details, data acquisition and the data processing will be described in Chapter 4.4, including nanofabrication in the UHV system and further characterization either in-situ (AES) or ex-situ (TEM, PolLux-STXM), as well as the novel nanofabrication technique FXBID with a scheme of the corresponding self-made gas supply system, and secondary carbon nanostructure growth via CVD experiments.

## 4.1 The UHV instrument

### 4.1.1 The preparation chamber

Sample preparation and analysis of reactive gases was performed in the preparation chamber. UHV conditions are achieved by an integrated pump system (rotary vane pump, turbomolecular pump, ion getter pump and titanium sublimation pump). A fast entry lock chamber is separated by a manual gate valve from the preparation chamber for sample transfer between ambient without breaking UHV conditions. Figure 4-1 depicts photographs of the chamber and the main components.

A manipulator provides the ability to heat (depending on the sample holders) and cool the sample (by liquid nitrogen), transform the sample inside the chamber to different functional attachments (LEED characterization, metal evaporation and surface preparation by sputtering and annealing). The transfer arm enables transformation of samples from the fast entry lock

## 4 Experimental details

chamber to the manipulator and also from the preparation chamber to the analysis chamber. Attached are the following instruments:

- Sputter gun (Scienta Omicron GmbH, ISE 10)
- Quartz microbalance (Syscon, OSC-100A)
- Electron evaporator (Focus, EFM 3i)
- Self-constructed Knudsen cell evaporator for organic compounds
- Quadrupole mass spectrometer (Pfeiffer Vacuum, Prisma QMS/QMA200)
- Retractable LEED system (Scienta Omicron GmbH, SPECTALEED)

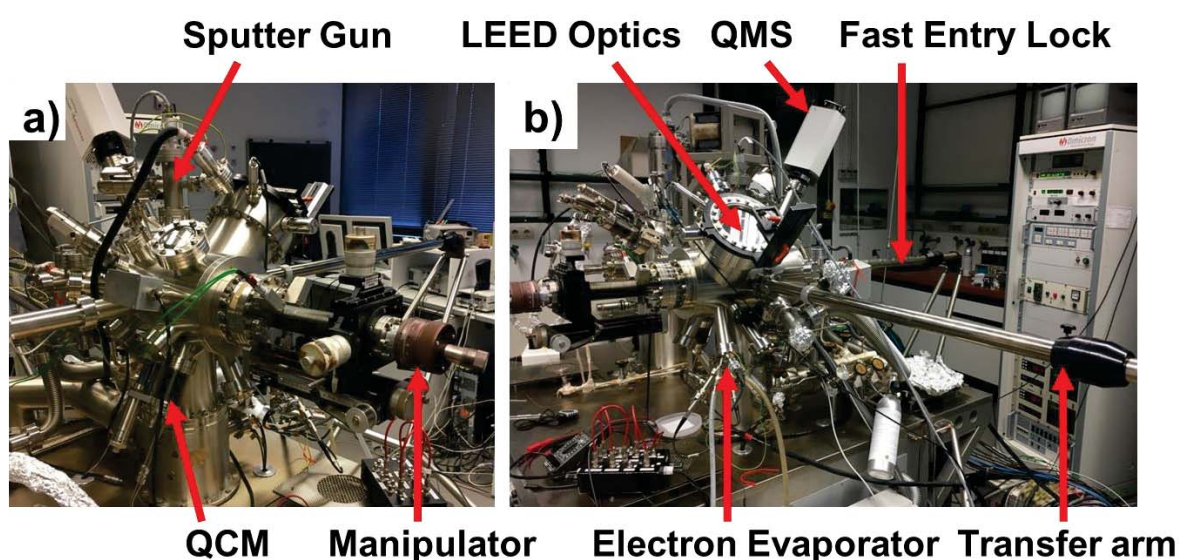


*Figure 4-1: Photographs of the preparation chamber of the UHV instrument with the most important attachments indicated.*

### 4.1.2 The analysis chamber

Surface science analysis tools used for nanostructure fabrication and characterization are located in the analysis chamber, in which UHV conditions are maintained by an integrated pump system, just as in the preparation chamber. A photograph of the analysis chamber is depicted in Figure 4-2, with the indicated attachments, including the sample stage.

## 4 Experimental details

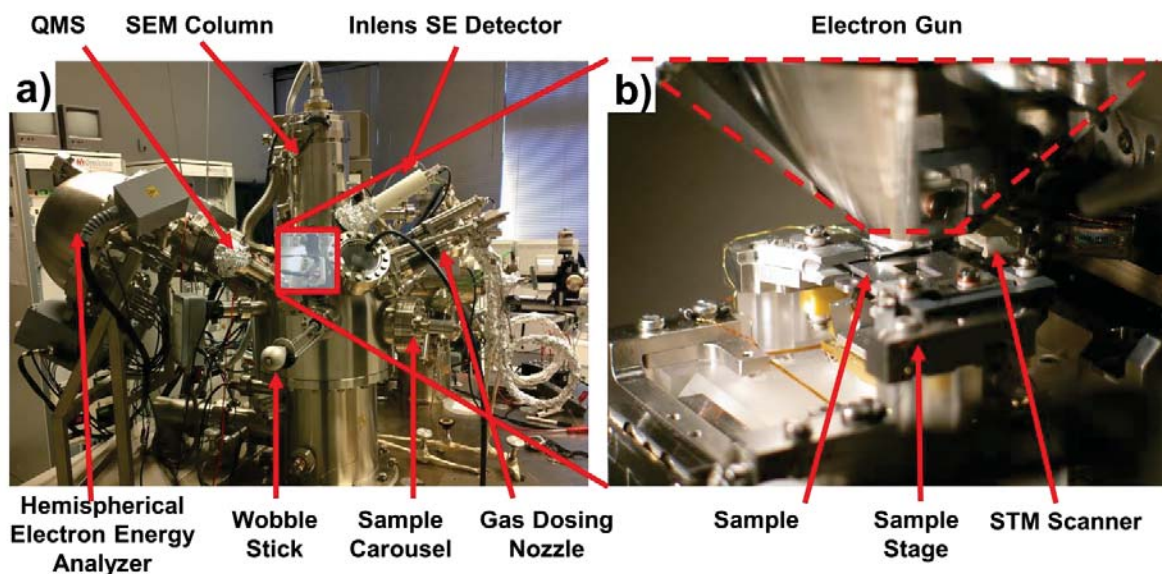


**Figure 4-2:** (a) Photograph of the analysis chamber of the applied UHV instrument with the attached components labeled correspondingly. (b) Overview of the sample stage of the analysis chamber. The STM scanner is positioned between the electron gun and the sample, with the ability to investigate the desired surface on atomic level resolution guided by SEM.

The linear transfer arm (Figure 4-1b) can transform the sample from the preparation chamber onto the sample carousel (Figure 4-2a). There are two identical floors which are each capable of storing up to six samples and/or tip holders. A wobble stick is employed for translation between the carousel and the sample stage.

One main component of the analysis chamber is the UHV SEM column (Zeiss, UHV Gemini), working as the electron source for SEM, AES and lithography. The ultimate resolution is below 3 nm at a beam energy of 15 keV and a beam current of 400 pA, evaluated according to the 20/80 criteria on a gold coated mica sample. A higher beam current is usually required for AES and SAM in order to reduce the noise to signal ratio. The resolution is correspondingly lowered to below 6 nm at 15 kV and a beam current of 3 nA [166, 167, 170].

Figure 4-3 presents the schematic diagram of the UHV Gemini column setup. The beam generator is a Schottky field emitter, consisting of a finely etched <100> oriented tungsten crystal tip with a sintered reservoir of zirconium oxide (ZrO) in the shank. The use of ZrO reduces the work function from 4.6 eV to 2.48 eV [171]. A suppressor is used for controlling the

## 4 Experimental details

emission at the position of the tip axes, leading to more defined energy distribution of the electron beam. The emitted electrons are then accelerated by the anode. The applied acceleration voltage is typically in the range of 0.1~30 kV [171].

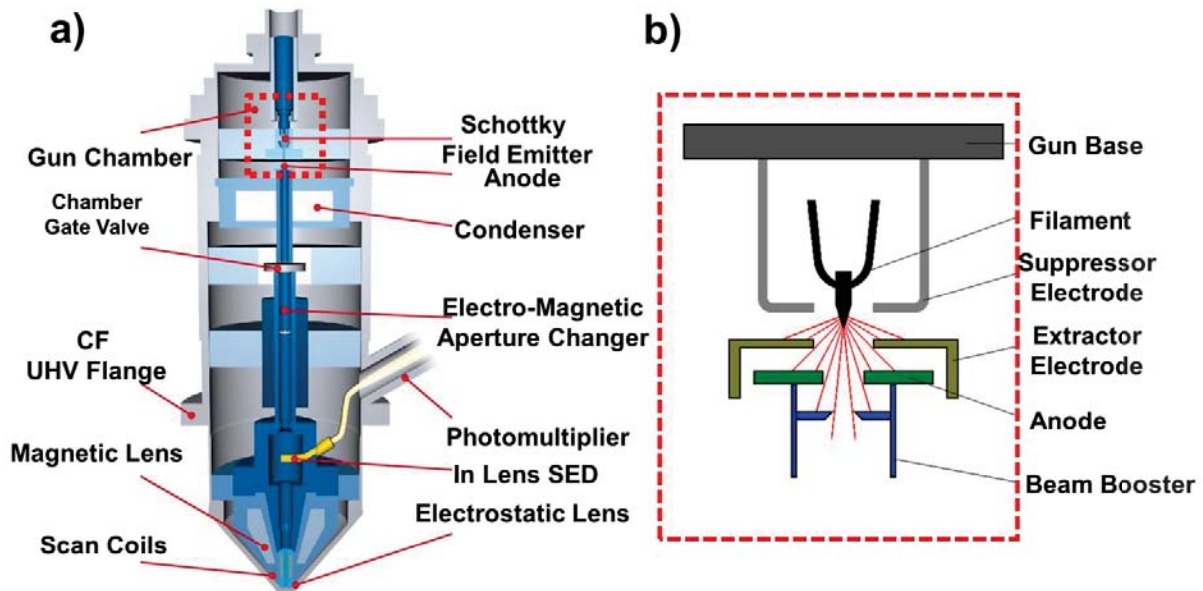


**Figure 4-3:** Scheme of the UHV Gemini column setup. (a) Overview of the inner part of the column. (b) Schottky field emitter electron gun. Adapted from references [172] and [171].

After the electrons are accelerated, the beam booster adds 8 keV to the energy of the electrons before they pass through the lens system. With this, aberrations are reduced, especially for electrons with low energies. The deceleration to the original energy before electrons hit on the sample is realized by a retarding field.

The sample stage can be rotated up to  $25^\circ$  into the direction of the hemispherical electron energy analyzer (Scienta Omicron GmbH, NanoSAM EA U7 analyzer), when chemical composition analysis is performed via AES or SAM. The composition of the residual gases can be monitored by a QMS (Pfeiffer Vacuum, Prisma QMS200) attached to the analysis chamber. An STM scanner can be positioned in between the SEM electron gun and the sample, enabling positional control of the STM tip in-situ by SEM.

## 4 Experimental details

A gas injection system is necessary for dosing metal-organic molecules as precursor during EBID experiments. Two separate gas lines are connected to the UHV analysis chamber with a linear translator which can approach the dosing nozzle to the sample surface (Figure 4-4). Two separate leak dosage valves (VG, LVM940) control the gas flow into the analysis chamber. A detailed description of the self-constructed gas injection system is given in the PhD theses of Thomas Lukasczyk and Michael Schirmer [166, 167].

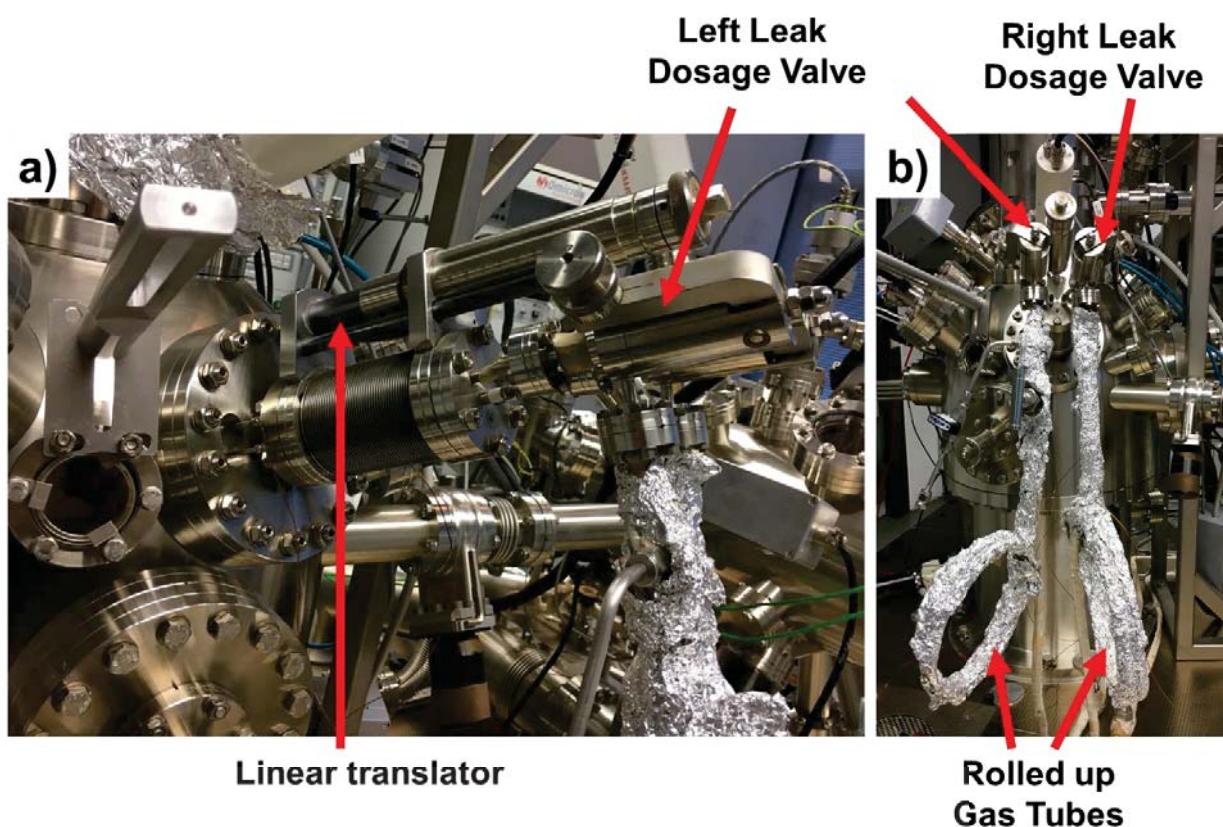


*Figure 4-4: Photographs of the gas dosage system. (a) side view, (b) front view.*

### 4.2 Sample holders

Various sample holders were used for transferring and heating samples in the instrument, depending on the type and geometry of the sample. They can be categorized into two different setups: the standard sample plate and the variable temperature (VT) sample holder. In the work

## 4 Experimental details

at hand, two sample holders were used, as shown in Figure 4-5. More details about the construction of the sample holders can be found in reference [167] and [170].

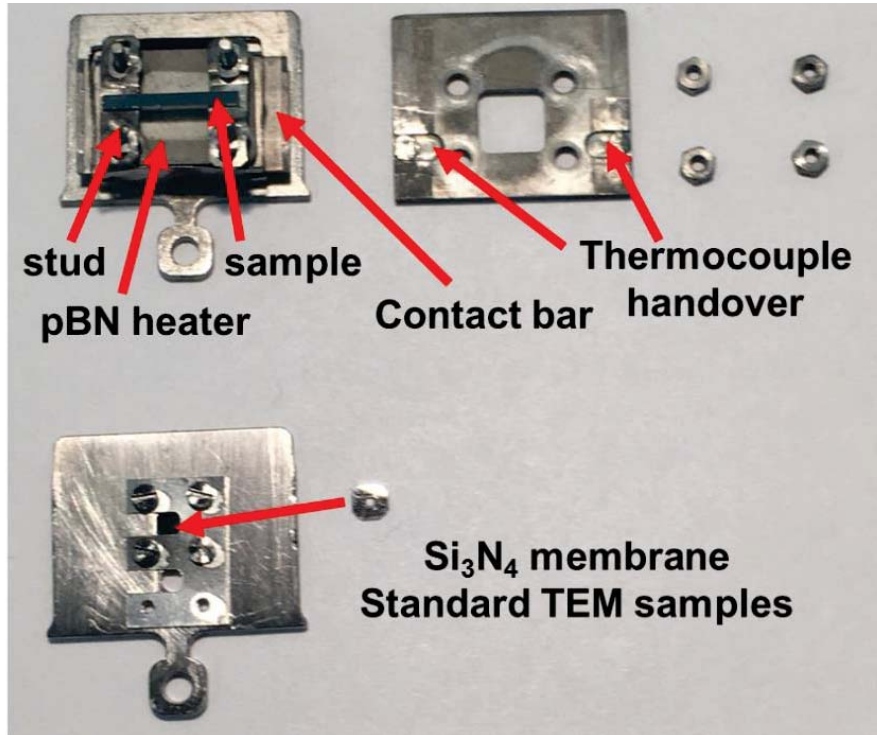


**Figure 4-5:** Setups of sample holders used in this thesis. The upper one is the top view of a VT sample holder. The lower one is a standard sample plate with windows used for mounting standard 3 mm TEM samples, e.g., Si<sub>3</sub>N<sub>4</sub> membrane.

The VT sample holder consists of a molybdenum base plate and a tungsten coated ceramic plate with a window at the top (Figure 4-4 upper). These two plates are connected with 4 molybdenum studs. Two contact bars realize the electrical contacts for heating the sample. Two thermocouple handover contacts on the top plate enable the temperature readout. Three heating techniques can be employed: direct current heating, radiative heating via a pyrolytic boron nitride (pBN) heater and electron bombardment heating by a specially modified sample holder with an integrated filament. Here, the pBN heater is used for surface preparation and thin oxide film growth, while the standard sample plate was employed for experiments on Si<sub>3</sub>N<sub>4</sub> membranes, which were used without further treatment.

### 4.3 Ingredients

#### 4.3.1 The precursors

Three metal-organic molecular precursors for fabricating nanostructures were used in this work. Iron pentacarbonyl ( $\text{Fe}(\text{CO})_5$ ) was purchased as a liquid from ACROS Organics with a specified purity of 99.5 %. The quality of the precursor gas was monitored via QMS in a dedicated gas analysis chamber with base pressure  $\sim 2 \times 10^{-9}$  mbar. The peak intensity ratios between Fe ( $m/z = 56$ ) and CO ( $m/z = 28$ ) was monitored and it is found that a ratio of at least 0.05 was necessary for successful nanofabrication experiments with subsequent autocatalytic growth. Color changes of the liquid precursor from dark red to green also indicate degradation of the precursor.

Cobalt tricarbonyl nitrosyl ( $\text{Co}(\text{CO})_3\text{NO}$ ) was purchased from abcr GmbH & Co. KG. It is similar to  $\text{Fe}(\text{CO})_5$  in that the intensity peak ratio between cobalt ( $m/z = 58$ ) and CO ( $m/z = 28$ ) acts as a good indicator for the quality of the precursor gas. This value was commonly observed to be above 0.15 and autocatalytic growth in EBID experiments was always observed. Characterization of both precursors via QMS and further discussion of the mentioned fragments can be found in references [166, 167, 170].

Methylcyclopentadienyl manganese tricarbonyl ( $\text{MeCpMn}(\text{CO})_3$ ) was purchased from abcr GmbH & Co. KG, with a specified purity of 97 %. Unlike the aforementioned precursors,  $\text{MeCpMn}(\text{CO})_3$  is a solid at RT with sufficient vapor pressure for EBID experiments. Figure 4-6 presents a reference of the mass spectrum of this compound with the probable fragments indicated.

All precursors were purified by evacuating the precursor container after installing it to the gas dosing system. Before each experiment, some cleaning cycles were performed in order to remove the residual gas inside the gas dosing tubes. The gas dosage system was repeatedly purged with gas from the precursor container and then evacuated via a turbo molecular pump. The gas quality was then evaluated by the QMS inside the gas dosing chamber.

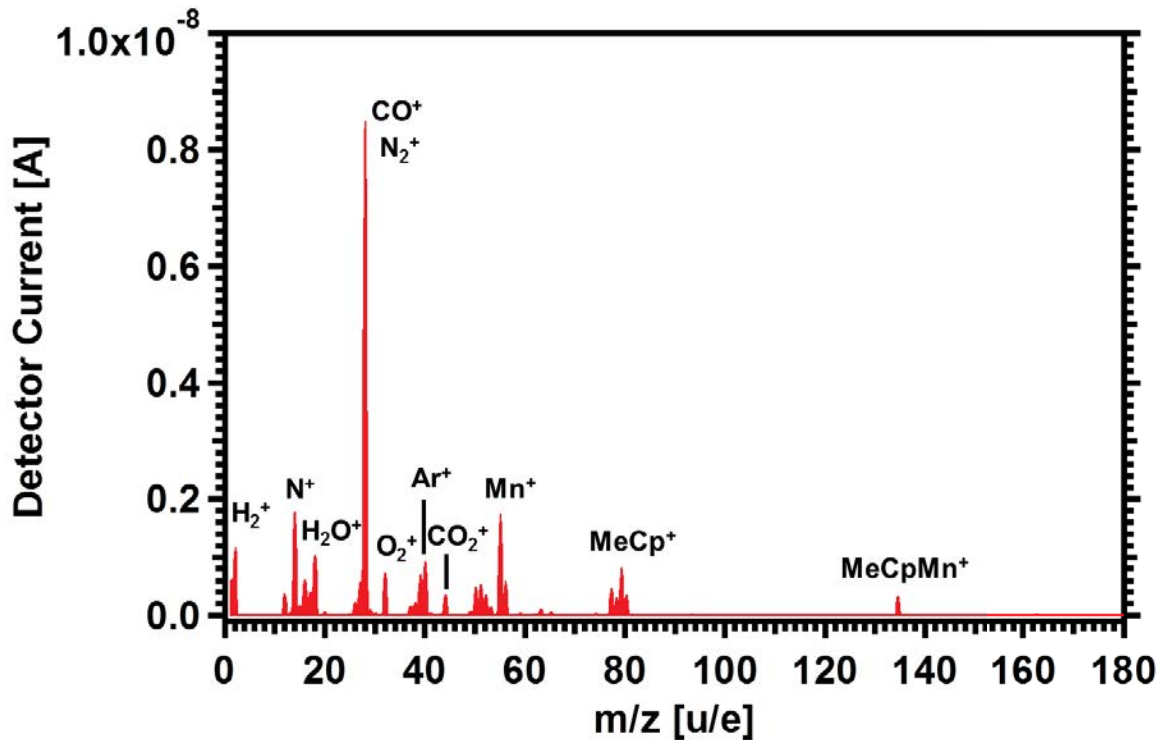


*Figure 4-6: Mass spectrum of  $\text{MeCpMn}(\text{CO})_3$  recorded in the gas dosing chamber at a pressure of  $3 \times 10^{-7}$  mbar. Likely fragments are indicated for the most prominent  $m/z$  features. This mass spectrum presents a good quality of the precursor for EBID experiments as a reference spectrum for latter experiments.*

#### 4.3.2 The substrates

Three types of substrates were used in this work at hand: silicon single crystals with different crystalline orientations, standard TEM  $\text{Si}_3\text{N}_4$  membranes, and a  $\text{Ag}(100)$  single crystal. The suppliers, parameters and preparation of these substrates are described in the following.

Silicon samples with the surface orientation (100) and (111) were used for EBID experiments due to the high relevance of the material in the semiconductor industry. They were purchased from the Institute of Electronic Materials Technology (Warszawa, Poland). The resistivity of  $\text{Si}(100)$  is  $0.065\sim 0.074 \Omega \text{ cm}$  with  $4.5 \times 10^{17}\sim 5.4 \times 10^{17} \text{ at./cm}^3$  boron doped, while the resistivity of  $\text{Si}(111)$  is at the range of  $0.01\sim 0.02 \Omega \text{ cm}$  with  $3.2 \times 10^{18}\sim 8.5 \times 10^{18} \text{ at./cm}^3$  boron doped. As silicon has a strong affinity towards oxygen and forms two stoichiometric oxides, i.e. silicon monoxide ( $\text{SiO}$ ) and silicon dioxide ( $\text{SiO}_2$ ) [173], a native oxide layer is

## 4 Experimental details

formed on the silicon single crystal after prolonged exposure to air. Therefore, EBID experiments were conducted on native  $\text{SiO}_x/\text{Si}(100)$  and  $\text{SiO}_x/\text{Si}(111)$  surfaces with X being most likely close to 2.

Standard TEM  $\text{Si}_3\text{N}_4$  membranes (30, 50, and 100 nm thick) were used with the purpose of further characterization of the fabricated nanostructures in transmission microscopy (STXM and TEM). They were purchased from Agar Scientific Ltd. with a thickness of 100  $\mu\text{m}$  of the surrounding silicon support substrate and a membrane size of 0.1 mm x 0.1 mm. As on silicon, a native oxide layer forms on the  $\text{Si}_3\text{N}_4$  membrane after exposure to air.

In order to prepare MgO thin films, a Ag(100) single crystal (9 x 2 mm<sup>2</sup>, 1 mm thick, 99.9999% purity, Surface preparation laboratory, The Netherlands) was used.

### 4.3.3 Other gases

Argon (Ar) and Oxygen ( $\text{O}_2$ ) are attached to the UHV system via lecture bottles and were purified by flushing the attached gas tubes. Ar was normally used for sputtering the Ag(100) surface, while  $\text{O}_2$  was used for oxide surface preparation, i.e. MgO thin film growth. Both reactive gases were purchased from Messer with 99.998 % purity. QMS was employed for monitoring the quality of the gases before their use.

## 4.4 Experimental details

### 4.4.1 Nanostructure fabrication and in-situ characterization with UHV-SEM

All precursor gas pressures given in EBID experiments are the background pressure in the chamber and are based on uncorrected ion gauge readings. All EBID experiments were performed at room temperature under UHV conditions.

The precursor gas was dosed through the nozzle (inner diameter 3 mm) with a distance of approximately 12 mm away from the sample surface. The local pressure on the sample surface was calculated using the GIS simulator (version 1.5) [174], which yields a local pressure increase on the sample surface by a factor of  $\sim 30$ . For a fixed background pressure of  $3 \times 10^{-7}$  mbar, this corresponds to a local pressure at the surface of  $9 \times 10^{-6}$  mbar. All the gases (precursors and reactive gases) used in this work were monitored via QMS with a pressure of  $3 \times 10^{-7}$  mbar in the gas dosage chamber [12-14, 36, 166].

## 4 Experimental details

All electron exposures for SEM and lithography were performed at a beam energy of 15 kV and a probe current of 400 pA (nominal resolution <3 nm). The lithographic processes were realized via a self-developed lithography application based on LabVIEW 8.6 (National Instruments) and a high speed DAC PCIe-card (M2i.6021-exp, Spectrum GmbH, Germany). Details on the self-developed LabVIEW lithographic programs can be found in reference [170].

In order to produce Fe/Co alloy nanostructures, Fe(CO)<sub>5</sub> and Co(CO)<sub>3</sub>NO were co-dosed during EBID experiments. First, Fe(CO)<sub>5</sub> was dosed through the right leak valve (Figure 4-4b) until the pressure reading reached  $1.5 \times 10^{-7}$  mbar. Then, Co(CO)<sub>3</sub>NO was dosed through the left leak valve to reach a pressure of  $3 \times 10^{-7}$  mbar.

For all AES characterizations, the sample was tilted to an angle of 25 ° between surface normal and the primary electron beam of the SEM. Under these conditions, the intensity of detected electrons in the hemispherical analyzer increases significantly. All AES measurements were performed with a primary beam energy of 15 kV and a beam current of 3 nA (minimum spot size < 6 nm). Local Auger electron spectra were recorded using the software MATRIX (Scienta Omicron GmbH, version 3.1). Surface irradiation for spectrum acquisition was performed with different scanning strategies: spot mode and area scanning.

All SEM micrographs were acquired with SmartSEM (Zeiss) and are shown with minor contrast and brightness adjustments only. AES spectra were treated via Igor Pro 6.22A.

### 4.4.2 Characterization with TEM

In order to characterize the Fe nanocrystal growth process during EBID and AG, ex-situ characterization was carried out at the Institute of Micro- and Nanostructure Research at the Friedrich-Alexander-Universität Erlangen-Nürnberg. An FEI Titan Themis<sup>3</sup> 300 was employed with the ability to perform both HRTEM and STEM. EELS was performed for chemical characterization while atomic level resolution imaging and electron diffraction were utilized for crystal structure analysis. Further information about the instrument can be found in reference [175].

As described in Chapter 3.4, the average size of the Fe nanocrystals can be calculated from the broadening of the diffraction ring at FWHM via Scherrer equation (Equation (3-11)). Further details of the calculation are described in the following:

## 4 Experimental details

$$\left\{ \begin{array}{l} \lambda = 2d\sin\theta_B \rightarrow \theta_B = \arcsin\left(\frac{\lambda g}{2}\right) \rightarrow \Delta(2\theta) = \arcsin\left(\frac{\lambda \Delta g}{2}\right) \\ L = \frac{K\lambda}{\Delta(2\theta)\cos(\theta_B)} = \frac{K\lambda}{\arcsin\left(\frac{\lambda \Delta g}{2}\right)\cos[\arcsin\left(\frac{\lambda g}{2}\right)]} \\ g = \frac{1}{d} \end{array} \right. \quad (4-1)$$

where  $g$  is the reciprocal lattice distance,  $L$  is the nanoparticle size,  $K$  is the shape factor (0.94 for cubic Fe nanocrystals fabricated via EBID plus AG),  $\theta_B$  is the Bragg angle in radians,  $\Delta(2\theta)$  is the broadening of the diffraction ring at FWHM in radians, and  $\lambda$  the electron wavelength. Here, a 200 keV beam was used for diffraction pattern measurements, corresponding to an electron wavelength of 2.508 pm with relativistic effects considered.

The atomic resolution micrographs achieved by HRTEM and STEM, electron diffraction patterns and EELS spectra were treated via Gatan Digital Micrograph and DM DiffTools while the FWHM in radians was measured by Fityk 0.9.8.

### 4.4.3 Characterization and nanofabrication with STXM

Scanning transmission soft X-ray spectromicroscopic measurements were carried out at the PolLux beamline located at the Swiss Light Source (SLS) in Villigen (CH) [176]. In STXM, high-brilliance synchrotron radiation is focused onto the specimen by a Fresnel zone plate (lateral resolution < 35 nm in routine operation). The chamber pressure ranges from high vacuum ( $1 \times 10^{-6}$  mbar) to 1 atm inert gas or He. Figure 4-7 presents the PolLux beamline instruments.

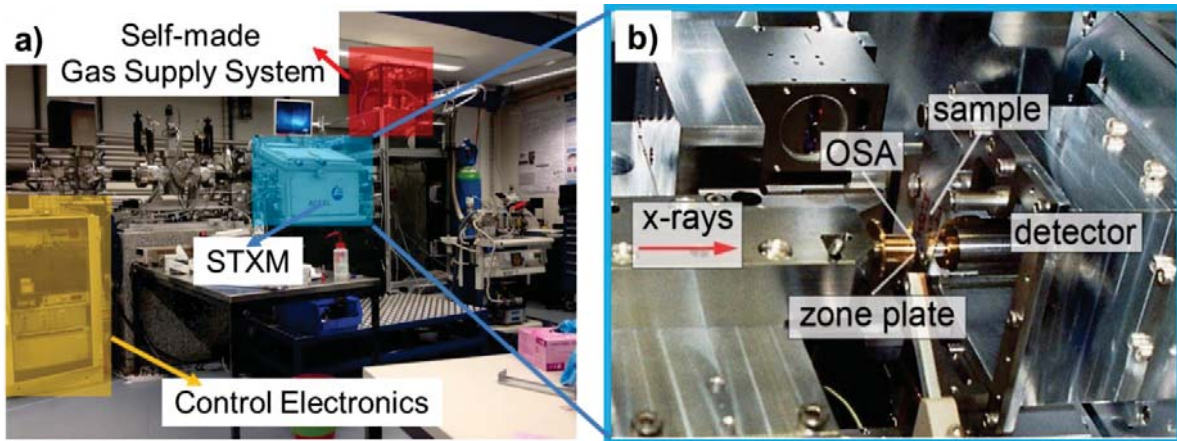


**Figure 4-7:** Photographs of the PolLux STXM. (a) Overview of the instrument including the connected self-made gas supply system. (b) Inner part of the STXM setup including X-ray focusing, sample stage and the detector.

## 4 Experimental details

For image recording, the focused X-ray beam at a certain energy (i.e. 708.7 eV, Fe  $L_3$ -edge for Fe nanostructures) raster-scans over the sample, while the transmitted photon intensity is recorded using a photomultiplier tube as a function of the position. The raster-scanning is realized via a coarse motor stage for steps larger than several  $\mu\text{m}$  and a piezo stage for smaller steps [170, 176]. The stage position is monitored via interferometric feedback. NEXAFS spectra were extracted from line scans, i.e., by consecutive scanning of the identical lines with varying photon energy and normalization to the energy dependent incident flux ( $I_0$ ).

The STXM data was analyzed using aXis2000 (Analysis of x-ray Images and Spectra, <http://unicorn.mcmaster.ca/aXis2000.html>), which is an IDL-based GUI for the processing of X-ray absorption micrographs and spectra. This includes convenient extraction of spectra from the recorded data and conversion from transmission to optical density data.

During the measurements, a variable in-plane external magnetic field can be applied using an electromagnet mounted in close proximity to the sample (Figure 4-8). Magnetic information was derived from XMCD microspectroscopy analyzing the dichroic signal with positive/negative circularly polarized X-rays. In order to observe the in-plane magnetization, the sample was tilted  $30^\circ$  with respect to the optical axis (along the z-direction).

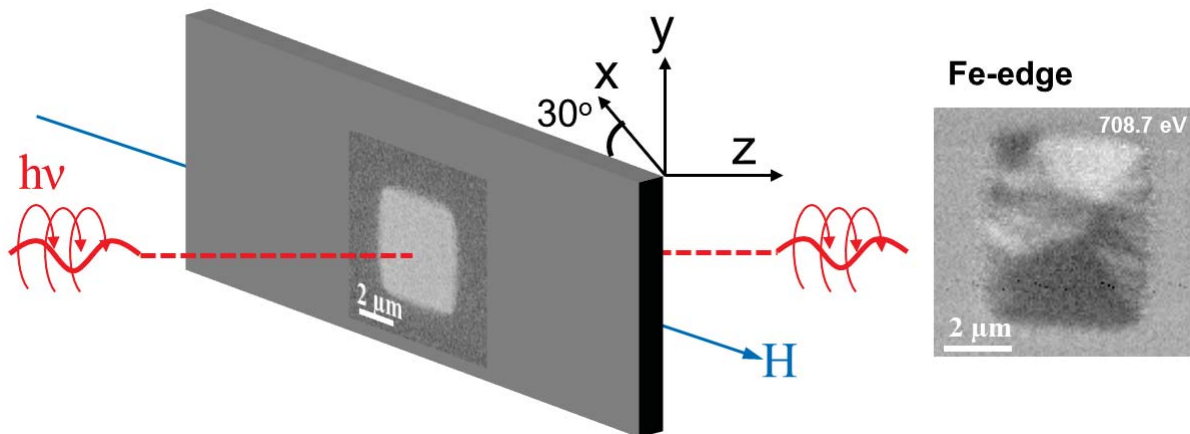


**Figure 4-8:** Scheme of the STXM experimental setup for measurements of magnetic properties. An in-plane magnetic field  $H$  was applied. The sample was tilted  $30^\circ$  with respect to the photon propagation direction to enhance the in-plane XMCD contrast. The sample was a  $4 \times 4 \mu\text{m}^2$  Fe deposit fabricated via EBID plus AG ( $0.1 \text{ C}/\text{cm}^2$ , 172 min). The STXM micrograph was recorded at the Fe  $L_3$ -edge energy resonance.

## 4 Experimental details

The PolLux-STXM enables also the implementation of a small gas flow around the sample position [177]. The respective gas cell is confined by two 50 nm thick  $\text{Si}_3\text{N}_4$  membranes that provide sufficient transmission over a broad photon energy range. Based on these unique instrumental possibilities, a novel technique to fabricate metal nanostructures via X-ray irradiation in an additive, direct write approach was explained in the framework of this thesis at hand (FXBID). A scheme of the modified STXM setup including the self-made gas supply system (details of the configuration can be seen in the Appendix) for FXBID studies and the interaction of the soft X-ray beam with the precursor molecules is depicted in Figure 4-9. A major advantage of the use of a STXM setup for these investigations is the inherent possibility to characterize the deposits directly after generation by means of NEXAFS and high-resolution X-ray microscopy [13, 14, 178].

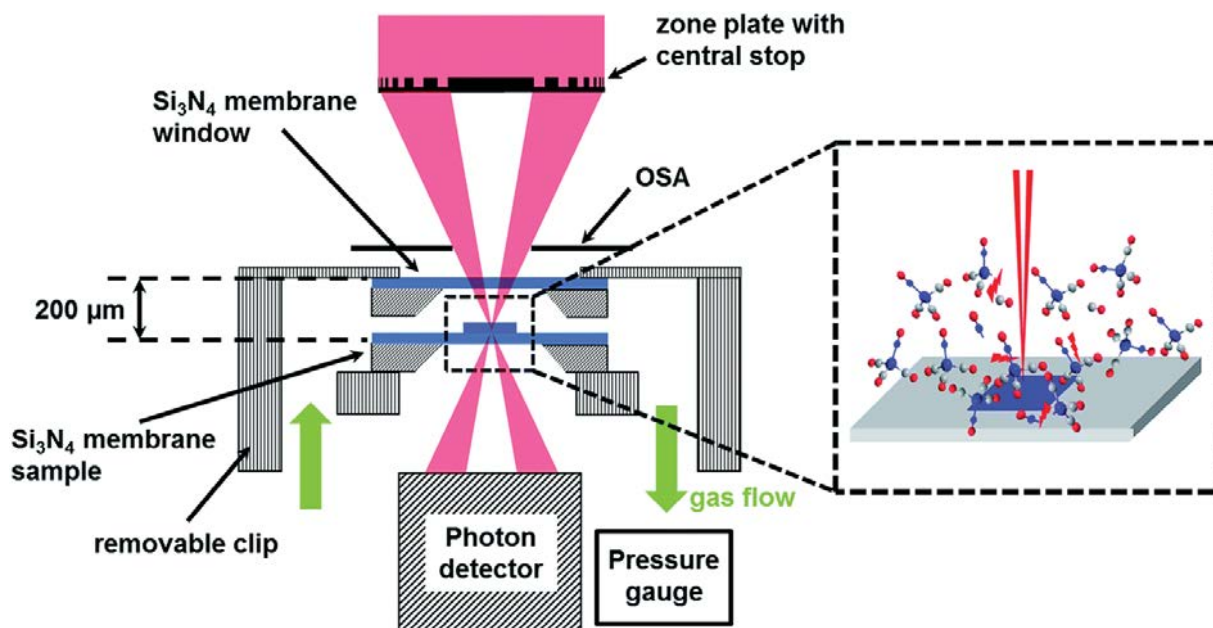


**Figure 4-9:** Scheme of the PolLux-STXM gas cell setup to allow precursor molecules (for example  $\text{Co}(\text{CO})_3\text{NO}$ ) flow on a 50 nm  $\text{Si}_3\text{N}_4$  membrane surface for nanofabrication via FXBID and further in-situ characterization.

During all FXBID processes, the residual pressure prior to precursor dosage was  $\sim 4 \times 10^{-7}$  mbar. It is important to note that within the current setup, the gas pressure is measured between the gas cell and the pumping system, indicating a slightly higher value within the gas cell than the recorded by the pressure gauge [178]. The size of the deposited nanostructures shown in the

## 4 Experimental details

present work is  $2 \times 1 \mu\text{m}^2$ , while a scan acceleration distance of  $0.5 \mu\text{m}$  was neglected on both sides of the fast (i.e., horizontal) scan direction in order to guarantee homogeneous irradiation of the specimen areas considered for quantitative analysis (effective size of the deposit:  $1 \times 1 \mu\text{m}^2$ ,  $100 \times 100$  acquisition points). The spot size during our experiments was approximately  $25 \text{ nm}$ .

Multi-sweep irradiations (40 sweeps, each with 2 ms dwell time) were performed at the Co (780 eV) and Mn (640.5 eV)  $L_{2,3}$ -edge resonances. The optical density was monitored between individual sweeps. The precursor pressures were  $9.2 \times 10^{-5} \text{ mbar}$  ( $\text{Co}(\text{CO})_3\text{NO}$ ) and  $2.5 \times 10^{-6} \text{ mbar}$  ( $\text{MeCpMn}(\text{CO})_3$ ).

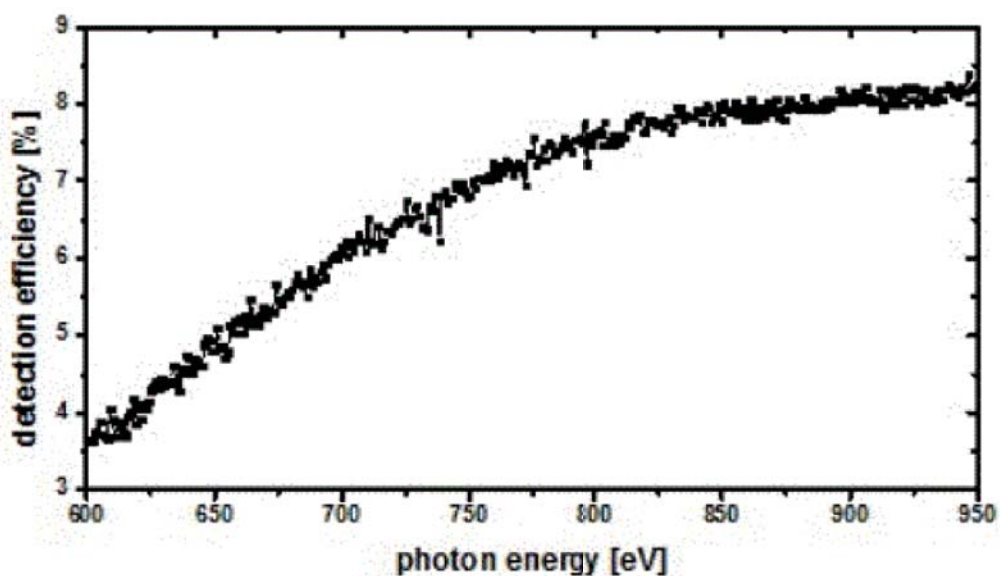


**Figure 4-10:** Efficiency of the PolLux detection setup during FXBID studies. The detection efficiency was measured with respect to a calibrated photodiode (100% collection efficiency and a quantum efficiency of  $E/3.65$  for photon energy  $E$ ). The energy dependence is mainly affected by the fluorescence efficiency of the phosphor powder scintillator and contamination artefacts. Note that the detection efficiency is also influenced by the threshold value of the discriminator that is implemented for noise suppression. Due to the comparably long acquisition times during the FXBID process, this threshold was set to a high value. Therefore the absolute values of the detection efficiency are about ten times smaller than for standard threshold (yielding optimized ratio of  $I_0$  and dark counts).

## 4 Experimental details

For the quantitative analysis of deposited mass versus incident photons, the efficiency of the detection setup (scintillator-based photomultiplier tube) was characterized (Figure 4-10), compared to a calibrated photodiode, and was also corrected for the respective absorption of the  $\text{Si}_3\text{N}_4$  membranes to evaluate the photon flux inside the gas cell [178]. An explanation of the thickness and material quantity evaluation can be found in reference [14].

### 4.4.4 CVD-CNTs growth

In order to produce CNTs at predefined patterns, a combination of EBID and CVD growth of CNTs was used, as EBID-Fe (Co) deposits can act as catalyst in the CVD-CNTs growth. Catalytic CVD experiments were carried out at atmospheric pressure in a horizontal quartz tube with an external diameter of 25.5 mm and a length of 1 m (MTA-SZTE Reaction Kinetic and Surface Chemistry Research Group, University of Szeged, Hungary), as depicted in Figure 2-5a. The tube is located inside a horizontal electrical furnace (Lenton PO BOX 2031), enabling heating to the desired CNT growth temperature. The system is equipped with a mass flow controller, allowing a precise flow of gas mixtures. The sample was placed in a quartz boat located in the quartz tube. As Laminar flow conditions and elevated temperatures for the decomposition of the carbon precursor were required to initiate the growth of nanotubes on the surface, the sample position in the quartz tube was chosen. Prior to the CVD reaction, the catalyst was reduced in a nitrogen/hydrogen flow mixture at the growth temperature of CNT for ~10 min. Ethylene ( $\text{C}_2\text{H}_4$ ) gas as carbon source was then introduced into the reactor to initiate the CNTs growth. Figure 4-11 presents the CVD strategy with a description in details of each step.

## 4 Experimental details

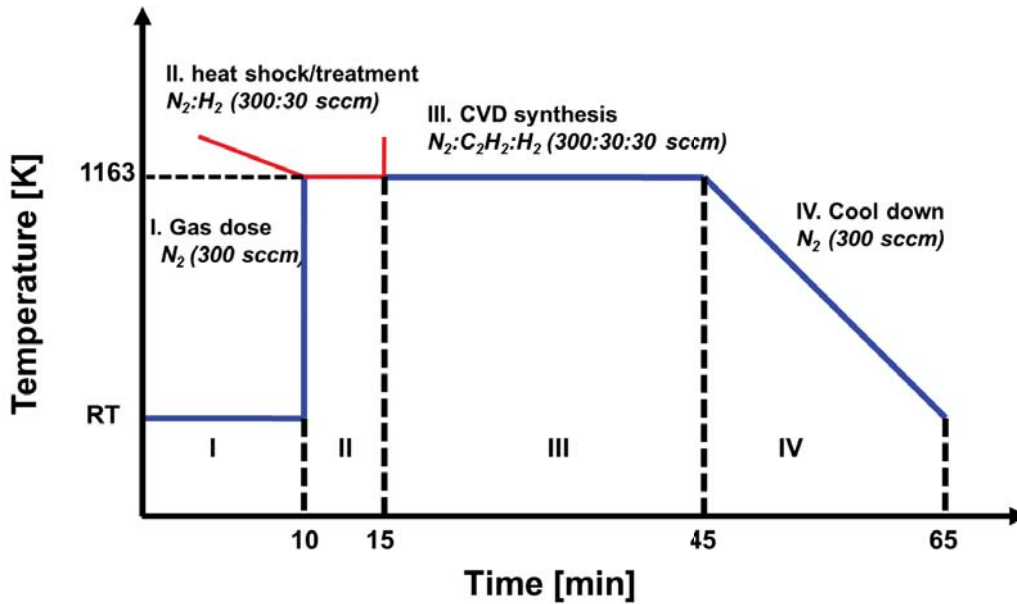


*Figure 4-11: CVD process with a description of the parameters of each step.*

### 4.4.5 MgO thin film growth

A Ag(100) single crystal was used as a substrate for MgO(100) thin film growth. The Ag(100) surface was prepared in UHV by repeated sputtering/annealing cycles, which is described in the following:

- |   |                           |                           |
|---|---------------------------|---------------------------|
| <u>i. Ar<sup>+</sup> ion sputtering</u> | Ar background pressure:   | 4 x 10 <sup>-6</sup> mbar |
|   | Ar ion energy:            | 1 keV                     |
|   | Temperature:              | Room temperature          |
|   | Time:                     | ~30-60 min                |
| <u>ii. Annealing</u>                    | Temperature:              | ~700-750 K                |
|   | Heating and cooling rate: | 1 K/s up, 0.5 K/s down    |
|   | Time:                     | ~30-60 min                |

The temperature during the preparation procedure was measured via a type K thermocouple directly attached to the Ag(100) sample. A PID controller (Eurotherm) was used to provide

## 4 Experimental details

reproducible conditions during heating. The surface quality was monitored via LEED and AES (Figure 4-12). Three Ag MNN peaks at 261.5, 296, and 352 eV are shown.

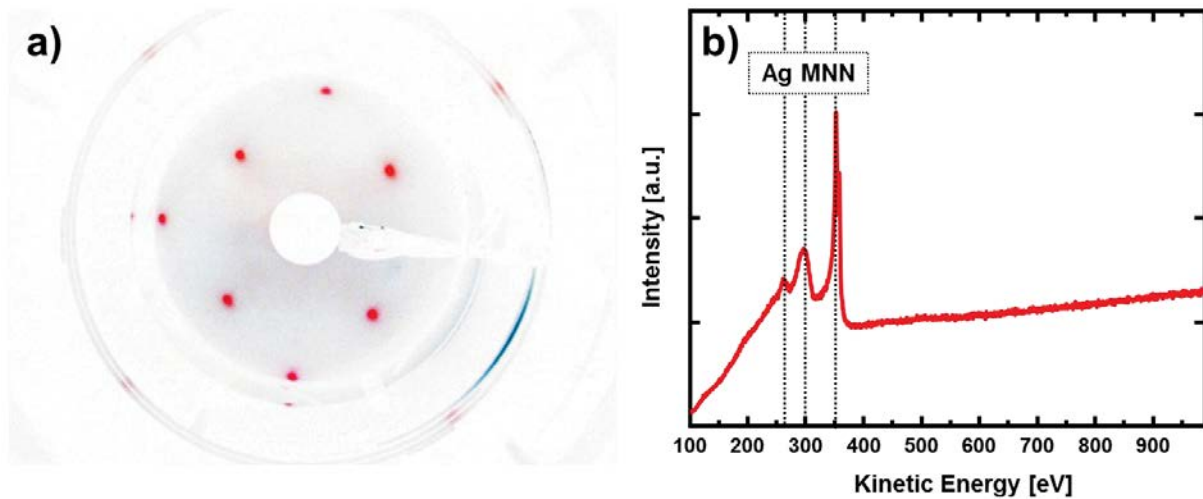


**Figure 4-12:** *Ag(100) single crystal surface prepared by several ( $> 10$ ) sputtering and annealing cycles as described above. (a) LEED pattern of the Ag(100) surface at an electron energy of 55 eV. (b) Local Auger spectrum of the prepared Ag(100) surface.*

For the preparation of MgO films, the same approach described in references [179-182] was used: evaporating Mg onto the Ag(100) surface in an O<sub>2</sub> atmosphere. Before deposition, the Ag(100) substrate temperature was increased to 700 K with 1.5 K/s. Simultaneously, the Mg evaporator was heated to the necessary evaporation temperature and the evaporation rate was set to  $\sim 3.5$  Å/min (calibrated by QCM). If the temperature of the Ag(100) substrate and the evaporation rate of Mg were stable, the desired O<sub>2</sub> (after several cycles of purification) pressure in the UHV chamber was adjusted to  $\sim 1 \times 10^{-6}$  mbar. After that, the substrate surface was rotated towards the Mg evaporator whose shutter was subsequently opened. After a certain MgO growth time, the shutter was closed and the substrate was cooled down to room temperature with 0.2 K/s in O<sub>2</sub>. A further annealing step up to 873 K in O<sub>2</sub> was carried out with the purpose of improving the MgO thin film quality, which can be monitored by the LEED, AES and STM (Figure 4-13).

#### 4 Experimental details

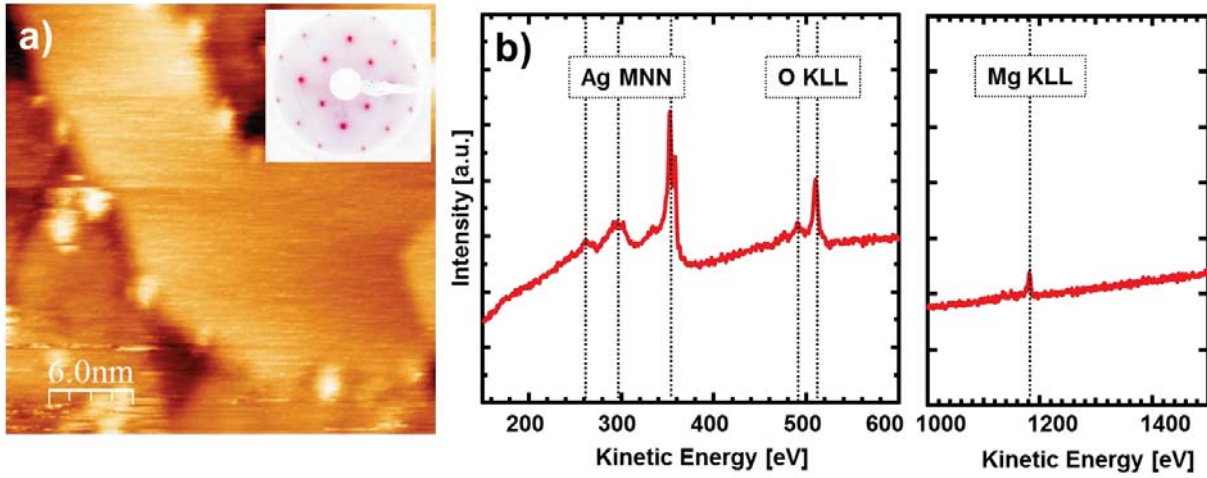


**Figure 4-13:** MgO film ( $\sim 3$  ML (1 ML  $\approx 0.23$  nm)) prepared on a Ag(100) substrate. (a) STM micrograph of MgO. The inserted image depicts the LEED pattern at an electron energy of 134 eV. (b) AE spectra of MgO with the corresponding transitions indicated. The thickness of the MgO film was evaluated also by AES using the damping of the Ag MNN peaks (as introduced in Chapter 3.2). The parameters are listed in Table 4-1.

**Table 4-1:** MgO thickness evaluation through Auger spectra according to Equation (3-3), (3-4), and (3-5).

$\lambda_{AL} / \text{nm}$	$Z$	$E / \text{eV}$	$a / \text{nm}$	$\mu / \text{g mol}^{-1}$	$\rho / \text{g cm}^{-3}$	$N_A / \text{mol}^{-1}$	$\theta$
1.14	10	351	0.285	40.3	3.58	$6.022 \times 10^{23}$	$35^\circ$

where  $Z$  is the average atomic number of MgO ( $\approx 0.5 \cdot Z_{Mg} + 0.5 \cdot Z_O$ ),  $E$  is the kinetic energy of the damped signal,  $a$  is calculated via Equation (3-5),  $\mu$  is the atomic mass,  $\rho$  is the density,  $N_A$  is the Avogadro constant and  $\theta$  is the angle between surface normal and electron spectrometer. The calculated thickness of MgO fits well with the growth rate measured by QCM. Further details concerning the attenuation length calculation can be found in reference [166].

## 5 TEM investigation of Fe nanocrystal growth

### 5.1 Introduction

Recently, it has been reported that Fe cubic nanocrystals can be fabricated on various surfaces (e.g., Si, Rh and TiO<sub>2</sub>) via EBID plus subsequent AG in UHV conditions with Fe(CO)<sub>5</sub> as a precursor [12, 15, 22]. Fe deposits have high potential for the application of magnetic logic circuits [17], biosensors [183], and catalysts for nanotube growth [32, 33]. However, the full picture of the AG process using Fe(CO)<sub>5</sub> to form nanocrystals in UHV is still unclear. Two main questions still remain unanswered: how does the cubic nanocrystal form? Is there a difference in the chemical composition between the deposits fabricated either via EBID only or combining the EBID and AG processes? In this sense, a better microscopic understanding of this process is necessary.

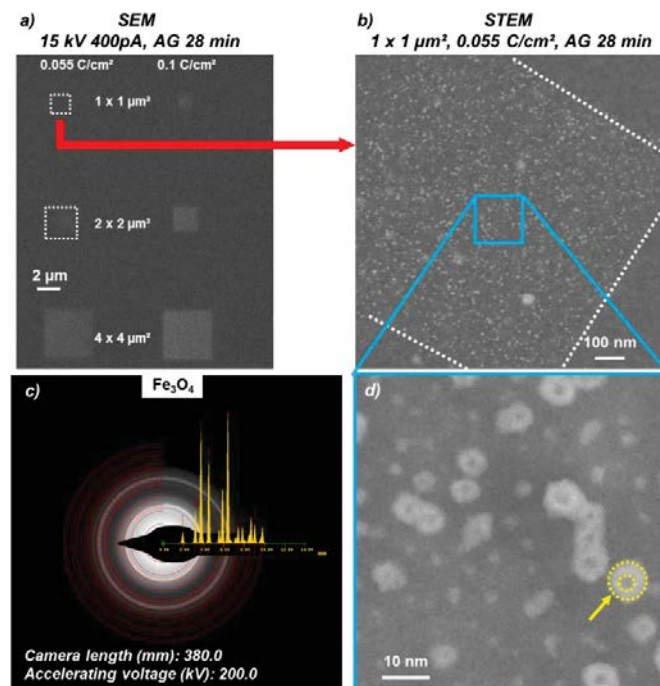
TEM is a powerful tool to investigate nanoscale objects [144]. Atomic level resolution provides the opportunity to monitor the AG process from the beginning. Through electron diffraction, the nanocrystallinity and average crystal size of the fabricated nanostructures can be evaluated. EELS allows tracking changes in the chemical composition as a function of the applied AG time.

In this chapter, a detailed analysis of the metallic nanostructures was carried out, which were fabricated with Fe(CO)<sub>5</sub> on a 30 nm Si<sub>3</sub>N<sub>4</sub> membrane by EBID and AG under UHV conditions. First, a morphological characterization of the structure was done by in-situ UHV-SEM. Second, an ex-situ chemical and morphologic characterization at the nanometer scale was performed via TEM. The powerful functions of TEM provide a further insight into the AG process, including changes of chemical composition and nanocrystallinity. A model describing the AG process is presented based on the experimental data. As Fe was natively oxidized during the transportation in air, it is necessary to transfer sample to the TEM in inert gas environment in order to avoid the shape changes due to the native oxidation process.

## 5.2 Results and discussion

### 5.2.1 Fabrication of iron nanostructures

Various Fe square structures were fabricated via EBID and the subsequent AG, as depicted in Figure 5-1. These Fe structures were investigated by not only the in-situ SEM, but also the high resolution TEM, so that the comparison between SEM and TEM micrographs on the same structure can be realized.



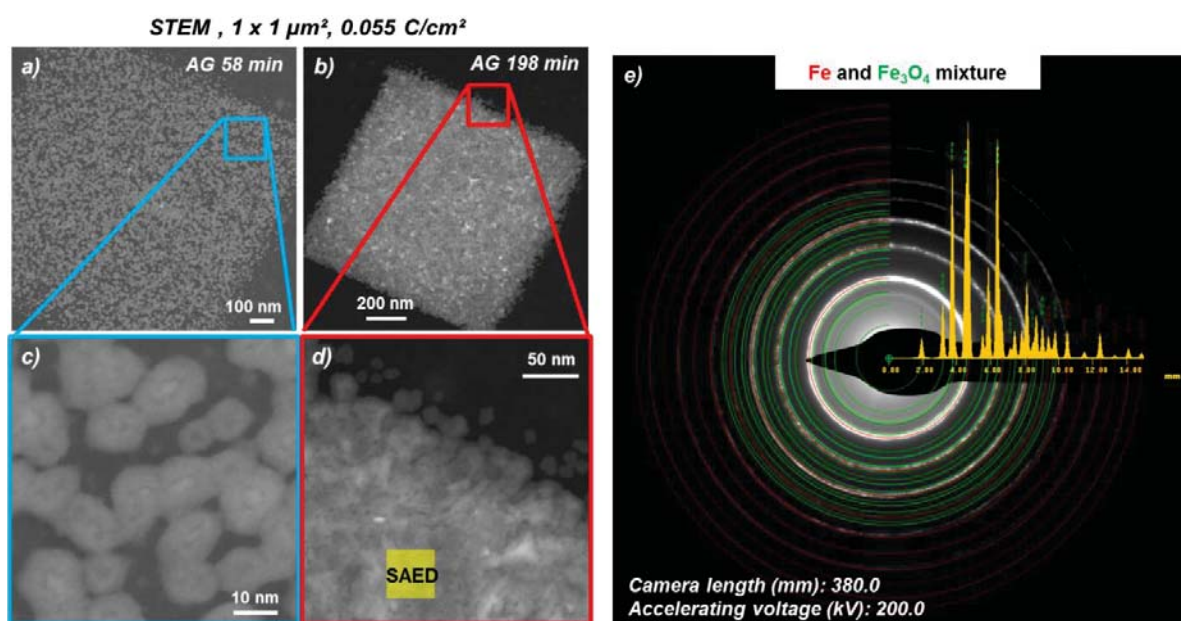
**Figure 5-1:** (a) In-situ SEM image of Fe nanostructures fabricated with EBID and AG, with the deposition parameters indicated. (b) STEM image of the 1 x 1 μm<sup>2</sup> Fe nanostructure, which exhibits no contrast in SEM. 1 x 1 μm<sup>2</sup> structure was rotated due to the characterizations in different instruments (SEM and STEM, respectively). (c) Electron diffraction pattern of the Fe nanostructure shown in (b), indicating fully oxidized iron nanoparticles Fe<sub>3</sub>O<sub>4</sub>. (d) Magnified STEM image with Z-contrast, suggesting a core-shell structure of the iron nanoparticles, as indicated by the arrow.

Figure 5-1a displays an in-situ SEM image of square structures (1 x 1, 2 x 2, and 4 x 4 μm<sup>2</sup>) fabricated by EBID on the native oxide of a 30 nm Si<sub>3</sub>N<sub>4</sub> membrane. It is obvious that small

## 5 TEM investigation of Fe nanocrystal growth

structures ( $1 \times 1$  and  $2 \times 2 \mu\text{m}^2$ ) fabricated with low electron doses ( $0.055 \text{ C/cm}^2$ ) can hardly be seen in SEM. Figure 5-1b presents the STEM image of the  $1 \times 1 \mu\text{m}^2$  Fe structure fabricated with  $0.055 \text{ C/cm}^2$  and 28 min AG time. Individual Fe nanoparticles are distributed over the irradiated area and exhibit a core-shell structure (Figure 5-1d). The Selective area electron diffraction pattern shows that the Fe nanoparticles are  $\text{Fe}_3\text{O}_4$  (Figure 5-1c).

It is worth to note that the Z-contrast was used in STEM, implying a reduced intensity in the center, as it shows a dark contrast. This is attributed to a void, which is due to the imbalance in the relative rates for the inward diffusion of O and outward diffusion of Fe during the native oxidation process [57]. Also the observed spherical shape of the Fe nanoparticles is caused by the strain induced morphological change [57], even though it is possible that cubic Fe nanocrystals were fabricated at beginning via EBID and AG.



**Figure 5-2:** AG process of a  $1 \times 1 \mu\text{m}^2$  nanostructure ( $0.055 \text{ C/cm}^2$ , AG times: 58 and 198 min). (a) and (c) STEM images of the deposit fabricated with 58 min AG time. (b) and (d) STEM images of Fe nanostructure with 198 min of AG time. (e) Selective area electron diffraction on (d) shows a mixture of Fe and  $\text{Fe}_3\text{O}_4$ .

Figure 5-2a-d depicts  $1 \times 1 \mu\text{m}^2$  Fe nanostructures fabricated by EBID ( $0.055 \text{ C/cm}^2$ ) and AG times of 58 and 198 min. Combined with Figure 5-1b ( $0.055 \text{ C/cm}^2$ , 28 min), this presents

## 5 TEM investigation of Fe nanocrystal growth

STEM images of Fe deposits with varying AG time. The core-shell structure can still be observed in Figure 5-2c and d. The small Fe nanoparticles at the edge of the structure in Figure 5-2d were deposited presumably due to proximity effects. From the images of deposits fabricated with different AG growth times, it can be concluded that Fe crystallites grow not only perpendicularly to the surface but also laterally. Selective area electron diffraction (SAED) provides information concerning the crystallinity of the Fe deposits, which can be identified as a mixture of  $\alpha$ -Fe and  $\text{Fe}_3\text{O}_4$  (Figure 5-2e).

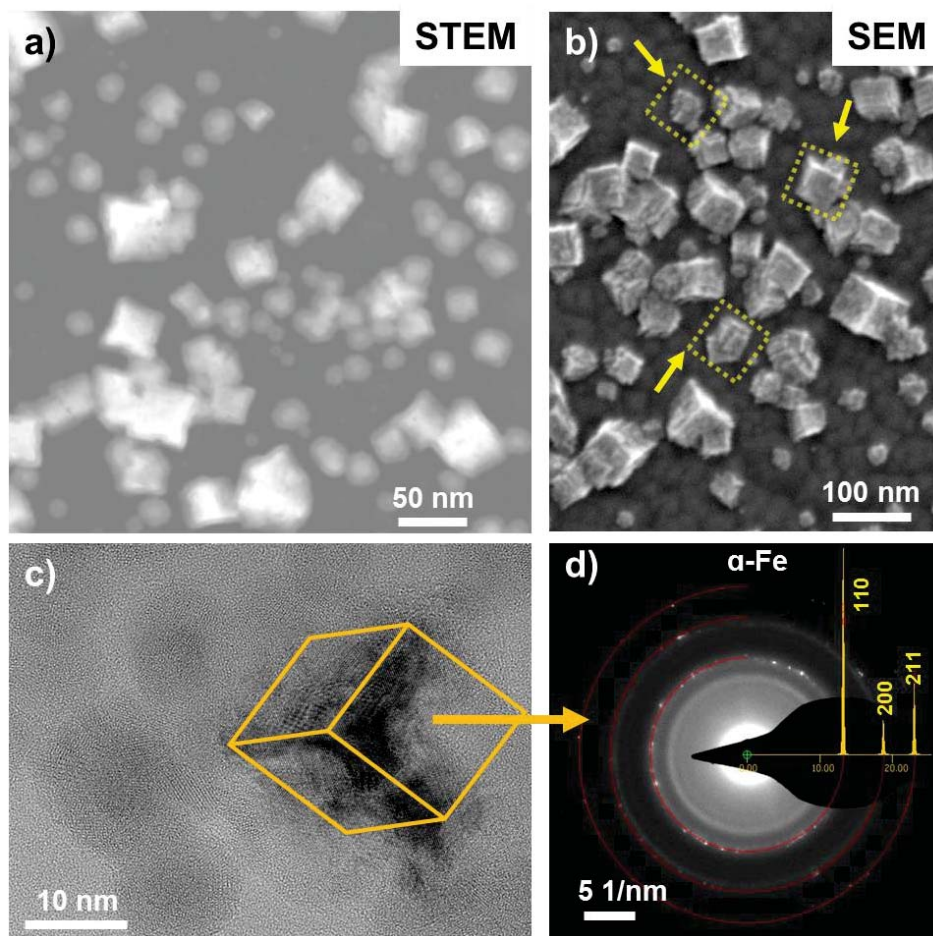


**Figure 5-3:** (a) STEM image of Fe nanocrystals fabricated via EBISA. (b) In-situ SEM image of Fe nanocrystals fabricated with EBISA. Fe nuclei were formed on Fe cubic nanocrystal surfaces, as indicated by arrows. (c) HR-TEM image of one cubic Fe nanocrystal. (d) Electron diffraction on the cubic Fe nanocrystal fabricated via EBISA, showing  $\alpha$ -Fe with the orientations (110), (200) and (211).

## 5 TEM investigation of Fe nanocrystal growth

Fe cubic nanocrystals can also be produced by EBISA. In a first step the sample is locally irradiated by the focused electron beam in the absence of  $\text{Fe}(\text{CO})_5$ . In a second step,  $\text{Fe}(\text{CO})_5$  is supplied and cubic nanocrystals grow on the pre-irradiated areas (Figure 5-3b). The STEM image of these cubic nanocrystals shows an outer shell which can again be identified as a oxide layer (Figure 5-3a). The HR-TEM image exhibits atomic resolution of the cubic Fe nanocrystal and electron diffraction shows the crystalline orientation as  $\alpha$ -Fe (110), (200) and (211). Figure 5-3b presents new Fe nuclei forming on the surface of Fe cubic nanocrystals, with different crystalline orientation. This can be identified in Figure 5-3c that Fe nanocrystals with different crystalline orientation have grown on each other.

### 5.2.2 AG growth model

In order to gain more insight into the AG process, a series of electron diffraction patterns was acquired on  $2 \times 2 \mu\text{m}^2$  Fe square structures fabricated with different AG times (28, 58, 87, 115, 149, 179 and 198 min). Figure 5-4a and b depict the electron diffraction patterns of two nanostructures fabricated with AG times of  $\sim 28$  and  $\sim 198$  min, respectively. It can be seen that Fe deposits are amorphous with shorter AG time ( $\sim 28$  min), whereas they are crystalline with longer AG time ( $\sim 198$  min).

By measuring the broadening of the diffraction ring at the FWHM, the average size of the nanocrystals in the selective area can be evaluated via the Scherrer equation (Chapter 4.4.2). The resulting plot is depicted in Figure 5-4c. First, the size of the Fe nanocrystals increases with increasing AG time and reaches a maximum value of 14-15 nm at around 100 min. A further increase of AG time results in a smaller average size of the fabricated Fe nanocrystals. This behavior is reasonable as the size here is the average value of the nanocrystals in the selective area. Therefore, most of the Fe nanocrystals grow with AG time while smaller Fe nucleus start to form simultaneously as long as the precursor is supplied. It is believed that the average size of the deposited Fe nanocrystals will change periodically with the applied AG time. Experiments with longer applied AG time are needed for further illustration.

## 5 TEM investigation of Fe nanocrystal growth

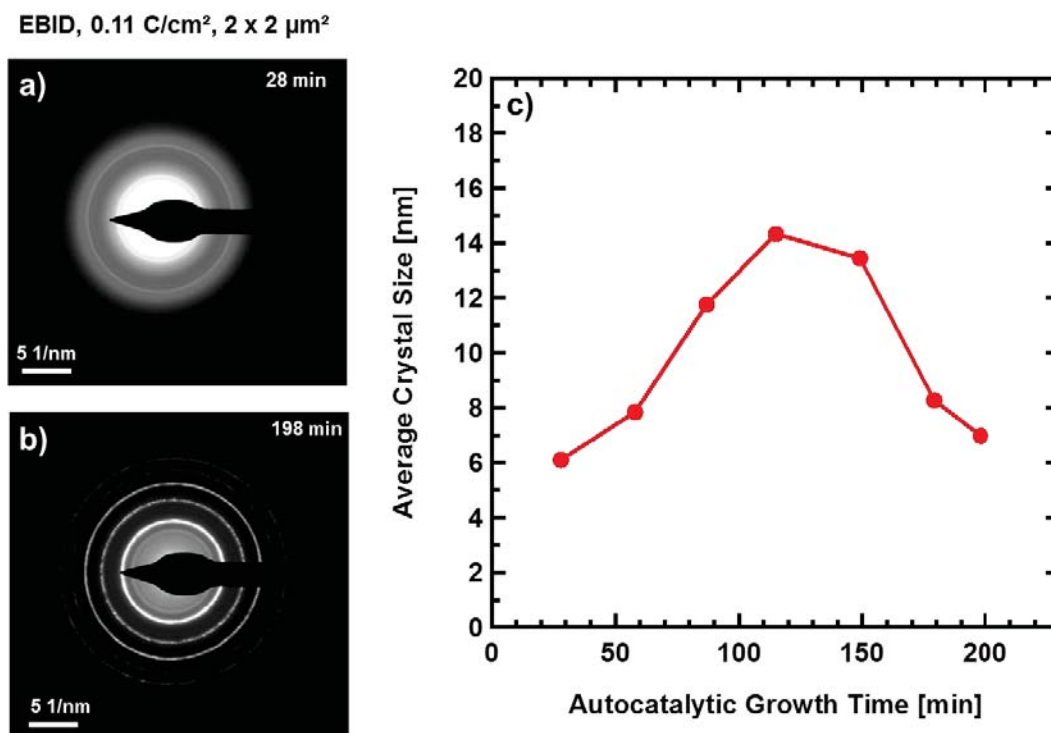


**Figure 5-4:** Average nanocrystal size evaluated via the Scherrer equation. (a) and (b) Electron diffraction patterns of 2 x 2 μm<sup>2</sup> nanostructures produced with EBID (0.11 C/cm<sup>2</sup>) plus different AG times (28 and 198 min respectively). (c) Average nanocrystal size vs. AG time.

### 5.2.3 Chemical composition analysis

The chemical composition of the fabricated Fe nanocrystals was obtained by carrying out EELS in the TEM instrument. Figure 5-5a and b present the electron energy loss spectra at both the oxygen and Fe energy range. It has to be emphasized that no carbon was detected on these Fe nanostructures (spectra are not shown here). The oxygen composition is attributed to either the dissociation of carbonyl ligand in EBID or the native oxidation process during transportation of the sample to the TEM instrument. Concerning qualitative analysis, the peak shifts of both oxygen and iron spectra are due to the change of the oxidation states during the AG process. The ratio between peak areas of Fe-L<sub>3</sub> and O-K sharply rises up with increasing AG time, indicating a self-passivation behavior of the native oxidation process. It is also possible that the ratio of bulk Fe atoms to the surface atoms increases with increasing nanocrystal size, which is related to the longer AG time. Therefore, the ratio between Fe-L<sub>3</sub> and O-K rises up as the bulk mainly

## 5 TEM investigation of Fe nanocrystal growth

consists of Fe while the surface contains O. The general composition of the deposits changes from  $\text{Fe}_3\text{O}_4$  to  $\text{Fe}_{3.4}\text{O}$ .

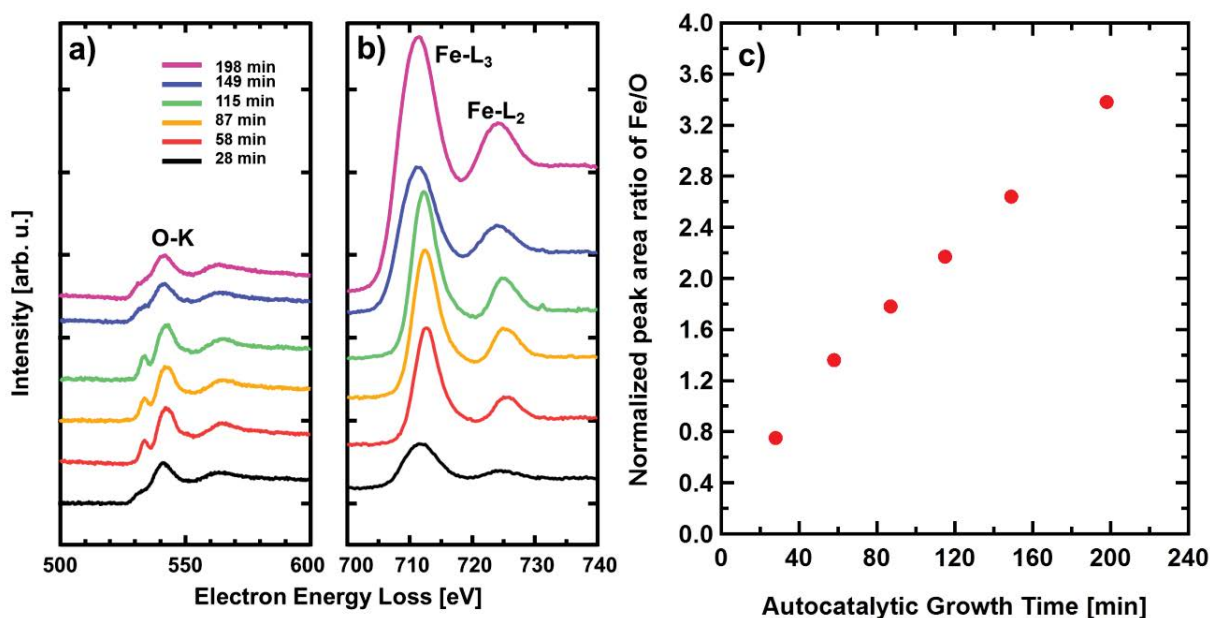


**Figure 5-5:** EELS of several Fe deposits fabricated with EBID ( $0.1 \text{ C/cm}^2$ ) plus different AG time. (a) EELS spectra in oxygen energy range. (b) Fe-L<sub>2,3</sub> spectra. (c) Ratio of Fe and O peak area versus AG time. Fe/O ratio of the Fe nanostructure with shortest AG time (28 min) is set to 0.75 as the Fe deposits are expected to be fully oxidized to  $\text{Fe}_3\text{O}_4$ .

### 5.3 Conclusions

TEM was employed for the investigation of the autocatalytic growth process after EBID deposition on a 30 nm  $\text{Si}_3\text{N}_4$  membrane using  $\text{Fe}(\text{CO})_5$  as a precursor. At shorter AG times, individual nanoparticles with spherical shape can be observed in high resolution STEM, revealing a core-shell structure with a void at the center. These nanoparticles are identified as  $\text{Fe}_3\text{O}_4$  by selective area electron diffraction. With longer AG times, continuous deposits are observed, indicating a 3D growth behavior. By using the longest AG time (198 min), a mixture of  $\alpha$ -Fe and  $\text{Fe}_3\text{O}_4$  is observed. This has also been proven by the electron energy loss spectra of Fe nanostructures ( $2 \times 2 \mu\text{m}^2$ ) fabricated with EBID ( $0.1 \text{ C/cm}^2$ ) plus different AG times. The peak area ratio between Fe and O sharply rises up with increasing AG time, changing from 0.75 to 3.4.

## 5 TEM investigation of Fe nanocrystal growth

Cubic Fe nanocrystals can also be fabricated via EBISA. They are shown to be  $\alpha$ -Fe with crystalline orientations of (110), (200) and (221). A thin oxide outer layer is also observed around the cubic nanocrystals, which can be ascribed to the oxidation during sample transportation in ambient.

The average crystal size of the Fe deposits has been evaluated via the electron diffraction patterns. The size increases with increasing AG time and reaches a maximum value of  $\sim 15$  nm at  $\sim 100$  min of AG time. Then it decreases to  $\sim 6$  nm (198 min), a similar value as the average size in beginning of the autocatalytic growth (28 min). This trend is explained by the small Fe nucleus forming simultaneously during the AG process. Longer AG times have to be applied to verify whether the average crystal size changes periodically.

It is important to note that the shape of the small Fe nanoparticles is influenced by the native oxidation process. The spherical shape of the Fe nanoparticles at the beginning of the AG process can be ascribed to either the strain induced morphological change or to the fact that they are directly fabricated via EBID. Thereby, a careful transportation of the sample in inert gas is necessary to reveal the AG process from the beginning.

## **6 On the magnetization properties of iron nanostructures via EBID plus AG**

### **6.1 Introduction**

Low dimension magnetic systems are of great interest, since they can not only promote the understanding of small scale magnetic mechanisms such as exchange coupling and magnetic anisotropy, but can also serve as prototype structures for their potential usage in devices [184-186]. STXM has been proven to be a powerful method for microscopical and element-specific investigation of the magnetic properties of thin film materials [159, 160, 162, 187-190]. In STXM, the polarization of the incoming X-ray probe can be changed in a controlled way, enabling the use of XMCD contrast to microscopically investigate magnetization patterns in thin magnetic samples [161, 191].

EBID has been used to fabricate magnetic nanostructures based on Fe [17, 73] and Co [45, 62, 192], considering the advantages of it compared to other techniques, e.g., the fabrication of extremely small structures, precise position control during fabrication, the realization of arbitrary shapes and a large variety of applicable precursors [60, 61, 63, 65]. In this context, it was demonstrated that the magnetic properties such as the coercive field ( $H_C$ ) can be influenced by the actual deposit thickness and shape.

The aim of this chapter is to investigate details of the magnetic properties of Fe nanostructures fabricated by EBID in our UHV system. With our specific “surface science” approach, it is able to overcome hitherto existing limitations concerning the purity of the corresponding deposits. The purity of Fe deposits can be higher than 95 at.%. In addition, by controlling the electron dose and AG time, clean iron nanostructures with controlled thickness (< 15 nm) can be fabricated, which consequently allows for depositing well-defined EBID structures significantly thinner than the ones reported [73]. In this respect, it is important to note that massive deposits can be grown via AG without further electron exposed and thus without proximity effects. Furthermore, the resulting deposits were characterized by synchrotron based STXM, with the ability for either chemical analysis (NEXAFS) or magnetic imaging (shift XMCD contrast in STXM).

## 6.2 Results and discussion

### 6.2.1 Iron nanostructures fabricated via EBID

Iron nanostructures were deposited from  $\text{Fe}(\text{CO})_5$  on the native oxide of 100 nm  $\text{Si}_3\text{N}_4$  membrane in the UHV setup. During EBID experiments, the primary beam energy was 15 keV with a beam current of 400 pA (nominal resolution better than 3 nm). By using the self-developed lithographic attachment, arbitrary shapes with varying primary electron doses can be fabricated via EBID in a controlled manner [170]. Figure 6-1 displays SEM micrographs of EBID structures (squares with dimensions of 1 x 1, 2 x 2, and 4 x 4  $\mu\text{m}^2$ , respectively) with focused electron beam doses ranging from 0.01 to 0.2  $\text{C}/\text{cm}^2$ . As indicated in Figure 6-1, the electron doses increase from left to right and the size of the irradiated squares from top to bottom. The individual square deposits were fabricated sequentially.

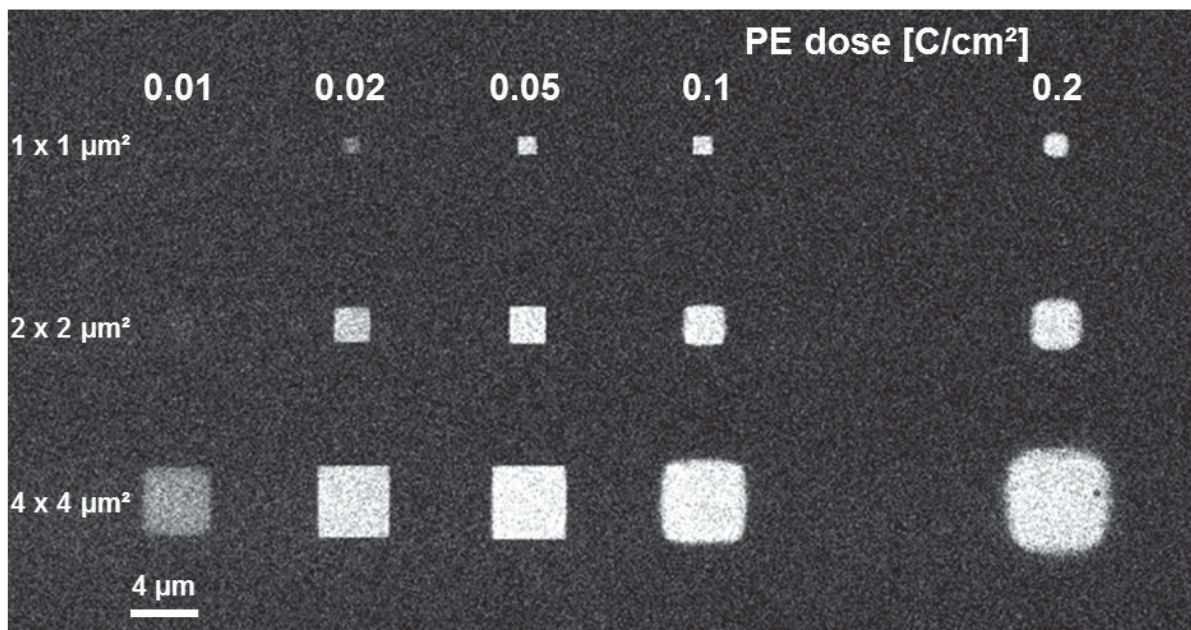


**Figure 6-1:** SEM micrographs of EBID square structures with different sizes and electron doses. EBID was performed on a 100 nm  $\text{Si}_3\text{N}_4$  membrane with  $\text{Fe}(\text{CO})_5$  as the precursor. All structures were prepared sequentially in one experiment. After the EBID, the precursor was further supplied for following autocatalytic growth. The minimum electron dose for detectable 4 x 4  $\mu\text{m}^2$  structures was 0.01  $\text{C}/\text{cm}^2$  while the proximity effect started to be observable at 0.1  $\text{C}/\text{cm}^2$ .

## 6 On the magnetization properties of iron nanostructures via EBID plus AG

The structures' appearance is influenced by the electron doses: the pattern prepared with a dose of  $0.1 \text{ C/cm}^2$  ( $4 \times 4 \text{ }\mu\text{m}^2$ ) starts to show observable proximity effects in the form of fringes around it, while below  $0.01 \text{ C/cm}^2$  structures are hardly visible in SEM. The so-called proximity effects mentioned above are a major challenge in EBID [11, 16]. Basically, these effects are caused by scattered and secondary electrons which lead to an effective broadening of the deposits compared to the diameter of the primary electron beam. As a result, the final deposit shape (i.e., asymmetry) can be significantly influenced by proximity effects [4, 16]. By applying a well-established “multi-sweeps” approach (consecutively sweeping the same area multi-sweep times), it is possible to enhance the uniformity of the targeted square shapes (compared to the single sweep irradiation). More details about the “multi-sweep” procedure as applied in this chapter can be found in reference [14] and its supporting information.

After the actual EBID process, the  $\text{Fe}(\text{CO})_5$  precursor supply was maintained for a certain amount of time to allow for AG of the deposited structures in a parallel fashion. Remarkably, for certain precursor molecules (e.g.,  $\text{Fe}(\text{CO})_5$ ), the AG occurs in the UHV system already at room temperature [10, 12, 14, 23, 36]. The corresponding deposit via AG not only yields pure iron from  $\text{Fe}(\text{CO})_5$  but also allows for depositing material without further electron dose and thus without any electron-related proximity effects. The overall deposition time, including AG time ( $t_G$ ) plus EBID duration, varied slightly from 223 min ( $0.2 \text{ C/cm}^2$ ,  $4 \times 4 \text{ }\mu\text{m}^2$ ) to 240 min ( $0.01 \text{ C/cm}^2$ ,  $1 \times 1 \text{ }\mu\text{m}^2$ ) for the structures shown in Figure 6-1. Due to material contrast, iron deposits on  $\text{Si}_3\text{N}_4$  membrane are expected to appear brighter than the substrate in SEM. This is simply because the backscattered electrons (BSE) and secondary electron yields are higher for more dense materials, i.e., elements with higher atomic number/mass [193]. At lower electron dose ( $0.01 \text{ C/cm}^2$ ), the smaller structures on the left in Figure 6-1 are hardly visible in comparison, e.g., to the  $4 \times 4 \text{ }\mu\text{m}^2$  structure even though the same primary electron dose was applied per surface area. This can be attributed to the proximity effects by forward- and backscattered-electrons which agglomerate for the larger  $4 \times 4 \text{ }\mu\text{m}^2$  structure. For higher doses (e.g.,  $0.1 \text{ C/cm}^2$ ,  $4 \times 4 \text{ }\mu\text{m}^2$ ), the structure starts to exceed the originally irradiated area again due to the proximity effects discussed above.

In the AG process, the additionally deposited material and thus the thickness of the structure can be controlled by the subsequent precursor dosage time  $t_G$ . In the current work, the corresponding  $t_G$  was varied from 26 min to 177 min. In Figure 6-2, a series of squares with three

## 6 On the magnetization properties of iron nanostructures via EBID plus AG

different  $t_G$  and various electron doses is shown. The images in the bottom row highlight the morphology of the corresponding deposits (white-dashed squares) at higher magnification. As indicated in Figure 6-2, there is a direct correlation between the brightness of the structures and the autocatalytic growth time. The brighter appearance of deposits with longer  $t_G$  can be attributed to the enhanced yield of BSE and thereby induced secondary electrons. This is a clear-cut indication that more Fe was deposited with longer autocatalytic growth times and is consistent with previous investigations [10, 12, 14, 23, 36]. The higher magnification images also reveal some insight into the AG process. As visible in the corresponding SEM images depicted in the bottom row of Figure 6-2, the deposit exhibits more bright features and an increasingly structured deposit with increasing  $t_G$  indicating the autocatalytic growth of clean iron nanocrystals.

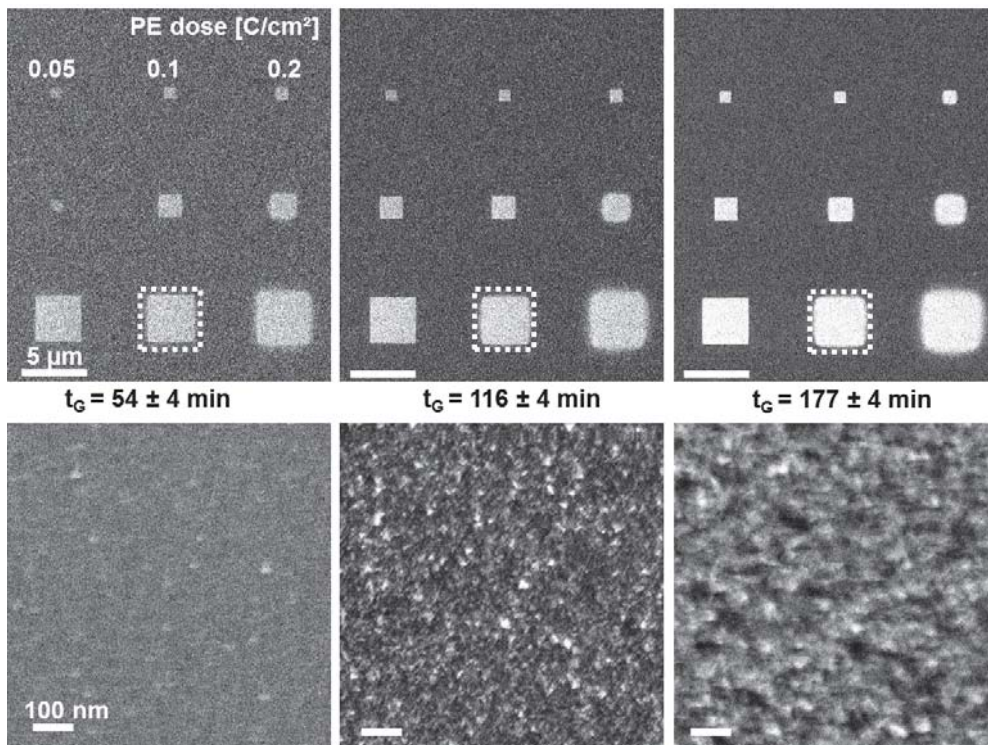


**Figure 6-2:** Sets of squares fabricated with EBID and autocatalytic growth with  $\text{Fe}(\text{CO})_5$  as the precursor on 100 nm  $\text{Si}_3\text{N}_4$  membrane. The electron doses are indicated and the time interval for each image is  $\sim 60$  min. The lower row presents the higher magnification images corresponding to the referred structures (highlighted-dashed squares). With increasing  $t_G$ , the images appear brighter, indicating that an increasing amount of Fe was deposited.

## 6 On the magnetization properties of iron nanostructures via EBID plus AG

After preparation via EBID and AG in our UHV system and subsequent characterization with SEM, the sample was transferred to the PoLux soft X-ray beamline at the Swiss Light Source (SLS) under ambient conditions for further investigation via STXM. In Figure 6-3a, Fe  $L$ -edge NEXAFS spectra of the deposits fabricated by EBID plus AG with  $\text{Fe}(\text{CO})_5$  are presented for different growth times.

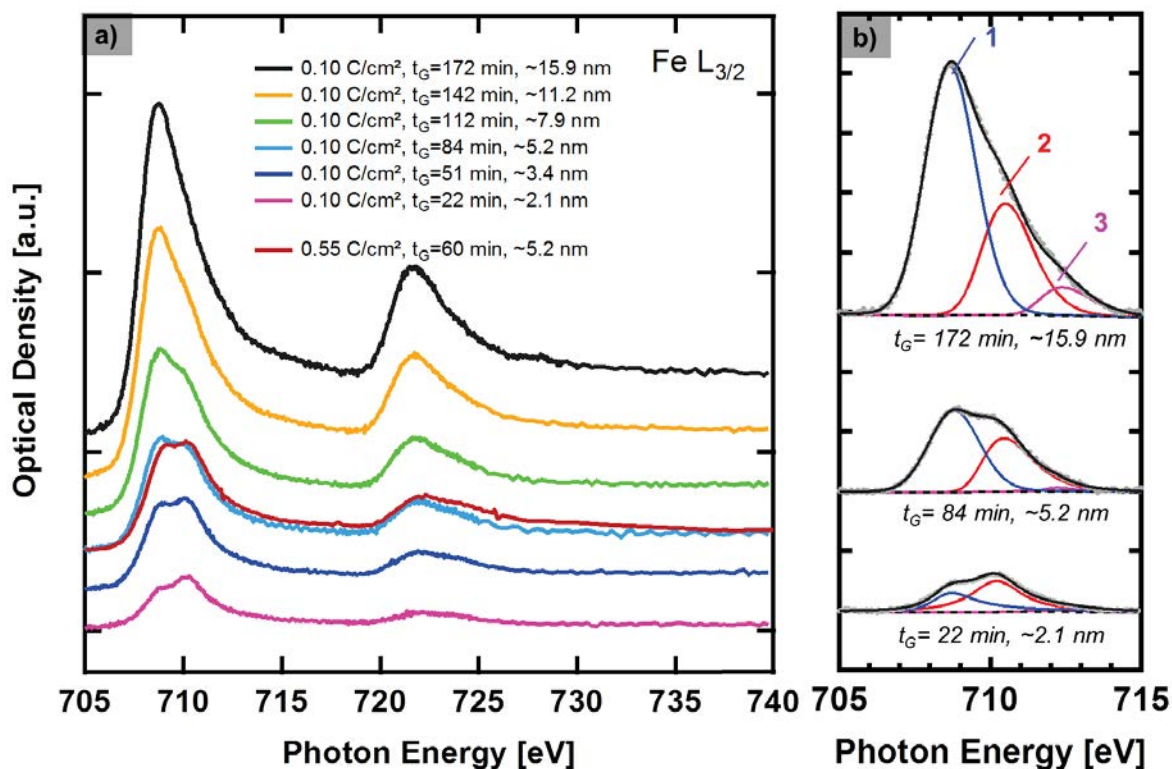


**Figure 6-3:** (a) Waterfall plot of Fe  $L$ -edge NEXAFS spectra extracted from line scans across the STXM micrographs of  $4 \times 4 \mu\text{m}^2$  deposits fabricated via EBID plus autocatalytic growth using  $\text{Fe}(\text{CO})_5$  with different growth times. (b) Selective three-peak fit of the low energy features in (a). Peaks 1, 2 and 3 can be ascribed to  $\text{Fe}^0$ ,  $\text{Fe}^{\text{II}}$  and  $\text{Fe}^{\text{III}}$  respectively.

A quantitative analysis of the iron oxidation states within the deposits was achieved by fitting of the Fe  $L_3$ -peak energy region (705-717 eV) with respective Lorentzian functions for each oxidation state (Figure 6-3b). It should be noted that a more elaborate analysis requires detailed information on the sample composition or respective simulations [194-197]. Three main peaks (708.9, 710.5 and 712.5 eV) at the Fe  $L_3$ -edge can be identified and assigned to different

## 6 On the magnetization properties of iron nanostructures via EBID plus AG

iron oxidation states ( $\text{Fe}^0$ ,  $\text{Fe}^{\text{II}}$ , and  $\text{Fe}^{\text{III}}$  respectively). After EBID with shorter AG time ( $t_G = 21$  min in Figure 6-3b), the deposit appears to consist mainly of iron oxide. With increasing  $t_G$  and thus increasing amount of deposited iron, the oxide component shrinks in comparison to the metallic Fe component, i.e., at 50 min AG time, the metallic state and oxide state are almost equal. After longer growth time (172 min), a large metallic peak dominates the spectrum. Based on these observations and the estimation that the thickest Fe layer is only  $\sim 15.9$  nm thick (the procedure for thickness evaluation is described below), it is proposed that the oxidation of Fe under ambient conditions is self-limited at a certain oxide thickness, yielding a  $\text{Fe}_x\text{O}_y$  protection layer restricting further oxidation of the iron deposit. With the ratio of the peak area between the oxidic and metallic state peaks, the iron oxide thickness with respect to total amount of iron can be estimated (Figure 6-4).

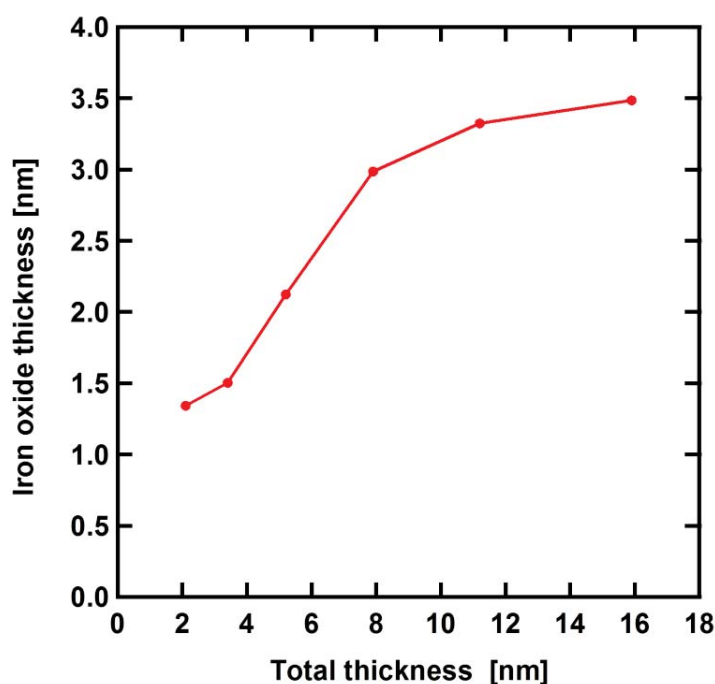


**Figure 6-4:** Iron oxide thickness vs. total thickness. With the NEXAFS peak fitting, iron oxide thickness can be evaluated through the peak area ratio between the peaks of oxidation and metallic state. The iron oxide thickness tends to saturate around 3.5 nm with the total thickness of 15.9 nm.

## 6 On the magnetization properties of iron nanostructures via EBID plus AG

It is found that saturation of the oxide species with increasing total iron thickness (saturated at around 3.5 nm with the total thickness of 15.9 nm) corroborates the model of preferential growth of  $\text{Fe}^0$  during AG. This result is in agreement with the oxidation theory of Fromhold and Cook and several experimental results [198, 199]. From the NEXAFS data discussed above, it is clear that a certain thickness of Fe deposits can be fabricated either via higher electron dose and subsequent shorter AG or by applying lower electron doses in EBID and longer AG. Another point is that for this particular thickness of Fe deposits, after the same native oxidation process, the one with lower electron dose and longer AG (0.10 C/cm<sup>2</sup>, 83 min, ~5.2 nm) shows less oxide component compared to the higher dose and shorter AG (0.55 C/cm<sup>2</sup>, 60 min, ~5.2 nm). Based on these observations, it can be concluded that the AG process results in Fe deposits with higher purity. The optical densities of the NEXAFS spectra in Figure 6-3 have been proven to be suitable for the direct determination of the layer thickness of the corresponding deposits [14]. According to this, deposits with higher brightness in SEM can be assigned to thicker layers and correspondingly appear darker in STXM (cf. Figure 6-5a).

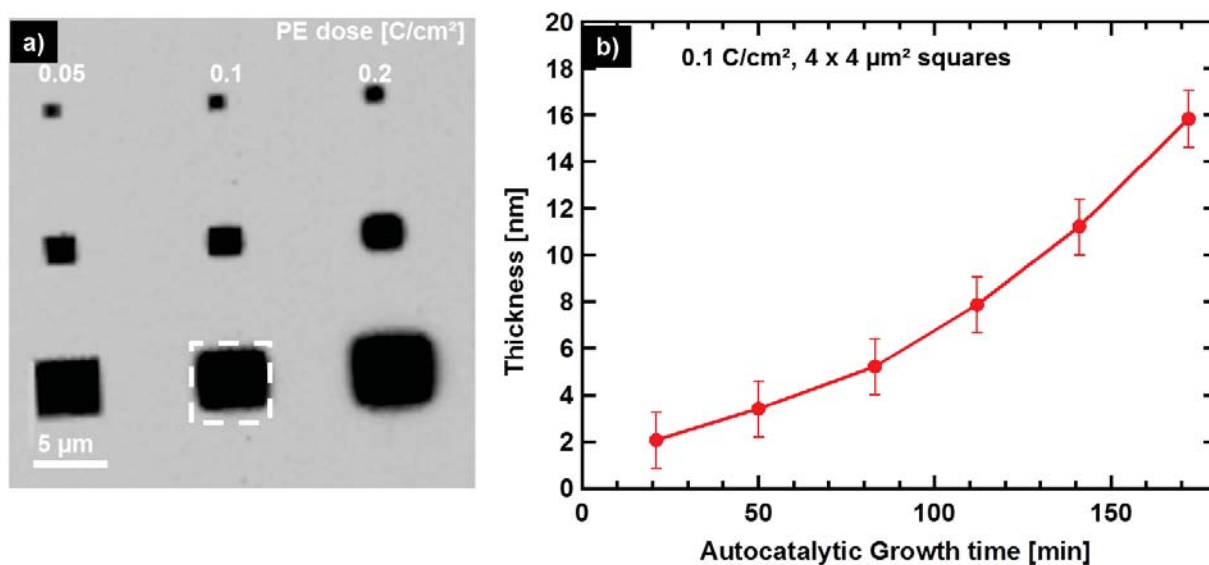


**Figure 6-5:** (a) Representatives STXM micrograph of the set of square deposits with  $177 \pm 4$  min growth time. The image was recorded at the resonant transition at 708.7 eV. Contrast enhanced as the electron dose increased. (b) Average thickness of the iron deposits (0.1 C/cm<sup>2</sup>, 4 x 4 μm<sup>2</sup>) at the Fe L<sub>3</sub>-edge (708.7 eV) versus autocatalytic growth time of Fe(CO)<sub>5</sub>. The growth process exhibits a non-linear behavior.

## 6 On the magnetization properties of iron nanostructures via EBID plus AG

As already reported in the previous work, STXM micrographs recorded at the resonant transition peak of the corresponding material can be used as a direct measure of the deposit thickness (Figure 6-5) [14]. Herein, images were recorded at 708.7 eV, which yield the strongest element-specific absorption for iron structures and thus maximize the contrast of the corresponding STXM micrographs (Figure 6-5a). Optical densities of the square structures were calculated by averaging the signal over the respective area and then referencing the signal to the background (i.e., bare Si<sub>3</sub>N<sub>4</sub> membrane). One representative STXM micrograph is depicted in Figure 6-5a for  $t_G = 177 \pm 4$  min (cf. Figure 6-2, right column). In order to apply Beer-Lambert's law, the corresponding photon energy-dependent linear absorption coefficient  $\mu(E)$  is required. Since the exact chemical composition (Fe<sub>x</sub>O<sub>y</sub>) of the deposits cannot be unequivocally determined, but certainly contains a high amount of Fe, the value of pure Fe (0.0497 nm<sup>-1</sup>) was used for the thickness evaluation according to Equation (6-1), where  $d$  represents thickness of the deposits,  $I$  and  $I_0$  indicate the incident and transmitted intensities respectively. As the contribution of the oxygen and carbon contaminations are expected to be much smaller than the Fe  $L_3$ -edge signals, the evaluated thickness value is a reasonable approximation:

$$O. D. = \mu(E) \cdot d = \ln(I_0/I) \quad (6-1)$$

Figure 6-5b depicts the thickness analysis for the selected deposits (Figure 6-5a, white-dashed square, 0.10 C/cm<sup>2</sup>, 4 x 4 μm<sup>2</sup>) produced by EBID plus autocatalytic growth with different autocatalytic growth times. It appears that the growth rate increased (steeper slope in Figure 6-5b) after a certain growth time (~100 min). By comparing with the corresponding morphology in SEM of the Fe square patterns, it seems that there is a critical size for the Fe seeds. It can be supposed that at 54 min (Figure 6-2), iron seeds are distributed statistically on the surface with considerable separations in between the particles. This may lead Fe deposits to grow not only in the vertical direction, but also laterally. When the Fe particles with critical size fully cover the surface (at ~100 min), the growth process might continue mainly in the vertical direction and Fe deposits will grow more homogeneously.

### 6.2.2 Magnetic properties of EBID iron nanostructures

First, XMCD measurements were conducted on the corresponding iron nanostructures produced by EBID plus AG with Fe(CO)<sub>5</sub> as precursor. The experiments were performed with positive and negative X-ray circular polarization. After changing the external magnetic field, an

## 6 On the magnetization properties of iron nanostructures via EBID plus AG

“equilibration time” was granted to ensure stable conditions. The applied external magnetic field could be varied in between the maximal values from -312 Oe to 312 Oe. Figure 6-6 depicts the XMCD spectra at maximum magnetic fields in reversal directions on a particular  $4 \times 4 \mu\text{m}^2$  structure ( $0.10 \text{ C/cm}^2$ ). The structure exhibits a pronounced XMCD effect at the Fe  $L$ -edge. The magnetic contrast of the Fe thin films can be achieved at the 708.8 eV (Fe  $L_3$ -edge), where magnetic circular dichroism is most pronounced.

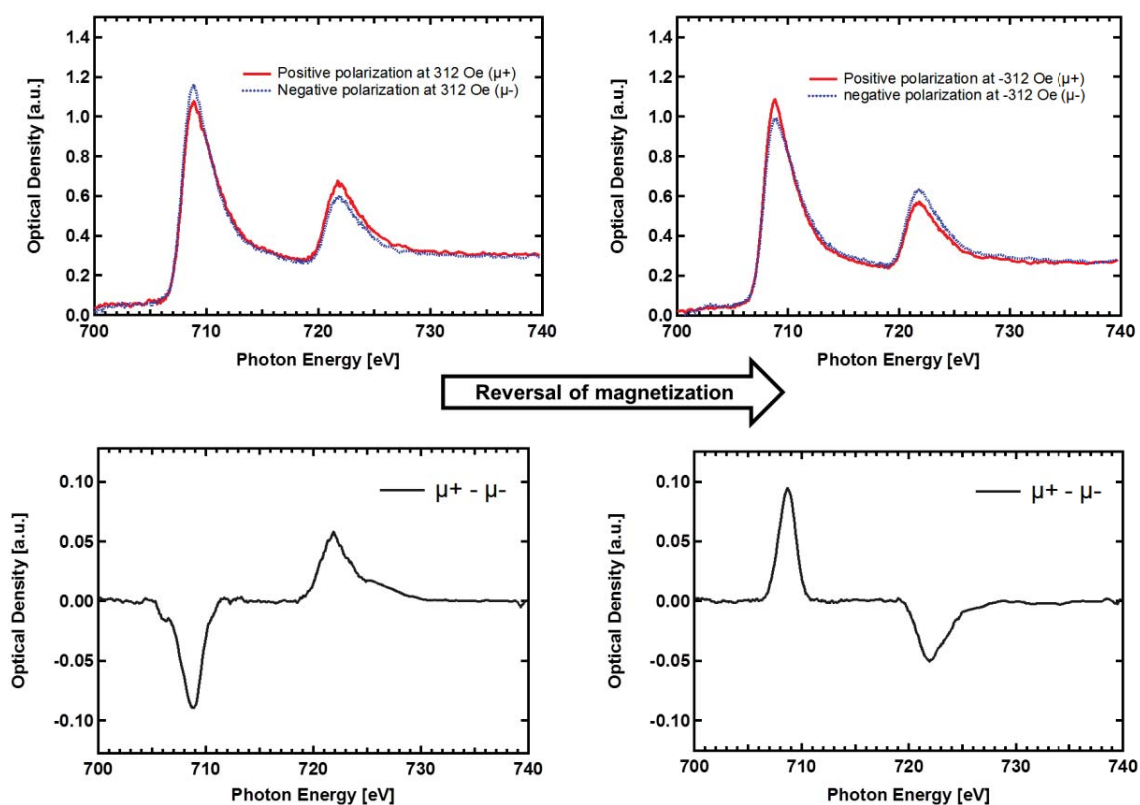


**Figure 6-6:** *Upper row:* XMCD spectra for the  $4 \times 4 \mu\text{m}^2$  structure produced by EBID ( $0.10 \text{ C/cm}^2$ ) plus autocatalytic growth of 172 min using  $\text{Fe}(\text{CO})_5$ . At both polarizations the XMCD peaks change in a characteristic way. **Lower row:** dichroic signals calculated from the one shown in the upper row.

In order to gain insight into the spatial development of the corresponding magnetic domains of the EBID structures, XMCD contrast at Fe  $L_3$ -edge has been used for STXM micrograph recording. By recording the STXM micrographs of the respective magnetic deposit for both

## 6 On the magnetization properties of iron nanostructures via EBID plus AG

positive and negative circular polarization, the XMCD contrast can be visualized. The individual images were normalized to the non-magnetic reference, i.e., the pristine membrane, to account for changes in overall image intensity, followed by a pixel-based evaluation of  $\mu^+ - \mu^-$ . Thus Equation (6-2) was used to obtain the magnetic signal for each applied field:

$$I_{mag} = \frac{P_{\mu^+}}{BG_{\mu^+}} - \frac{P_{\mu^-}}{BG_{\mu^-}} \quad (6-2)$$

While  $I_{mag}$  refers to the magnetic signal (which is used for XMCD images in Figure 6-7 and 6-8),  $P_{\mu^+}$ ,  $P_{\mu^-}$  are the average pixel intensities of the square structures recorded with positive and negative circular polarization respectively, and  $BG_{\mu^+}$ ,  $BG_{\mu^-}$  are the corresponding background intensities. This magnetic signal is displayed in the following XMCD contrast micrographs.

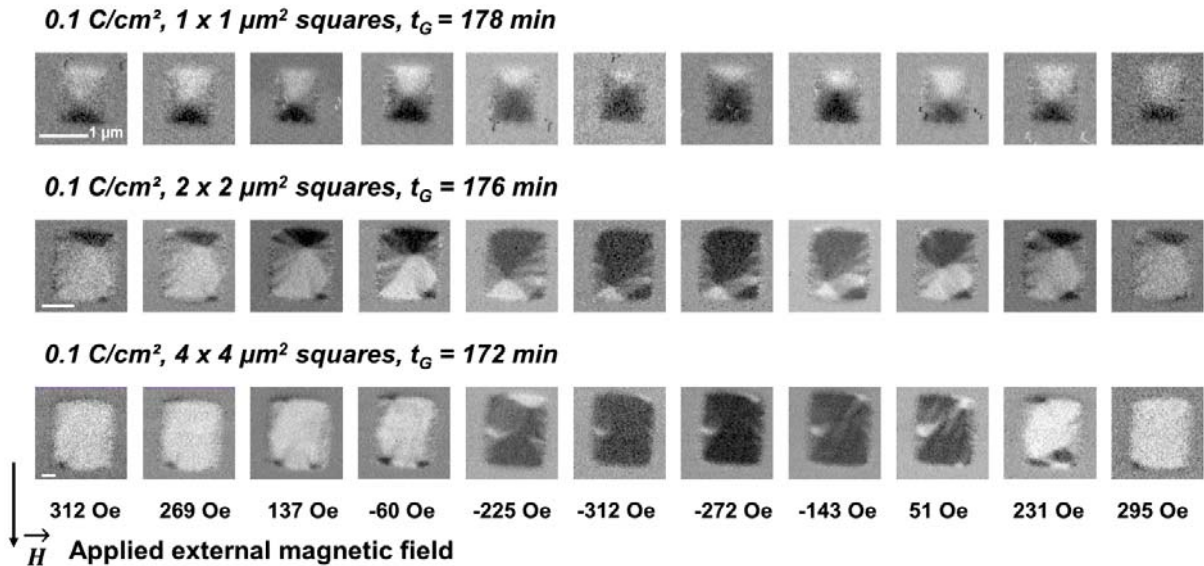


**Figure 6-7:** STXM micrographs with XMCD contrast upon variation of the external magnetic field of different square deposits fabricated with EBID plus autocatalytic growth with  $Fe(CO)_5$  precursor. The evolution of magnetic domains versus the applied magnetic field, in particular the shift of the vortex core is clearly visible for the upper two rows.

Figure 6-7 depicts the evolution of the magnetic domains with varying external magnetic field for squares with different sizes. For a 1 x 1 μm<sup>2</sup>, the sample is not fully saturated even at the highest achievable magnetic fields (±312 Oe). In this case, typical Landau structures can be observed with four triangular domains separated by 90° domain walls [184]. In the center of the

domain structure, a vortex core is located, which has a magnetization perpendicular to the plane. With the magnetic field variation, an apparent movement of the domain walls and the vortex core is observed. The white appearance reflects parallel alignment between the magnetization direction and the applied magnetic field, while a black appearance represents an antiparallel alignment. For a  $2 \times 2 \mu\text{m}^2$  pattern, similar Landau domains are observed. However, many smaller domain structures appear during the magnetic field variation.

When the size is increased to  $4 \times 4 \mu\text{m}^2$ , single vortex state cannot be distinguished and the magnetization switches rather abruptly compared to that of the smaller size square patterns. This behavior is attributed to an increased number of defects and/or grain boundaries of the nanocrystallites in the larger deposit as discussed for other magnetic microstructures [162, 184, 188, 200].

As mentioned above, two STXM micrographs can be achieved with positive and negative X-ray circular polarization for each applied magnetic field strength. By varying the magnetic field, the contrast in the STXM micrographs will follow the changes, reflecting different domain distributions. As the pixel intensity in the XMCD image is a direct measure of the local magnetization via  $(\mu^+ - \mu^-)$  at the  $L_3$  peak energy, an average magnetization of the structure at a given field can be calculated by taking the average of the pixel intensity. If this value is normalized to the average intensity at the maximum external field in both directions, magnetization curves are obtained as shown in Figure 6-8 and 6-9. All images were recorded at the resonant transition peak at 708.7 eV. The obtained magnetic signal for the  $4 \times 4 \mu\text{m}^2$  ( $0.10 \text{ C/cm}^2$ ) structures at different values of applied magnetic field has been normalized to that at the highest magnetic field. Figure 6-8 shows the hysteresis loop of the respective structure with 142 min AG time.

First, the maximum magnetic field strength of +312 Oe was applied to fully saturate the in-plane domain, which is in-line with the bright contrast in STXM micrographs with XMCD contrast. When the magnetic field was gradually reduced to -100 Oe, some domains with opposite magnetization (black in STXM micrographs with XMCD contrast) start to nucleate at the square nanostructure. An abrupt domain alignment can be observed as the magnetic field is varied from -100 Oe to -200 Oe and as a consequence most of the surface exhibits the opposite magnetization, which appears black contrast in the XMCD images. Upon further reduction of the

## 6 On the magnetization properties of iron nanostructures via EBID plus AG

magnetic field, the whole square will switch to the opposite magnetization state, i.e., homogenous black appearance. To drive the full hysteresis, the magnetic field is varied from -312 Oe to 312 Oe. At about 150 Oe, small domains with opposite magnetization are observed and finally, the magnetic state will recover to the initial state.

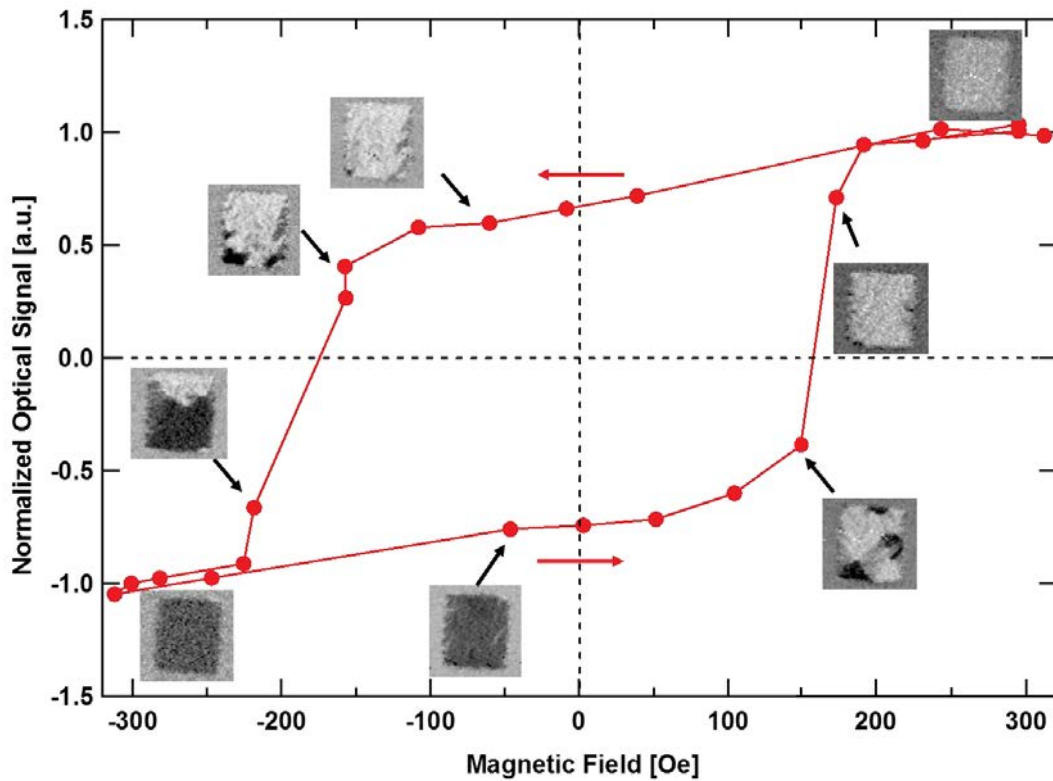


**Figure 6-8:** Hysteresis loop of  $4 \times 4 \mu\text{m}^2$  structure fabricated via EBID ( $0.10 \text{ C/cm}^2$ ) plus autocatalytic growth ( $t_G = 142 \text{ min}$ ) with  $\text{Fe}(\text{CO})_5$ . Domain distribution in the deposit for some values of the applied magnetic field is indicated with STXM micrographs. White contrast represents parallel alignment between the magnetization direction and the applied magnetic field, and black contrast vice versa.

With the same data evaluation, hysteresis loops of square nanostructures produced via EBID ( $0.10 \text{ C/cm}^2$ ) plus various autocatalytic growth times  $t_G$  were determined. A selection of corresponding hysteresis loops is depicted in Figure 6-9a. From this data, immediately a general trend can be extracted, that is: the width of the loops, which reflects the magnetic coercivity  $H_C$ , increases with increasing deposit thickness.

## 6 On the magnetization properties of iron nanostructures via EBID plus AG

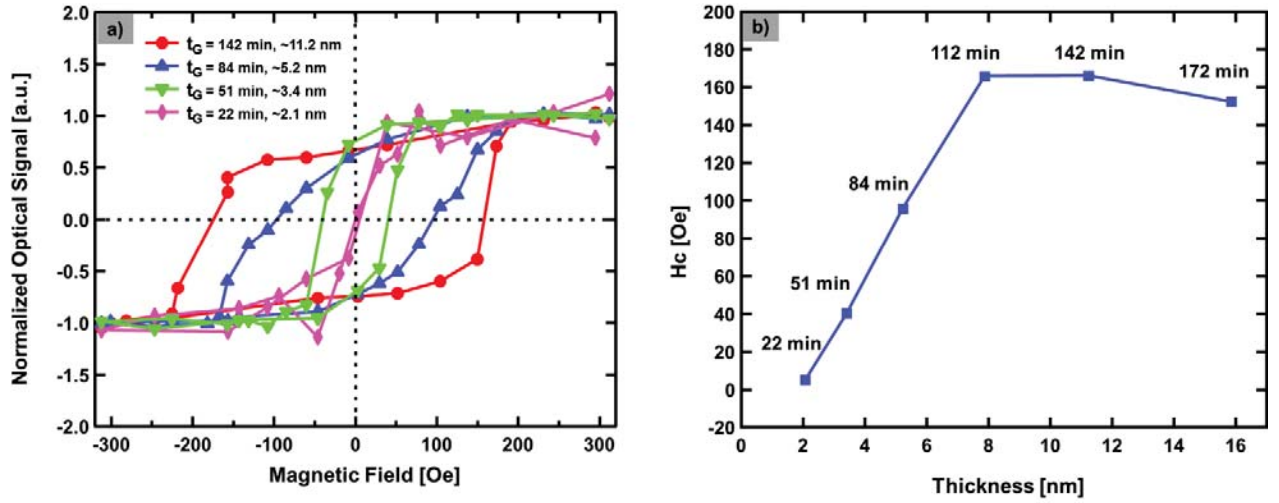


**Figure 6-9:** (a) Selected hysteresis loops of the  $4 \times 4 \mu\text{m}^2$  nanostructures produced via EBID ( $0.10 \text{ C/cm}^2$ ) with different autocatalytic growth times by using  $\text{Fe}(\text{CO})_5$  as precursor. (b) Magnetic coercivity ( $H_c$ ) measured from Figure 5.3-9a as a function of the deposit thickness. The corresponding autocatalytic growth times are indicated.

In the following, the thickness dependence of magnetic properties of the produced Fe deposits is discussed. Rodriguez et al [73] interpreted their results from Kerr microscopy of Fe nanowires as a bell-shape profile of the deposit and the assumption that a 5 nm thick oxide layer ( $\text{Fe}:\text{O} = 1:1$ ) forms at the deposit/vacuum interface. This thin FeO layer exhibits paramagnetic behavior, and thus does not contribute to the magnetic volume as the source for  $H_c$ . However, the thinner structure ( $0.10 \text{ C/cm}^2$ ,  $4 \times 4 \mu\text{m}^2$ , 51 min,  $\sim 3.4 \text{ nm}$ ) still shows ferromagnetic behavior even though it is expected to fully consist of natively oxidized Fe (exposure to the air) as indicated by the NEXAFS spectrum shown in Figure 6-3. It is also proved that Fe nanoparticles smaller than a critical size ( $\sim 8 \text{ nm}$ ) will fully oxidize in the air to  $\text{Fe}_2\text{O}_3$  [201]. Thus, it can be proposed that in this case the thin native oxide is not the paramagnetic FeO species but rather  $\text{Fe}_2\text{O}_3$  (used as material for magnetic storage and audio recording media as classical audio tapes) or  $\text{Fe}_3\text{O}_4$ , which both exhibit ferrimagnetism and therefore would contribute to a coercive field characterized by  $H_c$ . For the increase of the  $H_c$  with the thickness in our regime, a more general model used by Yuan and de Teresa should be applicable [73, 202]:

$$H_c = H_\infty + \alpha(t/w) \quad (6-3)$$

## 6 On the magnetization properties of iron nanostructures via EBID plus AG

where  $H_\infty$  is the coercive field of an infinite thin film,  $\alpha$  is the anisotropy factor and  $t/w$  is the ratio between thickness ( $t$ ) and width ( $w$ ) of the structure.

It also has been proved that the coercive field of cobalt nanowires grown by EBID follows this  $t/w$  dependence [70]. In this case, the width is constant (4  $\mu\text{m}$ ) and  $H_C$  increases approximately linearly from  $\sim 40$  Oe at 3.4 nm to  $\sim 160$  Oe at 8 nm thickness. For thicker deposits up to 16 nm,  $H_C$  appears to saturate or even slightly decrease around 160 Oe. This behavior of  $H_C$ , which is not reproduced by Equation (6-3), can be ascribed to the change of the magnetization reversal mode described in references [73, 202]. If the thickness increases, three-dimensional switching mechanisms, such as vortex formation, come into play and reduce the coercivity. As discussed above, complete hysteresis curves cannot be acquired for the structures smaller than 4 x 4  $\mu\text{m}^2$ , due to the fact that the maximum external field (in our present study) is not sufficient to induce complete magnetization reversal. This finding in combination with the clearly visible vortex domain/Landau structures (e.g., Figure 6-7, two upper rows) allows the conclusion that the corresponding coercivity values  $H_C$  rise with reduced lateral size of the deposited Fe square nanostructures, which is also in line with Equation (6-3).

### 6.3 Conclusions

The fabrication and microscopic, chemical and magnetic characterization of thin iron structures fabricated via a combined EBID and AG approach in UHV was reported and discussed. While the originally deposited structures are composed of practically pure iron, in particular when fabricated via AG, exposure to ambient conditions induces surface oxidation of the structures. In agreement with previous reports, the oxidation process appears to be self-limiting as discussed in the context of corresponding NEXAFS spectra of the deposits. The characterization of the magnetization reversal was achieved via XMCD contrast in STXM analysis. Thereby, the microscopic development of the corresponding magnetic domains could be observed as a function of the external magnetic field and used for the evaluation of the corresponding coercivity values  $H_C$ . Interestingly, even for very thin deposits in the range 3.4 – 8 nm hysteresis loops are observed, i.e., a ferromagnetic signature, even though the corresponding NEXAFS spectra as well as previous publications indicate that at least deposits thinner than 5 nm should be fully oxidized. This native oxide layer is proposed to consist of ferrimagnetic

## 6 On the magnetization properties of iron nanostructures via EBID plus AG

$\text{Fe}_2\text{O}_3$  or  $\text{Fe}_3\text{O}_4$  and not of the paramagnetic  $\text{FeO}$ .  $H_C$  values are determined for a set of  $4 \times 4 \mu\text{m}^2$  deposits with thicknesses ranging from 3.4 to 16 nm. When the thickness of the deposits varies between 3.4 and 8 nm, a steady increase of  $H_C$  from  $\sim 40$  Oe to more than 160 Oe is observed, which slightly decreases or almost remains constant upon increasing the thickness from 8 to 16 nm. The unique AG approach allows almost completely preventing the occurrence of electron-induced proximity effects, usually yielding thin deposits at the rim of the originally intended shape, which strongly influence the magnetic reversal properties.

In summary, it is possible to fabricate thin structures with controllable chemical composition (e.g., similar thickness with different oxide content) and thickness via EBID and AG. Thereby, the thickness and chemical composition of the nanostructures are found to be strongly correlated with their magnetic properties such as the magnetic coercivity, which gives perspective for designing functional magnetic structures with desired properties. Especially, the AG process can indeed provide a powerful route towards the fabrication of particularly clean metallic deposits and thus functional magnetic nanostructures, which deserves more investigation in the near future.



## 7 Secondary CNT growth on EBID-deposits

### 7.1 Introduction

CNTs have attracted enormous interest concerning their potential as functional building blocks in applications like molecular electronics, sensors and energy storage [24, 26, 80, 83]. As introduced in Chapter 2, one of the common synthesis methods for CNTs is CVD [78, 79, 81], in which usually statistically distributed metal-containing particles act as catalysts for the CNT growth. Thereby not only the more or less random position of the catalyst particles determine the position of the CNT but also the size, chemical composition and the surface structure of the catalyst influence the growth of the CNTs [105, 106, 108, 109]. Therefore, it is important to fabricate catalysts with controllable size and chemical composition at the desired spatial position, in order to fabricate CNTs in well-defined configurations towards building integrated systems for micro- and nanoelectronics.

In this contribution, EBID is explored for the controlled and localized fabrication of catalytic active deposits for the subsequent growth of corresponding CNTs with precise positioning. In previous publications, it was shown that either Fe or Co deposits fabricated via EBID are principally feasible for CNT growth [32-34]. However, the reported results either lack in the control of the CNT morphology, showing only initial states of CNT growth, or usually the corresponding EBID deposits contain high amounts of carbon as contamination. For example, Sharma et al. [33] presented the possibility to control the deposited particle size through varying the EBID parameters (i.e., electron dose and beam current) but no further CNTs grown on these different Fe nanoparticles were shown. Carbon contamination had a pronounced negative influence on the activity of EBID deposits. The yield of CNTs on these deposits was low and post-treatments such as oxygen plasma exposure were necessary to clean the EBID-Co deposits before the corresponding CVD experiment could be conducted [34]. The existence of the corresponding carbon contaminations were traced back to deposits from the residual gas of the high vacuum environment and the dissociation of the carbon containing precursor ligands [32]. With our “surface science approach” to EBID, i.e., working in an ultra-high vacuum environment, we are able to fabricate clean metallic deposits in particular from the precursor  $\text{Fe}(\text{CO})_5$  [10, 12, 13, 15, 22, 23, 203].

## 7 Secondary CNT growth on EBID-deposits

In the present work, Fe nanostructures fabricated via EBID and AG with the precursor  $\text{Fe}(\text{CO})_5$  in a UHV instrument were used as catalysts to synthesize well-defined CNTs with controllable morphology via CVD. The influence of the chemical composition and in particular of the fabrication parameters (electron dose and AG time) of Fe deposits were investigated, in respect to their suitability and properties as seeds for secondary CNT growth via subsequent CVD. One ultimate goal in that respect is to fabricate Fe deposits on which only one CNT grows, i.e., to exactly position an individual CNT. Another desirable CNT arrangement is to grow the so-called CNT forests.

In order to control the morphology of CNTs such as forming high density vertically aligned CNTs referred to as forest, a thin  $\text{Al}_2\text{O}_3$  layer was introduced to improve the yield of CNTs grown on EBID-Fe deposits. The significant increase of the yield can be attributed to a reduced Fe deposits mobility on the  $\text{Al}_2\text{O}_3$  substrate, hindering the coalescence of Fe nanoparticles, resulting in more active sites for CNT nucleation [50, 92, 101]. A peculiar lifted-up CNTs nanostructure was also observed for the first time. On the basis of EDX spectroscopy and SEM data, the corresponding mechanism will be discussed.

With the purpose of synthesizing single-walled carbon nanotubes (SWNTs) with a site-specific control, Co nanostructures can be fabricated with EBID and AG in the UHV, using  $\text{Co}(\text{CO})_3\text{NO}$  as the precursor. The subsequent CVD experiment was carried out on these Co containing deposits without any post-treatments. The temperature of the CVD process was lower than the one used in the case of Fe catalysts. CNTs with high yield and long length were fabricated on the Co deposits.

## 7.2 Results and discussion

### 7.2.1 CNT growth on EBID-Fe deposits

The first aim of experiments was to obtain proof of principle that the localized fabrication of CNTs at EBID deposits works with the approach as proposed. Figure 7-1 depicts the result of an exploratory experiment to locally synthesize CNTs via CVD on  $\text{SiO}_x/\text{Si}(100)$ , using Fe-containing deposits (Figure 7-1b) as CVD catalysts. The latter were fabricated via EBID (1.2 nC/point) and subsequent AG (~60 min autocatalytic growth time) in our UHV instrument. Here,

## 7 Secondary CNT growth on EBID-deposits

the EBID process was performed as a point irradiation, i.e., the electron beam rests at a fixed position for a certain amount of time and thus a certain local electron dose.

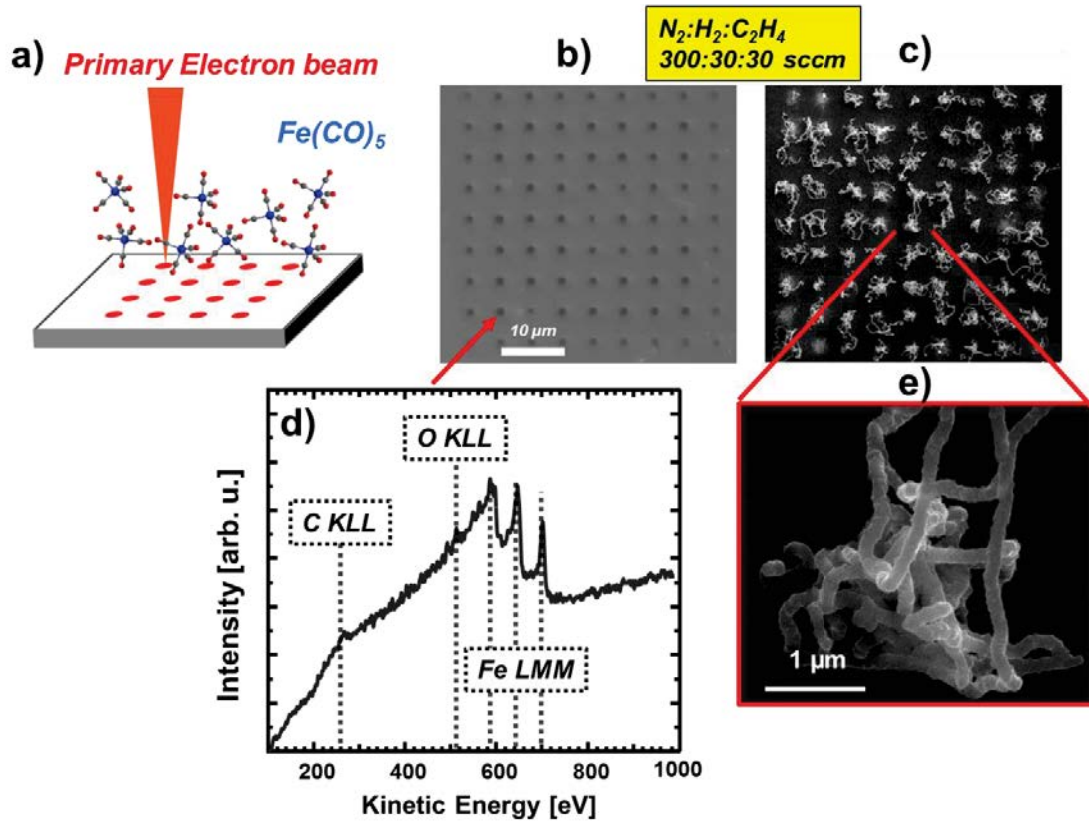


**Figure 7-1:** (a) Scheme of the EBID process with  $\text{Fe}(\text{CO})_5$  as precursor molecule, producing a point-matrix of Fe deposits. (b) SEM micrograph of a point-matrix of Fe deposits on  $\text{SiO}_x/\text{Si}(100)$  fabricated via EBID (1.2 nC/point) plus AG (~60 min growth time). (c) and (e) SEM micrographs of CNTs grown site selectively on the pre-deposited Fe structures. The CVD temperature was 1163 K with a gas flow of  $\text{N}_2$ ,  $\text{H}_2$  and  $\text{C}_2\text{H}_4$  (300:30:30 sccm) mixture. (d) Auger electron spectrum of the indicated Fe deposit.

The enlargement of the deposits with increasing electron dose is due to complex proximity effects like electron backscattering and electron forward scattering in the already built deposit [11, 16]. In the depicted micrograph (Figure 7-1b), the actual iron deposits obviously appear darker than the substrate in SEM. The CVD experiment was carried out at 1163 K, with the following precursor composition  $\text{N}_2:\text{H}_2:\text{C}_2\text{H}_4$  (300:30:30 sccm). The chemical composition of Fe deposits before the CVD experiment was characterized by in-situ AES as depicted in Figure 7-1d.

## 7 Secondary CNT growth on EBID-deposits

The investigated deposit (by EBID plus AG) consists of Fe (~87 at.%), C (~7 at.%) and O (~6 at.%). The low carbon and oxygen contaminations in the deposits can be attributed to residual gases adsorbed within the time span between electron beam induced (EBI) deposition and acquisition of the Auger electron spectra (>24 h). It is important to note that the EBID-Fe samples were transferred under ambient conditions to the CVD apparatus at the University of Szeged, Hungary. Therefore, oxidation of the Fe deposits is anticipated, forming  $\text{Fe}_2\text{O}_3$  and  $\text{Fe}_3\text{O}_4$ , as discussed previously [13]. However, exposure to  $\text{H}_2$  for ten minutes before the CVD and simultaneous dosage of the latter reducing agent during CVD is a powerful method to reduce the eventually oxidized Fe deposits [204]. Therefore, the influence of the oxidation due to the prior exposure to ambient is regarded as minor if not negligible.

The comparison of Figure 7-1b and Figure 7-1c, i.e., the sample before and after the CVD process, reveals that the approach was indeed successful. The blow-up of the indicated region depicted in Figure 7-1c reveals the typical appearance of CNTs in SEM. The result is striking since each individual EBID-Fe deposit acted as a catalyst for the growth of a “knawel” of CNTs. This proves that Fe deposits fabricated via EBID and AG from  $\text{Fe}(\text{CO})_5$  in the UHV are very suitable for localized CNT growth with high yield at predefined positions. Even though the results obtained in this experiment are a proof of principle, one certainly targets to gain more control over the CNT fabrication process, e.g., one ultimate goal is to grow exactly one CNT at each EBID deposit position. To do so, it is necessary to investigate the influence of various parameters (e.g., electron dose and AG time), which will be addressed and discussed in the following sections.

### 7.2.2 Optimization of Fe deposits fabrication

As already mentioned earlier the chemical nature and the size of the catalytic active particles are anticipated to be one determining factor for the length and diameter of the CNTs grown subsequently via CVD. To get more insight into the corresponding relations we systematically varied main fabrication parameters for the Fe deposits, i.e., the electron dose and the autocatalytic growth time [13, 14].

The left column in Figure 7-2 depicts matrixes of 9 x 9 EBID deposits from  $\text{Fe}(\text{CO})_5$  fabricated via point exposure with different electron doses (0.25 nC, 0.5 nC and 1.2 nC) which all experienced an subsequent AG time of ~60 min along with zoom-ins of representative

## 7 Secondary CNT growth on EBID-deposits

deposits. As expected the diameter of the black core, which we identify as the main iron deposit, grew with the applied electron dose from barely visible at 0.25 nC over ~120 nm at 0.5 nC to ~330 nm at 1.2 nC. The bright fringes around the black spots in the left column of Figure 7-2 are attributed to the proximity effects [11, 16]. The size of the black center and the white features both increases with the applied electron dose as expected.

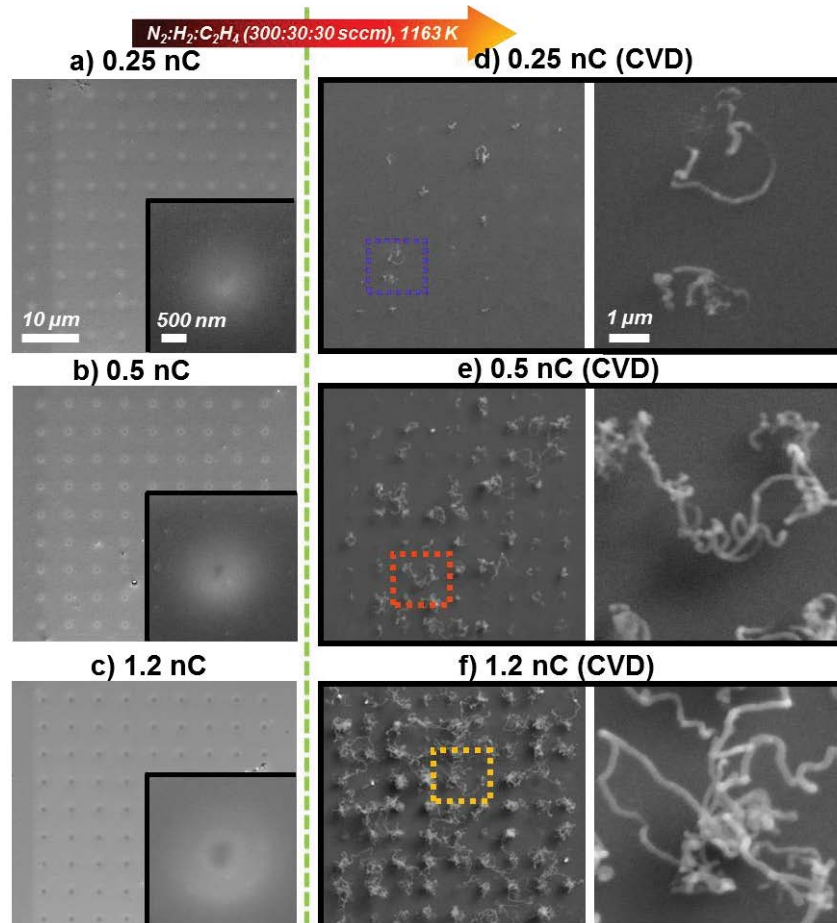


**Figure 7-2:** SEM micrographs of Fe EBID deposits before and after CVD experiment (1163 K,  $N_2:H_2:C_2H_4 = 300:30:30$  sccm). Fe deposits fabricated with (a) 0.25 nC (b) 0.5 nC, (c) 1.2 nC electron dose per point. (d), (e) and (f) are the corresponding results after the CVD experiment. An AG time of ~60 min was applied in all cases depicted.

The SEM micrographs in the right column of Figure 7-2 depict the same areas after the corresponding CVD experiment. Inspection of these images reveals that indeed CNTs were grown with different yield and appearance on the pre-fabricated Fe deposits. It becomes

## 7 Secondary CNT growth on EBID-deposits

immediately clear that the yield of CNTs increases with the applied electron dose for EBID fabrication and thus the determined diameters of the deposits. In the case of 0.25 nC, roughly only about 15% of the point deposits acted as seeds for CNT growth, i.e., only few rather short CNTs were synthesized on the Fe point-matrix deposits (Figure 7-2d, see also Appendix Figure 13-2 for full statistics and evaluation scheme). This number significantly increases to ~70% active EBID deposits for the point exposure of 0.5 nC (Figure 7-2e). Finally, in the case of 1.2 nC, all Fe deposits were active for localized CNT growth and their length is also obviously significantly increased in comparison to the CNTs grown on EBID deposits with lower electron dose (Figure 7-2f). Considering the above formulated goal to produce one individual CNT on each Fe deposit of the point-matrix, one has to state that it is difficult to judge if one or maybe more than one CNT grew at the deposit position. This is due to the fact that in particular for the highest electron dose the CNTs appear as knawels in SEM, which makes it difficult to identify individual CNT. However, at this point, one can conclude that an electron point dose between 0.5 nC and 1.2 nC in combination with AG for ~60 min is well suitable to fabricate deposits from  $\text{Fe}(\text{CO})_5$  for the localized growth of one CNT.

With the next experiment the influence of the AG time was investigated. Therefore, again three 9 x 9 point-matrixes of Fe deposits were fabricated this time with varying AG times (~37 min, ~58 min and ~92 min) but always with 1.2 nC electron point dose, as depicted in Figure 7-3. As expected the Fe deposits can be assigned to the black features in SEM, which are depicted in the zoom-ins in the left column of Figure 3. The diameter of the corresponding deposits from  $\text{Fe}(\text{CO})_5$  increases from ~220 nm at ~37 min AG time, ~330 nm at ~58 min AG time to ~340 nm at ~92 min AG time. First of all, it can be stated that the size of the deposits is reproducible by comparing the current result of ~330 nm at ~58 min/1.2 nC with the same result from the previous experiment for the very similar deposition parameters of ~60 min/1.2 nC. The same holds true for the results shown in Figure 7-1. Thus three very similar results were achieved with the same parameters from three different experimental runs, which indicate that the reproducibility is indeed quite good. Otherwise, from ~37 min to ~58 min AG time, the diameter increases by 110 nm, whereas from ~58 min to ~92 min the diameter only increases by ~10 nm. Indeed, the yield and appearance of the CNTs grown on the Fe deposits with very similar diameters, i.e., the ones with ~58 min and ~92 min AG time are also very similar. On both of the latter 9 x 9 matrixes practically all Fe deposits were active towards the growth of CNTs.

## 7 Secondary CNT growth on EBID-deposits

However, for the matrix with the lowest AG time of ~37 min about 30% of the EBID deposits turned out to be not active towards the secondary CNT growth and roughly half of the active ones only yield shorter CNTs and not the apparent knowels (c.f. Figure 7-3d and Appendix Figure 13-2). Based on the results discussed so far, it can be concluded that the yield and appearance of the fabricated CNTs are directly related to the size of the catalyst particle fabricated via EBID and AG.

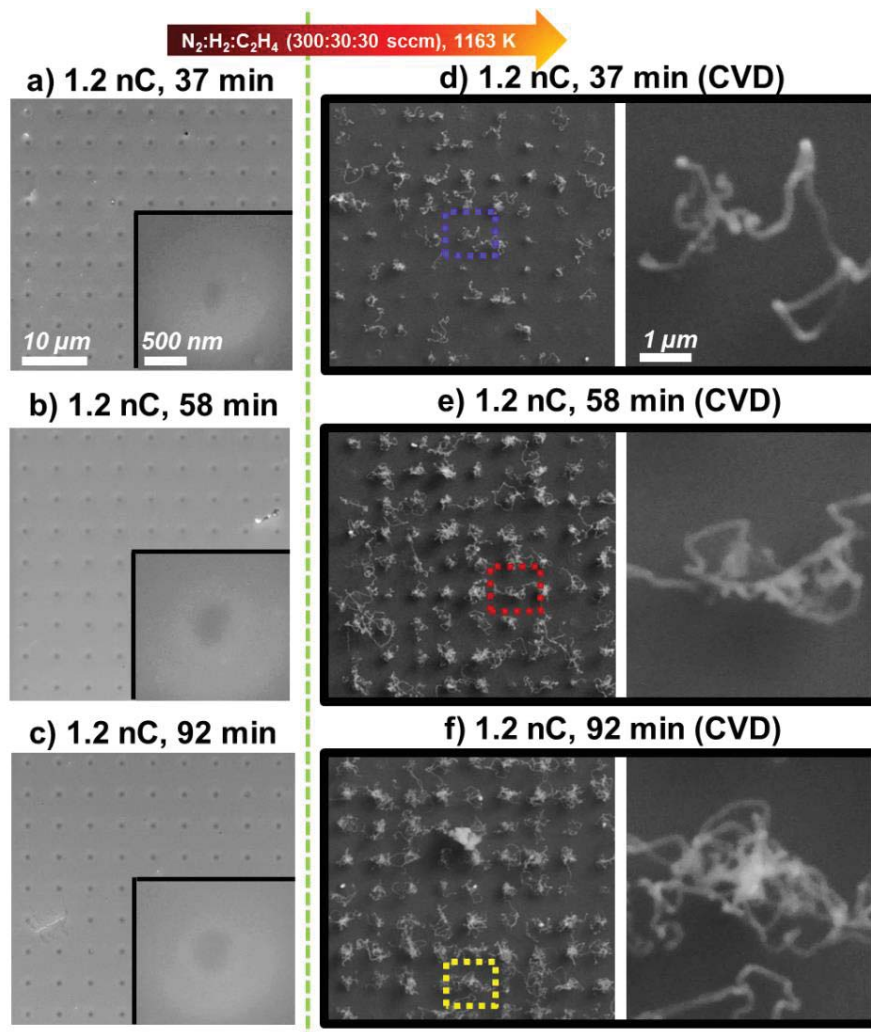


**Figure 7-3:** SEM micrographs of Fe EBID deposits before and after CVD experiment (1163 K,  $N_2:H_2:C_2H_4 = 300:30:30$  sccm). Fe deposits fabricated with (a) ~37 min, (b) ~58 min and (c) ~92 min AG time. All deposits were fabricated with 1.2 nC electron point dose. (d), (e) and (f) are the corresponding results after the CVD experiment.

## 7 Secondary CNT growth on EBID-deposits

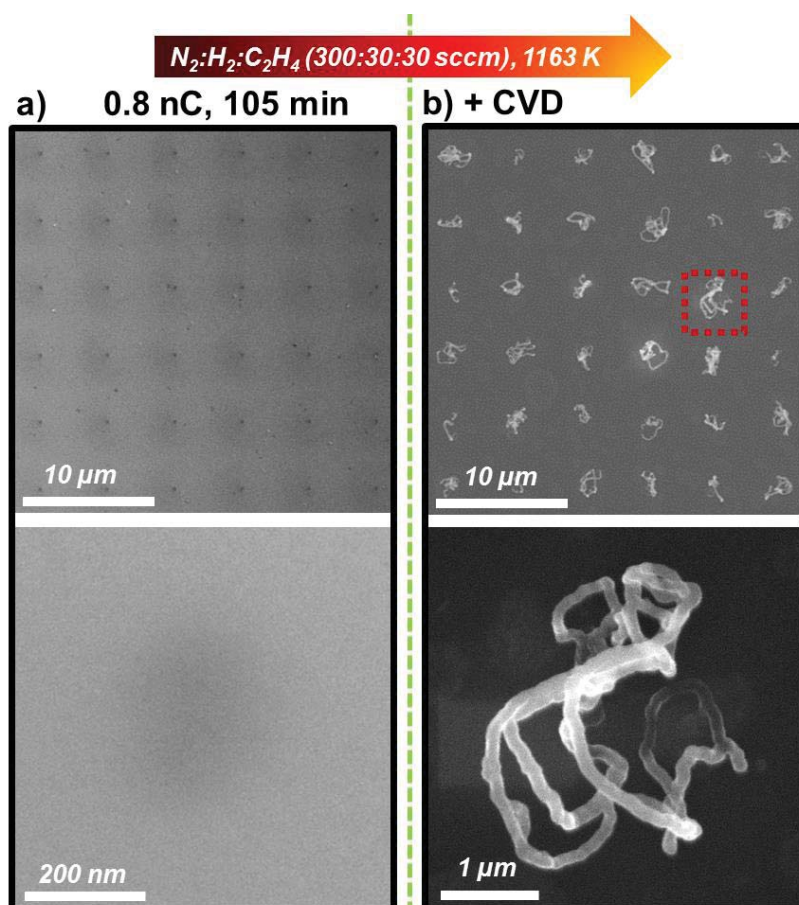


**Figure 7-4:** (a) 6 x 6 point-matrix of Fe deposits which were fabricated via EBID (0.8 nC) with subsequent ~105 min AG. (b) Well-defined individual CNTs grown on the deposits depicted in a. Parameters used in the CVD experiment: 1163 K with  $N_2:H_2:C_2H_4$  (300:30:30 sccm).

According to the previous results we now revisit one of the main goals, which was the fabrication of one individual CNT per EBID deposit. As evident from Figure 7-2, electron doses between 0.5 nC and 1.2 nC appear promising. In addition a sufficient AG time  $\geq 60$  min should be applied as extracted from the data depicted in Figure 7-3. Indeed, a successful attempt is depicted in Figure 7-4 with a 6 x 6 point-matrix realized with 0.8 nC and ~105 min AG time. The corresponding SEM micrographs after CVD in Figure 7-4b document that exactly one CNT was grown via CVD at each of the 36 EBID deposits. Even though with this result an important goal was reached, one also has to state that the length and shapes of the individual CNTs vary a bit, i.e., the tubes are not uniform. This can be explained to some extent by the inherent nonlinearity of catalytic processes. Considering the large number of tunable parameters within

the complex CNT fabrication process (EBID, AG and CVD) it is also clear that there is still plenty of room for improvements.

### 7.2.3 Fabrication of CNT forests on Al<sub>2</sub>O<sub>3</sub> support layer

After the successful exploration of the localized fabrication of individual CNTs at predefined position, the next step was to target the growth of CNT forests which represent appealing materials for different applications, such as super-capacitor electrodes [26, 205], nanoscale actuator [206], and cooler on chips [24]. A CNT forest is defined as CNTs grown with high density and vertical alignment. Therefore, it is necessary to increase the number of the CNTs per surface area. Corresponding attempts on the native oxide surface on Si(100) used for the results presented and discussed above were not satisfying, i.e., the density of CNTs on 2-dimensional deposits, like Fe-squares, was not sufficient to form the desired forest material. An important point in this regard is probably diffusion along with Oswald ripening and segregation of the Fe deposits during the pretreatment and the CVD process itself [92, 207-209]. In this regard, an Al<sub>2</sub>O<sub>3</sub> support layer was discussed by Kim et al. as a suitable substrate to reduce the mentioned degradations of Fe catalyst structures for CNT CVD [92]. Following the latter work we also explored an Al<sub>2</sub>O<sub>3</sub> layer as support the Fe EBID structures. Figure 7-5 depicts SEM micrographs of CNTs grown on Fe EBID square structures (1 x 1, 2 x 2, and 4 x 4 μm<sup>2</sup>) on an Al<sub>2</sub>O<sub>3</sub> support. Different electron doses were applied (0.22, 0.55, and 1.10 C/cm<sup>2</sup>) with a constant AG time of ~240 min. It is important to note that the corresponding CVD experiment was carried out at 1073 K, at which no CNT growth was observed on the SiO<sub>x</sub>/Si(100) substrate with identically fabricated Fe squares. The zoom-ins in Figure 7-5 illustrate two clear trends: increased yield of CNTs with increasing square size (right column) and also increasing yield with increasing electron dose (bottom row). Both observations are in line with the previous observations and can be understood by apparent consideration.

It can also be stated that the overall yield of the CNTs increased significantly when an Al<sub>2</sub>O<sub>3</sub> layer was used as the substrate. As discussed before this can be conclusively explained by the reduction of the Fe mobility on the Al<sub>2</sub>O<sub>3</sub> surface, resulting in less Fe coarsening /segregation during the heating process and thus leaving more catalytically active Fe sites for CNT growth [92]. According to literature, the Al<sub>2</sub>O<sub>3</sub> itself does not directly contribute to the CNT growth, e.g., by catalytic carbon source dissociation [101]. As depicted in Figure 7-5f, a spatially well-defined

## 7 Secondary CNT growth on EBID-deposits

4 x 4  $\mu\text{m}^2$  CNT nanostructure with high density was synthesized, indicating the possibility to produce CNT forest structures by further exploring the experimental parameters during CVD.

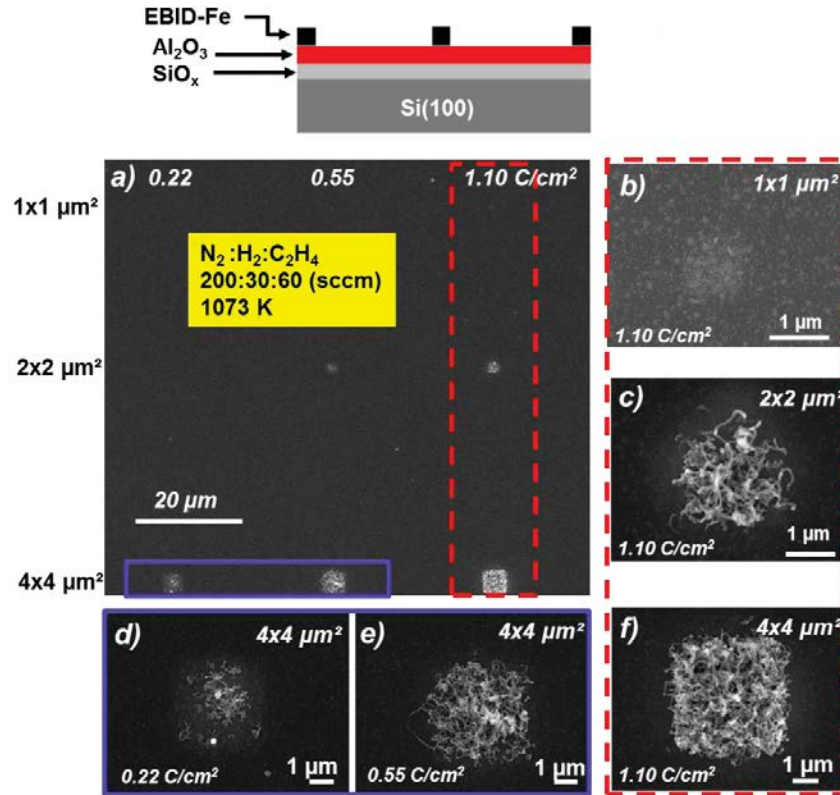


**Figure 7-5:** SEM micrographs of CNTs grown by CVD on Fe nanostructures (1 x 1, 2 x 2, and 4 x 4  $\mu\text{m}^2$ ) fabricated via EBID (various electron doses: 0.22, 0.55 and 1.10 C/cm<sup>2</sup>) with similar AG time of ~240 min. (a) Overview of the CNTs growth. (b)-(f) SEM micrographs of CNTs on corresponding nanostructures with high magnification.

In order to synthesize CNTs forest nanostructures, exploratory CVD experiments at two different temperatures were carried out on the EBID-Fe (1.1 C/cm<sup>2</sup> and ~100 min AG). Following the trend of increased CNT yield with larger 2D structures, the side length of the squares was enlarged to 10  $\mu\text{m}$  (Figure 7-6a). Correspondingly Figure 7-6b and c depict the results of CNT growth via CVD at two different temperatures: 1073 K and 1133 K. At the lower CVD temperature of 1073 K, CNTs were obtained, appearing high yield but not a consistently vertical alignment. However, after growth at 1133 K, a very peculiar structure as depicted in Figure 7-6b and d can be observed. First of all, the CNTs are indeed organized in a very dense, nearly parallel arrangement which can be identified as the desired forest structure. Secondly, the

## 7 Secondary CNT growth on EBID-deposits

whole catalytic active 2D structure was obviously lifted-up by the CNT growth process. On top of the lifted square structure, only very few CNTs with reduced length are observed.

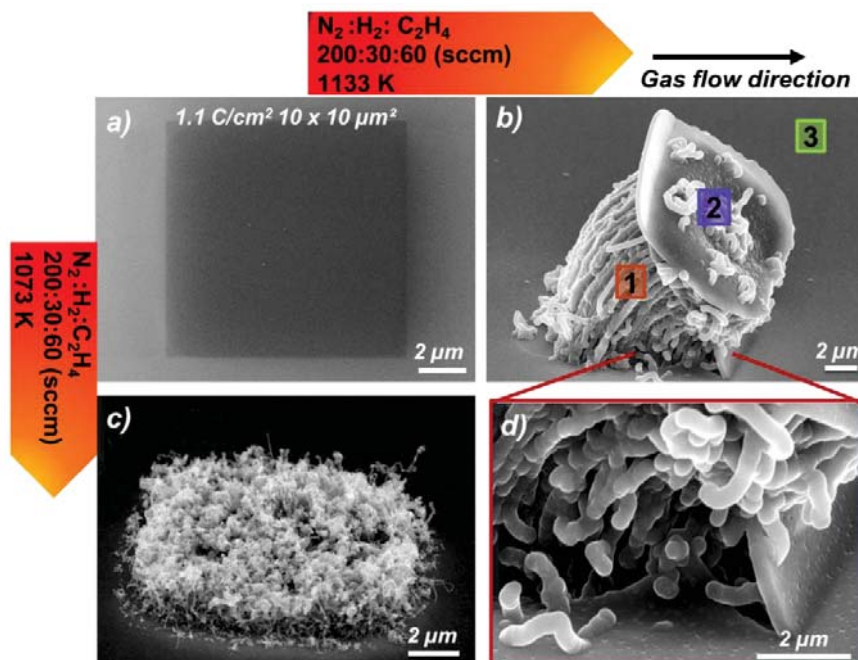


**Figure 7-6:** CNT growth at different temperature on  $10 \times 10 \mu m^2$  EBID-Fe deposits fabricated with  $1.1 C/cm^2$  and AG time of  $\sim 100$  min. (a) SEM micrograph of a Fe deposit before the CVD experiment. (b) and (d) CNT growth after a CVD experiment at 1133 K. (c) CNT growth after CVD experiment at 1073 K. EDX spectra were recorded at the indicated positions (1, 2 and 3) in (b), which can be found in Appendix Figure 13-3.

Further characterization was performed with local EDX (Appendix Figure 13-3) at the positions indicated in Figure 7-6b. At positions 1 and 2 a large carbon signal was detected which is in line with the growth of CNTs. In addition also signals for Si are detected at the position 2, probably originating from the underlying substrate. At position 3 a large Si signal was detected along with minor carbon and aluminum signals. While the carbon signal might derive from corresponding surface contaminations, the origin of the aluminum signal is certainly the  $Al_2O_3$  layer. In addition we have to state that we were not able to detect the Fe signal at this instance. This is especially remarkable at position 2 in Figure 7-6b, however this can be explained considering that EDX is not a surface sensitive method. Therefore the composition of the bulk material dominates the detected EDX signals. For example the penetration depth  $d$  of the focused

## 7 Secondary CNT growth on EBID-deposits

electron beam with a primary energy of 10 keV within amorphous carbon or silicon can be estimated to be in the range of 1.8  $\mu\text{m}$  by the following equation [27]:

$$d(\mu\text{m}) = \frac{0.1E^{1.5}}{\rho}$$

where  $E$  is the accelerating voltage in keV and  $\rho$  is the density of the detected sample. Considering the thickness of Fe nanostructure is approximately  $\sim 30$  nm, this would make  $\sim 1.6\%$  Fe signal, which can be regarded as below the detection limit of the method [210].

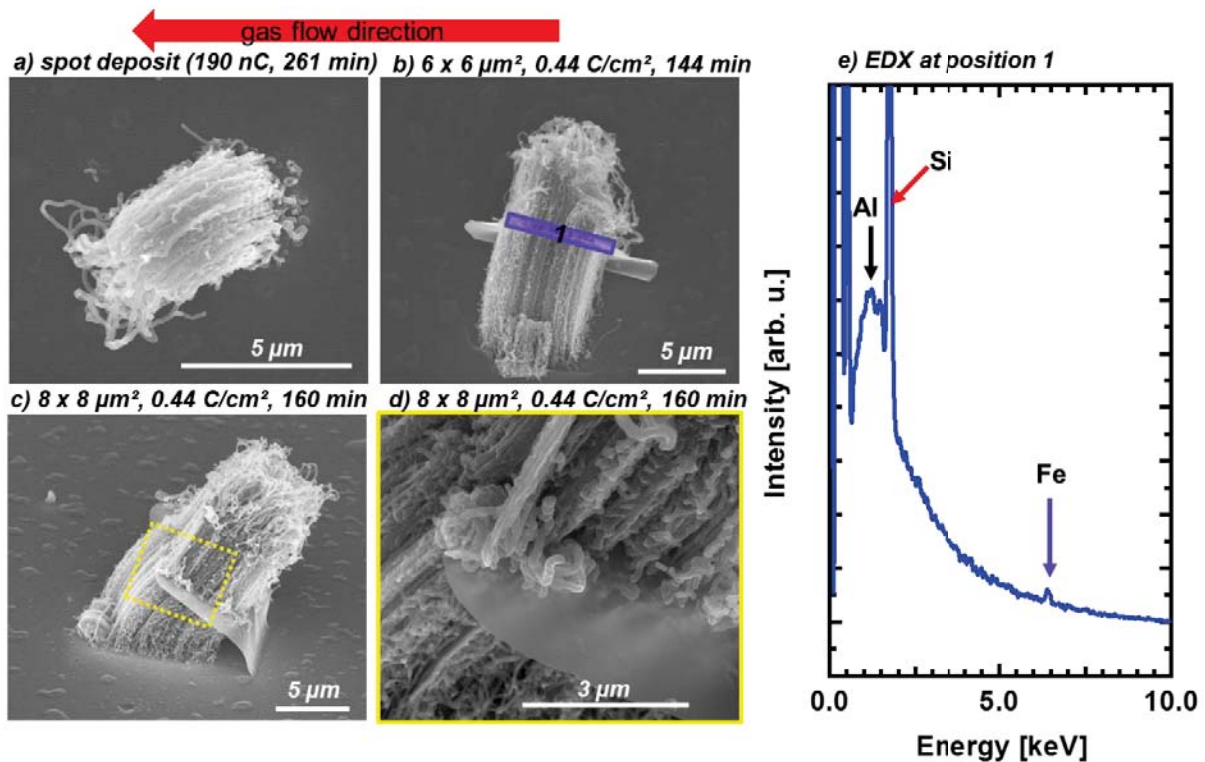


**Figure 7-7:** Lifted up CNT forest structures produced on various Fe nanostructures. (a), (b) and (c) Bending forests grown on EBID-Fe nanostructures with different shapes. (d) SEM micrographs with high magnification at the position indicated in (c). (e) EDX spectrum at the desired position in (b).

In additional experiments on other samples the fabrication of CNT forests and the peculiar lifting effect of the FEBIP deposit could be verified. Further investigations on the growth mechanism of the lifted-up flake nanostructure were carried out by performing CVD experiments

## 7 Secondary CNT growth on EBID-deposits

at slightly different conditions (1133 K ,  $N_2:H_2:C_2H_4 = 200:30:30$  sccm ) on EBID + AG Fe deposits with varying shapes fabricated on the  $Al_2O_3$  substrate. Figure 7-7 depicts SEM micrographs of three different correspondingly fabricated CNT forests along with the indicated direction of the gas flow during CVD. Close inspection of the SEM images reveal that the bending direction of the forests is independent of the flow direction. The SEM image with high magnification on the lifted-up flake (Figure 7-7c on the right) reveals different morphologies of the CNTs on top and below the flake. An EDX spectrum was obtained at position 1 as indicated in Figure 7-7b with the direction of electron beam parallel to the lifted-up flake. In this geometry the detected volume of the lifted flake is obviously significantly increased in comparison to the perpendicular orientation at position 2 in Figure 7-6b. As a result a small signal of Fe can be detected in the spectrum depicted in Figure 7-7e. In addition to Fe also significant Al and Si signals are visible at the same position. Therefore, it can be concluded that the lifted-up flake also consists in part of  $Al_2O_3$  and Si in addition to the deposited Fe.

Considering the chemical composition of the lifted-up flake, the growth mechanism of these nanostructures can be summarized as sketched in Figure 7-8. We speculate that the Fe EBID deposits eventually sinter or alloy to a certain extent with the underlying alumina layer. By chance this process might lead to increased tension within the deposited structure and could cause a lifting at the rim of the latter. During CVD the lifted corner of the structure allows precursor molecules to enter in between this edge and the substrate and consequently CNTs can grow underneath and lift the deposit structure as a flake starting from this “initial” edge position. Within this picture the flake is lifted in a tilted fashion and the direction of the tilt is not determined by the flow direction but by the position of the initially lifted corner. Since the top side of the flake is anyway accessible to precursor molecules the CNT grow can occur in a parallel fashion on both sides of the flake yielding the structures depicted in Figures 7-6 and 7-7.

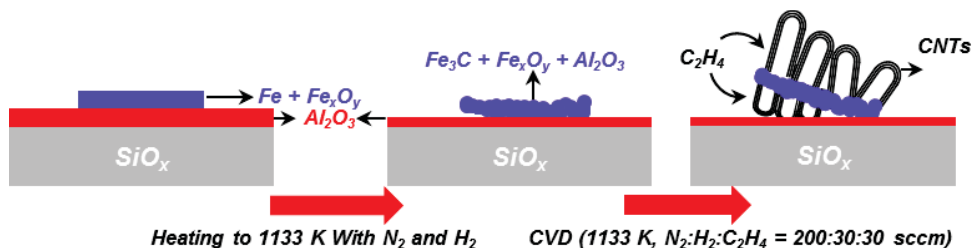


**Figure 7-8:** Scheme of growth mechanism of the lifted-up CNT nanostructure.

### 7.2.4 Co containing EBID deposits as catalyst for CNT growth

Finally the investigations concerning the localized growth of CNTs on EBID deposits were expanded to a Co precursor, namely  $\text{Co}(\text{CO})_3\text{NO}$ , which has been studied in detail recently [14, 203]. However, it turned out that even under UHV condition the deposits from  $\text{Co}(\text{CO})_3\text{NO}$  always contain significant amounts of oxygen and nitrogen (probably from the nitrosyl group) and partially also carbon. Generally, Co is a very common catalyst for CNT growth via CVD, in particular for SWNT growth [84, 211, 212].

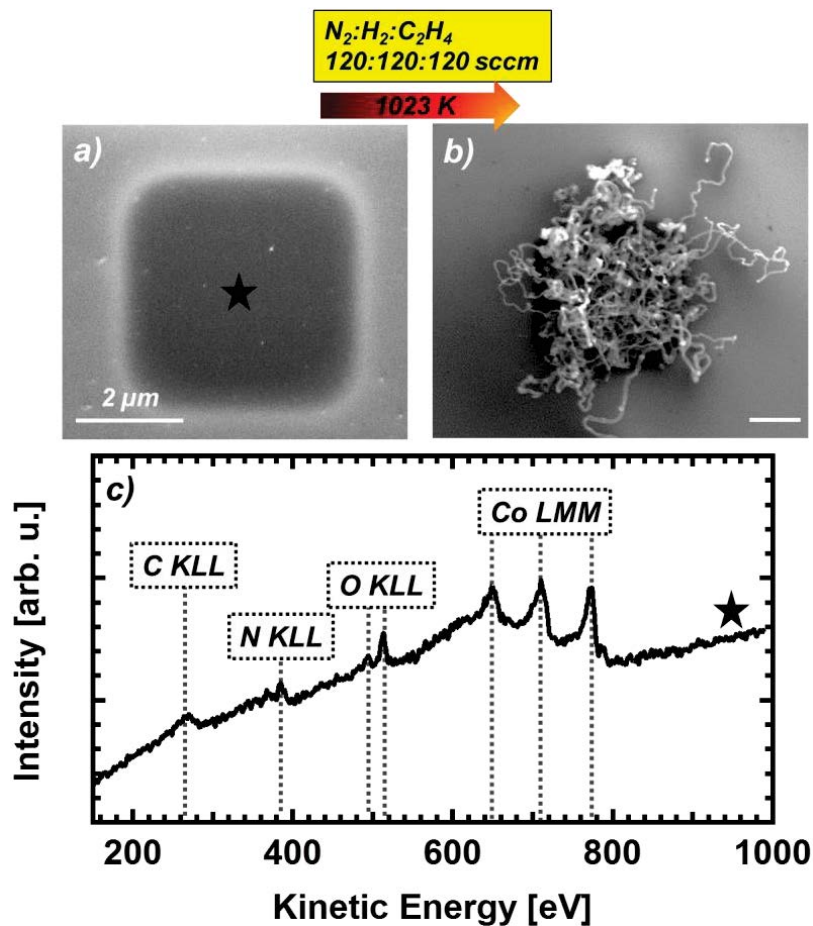


**Figure 7-9:** (a) SEM micrograph of  $4 \times 4 \mu\text{m}^2$  Co nanostructure fabricated via EBID ( $1.1 \text{ C}/\text{cm}^2$ ) with AG time of  $\sim 80 \text{ min}$ . (b) CNTs growth on the Co  $4 \times 4 \mu\text{m}^2$  structure via CVD experiment ( $1023 \text{ K}$ ,  $\text{N}_2:\text{H}_2:\text{C}_2\text{H}_4 = 120:120:120 \text{ sccm}$ ). (c) In-situ Auger electron spectrum of EBID-Co deposits before the CVD.

## 7 Secondary CNT growth on EBID-deposits

Figure 7-9a depicts a  $4 \times 4 \mu\text{m}^2$  square structure as fabricated via EBID and AG from  $\text{Co}(\text{CO})_3\text{NO}$  on  $\text{SiO}_x/\text{Si}(100)$  in the UHV instrument. The chemical composition was characterized by in-situ AES (Figure 7-9c), indicating that the deposit consists of C (~17 at.%), N (7 at.%), O (13 at.%) and Co (63 at.%). A subsequent CVD experiment was carried out with a precursor gas of  $\text{N}_2$ ,  $\text{H}_2$  and  $\text{C}_2\text{H}_4$  (120:120:120 sccm) at 1023 K. This temperature is even lower than the low temperature used in the case of Fe deposits on the substrate of  $\text{Al}_2\text{O}_3$ . Figure 7-9b depicts the Co-containing deposit after CVD. Obviously CNTs grew with high yield and increased length on the square deposit from the Co precursor. In conclusion the result demonstrates that indeed EBID deposits from  $\text{Co}(\text{CO})_3\text{NO}$  are very well suitable catalyst for CNT growth, even though the initial metal content of the deposited material is much lower than the one of the Fe deposits described above.

### 7.3 Conclusions

Protocols for the fabrication of well-defined CNTs with positional control on the nanoscale and different morphologies were successfully established, based on lithographically generated catalytic active EBID templates. Fe deposits were fabricated via EBID and subsequent AG in UHV with  $\text{Fe}(\text{CO})_5$  as precursor molecule. Evidence was presented that the Fe deposits can act as catalysts for localized CNT growth. The influence of the Fe deposits fabrication parameters (i.e., electron dose and AG time) on the shape of the latter deposits and finally on the yield and the morphology of the resulting CNTs after CVD was investigated. By adjusting these parameters, an important first goal could be reached, that is the fabrication of well-defined individual CNT on all 36 Fe deposits within a  $6 \times 6$  point-matrix.

In a next step CNTs with high density and vertical alignment, referred to as the CNT forest, were produced on Fe deposits, fabricated on an  $\text{Al}_2\text{O}_3$  substrate. It can be stated that the  $\text{Al}_2\text{O}_3$  supports the growth and enhances the yield of CNTs, i.e. lower temperatures are sufficient in CVD and a significant increase of the CNTs yield was observed compared with the ones synthesized with corresponding Fe deposits on a  $\text{SiO}_x/\text{Si}(100)$  substrate at higher temperatures. A peculiar lifting-up of corresponding 2D EBID deposits as “flakes” was observed. This lifting was conclusively interpreted as due to the growth of CNTs underneath the catalytic active deposit, effectively raising the latter structure from the support. As a result the CNT forest

## 7 Secondary CNT growth on EBID-deposits

structure was observed on both sides of the lifted flake. Furthermore, proof of principle is presented that Co-containing EBID + AG structures from the precursor  $\text{Co}(\text{CO})_3\text{NO}$  are also very effective as seeds for the secondary growth of CNTs. Interestingly, even though the metal contents of these structures were significantly lower than the ones of the Fe deposits the Co containing catalyst structures were active in CVD at lower temperatures.

In summary, an unprecedented degree of control can be realized, in respect to the localized growth and also morphology of secondary CNT nanostructures on EBID. Considering the huge number of variable processing parameters for EBID and AG as well as for CVD, it is clear that there is plenty of room to further tweak the fabrication process. If one also considers the exploration of other precursors for both processes and surfaces even more possibilities to tailor-make secondary nanostructures, which could also be, e.g., Si or Ge nanowires. One more specific direction might be to target the localized production of single walled CNTs. Also the combination of  $\text{Fe}(\text{CO})_5$  and  $\text{Co}(\text{CO})_3\text{NO}$  as precursors in EBID might be worth to investigate, since binary mixtures of active catalysts such as Ni, Fe and Co are reported to exhibit higher activity than individual elements [213]. A last topic to be mentioned for future investigations is the fabrication of EBID seed structures with different geometries to trigger novel carbon nanostructures like “twisted rope” structures or extended 2D materials.

## 8 A novel nano-fabrication technique: FXBID

### 8.1 Introduction

An additive form of lithographic nanofabrication involves using radiation to induce the local dissociation of precursor molecules and the subsequent deposition of one of the dissociation products. An example of such a technique is EBID, in which a focused electron beam is employed to induce the local dissociation of surface-adsorbed metal organic precursor molecules supplied from the gas phase [5, 18, 19]. As introduced in previous chapters, the non-volatile dissociation products remain as a deposit on the surface while the volatile ones are pumped away. The non-volatile portion usually contains the metal center of the precursor and forms a defined metal-containing deposit that can be purified to almost clean metal nanostructures [20].

Despite the various and promising applications of EBID, electron induced deposition processes with focused electron beams have an inherent drawback considering material selectivity. Since the primary energy of such a focused electron beam is usually well above 10 keV, all sorts of secondary and backscattered electrons are also generated. So even if the incident electron beam would be monochromatic, the full energy range of electrons, from zero to the primary beam energy, is present in close proximity to the incident beam. Hence, one does not anticipate selectivity within different precursors, even though the energy dependent cross section of electron induced precursor dissociation might vary between them. Therefore, precursors with comparable deposition rates are expected to generate mixed deposits when dosed simultaneously. In the present work this issue was addressed by replacing the incident electron beam by a focused beam of monochromatic X-rays.

Absorption of X-rays in the energy region of the *K*- and *L*-edges of the specimen leads to the formation of core holes and subsequent relaxation via fluorescence and Auger cascades [214, 215]. The radiochemical processes induced by X-ray beams – usually referred to as radiation damage – are mostly governed by interaction of the specimen with low energy secondary electrons produced by the Auger cascade [215]. Therefore, the basic radiochemical processes are expected to be very similar for electron and X-ray irradiation, except that the latter requires a higher incident dose for a comparable quantitative effect [215]. However, switching the primary

irradiation from electrons to X-rays offers the possibility of resonant, and therefore chemically selective, excitation. For most materials, the X-ray absorption spectra tend to show distinctive discrete peaks in the near-edge energy region. This behavior is often employed in NEXAFS spectroscopy and resonant microscopic imaging and could be utilized to tailor the deposition rates by appropriate tuning of the incident photon energy [214, 216]. There is a great potential for sequential deposition of materials from various precursors without intermediate pumping and atmosphere exchange. This would be most useful for the fabrication of structures involving alternating multilayers, where a single precursor mixture could be used and the deposition material chosen by simply switching the incident photon energy.

The idea of FXBID combines the energy-selectivity of X-ray lithography with the idea of deposition of metal nanostructures from suitable precursor gases [178]. The use of a STXM setup for these experiments offers several advantages. First, STXM is a raster-scanning technique which avoids the necessity of shadow masks [123]. Furthermore, the minimum feature size of the metal structures is mainly determined by the spot size of the incident beam. Based on modern zone-plate technology a resolution of 10 nm has been reached so far [129, 130], while recent developments suggest a significant improvement within the next years [127, 217]. Finally, STXM can be directly employed for an in-situ analysis of the metallic deposits directly after fabrication by means of resonant imaging and NEXAFS spectroscopy to evaluate confinement, growth rates, oxidation state and purity [14]. XMCD can be employed to characterize magnetic deposits with respect to their magnetization such as the coercivity [13].

This Chapter presents a comparative study of the Co and Mn nanostructures fabrication from  $\text{Co}(\text{CO})_3\text{NO}$  and  $\text{MeCpMn}(\text{CO})_3$  in terms of growth rates, purity and energy-selectivity of the FXBID process. In the case of Co, illumination at several absorption edges will be compared, addressing resonant absorption for Co, O and N. Furthermore, one-sweep versus multi-sweep irradiation at constant cumulated dwell time is shown, for a deeper understanding of growth kinetics.

## 8.2 Results and discussion

### 8.2.1 Cobalt nanostructures fabricated via FXBID

Figure 8-1a shows an optical density STXM micrograph (780.4 eV, Co  $L_3$ -edge), of an array of cobalt nanostructures fabricated via FXBID with  $\text{Co}(\text{CO})_3\text{NO}$  precursor ( $8.5 \times 10^{-6}$  mbar) on the native oxide of a 50 nm  $\text{Si}_3\text{N}_4$  membrane in the high vacuum PolLux gas cell setup described in Chapter 4. As indicated in Figure 8-1a, the dwell time was varied from 20 ms to 80 ms, while the photon energies were well below and above the Co  $L$ -edge (770 and 800 eV, respectively), as well as at the resonant excitation energy (780 eV). The appearance of the nanostructures is, as to be expected, influenced by the applied dwell time. Structures with increasing irradiation time per pixel (20, 40, 80 ms) exhibit an increased brightness (higher optical density) in the STXM micrograph (optical density contrast). As already reported in the previous works, the optical density recorded at the resonant transition peak of the corresponding material can be used as a direct measure of the deposit thickness [13, 14, 178]. Herein, the strongest element-specific absorption for cobalt structures can be achieved by acquisition of STXM micrographs recorded at 780.4 eV. It is possible that FXBID deposits prepared by the present simple approach contain significant amounts of light elements from the precursor molecules (e.g., C  $K$ -edge NEXAFS spectra of the deposits presented within this work, cf. Figure 8-2b). However, the absorption coefficients of these elements are comparably low at the Co (and Mn in the latter part of this chapter)  $L_{2,3}$ -edges and can be neglected in resonant Co (or Mn) imaging [216, 218]. Hence, the linear absorption coefficient of pure Co is used as an approximation ( $\mu \sim 0.102 \text{ nm}^{-1}$ ) for the calculation of the thickness of the respective deposits. Following this procedure, the thickness given for the respective deposits denotes the amount of deposited Co, while the overall thickness including lighter elements is certainly underestimated to some extent.

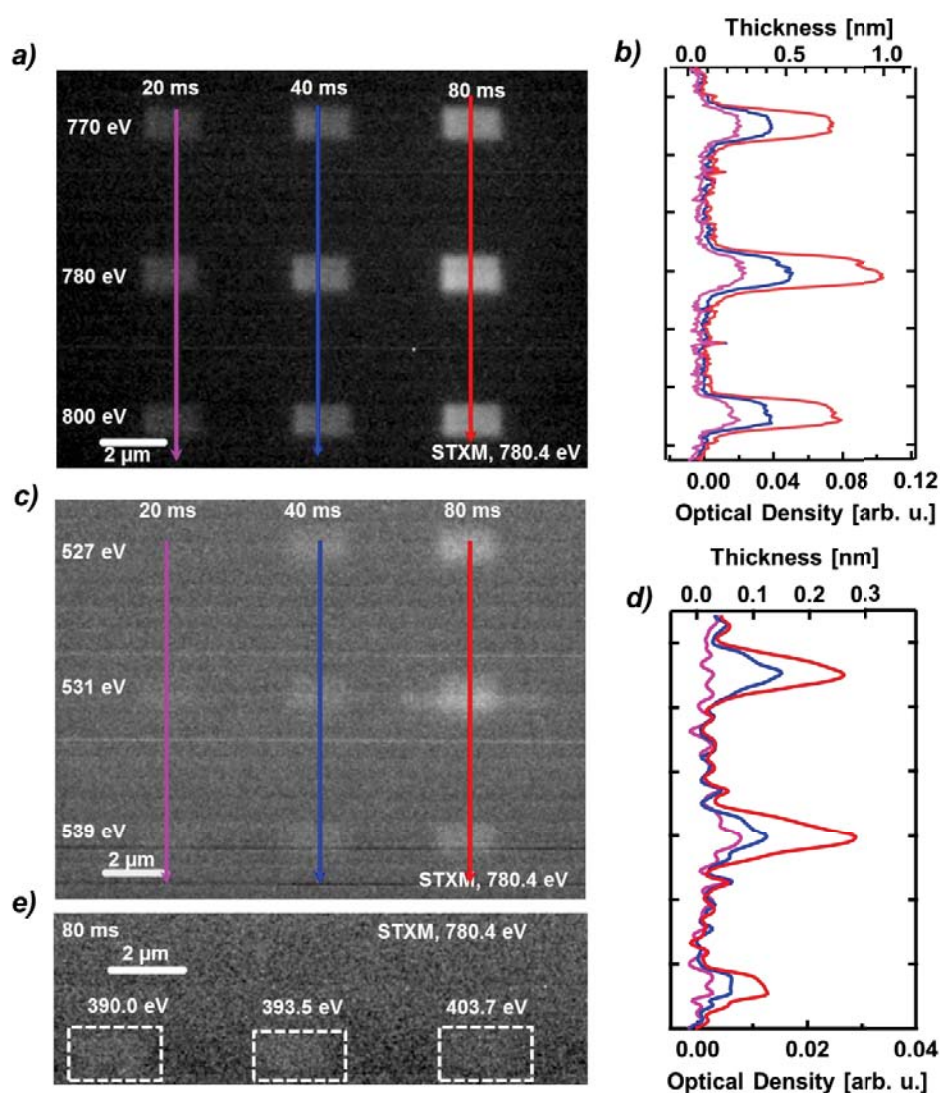


**Figure 8-1:** (a) STXM micrograph (optical density) of Co deposits from FXBID using  $\text{Co}(\text{CO})_3\text{NO}$  as precursor ( $8.5 \times 10^{-6}$  mbar) at varied irradiation times per pixel (columns) and photon energies near the Co  $L_{2,3}$ -edge (rows). The STXM micrograph was recorded at the Co  $L_3$  resonant energy which gives the strongest element-specific absorption for cobalt structures. (b) Line profiles across the deposits, illustrating the variations of the resulting optical density which is proportional to the quantity of deposited Co. (c) STXM micrograph of Co deposits fabricated by using photon energies at the O  $K$ -edge with varying dwell time. (d) Line profile of the optical density and evaluated effective Co thickness across Co nanostructures in (c). With the shortest dwell time (20 ms), almost no Co was deposited. (e) STXM micrograph of Co deposits fabricated by using photon energies at the N  $K$ -edge (dwell time 80 ms).

## 8 A novel nano-fabrication technique: FXBID

The evaluation of deposited Co atoms per area (Figure 8-2) can be quantitatively well approximated. A comparison of the optical densities of the deposits or, for better visualization, of the respective linear profiles depicted in Figure 8-1b, shows directly that the deposit thickness is proportional to the dwell time and energy-dependent. Resonant illumination yields significantly more Co deposition at identical dwell times compared to off-resonant excitation. For a dwell time of 80 ms and resonant excitation at 780 eV ( $1.8 \times 10^5$  photons per  $\text{nm}^{-2}$ ), a maximum deposit thickness of  $\sim 1.1$  nm can be achieved. Further deposits were fabricated at and around the O and N *K*-edge resonant energies (Figure 8-1c-e). The optical densities shown in the STXM micrographs are lower compared to the ones fabricated at the Co  $L_{2,3}$ -edge, indicating significantly thinner deposits fabricated via FXBID at the O *K*-edge. However, also the incident flux was lower for this energy. No clearly detectable amount of Co was deposited at the N *K*-edge at all applied dwell times and incident photon energies (Figure 8-1e). This effect is attributed mainly to a very low incident flux inside the gas cell due to the use of  $\text{Si}_3\text{N}_4$ -windows. N from  $\text{Si}_3\text{N}_4$  might contribute to the absorption of photons at N *K*-edge resonance. Therefore it would be reasonable to analyze deposition at the N *K*-edge with a gas cell based on nitrogen-free membranes (i.e., Si membranes).

Figure 8-2 presents the analysis of the energy-dependent deposition rate at the O *K*-edge and at the Co  $L_{2,3}$ -edge respectively. A calibration to the beamline photon flux, detection efficiency and absorption of the  $\text{Si}_3\text{N}_4$  membranes of the gas cell was carried out to evaluate the correct number of photons inside the gas cell (c.f. Figure 4-10). Especially the consideration of the incident photon flux is crucial for the determination of absolute growth rates, since it may vary strongly with the photon energy. With respect to these corrections, a clear linear dependence of the effective Co thickness on the illumination time per pixel (directly proportional to number of absorbed photons) is observed for each excitation energy. Furthermore, the energy-dependence of the deposition rate can be quantified from the slope of the respective linear fits. At both absorption edges the resonant photon energy yields the highest deposition rate outscoring pre-edge excitation by 20% (Co  $L_{2,3}$ -edge) or 10% (O *K*-edge) and post-resonant illumination even by 40% (Co  $L_{2,3}$ -edge) or 30% (O *K*-edge). Based on the standard models of X-ray induced radiochemistry, it is expected a correlation of radiation damage and the absorption cross section of the precursor molecule within this energy regime [219]. Therefore, it is not surprising that the resonant energies show higher deposition rates. However, the post-edge rates

would be expected to be higher than the pre-edge rates. As the exact absorption spectrum of the precursor molecule is not known and pre-edge absorption peaks might contribute to the observed behavior [216]. The presence of threshold-dependent deactivation processes is speculated and these processes lead to selective radiochemistry with respect to pre- and post-edge excitation [220].

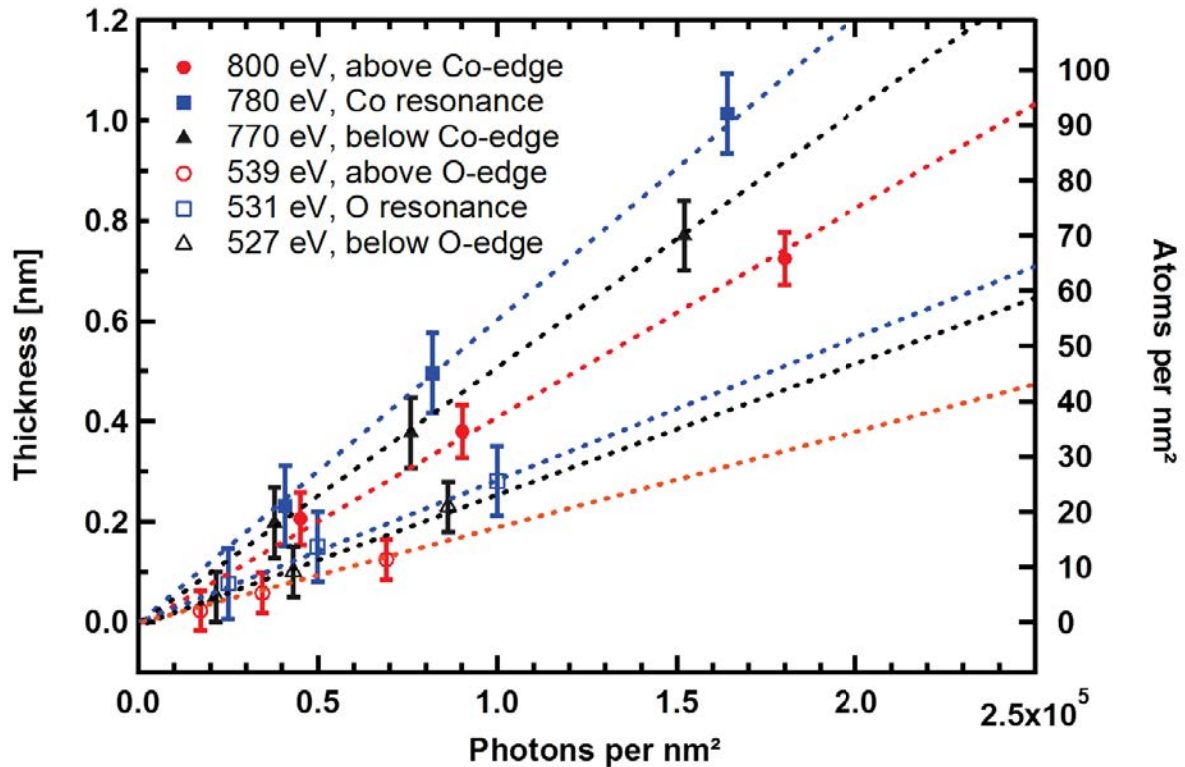
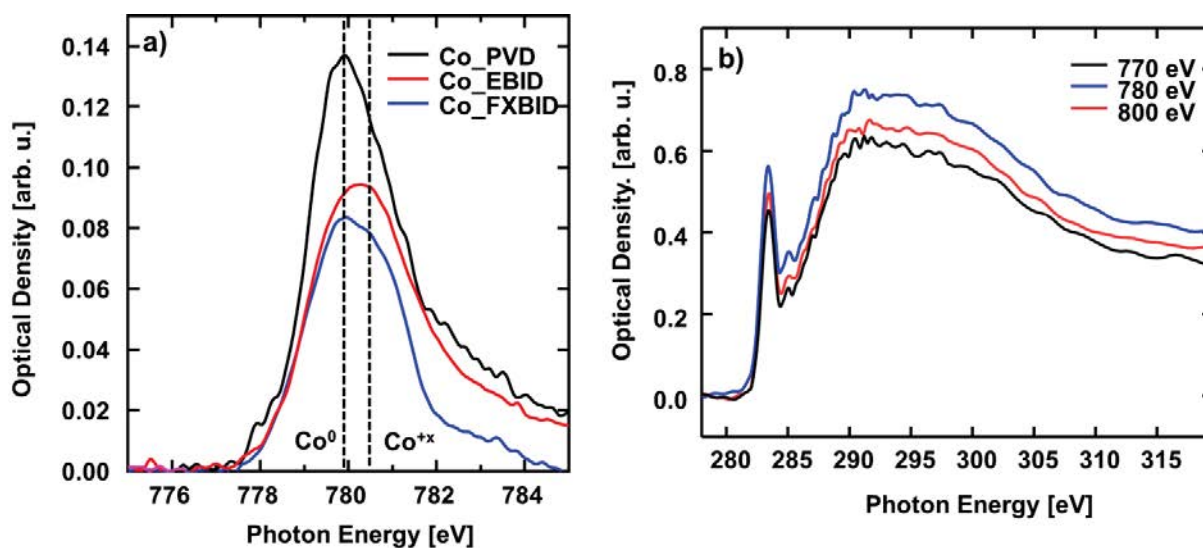


**Figure 8-2:** Quantitative analysis of FXBID deposits fabricated at and around the O K-edge and Co  $L_{2,3}$ -edge energies. The effective Co thickness and correlated number of atoms per  $\text{nm}^2$  is plotted versus the calibrated amount of impinging photons per area. The number of incident photons is directly proportional to irradiation time.

Another finding is that the deposition rate with respect to the number of incident photons at the Co  $L_{2,3}$ -edge is in all three cases roughly twice as high as for the respective energy at and around the O K-edge. This result does not correlate with the ratios of the respective tabulated photo-absorption cross sections. According to literatures [218, 221] the pre-edge absorption cross section at the Co  $L_{2,3}$ -edge is 1.6-times higher than for the O K-edge, while for the post-

edge cross section the O *K*-edge outscores by a factor of 1.3. Resonant excitation is not properly treated by these tables, but it should be noted that the tabulated cross section directly at the O *K*-edge exceeds the Co *L*<sub>3</sub>-edge by a factor of 1.9. Furthermore, Co(CO)<sub>3</sub>NO contains four O atoms, but just one Co. Hence, at a given precursor pressure, each incident photon can interact with four times more O than Co atoms resulting in an overall higher probability of O excitation at each of the considered O *K*-edge energies compared to Co excitation at the respective Co *L*<sub>2,3</sub>-energies with respect to cross section and atom number ratios. This contradiction to the experimental results leads to the hypothesis that photoexcitation at the CO and NO ligands of Co(CO)<sub>3</sub>NO has a lower probability to cause precursor decomposition than absorption of a photon at the metal center. In conclusion, in the case of Co(CO)<sub>3</sub>NO resonant excitation at the Co *L*<sub>3</sub>-edge is superior for the purpose of metal nanostructure fabrication compared to all other evaluated incident photon energies.

Figure 8-3 presents an analysis of the purity of the FXBID deposits by means of NEXAFS spectroscopy of an exemplary Co deposit. In Figure 8-3a, the NEXAFS spectra of Co deposits fabricated via different techniques to determine and compare Co oxidation states are depicted. The comparison of the Co peak positions between a metallic cobalt film prepared by physical vapor deposition (PVD) and the structures prepared by EBID and FXBID reveals a chemical shift, indicating different Co oxidation states in the fabricated deposits. Deposits fabricated via PVD serve as metallic cobalt reference with a peak maximum at 779.9 eV, while the spectra of deposits fabricated with EBID and FXBID show a mixture of metallic and oxidized states. However, it is obvious that Co<sup>0</sup> is the dominant oxidation state within FXBID deposits. This finding is remarkable, considering that EBID-Co deposit with comparable thickness (~0.9 nm) was found to be strongly oxidized (main peak shifts to 780.4 eV). However, it should be noted that the spectroscopic investigations of FXBID deposits were performed in-situ after deposition, while the respective EBID deposits could be oxidized during transport in ambient to the synchrotron for NEXAFS inspection.



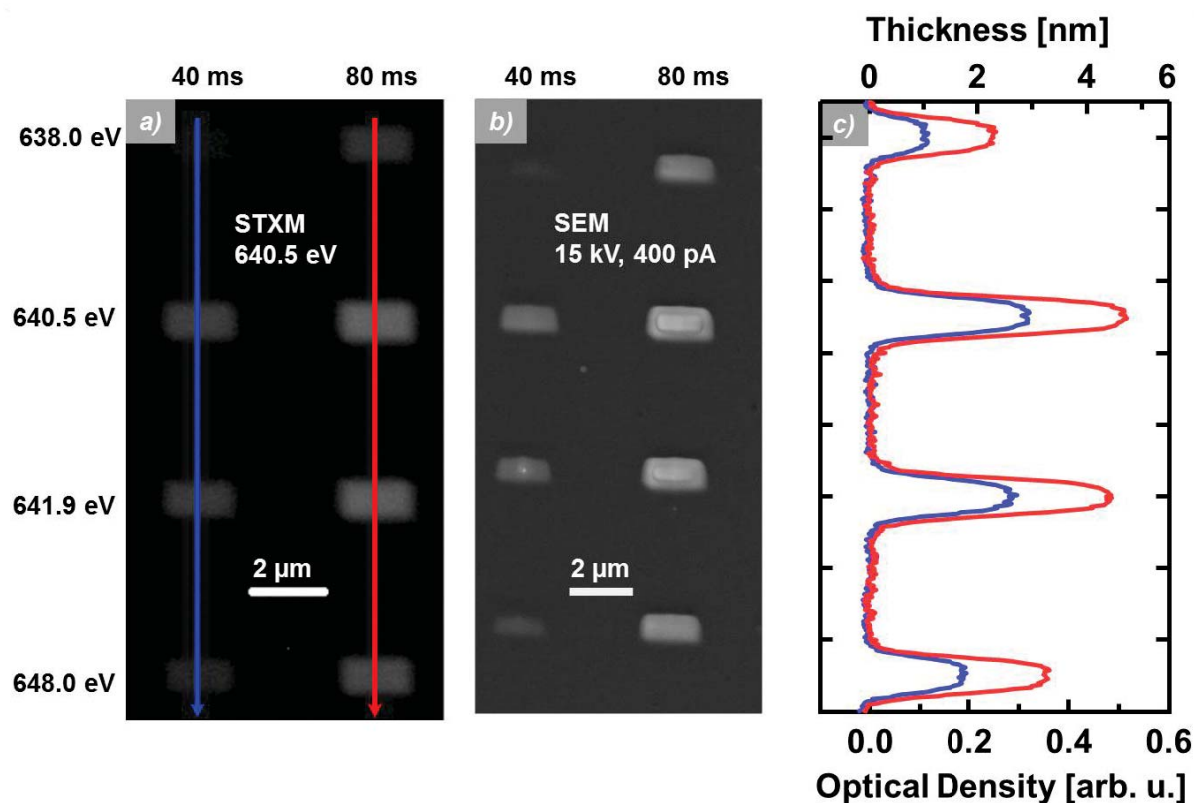
**Figure 8-3:** (a) Co  $L_3$ -edge spectra of deposits fabricated with physical vapor deposition (PVD), FXBID and EBID. The pure cobalt layer prepared via PVD acts as a  $\text{Co}^0$  reference. The FXBID deposit was fabricated by using 780 eV photon energy with a  $\text{Co}(\text{CO})_3\text{NO}$  pressure of  $9.2 \times 10^{-5}$  mbar and 40 ms dwell time per pixel, while the EBID deposit was fabricated by using 0.2  $\text{C}/\text{cm}^2$  primary electron dose and 113 min autocatalytic growth time. Different Co oxidation states were indicated at different peaks. The thickness of the FXBID and EBID deposits is  $\sim 0.9$  nm for both. (b) C  $K$ -edge NEXAFS spectra of FXBID-Co deposits with respect to the incident photon energy (dwell time: 80 ms) using  $\text{Co}(\text{CO})_3\text{NO}$  as a precursor.

Figure 8-3b displays the C  $K$ -edge spectra of FXBID deposits generated under similar conditions. The spectral shape indicates a crude mixture of different typical radiochemical end products containing a strong  $\pi_{\text{C}=\text{C}}^*$  signal at about 285.0 eV from unsaturated C-C bonds [222]. The amount of C correlates with the optical density at photon energies above the C  $K$ -edge jump (e.g., 320 eV) [216]. Considering the three different photon energies, a similar quantitative trend is found, compared to the amount of deposited Co. Resonant irradiation leads to an increased quantity of carbonaceous material within the deposits. Therefore, it can be concluded that the carbon source within the experiment is mainly the precursor molecules and to a minor portion caused by residual gases. Although a significant amount of C within the deposits is observed, the spectral analysis reveals a similar purity of FXBID deposits compared to EBID with a higher amount of  $\text{Co}^0$  species [14]. In addition, the established purification techniques for EBID

structures could be applied to the fabricated deposits, especially substrate heating, reactive gas mixtures and hydrogen radical treatment [20] should be applicable with minor modifications of the present setup.

### 8.2.2 Mn nanostructures fabricated via FXBID

NEXAFS spectroscopy of a first exploratory test pattern deposited by FXBID from  $\text{MeCpMn(CO)}_3$  suggested the presence of a mixture of Mn oxidation states within the deposits. The main contributions have been identified as  $\text{Mn}^{2+}$  (640.5 eV) and  $\text{Mn}^{3+}$  (641.9 eV) [223]. Hence, the FXBID experiments were performed at four photon energies: well below the  $\text{Mn}^{2+}$  resonant energy (638.0 eV), at the  $\text{Mn}^{2+}$  (640.5 eV) and  $\text{Mn}^{3+}$  (641.9 eV) resonances, as well as above the edge jump (648 eV). The  $\text{MeCpMn(CO)}_3$  pressure was kept at  $3.7 \times 10^{-6}$  mbar and the dwell times 40 ms and 80 ms, respectively, were utilized. Figure 8-4a shows the STXM micrograph, recorded at the  $\text{Mn}^{2+}$  resonant energy, of a set of  $2 \times 1 \mu\text{m}^2$  Mn nanostructures. Again, the optical density, referencing the thickness of Mn within the nanostructures, is directly proportional to the applied dwell-time, i.e., the number of impinging photons. This can be extracted from the different brightness levels and is further illustrated by the linear profiles across the array of nanostructures (Figure 8-4c). The morphology of the deposits was also investigated by UHV-SEM, shown in Figure 8-4b. As material contrast is dominant in this case, it is confirmed that FXBID with 80 ms dwell time at the  $\text{Mn}^{2+}$  and  $\text{Mn}^{3+}$  resonant energies results in a higher amount of deposited Mn. Both micrographs show that the Mn nanostructures were spatially defined and no obvious proximity effect was observed (the pad size is  $1 \times 2 \mu\text{m}^2$ ) [11, 13, 14].



**Figure 8-4:** Mn nanostructures ( $2 \times 1 \mu\text{m}^2$ ) produced via FXBID, using  $\text{MeCpMn}(\text{CO})_3$  as precursor with 40 and 80 ms dwell time, respectively. (a) STXM micrograph of the fabricated nanostructures, recorded at the  $\text{Mn}^{2+}$   $L_3$ -edge resonant energy (640.5 eV). (b) SEM micrograph of the same nanostructures. Material contrast is dominant here, indicating more Mn deposited. (c) Linear profile extracted from the STXM micrograph, displaying the energy selectivity of the Mn precursor dissociation.

Figure 8-5a depicts the quantitative analysis of the energy-dependent deposition rate at and around Mn resonant energy. A linear fitting was carried out with a line passing through zero point, indicating the deposition rate from the slope of the fitted lines. The linear absorption coefficient of Mn oxide is evaluated to be  $\sim 0.109 \text{ nm}^{-1}$ . It is obvious that irradiation with  $\text{Mn}^{2+}$  resonant energy (640.5 eV) gives rise to the highest deposition rate, which is 50% higher compared to the pre-edge (638.0 eV) and almost 40% higher compared to the post-edge (648.0 eV) energy. The second most effective dissociation energy is the  $\text{Mn}^{3+}$  resonance (641.9 eV).

## 8 A novel nano-fabrication technique: FXBID

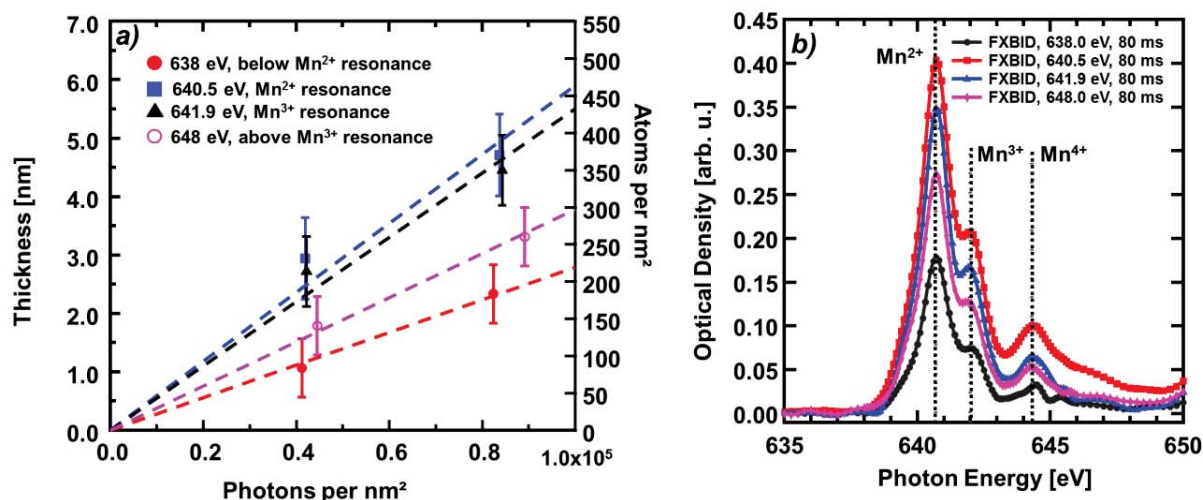


**Figure 8-5:** (a) Quantitative analysis of the Mn nanostructures depicted in Figure 8-4. The effective Mn thickness and correlated number of atoms per nm<sup>2</sup> is plotted versus the calibrated amount of impinging photons per area. The number of incident photons is directly proportional to irradiation time. (b) Mn L<sub>3</sub>-edge spectra of FXBID deposits fabricated at different photon energies with 80 ms dwell time.

For an analysis of the Mn oxidation states presented within the deposits, NEXAFS spectra were recorded on all deposits fabricated with 80 ms dwell time (Figure 8-5b). From these spectra, a superposition of different Mn oxidation states can be observed, the main one being Mn<sup>2+</sup> with smaller amounts of Mn<sup>3+</sup> and Mn<sup>4+</sup>. As Mn(I) is the original oxidation state in the precursor, the nanostructures must be oxidized either via the oxygen residual gas inside the gas-cell, or the CO ligand from the precursor upon photon-induced decomposition. It has been reported that under electron excitation (70~100 eV), decomposition of MeCpMn(CO)<sub>3</sub> is dominated by decarbonylation steps. The methylcyclopentadienyl moiety is retained as other carbonyl ligands are easier to be desorbed from the active ions MeCpMn(CO)<sup>x+</sup> (x = 0~3). This dominant organic ligand in the precursor does not decompose upon electron excitation (< 100 eV). Hence, this dissociation mechanism may contribute to the higher carbon residuals in the FXBID-Mn nanostructures (Figure 8-6).

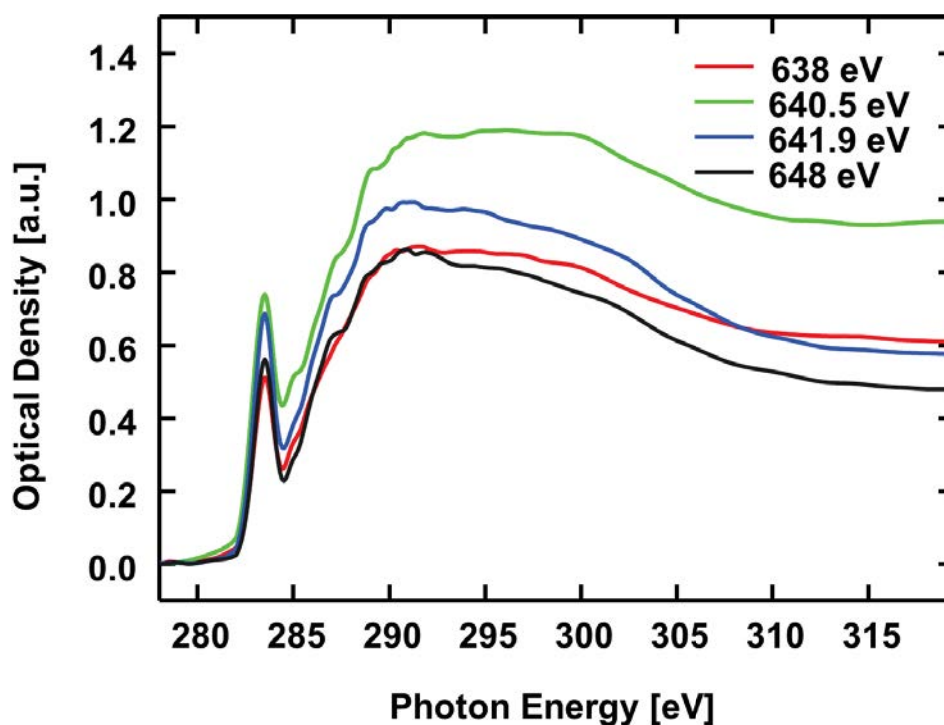


**Figure 8-6:** C K-edge NEXAFS spectra of FXBID-Mn deposits from  $\text{MeCpMn}(\text{CO})_3$  with respect to the incident photon energy (dwell time: 80 ms). The presented C K-edge spectra exhibit the typical spectral shape as the one of FXBID-Co deposits. The amount of C correlates with the optical density at photon energies above the C K-edge jump (e.g., 320 eV) [216]. Similar quantitative trends are observed compared to the amount of deposited Mn corroborating the conclusion that the carbon source in the setup is mainly the respective precursor molecules. This trend is also observed in Co deposits. Since  $\text{MeCpMn}(\text{CO})_3$  does abstract the MeCp ligand only under very harsh conditions, the C content of the respective deposits is significantly higher resulting in higher optical density within the C spectra compared with the one in Co deposits (Figure 8-3b).

### 8.2.3 Growth mode of Mn and Co precursors

Figure 8-7 indicates the evolution of the optical density of the fabricated deposits (for both Co and Mn) as a function of the number of sweeps (or amount of photon dosage). It is obvious that the dissociation rate is constant for  $\text{Co}(\text{CO})_3\text{NO}$  while it decreases slightly for the Mn precursor. Two kinetic regimes for the photon beam induced dissociation can be expected: precursor- and photon-limited regime. The applied pressure during Mn deposition ( $2.5 \times 10^{-6}$

mbar) was lower than the one during Co deposition ( $9.2 \times 10^{-5}$  mbar) due to a lower vapor pressure of  $\text{MeCpMn}(\text{CO})_3$ , presumably resulting a precursor-limited dissociation behavior of  $\text{MeCpMn}(\text{CO})_3$  and photon-limited deposition kinetics for  $\text{Co}(\text{CO})_3\text{NO}$ . Another important influence on the deposition kinetics is the surface diffusivity of the two precursors. The lower mobility of the Mn precursor at the surface, due to the heavy methyl cyclopentadienyl ligand, will also contribute to a precursor-limited regime of the photon induced molecular dissociation. This is similar to the use of trimethyl (methylcyclopentadienyl) platinum (IV) in EBID processes [4, 224, 225].

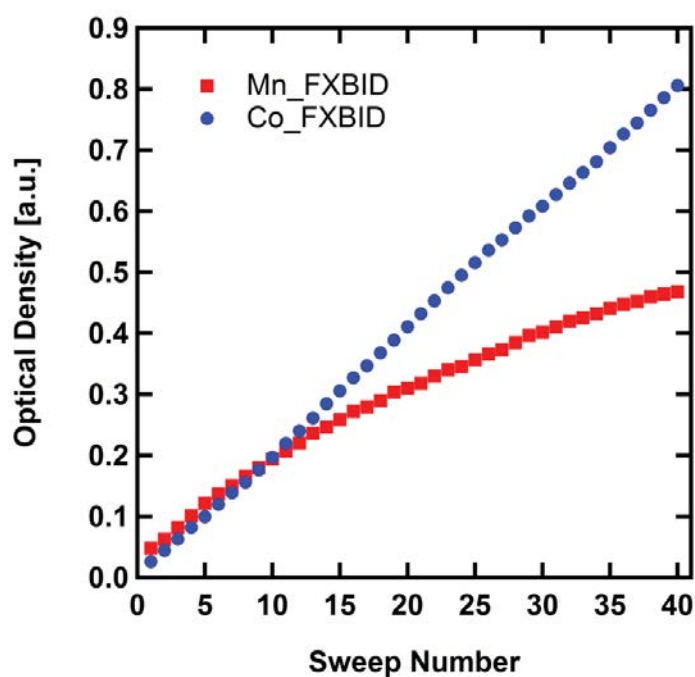


**Figure 8-7:** Optical density as a function of the number of sweeps for Mn and Co deposits. The applied photon energies were the Co  $L_3$ -edge resonance (780 eV,  $\text{Co}(\text{CO})_3\text{NO}$ ) and the  $\text{Mn}^{2+}$   $L_3$ -edge resonant energy (640.5 eV,  $\text{MeCpMn}(\text{CO})_3$ ). The pressures were  $9.2 \times 10^{-5}$  mbar ( $\text{Co}(\text{CO})_3\text{NO}$ ) and  $2.5 \times 10^{-6}$  mbar ( $\text{MeCpMn}(\text{CO})_3$ ).

### 8.3 Conclusions

In summary, the fabrication, microscopic and in-situ chemical characterization of cobalt and manganese nanostructures produced via the novel FXBID technique was reported. An apparent energy-selective optical density was observed, depending on the resonant energies of the metal

center. In agreement with the previous work [178], it can be concluded that  $\text{Co}(\text{CO})_3\text{NO}$  as well as  $\text{MeCpMn}(\text{CO})_3$  dissociate most effectively at resonant energies of the respective absorption edges. In addition it is revealed for Co deposition that excitation at the  $L_3$ - absorption edge of the metal center of the precursor yields clearly superior deposition rates compared to excitation at the ligands. Deposits fabricated from  $\text{MeCpMn}(\text{CO})_3$  exhibit an energy dependent dissociation at the Mn  $L_{2,3}$ -edge, analogous to  $\text{Co}(\text{CO})_3\text{NO}$ . These findings expand the scope of FXBID, which might work with a larger amount of organometallic molecules, with the energy selectivity of the precursor dissociation mainly driven by the X-ray absorption cross section at the respective metal transitions. All nanostructures have been fabricated via FXBID with less or no BSE proximity effects, which is a phenomenon that always has to be considered in EBID [11, 16].

The results suggest that FXBID could be a valuable approach to produce combined nanostructures of more than one metal with controlled material distribution within a batch process of consecutive illumination with adjusted photon energy. Gases could be dosed simultaneously without time consuming pumping steps or even breaking the vacuum. Deposition from gas mixtures, however, is expected to require precursors with comparable deposition rates. This was not achieved with the so far tested precursors, due to the comparably low vapor pressure of  $\text{MeCpMn}(\text{CO})_3$ .

In order to get more insight into the basic dissociation and growth mechanisms in FXBID, further studies are required. This specifically refers to the initial X-ray absorption process which could be examined by photon-energy dependent studies with precursor molecules in the gas phase and resulting fragmentation [226]. The resolution limit of FXBID will be evaluated in detail in the future work, as it is expected that the resolution will mainly be limited by the X-ray optics of the STXM, which is rapidly improving [127-130, 176]. Single-line deposits with ultimately resolving zone plate optics may also shed light on the question how the substrate influences molecular decomposition (e.g., due to secondary electrons from the substrate). Effects of other parameters such as substrate temperature and surface chemical composition on the chemical dissociation behavior during FXBID process are also interesting. It is expected that the principles and examples presented in this work will stimulate further researches and possibly lead to practical applications of this novel technique.

## 9 EBID and EBISA on MgO(100)/Ag(100)

### 9.1 Introduction

The surface activation process in EBISA has been investigated on silicon oxide and TiO<sub>2</sub> [12, 15]. The mechanism was summarized as reduction and restructuring of the substrate due to the electron stimulated oxygen desorption, presumably following the Knotek-Feibelman mechanism [15]. The first purpose of this chapter is to expand the EBISA technique further to another oxide thin film and to obtain information about the activation mechanism. In addition, expanding EBISA to other oxide thin films might allow drawing conclusions about the electron beam induced activation of oxide substrates in general.

MgO thin film was chosen because of its attractive properties. It can act as an insulating barriers in magnetic tunnel junctions (i.e., Fe/MgO/Fe), providing a large magnetoresistance ratio at room temperature [227]. Additionally, the catalytic activity of metal clusters on MgO thin film is subject to the surface statement [228]. It was reported that Au<sub>8</sub> clusters bound to oxygen vacancies of MgO surface can catalytically oxidize CO into CO<sub>2</sub> at low temperature [228]. Therefore, not only the EBISA, but also the EBID experiments were carried out on the well-prepared MgO substrate, to fabricate metal nanostructures for further magnetic and catalytic investigations in the near future.

MgO(100) thin films were epitaxially grown on a Ag(100) surface as introduced in Chapter 4 [181]. The quality of the thin film was monitored by SEM, LEED and AES. EBID and EBISA with subsequent AG performed on the as-prepared oxide thin film substrate in the UHV instrument. Fe nanostructures with varying shapes were fabricated by using Fe(CO)<sub>5</sub> as precursor molecule. In-situ SEM and AES were used to investigate the morphology and chemical composition, respectively. Series of Auger spectra were recorded with different electron doses, to scrutinize the electron stimulation process on the MgO surface. Ratios between the oxygen and the respective metal Auger peak areas were estimated and plotted versus the applied electron doses. An obvious electron stimulated desorption of oxygen can be observed, which is similar to other oxide surfaces, such as silicon oxide, and TiO<sub>2</sub> [15, 23].

## 9.2 Results and discussion

### 9.2.1 Nanostructure fabrication

Fe structures were fabricated via both EBID and EBISA with  $\text{Fe}(\text{CO})_5$  as the precursor on the MgO(100) substrate. SEM imaging and lithography were carried out with a beam energy of 15 keV and a probe current of 400 pA. Auger electron spectra were recorded with 15 keV electron beam energy and 3 nA probe current.

Firstly, the fabrication of EBID was investigated. Therefore spot and line patterns of Fe nanostructures were fabricated via EBID and the subsequent AG (~249 min), as depicted in Figure 9-1. For the spot pattern, the spot mode of the SEM software was used, while a single sweep with a step size of 12 nm was applied for the line pattern. Figure 9-1c and d show zoom-ins of the line patterns, which both have a total length of 45  $\mu\text{m}$ . The applied electron dose is realized by the actual dwell times and step sizes in the case of line patterns. All fabricated Fe deposits on MgO surface appear dark in SEM. This might be due to an increased work function of the Fe deposits compared to the one of the MgO substrate. The spot patterns demonstrate a straightforward relation between the applied electron dose and the diameter of the deposits. High electron dose (48 nC) results in large diameter of the deposits, due to increasing proximity effects [11, 16]. A local Auger electron spectrum, at the indicated position (red star) in Figure 9-1b, reveals a purity of ~93 at.% of the corresponding Fe deposits. The small oxygen peak can be attributed either due to residual gases in the UHV chamber or the MgO surface, while no significant carbon peak is observed.

## 9 EBID and EBISA on MgO(100)/Ag(100)

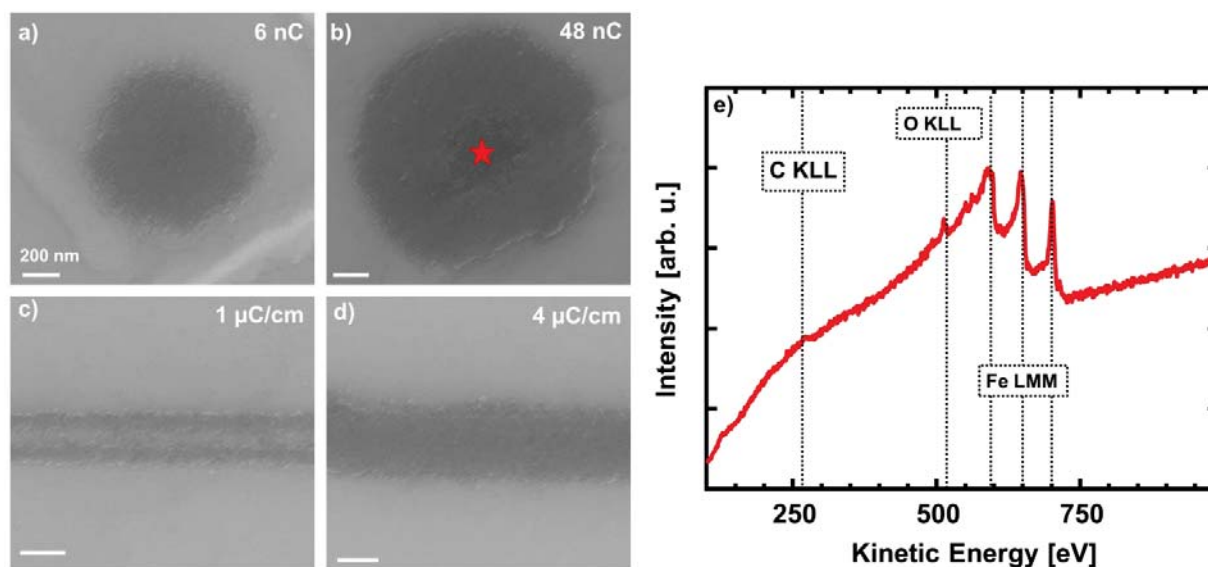


**Figure 9-1:** Spot (a, b) and line (c, d) patterns fabricated via EBID on MgO(100)/Ag(100) using  $Fe(CO)_5$  as precursor (approx.  $3 \times 10^{-7}$  mbar base pressure) with AG time  $\sim 249$  min. Electron doses are indicated on the top right. The spot diameter and line width increase with increasing electron dose. (e) AE spectrum of the Fe deposit depicted in (a), with the position indicated by the red star.

Since EBID obviously works fine on MgO, the next step was to investigate if the substrate is also susceptible to EBISA. Therefore, EBISA with subsequent AG of  $\sim 270$  min was also for Fe nanostructures fabrication on the MgO substrate. Figure 9-2 depicts spot pattern and line pattern of Fe nanostructures with further in-situ chemical characterization via AES. The deposits are composed of  $\sim 95$  at.% Fe with a small amount of oxygen ( $\sim 4$  at.%) and carbon ( $\sim 1$  at.%). The broadening of the fabricated structures is due to the proximity effects caused mainly by BSEs and associated SEs, as no forward scattering occurs in EBISA [11]. It is important to note that Fe nanocrystals grew in a rectangular fashion, i.e., with the edges along the [010] and [001] directions of the MgO (100) substrate as indicated by the dashed-lines in Figure 9-2a).

## 9 EBID and EBISA on MgO(100)/Ag(100)

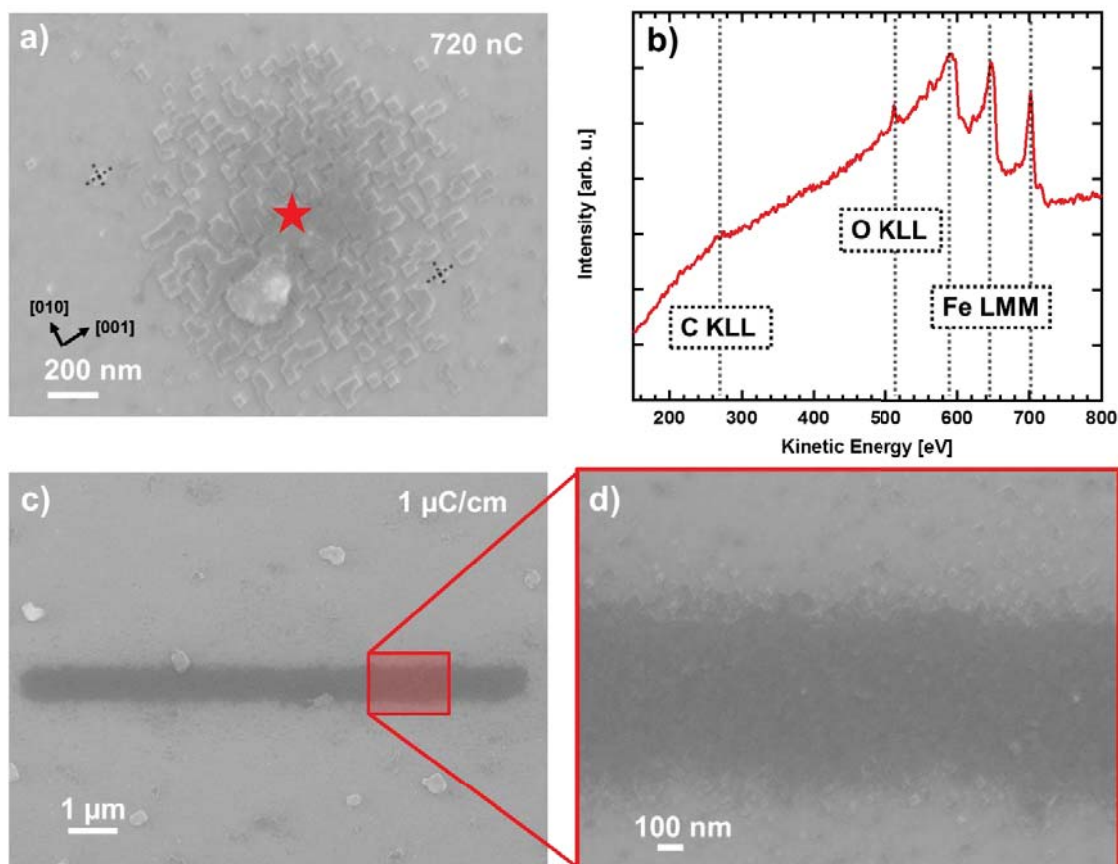


**Figure 9-2:** Fe nanostructures fabricated via EBISA plus AG, with  $\text{Fe}(\text{CO})_5$  as precursor. (a) Spot pattern Fe deposit (720 nC). (b) AE spectrum recorded on the indicated position in (a). (c) and (d) show a line Fe nanostructure with a length of  $10\ \mu\text{m}$  and step size of 12 nm. The total electron dose of the line is  $1\ \mu\text{C}/\text{cm}$ . Crystallographic axes were determined by LEED.

### 9.2.2 Activation mechanism

It was reported that on rutile  $\text{TiO}_2(110)$  surfaces, oxygen vacancies caused by the electron stimulated desorption of oxygen are the catalytically active sites that lead to precursor dissociation [15]. In order to investigate the effect of electron beam irradiation on the MgO surface, a spectroscopic investigation was carried out by AES.

Local Auger spectra were recorded while scanning the surface at different magnifications and therefore applying different electron doses. In this regard, the intensity changes of the Auger spectra as a function of the electron dose can be monitored. Figure 9-3 depicts the ratios between the oxygen and the respective Auger peak areas of Ti and Mg versus the applied electron doses.

### 9 EBID and EBISA on MgO(100)/Ag(100)

It is obvious that the amount of oxygen on the MgO surface is reduced by prolonged electron beam irradiation, which is quantitatively in line with what was observed on the other oxide surface [15]. For  $\text{TiO}_2(110)$  at high electron doses ( $\sim 10^6 \text{ C/cm}^2$ ), the O:Ti ratio is  $\sim 1.0$ , as half amount of oxygen atoms desorbed due to the electron stimulation. On the MgO(100) substrate, the O:Mg ratio saturates after  $\sim 100 \text{ C/cm}^2$ , and indicates half of the oxygen atoms desorption, as observed on the  $\text{TiO}_2$  surface. This observed reduction by electron irradiation is also in line with reports from the literature, where color center (oxygen vacancy) formation has been observed by exposing MgO films to electrons with an energy of 100 eV [229]. These defect were explained by electron stimulated desorption of oxygen atoms or ions via a multielectron Auger decay [230]. It is important to note that the chemical composition of the surface is likely to be non-uniform after the reduction process.

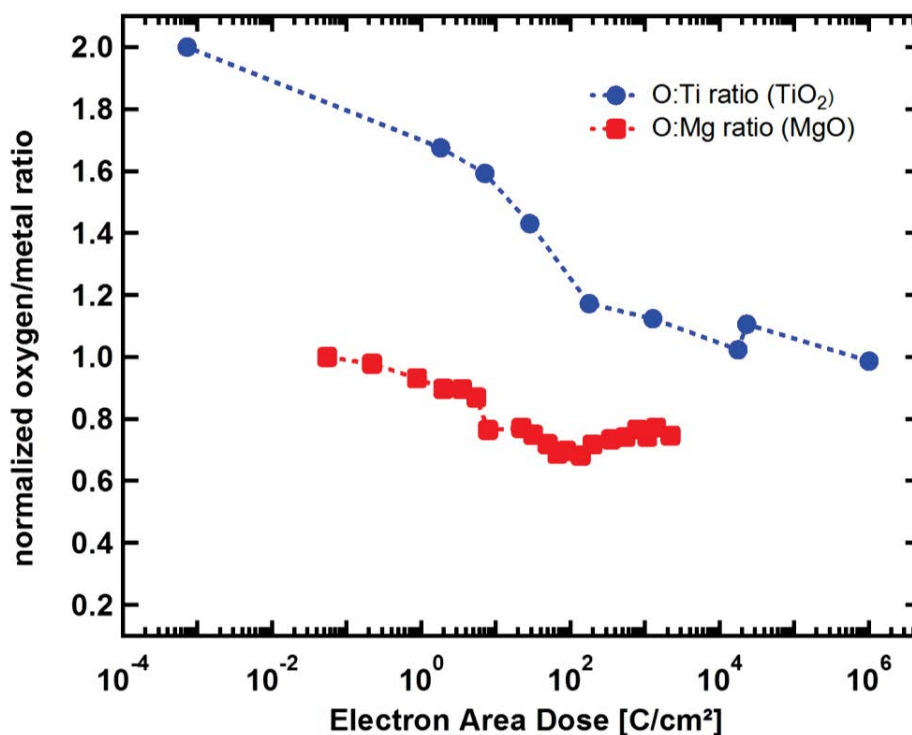


**Figure 9-3:** Quantitative evaluation of the ratio between normalized O and (semi-)metal peak areas versus applied electron area dose. At the lowest electron doses, the O:Mg peak area ratio is set to 1:1, while O:Ti is set to 2:1. Electron stimulated desorption causes a loss of oxygen atoms.

### 9.3 Conclusions

EBID and EBISA experiments were expanded to a well-prepared MgO(100)/Ag(100) substrate. Iron nanostructures with different shapes were fabricated using Fe(CO)<sub>5</sub> as precursor. It was proved by Auger spectra that Fe deposits with high purity can be obtained with both EBID and EBISA. It is interesting to observe that Fe nanocrystals grew solely along two-fold directions ([010] and [001]) on the MgO(100), which is different from other oxide surfaces.

The effect of electron beam irradiation on the MgO(100) surface has been studied via AES. These oxygen vacancies presumably play the key role in the dissociation of the subsequently dosed Fe(CO)<sub>5</sub>, resulting in Fe cubic nanocrystals growth on the surface. In particular, it could be demonstrated that MgO as a substrate is susceptible to electron beam induced activation via electron stimulated desorption of oxygen.

As described previously, there are various precursors applied in EBID and EBISA experiments. It is interesting to carry out exploratory experiments with other precursors such as Co(CO)<sub>3</sub>NO on MgO(100)/Ag(100) surface, as Co deposits present also attractive magnetic properties.

## 10 Binary Fe/Co alloy fabrication

### 10.1 Introduction

Magnetic nanostructures have generated a large scientific interest due to their potential applications in micro- and nano-electronics, spintronics, and data storage media [1-3]. One attractive type of magnetic materials is the binary alloy. For example, it has been reported that Fe-Pt alloy possesses high uniaxial magnetocrystalline anisotropy with good chemical stability, which can be applied as high performance permanent magnets [4]. Considering the synthesis of these magnetic binary alloys, it is important to control the shape and size of the magnetic nanostructures, as these factors have a strong influence on the magnetic properties [5].

As discussed previously, EBID is one of the most promising techniques for direct writing of nanostructures with controllable size and position [6-8]. Various magnetic nanostructures can be fabricated via EBID by using magnetic element containing precursor molecules [9-11]. In the last decades, magnetic iron and cobalt nanostructures have been produced through EBID using single metallic element molecules such as  $\text{Fe}(\text{CO})_5$  [12], and  $\text{Co}_2(\text{CO})_8$  [10]. Currently, investigations are focusing on the fabrication of binary alloys via EBID to expand the types of magnetic materials [13-15]. One way is to mix precursor gases by employing suitable precursor gas injection systems. Che et al. [15] showed that Fe-Pt alloy nanorods can be fabricated via EBID in an UHV SEM, using  $\text{Fe}(\text{CO})_5$  and cyclopentadienylplatinum trimethyl  $[(\text{CH}_3)_3(\text{C}_5\text{H}_5)\text{Pt}]$  as precursors. The corresponding binary nanostructures exhibited two or three times larger magnetic flux density than that of the Fe-containing nanorods. It is important to note that significant carbon contaminations were observed in the Fe-Pt deposits by EDX. Another way of synthesizing binary alloys via EBID is using a heteronuclear precursor containing two metallic elements. Porrati et al. [13] fabricated Co-Fe alloy magnetic nanostructures with high metallic content (~84 at.%) and lateral size down to 50 nm, by means of EBID from the  $\text{HFeCo}_3(\text{CO})_{12}$  heteronuclear carbonyl precursor.

One drawback of the heteronuclear precursor application is the requirement of well-designed precursor synthesis, such as chemical stability, enough vapor pressure and suitable ligands [8]. Another significant flaw is the lack of chemical composition control of the deposits during EBID process. Therefore, in this work, gaseous precursor mixtures were applied in EBID

## 10 Binary Fe/Co alloy fabrication

experiments and dosed through one single gas injection nozzle on the surface, in order to fabricate clean binary alloys nanostructures. With this method, alloys with variable chemical composition can be obtained by varying the partial pressure of the precursors [16].  $\text{Fe}(\text{CO})_5$  and  $\text{Co}(\text{CO})_3\text{NO}$  were chosen as they are chemically stable at room temperature and provide proper vapor pressure during EBID experiments. Another important point is that these two precursors yield Fe and Co nanostructures with high metal content [17, 18]. Additionally, AG process in our UHV system with these two precursors bear the possibility of fabricating well-defined nanostructures with high purity, as no electron dose is required during AG and thus no proximity effects occur [5]. In the following sections, it will be shown that the gas pressure ratio of the precursors indeed determines the chemical composition of the fabricated nanostructures. By characterizing series of binary nanostructures by the same electron dose but different AG time with in-situ AES, it turned out that the Fe/Co ratios of the deposits change with AG times. At last, it is highlighted that carbon free binary Fe-Co nanostructures can be fabricated via EBID and the subsequent AG in the UHV.

### 10.2 Results and discussion

#### 10.2.1 Precursors

As mentioned above,  $\text{Fe}(\text{CO})_5$  and  $\text{Co}(\text{CO})_3\text{NO}$  are two commonly used precursors in our UHV instrument for Fe and Co nanostructures fabrication via EBID and subsequent AG [17, 18]. In order to fabricate Fe-Co binary alloy nanostructures,  $\text{Fe}(\text{CO})_5$  and  $\text{Co}(\text{CO})_3\text{NO}$  were dosed simultaneously to the substrate surface through one gas dosing nozzle. It is well-known that the quality of the precursor molecules are important as it has great influence on the purity of the metal deposits fabricated via EBID using these precursors [19]. Therefore, before each EBID experiment, the quality of the precursor gas mixture was monitored by QMS in the gas dosing chamber. Different gas pressure ratios and dosing sequences for simultaneous dosing precursors were used, as listed in Table 10-1. The peak intensity ratio between  $\text{Fe}^+$  and  $\text{Co}^+$  in mass spectra changes with the corresponding gas pressure ratio. The QMS spectra were recorded only when the background pressure was stable after a sufficient equilibrium time.

In the case No.1,  $\text{Fe}(\text{CO})_5$  was first dosed until the background pressure of the gas dosing chamber reached  $1.5 \times 10^{-7}$  mbar, then  $\text{Co}(\text{CO})_3\text{NO}$  was dosed to achieve an accumulated background pressure of  $3 \times 10^{-7}$  mbar. The partial pressure of  $\text{Co}(\text{CO})_3\text{NO}$  was  $1.5 \times 10^{-7}$  mbar.

## 10 Binary Fe/Co alloy fabrication

The mass spectrum of the mixture gas is presented in Figure 10-1. The ratio between  $\text{Fe}^+$  ( $m/z = 56$ ) and  $\text{Co}^+$  ( $m/z = 58$ ) is estimated as  $\sim 0.77$ , unlike the partial pressure ratio in the gaseous mixture (both  $1.5 \times 10^{-7}$  mbar). This can be explained by the different ionization cross section of the precursors in the QMS.

In the case No.2, with the same dosing sequence, the background pressure of  $\text{Fe}(\text{CO})_5$  was increased to  $2 \times 10^{-7}$  mbar, then  $\text{Co}(\text{CO})_3\text{NO}$  until  $3 \times 10^{-7}$  mbar of the accumulative background pressure. It is as expected that the ratio between  $\text{Fe}^+$  and  $\text{Co}^+$  reaches  $\sim 1.56$ , which is two times higher than the value in the case No.1, due to the increase of the pressure ratio between iron and cobalt precursors in the mixture. This simple linear relation opens a route to adjust the ratio between Fe and Co in the mixture gas thus further control the chemical composition of the Fe-Co binary alloys fabricated using these mixture as the precursor via EBID.

Additionally, in the case No.3, the sequence of dosing these two precursors was reversed but with the same background pressure as in case No.1.  $\text{Fe}^+/\text{Co}^+$  ratio increases  $\sim 22\%$  compared to the value in case No.1. This might be attributed to the errors in the mass spectroscopy intensity reading. Mass spectra of the mixture precursor gases in case No.2 and No.3 can be found in Appendix Figure 12-4 and 12-5.

**Table 10-1:** Ratios between  $\text{Fe}^+$  and  $\text{Co}^+$  peak intensity in mass spectra by using different gas pressure ratios and dosing sequences.

Case No.	$\text{Fe}(\text{CO})_5$	$\text{Co}(\text{CO})_3\text{NO}$	$\text{Fe}^+/\text{Co}^+$
1	$1.5 \times 10^{-7}$ mbar	$1.5 \times 10^{-7}$ mbar	0.77
2	$2.0 \times 10^{-7}$ mbar	$1.0 \times 10^{-7}$ mbar	1.56
3*	$1.5 \times 10^{-7}$ mbar	$1.5 \times 10^{-7}$ mbar	0.94

\* In the case No.3, the sequence of dosing precursors is  $\text{Co}(\text{CO})_3\text{NO}$  first then  $\text{Fe}(\text{CO})_5$

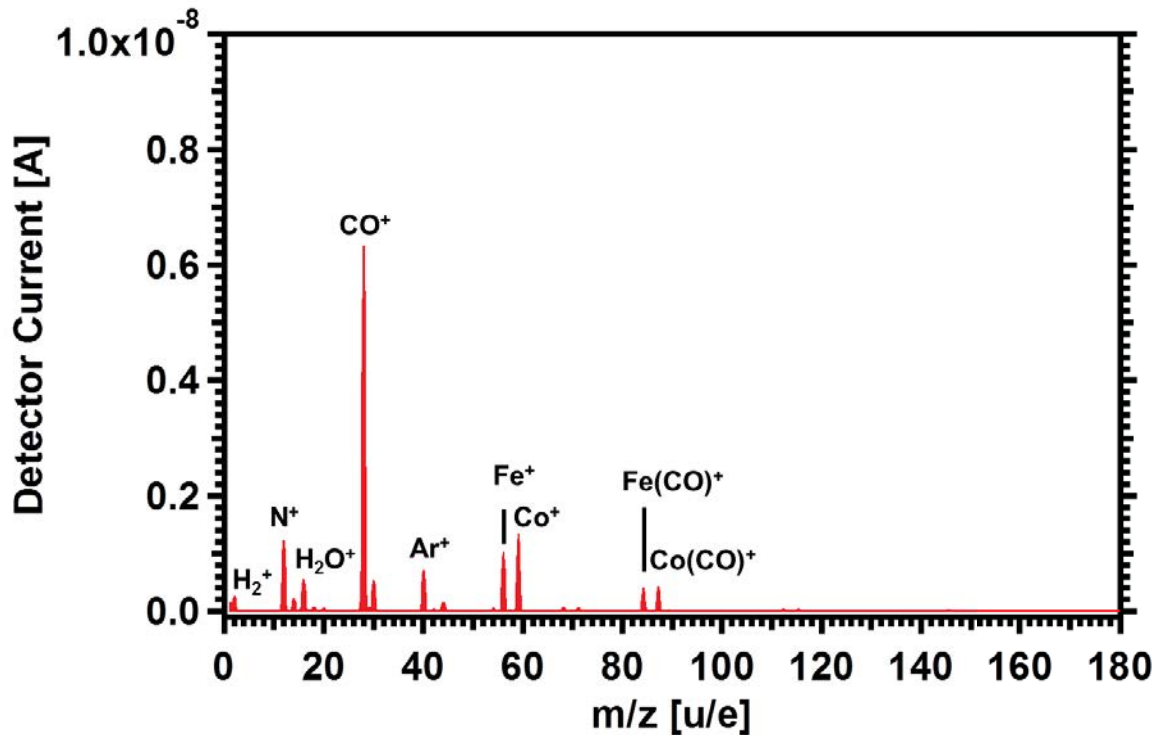


*Figure 10-1: Mass spectrum of a gas mixture of  $\text{Fe}(\text{CO})_5$  and  $\text{Co}(\text{CO})_3\text{NO}$ .  $\text{Fe}(\text{CO})_5$  was first dosed to  $1.5 \times 10^{-7}$  mbar, then  $\text{Co}(\text{CO})_3\text{NO}$  was dosed to  $3 \times 10^{-7}$  mbar. The ratio between  $\text{Fe}^+$  and  $\text{Co}^+$  peak intensity is 0.77. Likely fragments are indicated for the most prominent  $m/z$  features.*

By monitoring the ratio of  $\text{Fe}^+/\text{Co}^+$  in the mass spectra, the chemical composition of the gaseous mixture can be monitored. An in-situ measurement of the precursor mixture during the EBID and subsequent AG is necessary to understand the influence of the gas composition on the chemical composition of fabricated Fe-Co binary nanostructures.

### 10.2.2 Fe-Co binary nanostructures fabricated via EBID

EBID experiments were carried out on native oxidized Si(100) substrate with different electron doses and AG times, using gaseous mixture of two precursors ( $\text{Fe}(\text{CO})_5$  and  $\text{Co}(\text{CO})_3\text{NO}$ ), in order to fabricate Fe-Co binary alloy nanostructures. Simple  $4 \times 4 \mu\text{m}^2$  patterns were chosen for in-situ characterization in the UHV instrument by SEM and AES. The step size during EBID process was 6.2 nm and multi-sweep-scanning was applied (10 sweeps) [5, 17]. 15 keV electron beam energy and 400 pA beam current were used for all SEM micrographs and

## 10 Binary Fe/Co alloy fabrication

lithography. Auger spectra were recorded on the corresponding nanostructures with a beam energy of 15 keV and a beam current of 3 nA. Different gas partial pressure ratios between these two precursors were used, as listed in Table 10-1. After dosing each precursor, an “equilibration time” (~15 min) was granted to ensure a stable background pressure.

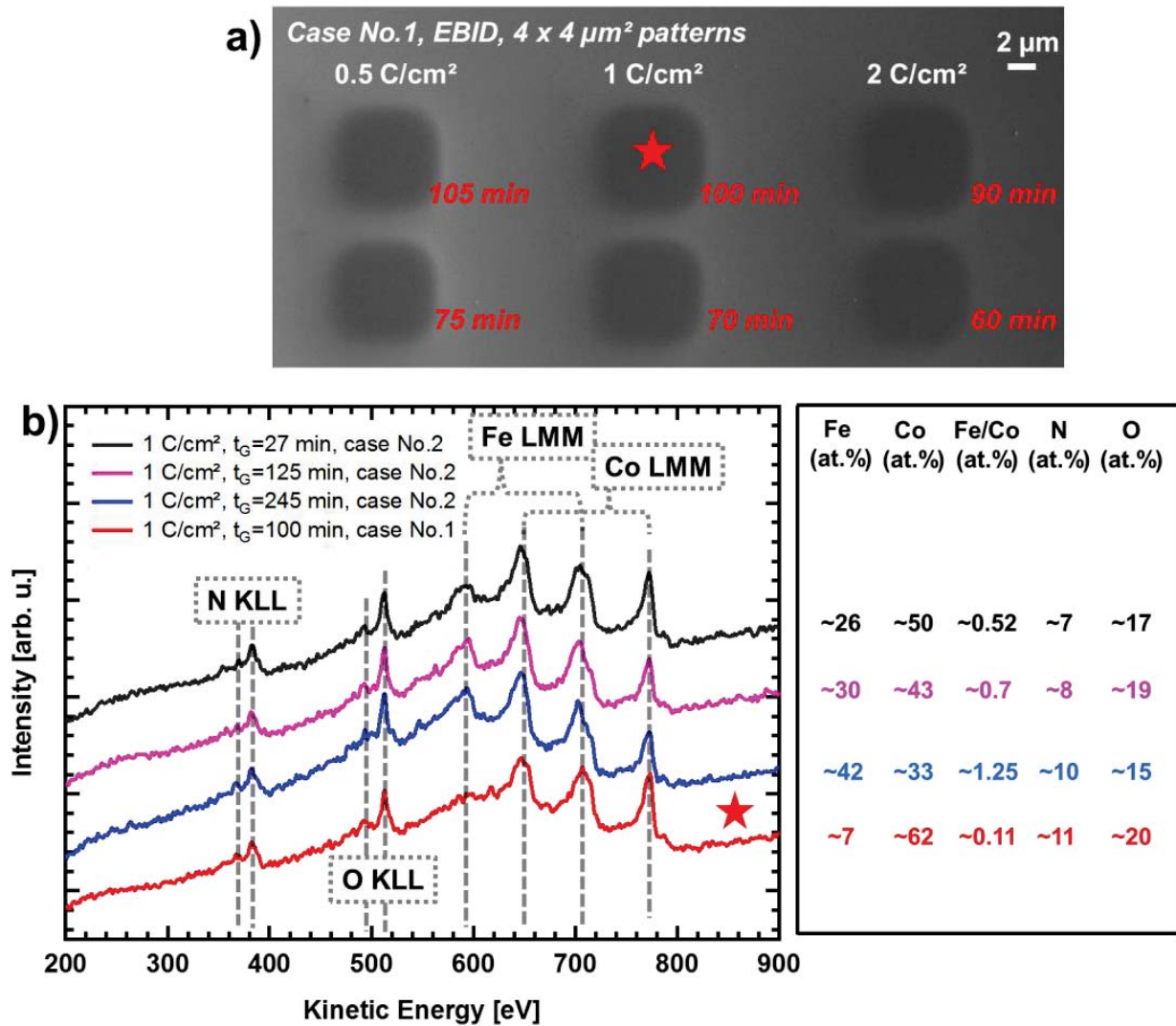


**Figure 10-2:** (a)  $4 \times 4 \mu\text{m}^2$  Fe/Co binary alloy patterns fabricated via EBID with different AG times, and the gas mixture case No.1 (cf. Table 10-1). The applied electron doses and AG times are indicated. (b) Auger spectra of the fabricated Fe/Co alloys with EBID ( $1 \text{ C/cm}^2$ ) and different AG times, with case No.1 and case No.2 gas mixtures. The position of the spectrum on deposit in case No.1 ( $1 \text{ C/cm}^2$ , 100 min AG time) is labeled in (a). As indicated in the figure, two peaks of the Fe LMM and Co LMM transitions are overlapping.

## 10 Binary Fe/Co alloy fabrication

Figure 10-2a depicts the fabricated nanostructures via EBID and the corresponding AG time as indicated, using gaseous mixture of the case No.1 as precursor molecules. The fringes around the structures can be attributed to proximity effects caused by forward scattering and backscattered electrons [20, 21]. Dark appearance of fabricated nanostructures might be due to the higher work function of the deposits compared to the one of the native oxide Si(100) surface. Auger spectrum was recorded at the center of the indicated nanostructure in Figure 10-2a (1 C/cm<sup>2</sup>, 100 min of AG), indicating a chemical composition of Fe (~7 at.%), Co (~62 at.%), N (~11 at.%), and O (~20 at.%). As depicted in Figure 10-2b of the Auger spectra, the first Fe LMM (597 eV) and last Co LMM peak (773.5 eV) were used for Fe and Co composition evaluation. The metal content of the deposits is as high as ~70 at.%, which can be attributed to the UHV fabrication environment and also the long AG time. There is no carbon detectable in the nanostructure. The oxygen and nitrogen KLL peaks are suspected to derive from the nitrosyl ligands of the cobalt precursor and the residual gas in the chamber. Therefore, it has been demonstrated that carbon free Fe-Co binary alloy can be fabricated via EBID and the subsequent AG in the UHV, using gaseous mixture of Fe(CO)<sub>5</sub> and Co(CO)<sub>3</sub>NO as the precursor. However, only 0.11 of Fe/Co was obtained, which is 7 times lower than the ratio between Fe<sup>+</sup>/Co<sup>+</sup> of the mixture precursor in the QMS. This lower value might be caused by various factors, such as the diffusion ability of the molecules on the surface, the cross sections, and the autocatalytic decompositions on pre-formed deposits.

With the purpose of increasing the Fe concentration inside the EBID-binary alloys, a mixture gas with higher iron precursor pressure (case No.2) was applied. 4 x 4 μm<sup>2</sup> Fe-Co binary nanostructures were produced via EBID (1 C/cm<sup>2</sup>) with different AG times. In-situ AES was carried out to monitor the chemical compositions of the nanostructures (Figure 10-2b). It is obvious that Fe peak (597 eV) increases compared to the previous one using gaseous mixture of case No.1. Fe-Co deposits by 1 C/cm<sup>2</sup> and 125 min of AG time consist of Fe (~30 at.%), Co (~43 at.%), N (~8 at.%), and O (~19 at.%). Two time higher iron precursor pressure in the gaseous mixture precursor results in 7 times higher Fe/Co ratio (~0.7) compared to the one of the nanostructure fabricated with similar parameters (1C/cm<sup>2</sup> and 100 min of AG), using mixture precursor of case No.1. This demonstrates that changing the precursor pressure is a simple route to control the chemical composition of the deposits via EBID, when two precursors were dosed

## 10 Binary Fe/Co alloy fabrication

simultaneously. It is expected that higher Fe concentration can be obtained if higher pressure of  $\text{Fe}(\text{CO})_5$  in the gaseous mixture is applied.

Furthermore, nanostructures fabricated with the same electron dose ( $1\text{C}/\text{cm}^2$ ) and precursor composition (case No.2) but different AG time exhibit changes in the chemical composition, as shown by the composition values in Figure 10-2b. The intensity of the first Fe LMM peak (597 eV) increases, while the one of the last Co LMM peak (773.5 eV) decreases with increasing AG time. This indicates a higher Fe/Co ratio of the deposits with longer AG time.

In order to investigate the influence of the AG time on the composition of the fabricated Fe/Co binary alloy nanostructures, series of Auger spectra were recorded on the nanostructures produced by various electron doses and AG times, using precursor mixture of the case No.2. Quantitative analysis was carried out by evaluating the ratios between Fe and Co peak areas and plotting them versus the applied AG times, as depicted in Figure 10-3. It can be observed that Fe/Co increases with the AG time for all applied electron doses ( $0.5$ ,  $1$ , and  $2\text{C}/\text{cm}^2$ ). The ratio seems to saturate at around 180 min of the AG time. There is no difference of the chemical composition for the nanostructures fabricated with different electron doses but the same AG times and the same precursor gases.

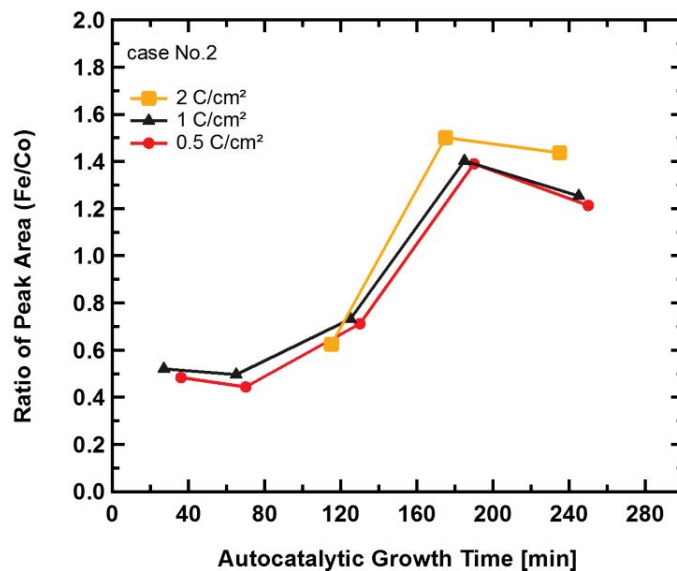


**Figure 10-3:** Influence of AG time and applied electron dose during EBID process on the chemical composition of fabricated Fe/Co alloy nanostructures. Quantitative analysis of the ratio between Fe and Co peak areas was done by using the Fe LMM peak at 595 eV and the Co LMM peak at 773.5 eV with background subtraction.

## 10 Binary Fe/Co alloy fabrication

The increase of the Fe/Co with the AG time can be simply explained by the autocatalytic decomposition of iron and cobalt precursors. It is obvious that both  $\text{Fe}(\text{CO})_5$  and  $\text{Co}(\text{CO})_3\text{NO}$  decomposed autocatalytically on the pre-formed Fe-Co binary deposits. As the Fe/Co ratio increases, it can be speculated that  $\text{Fe}(\text{CO})_5$  exhibits higher decomposition rate than the one of  $\text{Co}(\text{CO})_3\text{NO}$ . After a long AG time (~180 min), the decomposition of both iron and cobalt precursors reaches an equilibrium state and the Fe/Co ratio becomes saturated. With this result, it is demonstrated that the chemical composition of Fe-Co binary deposits can be not only controlled along the EBID process by changing the partial pressure of the precursors, but also adjustable through the AG process (i.e., different AG time applied). Furthermore, the equilibrium value of the Fe/Co ratio during AG can even be changed by applying different partial pressure of the precursors.

Further experiments will be carried out to extend the curves in Figure 10-3 to longer AG time part so that the saturation behavior can be identified. TEM investigations on the morphology of the deposits in atomic level resolution can be helpful for understanding the mechanism of the changes in the Fe/Co ratio. As there is no influence of the applied electron dose on the chemical composition, it can be suspected that the whole EBID process is in the precursor limited region.

### 10.3 Conclusions

This chapter aimed at investigating the fabrication of Fe/Co binary alloy nanostructures via EBID and subsequent AG processes using mixtures of  $\text{Fe}(\text{CO})_5$  and  $\text{Co}(\text{CO})_3\text{NO}$  on  $\text{SiO}_x/\text{Si}(100)$ . It has been demonstrated that carbon free Fe-Co binary nanostructures can be fabricated. The metallic composition of the fabricated nanostructures can be controlled via adjusting the precursor pressure in the gaseous mixture or the subsequent AG time.

As the quality of the precursor is important for further EBID and AG process, QMS was employed to monitor the gas mixture compositions. It has been shown that the Fe/Co intensity ratio in the mass spectrum can be increased two times by simply increasing two times of the partial pressure of  $\text{Fe}(\text{CO})_5$  in the precursor mixture.

EBID-Fe/Co binary alloy nanostructures have been fabricated by changing various parameters: the composition of the precursor mixture, electron dose and AG time. Auger spectra showed that the Fe-Co nanostructure composition can be varied by changing the composition of

## 10 Binary Fe/Co alloy fabrication

the mixed precursor. With increasing AG time, Fe/Co ratios in deposits increase and tend to saturate at ~180 min. No significant influence of the electron dose on the composition of the EBID binary deposits has been observed. No carbon is detectable and a high metal content (~70 at.%) was observed on the Fe-Co deposits, which is due to the UHV environment and also the subsequent AG. Oxygen and nitrogen inside the deposits can be attributed to the nitrosyl ligands and the residual gas of the chamber. It is possible to increase the metal content of the binary deposits further by using  $\text{Co}_2(\text{CO})_8$  instead of  $\text{Co}(\text{CO})_3\text{NO}$ , as carbonyl ligands are expected to dissociate completely by the electron stimulation.

The results provide various routes to adjust the chemical composition of the fabricated carbon-free binary alloys. Fe/Co ratio can be controlled along the deposition process (EBID) by changing the gas partial pressure. Different subsequent AG times also have influence on the chemical compositions. Additionally, the equilibrium value of the Fe/Co ratio during AG can also be adjustable by changing the gas partial pressure.



## 11 Summary

This thesis focuses on two aspects: firstly, to explore and investigate novel nanolithographic processes to fabricate Fe and Co nanostructures from the precursor molecules  $\text{Fe}(\text{CO})_5$  and  $\text{Co}(\text{CO})_3\text{NO}$  and secondly, to further characterize the physical and chemical properties and explore novel applications (seeds for the localized growth of CNTs) of the latter metal containing deposits. Fe and Co nanostructures with controllable shape and desired chemical composition (i.e., high purity) were fabricated via electron beam induced deposition (EBID) and electron beam induced surface activation (EBISA) techniques, using  $\text{Fe}(\text{CO})_5$  and  $\text{Co}(\text{CO})_3\text{NO}$  as precursor molecules. In EBID, a focused electron beam is applied to locally dissociate precursor molecules on a substrate, generating a deposit from the non-volatile fragments. Surface activation is utilized in EBISA stimulated by focused electron beam and presents autocatalytic decomposition property for certain precursors, resulting in desired deposits.

Under ultra-high vacuum (UHV) condition, pre-formed deposits (Fe or Co) will exhibit autocatalytic growth (AG) already at room temperature as long as the corresponding precursors ( $\text{Fe}(\text{CO})_5$  and  $\text{Co}(\text{CO})_3\text{NO}$  respectively) are supplied. Combining EBID with AG, massive deposits can be fabricated with reduced proximity effects as no further electron dose is required during AG. Thereby, it is necessary to investigate the evolution of the iron deposits morphology during AG procedure via in-situ scanning electron microscopy (SEM) and high resolution transmission electron microscopy (HRTEM). Electron diffraction and electron energy loss spectroscopy (EELS) provided further characterization of the crystalline orientation and chemical composition of the deposits. Just after EBID experiments, Fe nanoparticles with spherical shape were observed, which were identified as  $\text{Fe}_3\text{O}_4$ . It is important to note that the spherical shape can also be due to the strain induced morphological change during the native oxidation process when exposed to ambient conditions, as occurred for the transport from the UHV instrument to the HRTEM. EBID and EBISA combined with long AG time produced pure cubic  $\alpha$ -Fe nanocrystals, indicating complete dissociation of  $\text{Fe}(\text{CO})_5$  during AG. Further characterization with TEM by transporting samples in inert gas atmosphere is suggested in order to clarify the morphology and chemical composition of Fe deposits just after EBID (Chapter 5).

In the next step, the magnetic properties such as coercivity field of the Fe nanostructures fabricated via EBID plus AG were investigated. Chemical information was provided by the near

## 11 Summary

edge X-ray absorption fine structure (NEXAFS) spectra on the produced Fe nanostructures and a self-limiting native oxidation process was found and discussed. The characterization of the magnetization reversal was achieved via X-ray magnetic circular dichroism (XMCD) contrast in scanning transmission X-ray microscopy (STXM) analysis. The shape of the magnetic domains could be observed as a function of the external applied magnetic field and further utilized for the evaluation of the corresponding coercivity values  $H_C$ . It was observed that hysteresis loops still exist for thin deposits in the range of 3.4~8 nm, which are implied to be fully natively oxidized. These native iron oxide nanostructures consist of  $Fe_3O_4$  and  $\alpha$ -Fe crystals, as verified via TEM measurements. A steady increase of  $H_C$  from ~40 Oe to more than ~160 Oe was observed in the range of the thickness mentioned above. The acquired results indicate perspectives for designing functional magnetic structures with desired properties. Especially, the unique AG approach can indeed open a powerful route towards the fabrication of particularly clean metallic deposits and thus functional magnetic nanostructures (Chapter 6).

Protocols for the fabrication of well-defined CNTs with positional control on the nanoscale and different morphologies were successfully established, based on lithographically generated catalytic active EBID templates. In this work at hand, Fe deposits fabricated via EBID and subsequent AG in UHV with  $Fe(CO)_5$  as precursor molecule. Evidence was presented that the Fe deposits can act as catalysts for localized CNT growth. The influence of the Fe deposits fabrication parameters (i.e., electron dose during EBID and the subsequent AG time) was investigated. By adjusting these parameters, well-defined individual CNT on each EBID-Fe point-deposit of a point-matrix can be realized, via the corresponding CVD experiment. In the next step, CNTs with high density and vertical alignment, referred as CNT forest, were produced on EBID-Fe deposits, fabricated on an  $Al_2O_3$  substrate. It is obvious that the  $Al_2O_3$  thin film enhances the yield of CNTs. A peculiar lifting-up of corresponding 2D EBID structures as “flakes” was observed. This lifting-up structure can be attributed to the growth of CNTs underneath the catalytic active deposit, raising the latter structure from the support. Additionally, proof of principle is presented that Co structures fabricated via EBID plus AG from the precursor  $Co(CO)_3NO$  are also very effective as catalysts for the secondary growth of CNTs. Even though the metal contents of these structures were significantly lower than the ones of the Fe deposits, the Co containing structures still active in CVD at lower temperatures (Chapter 7).

## 11 Summary

Utilizing a synchrotron based STXM instrument, a novel focused X-ray beam induced deposition (FXBID) technique has been developed. In this regard the fabrication, microscopic and in-situ chemical characterization of cobalt and manganese nanostructures produced via this FXBID technique has been reported and discussed. An apparent energy-dependent dissociation of the precursor molecules was observed. It can be concluded that  $\text{Co}(\text{CO})_3\text{NO}$  and  $\text{MeCpMn}(\text{CO})_3$  dissociated most effectively at resonant energies of the respective absorption edges of the metal center. These findings indicate that FXBID can be performed with a large amount of organometallic molecules with the energy selectivity of the precursor dissociation mainly driven by the X-ray absorption cross section at the respective metal transitions. There is less or no backscattered electron (BSE) proximity effects for the fabricated nanostructures via FXBID compared to FEBIP. It is also possible to produce binary alloy nanostructures through FXBID, using gas mixture with more than one metal center. High purity of binary nanostructures can be deposited without time consuming pumping steps or even breaking the vacuum, by controlling the resonant energy during FXBID process. Further photon-energy dependent studies with precursor molecules in the gas phase are required, with purpose of getting insight into the basic dissociation and growth mechanisms. The limitation of the resolution in FXBID is also interesting in the near future work (Chapter 8).

As an important technique, EBID and EBISA experiments were expanded to an ultra-thin oxide films namely MgO with  $\text{Fe}(\text{CO})_5$  as precursor. Cubic Fe nanocrystals were fabricated and characterized by in-situ SEM and Auger electron spectroscopy (AES). Electron irradiation on MgO was studied via Auger spectra. It could be verified that oxygen vacancies were generated by electron stimulated desorption, similar as on  $\text{TiO}_2$  and  $\text{SiO}_2$  surfaces. These vacancies presented catalytic active sites for the decomposition of  $\text{Fe}(\text{CO})_5$ , leading to the fabrication of Fe nanostructures with high purity. Further work will be continued by using  $\text{Co}(\text{CO})_3\text{NO}$  as the precursor of EBID on the MgO thin film (Chapter 9).

Last but not least, binary Fe-Co nanostructures were fabricated on an  $\text{SiO}_x/\text{Si}(100)$  substrate via EBID combined with AG in the UHV, using a gas mixture of  $\text{Fe}(\text{CO})_5$  and  $\text{Co}(\text{CO})_3\text{NO}$ . It could be demonstrated for the first time that carbon-free Fe-Co binary alloys with high metallic content ( $> \sim 70$  at.%) can be fabricated. Various routes for adjusting the chemical composition of deposits can be concluded. During the EBID process, the chemical composition, i.e., the Fe/Co ratio can be adjusted by simply changing the partial pressure of the precursors in the gas mixture.

## 11 Summary

Additionally, Fe/Co ratios change with the subsequent AG time, which can be ascribed to the different autocatalytic decomposition yield of iron and cobalt precursors. Therefore, certain Fe/Co composition corresponds to a specific AG time. Furthermore, it is also possible to control the Fe/Co ratio by changing the gas partial pressure during the AG (Chapter 10). Fe/Co binary alloy nanostructures fabricated in this work are attractive for their magnetic and catalytic properties. Further investigations can be carried out with STXM for magnetic properties and also CNTs can be grown on these binary nanostructures.

From all the results presented, it is obvious that focused electron and photon beam are promising tools to fabricate well-defined functional nanomaterials on various surfaces. Especially concerning the properties of the fabricated nanomaterials, a new route can be opened for the investigations of the nanodevices.

## 12 Zusammenfassung

Diese Arbeit beschäftigt sich im Wesentlichen mit zwei Aspekten: Der Erste, ist die Untersuchung und Erforschung neuer nanolithographischer Prozesse zur Herstellung von Fe und Co Nanostrukturen aus den Precursormolekülen  $\text{Fe}(\text{CO})_5$  und  $\text{Co}(\text{CO})_3\text{NO}$ . Der Zweite Aspekt ist die weitere Charakterisierung der physikalischen und chemischen Eigenschaften, sowie die Erforschung neuer Anwendungen (Keime für das lokalisierte Wachstum von CNTs) der metallhaltigen Abscheidungen. Die Fe und Co Nanostrukturen wurden, mit kontrollierter Form und chemischer Zusammensetzung (z.B.: hohe Reinheit), durch Elektronenstrahlinduzierte Abscheidung (EBID) und Elektronenstrahlinduzierte Oberflächenaktivierung (EBISA) mit den Precursormolekülen  $\text{Fe}(\text{CO})_5$  und  $\text{Co}(\text{CO})_3\text{NO}$  hergestellt. Bei EBID wird ein hochfokussierter Elektronenstrahl benutzt, um lokal Precursormoleküle auf einem Substrat zu dissoziieren, wobei eine Abscheidung aus den nichtflüchtigen Fragmenten entsteht. In EBISA wird eine lokale Aktivierung der Oberfläche, durch einen fokussierten Elektronenstrahl erreicht, an diesen aktivierten Bereichen findet eine autokatalytische Zersetzung bestimmter Precursormoleküle statt, was zu den gewünschten Abscheidungen analog zum EBID Prozess führt.

Unter Ultrahochvakuum (UHV) Bedingungen, zeigen zuvor geformte Abscheidungen (Fe oder Co), bereits bei Raumtemperatur, autokatalytisches Wachstum (AG), so lange der entsprechende Precursor ( $\text{Fe}(\text{CO})_5$  beziehungsweise  $\text{Co}(\text{CO})_3\text{NO}$ ) dosiert wird. Durch die Kombination von EBID und AG können massive Abscheidungen, mit reduzierten Proximity-Effekten, hergestellt werden, da während der AG keine weitere Elektronendosis benötigt wird. Dadurch ist es notwendig, die Entwicklung der Morphologie der Eisenabscheidungen, während des AG Prozesses, mit Hilfe von in-situ Rasterelektronenmikroskopie (SEM) und hochauflösender Transmissionselektronenmikroskopie (HRTEM) zu untersuchen. Elektronenbeugungs- und Elektronenverlustspektroskopie (EELS) lieferten eine weitere Charakterisierung der Kristallorientierung und chemischen Zusammensetzung der Abscheidungen. Direkt nach EBID Experimenten wurden kugelförmige Fe Nanopartikel, welche als  $\text{Fe}_3\text{O}_4$  identifiziert wurden, beobachtet. Hierbei ist es wichtig festzustellen, dass die Kugelform auch durch Spannungsinduzierte Morphologieänderungen während des natürlichen Oxidationsprozesses in Umgebungsbedingung entstehen kann. Die Probe wurde beim Transport vom UHV Instrument zum HRTEM Umgebungsbedingungen (also auch Luftsauerstoff)

## 12 Zusammenfassung

ausgesetzt. EBID und EBISA kombiniert mit langen AG Zeiten führen zu kubischen  $\alpha$ -Fe Nanokristallen, was auf eine komplette Zersetzung von  $\text{Fe}(\text{CO})_5$  während des AG hinweist. Weitere Untersuchungen mit TEM, wobei die Proben unter Inertgas transportiert werden sollten, sind notwendig, um die Morphologie und die chemische Zusammensetzung der Fe Abscheidungen direkt nach dem EBID Prozess zu bestimmen (Kapitel 5).

Im nächsten Schritt wurden die magnetischen Eigenschaften, wie die Koerzitivität, der Fe Nanostrukturen, welche mit EBID plus AG hergestellt wurden, untersucht. Mit Hilfe von Röntgen-Nahkanten-Absorptions-Spektroskopie (NEXAFS) konnten tiefergehende Erkenntnisse über die chemische Zusammensetzung der produzierten Fe Nanostrukturen gewonnen werden. Dabei wurde ein selbst-limitierender, natürlicher Oxidationsprozess festgestellt und diskutiert. Die Charakterisierung der Magnetisierungsumkehrung durch ein äußeres Feld, wurde mit Röntgendichroismus (XMCD) Kontrast während der Raster-Transmission-Röntgenmikroskopie (STXM) Analyse erhalten. Die Form der Magnetischen Domänen konnten als Funktion des angelegten externen magnetischen Feldes beobachtet werden und entsprechende Hysteresekurven extrahiert werden. Diese Daten wurden weiter benutzt, um die entsprechenden Koerzitivfeldstärken  $H_C$  (Breite der Hystereseschleife) zu ermitteln. Eine stetige Zunahme von  $H_C$ , beginnend bei  $\sim 40$  Oe bis hin zu  $\sim 160$  Oe, wurde im Bereich der erwähnten Dicke festgestellt. Die erlangten Ergebnisse deuten Möglichkeiten für das Design von funktionellen magnetischen Strukturen mit gewünschten Eigenschaften an. Besonders der einzigartige AG Ansatz kann in der Tat eine vielversprechende Route, zur Herstellung von besonders reinen Metallabscheidungen und somit funktionellen magnetischen Nanostrukturen, sein (Kapitel 6).

Basierend auf katalytisch aktiven EBID Masken, hergestellt via FEBIP-Lithographie, wurden Protokolle für die Herstellung von wohldefinierten CNTs, mit Positionkontrolle auf der Nanoskala und unterschiedlicher Morphologie, eingeführt. In dieser Arbeit handelte es sich um Eisenabscheidungen, hergestellt via EBID und darauffolgendem AG im UHV, aus dem Precursormolekül  $\text{Fe}(\text{CO})_5$ . Es wurde gezeigt, dass diese Eisenabscheidungen als Katalysator für das lokalisierte Wachstum von CNTs eingesetzt werden können. Der Einfluss der Parameter zur Herstellung der Eisenabscheidungen (z.B. Elektronendosis während EBID und die folgende AG Zeit) wurde untersucht. Durch die Optimierung dieser Parameter konnten wohldefinierte, einzelne CNTs auf jeder EBID-Fe-Punkt-Abscheidung, einer Punktmatrix, realisiert werden. Im

## 12 Zusammenfassung

nächsten Schritt wurden CNTs mit hoher Dichte und vertikaler Anordnung hergestellt. Diese „CNT Wälder“ wurden auf EBID-Fe Abscheidungen, welche auf  $\text{Al}_2\text{O}_3$  geschrieben wurden, mit dem entsprechenden CVD Experiment gewachsen. Es ist offensichtlich, dass der dünne  $\text{Al}_2\text{O}_3$  Film die Ausbeute an CNTs erhöht. Ein „Anheben“ der 2D EBID Strukturen auf sog. „flakes“ wurde beobachtet. Diese erhobenen Strukturen sind auf das Wachstum von CNTs unter den katalytisch aktiven Abscheidungen zurück zu führen. Dadurch werden diese Abscheidungen vom Support angehoben. Zusätzlich wurde gezeigt, dass Co Strukturen, welche mit EBID plus AG aus dem Precursor  $\text{Co}(\text{CO})_3\text{NO}$ , hergestellt wurden ebenfalls sehr effektive Katalysatoren für das sekundäre Wachstum von CNTs sind. Obwohl der Metallgehalt dieser Strukturen deutlich geringer, verglichen mit den Eisenabscheidungen, war, waren die Co enthaltenden Strukturen noch in CVD bei geringeren Temperaturen aktiv (Kapitel 7).

Eine neue Fokussierte-Röntgenstrahl-Induzierte-Abscheidungs-Technik (FXBID) wurde mit Hilfe eines Synchrotron basierten STXM Instruments entwickelt. In diesem Zusammenhang wurden die Herstellung, die mikroskopische und die in-situ chemische Charakterisierung von Cobalt und Mangan Nanostrukturen, welche mit diesem FXBID Prozess hergestellt wurden, realisiert und diskutiert. Eine energieabhängige Dissoziation der Precursormoleküle wurde beobachtet. Daraus konnte gefolgert werden, dass  $\text{Co}(\text{CO})_3\text{NO}$  und  $\text{MeCpMn}(\text{CO})_3$  am effektivsten bei Resonanzenergien der entsprechenden Absorptionskante des Metallzentrums dissoziieren. Diese Beobachtungen deuten an, dass FXBID mit einer großen Menge an organometallischen Molekülen realisiert werden kann. Dabei wird die Energieselektivität, der Dissoziation der Precursormoleküle, hauptsächlich durch das Röntgenabsorptionsprofil des entsprechenden Metallübergangs bestimmt. Es tritt weniger oder kein Rückstreuelektronen-Proximity-Effekt, verglichen mit FEBIP, bei der Herstellung von Nanostrukturen via FXBID auf. Außerdem ist es mögliche binäre Legierungen herzustellen, in dem man Gasmischungen mit mehr als einem Metallzentrum benutzt. Man kann durch die Kontrolle der Resonanzenergie, während des FXBID Prozesses, eine hohe Reinheit an binären Nanostrukturen erreichen, ohne zeitraufwändige Pumpschritte oder sogar Unterbrechungen des Vakuums zu benötigen. Um einen Einblick in den grundlegenden Dissoziations- und Wachstumsmechanismus zu bekommen, sind weitere photonenergieabhängige Studien mit gasförmigen Precursormolekülen notwendig (Kapitel 8).

## 12 Zusammenfassung

Die wichtigen Techniken, EBID und EBISA, wurden erstmals auf einem ultra-dünnen MgO Oxidfilm mit dem Precursor  $\text{Fe}(\text{CO})_5$  angewandt. Kubische Fe Nanokristalle wurden hergestellt und durch in-situ SEM und Auger-Elektronen-Spektroskopie (AES) charakterisiert. Die Elektronenbestrahlung von MgO wurde mit Augerspektren analysiert. Ähnlich wie bei  $\text{TiO}_2$  und  $\text{SiO}_2$  Oberflächen, wurden durch elektronenstimulierte Desorption Sauerstofffehlstellen geschaffen. Diese Fehlstellen weisen eine katalytische Aktivität gegenüber der Zersetzung von  $\text{Fe}(\text{CO})_5$  auf, was zur Entstehung von Fe Nanostrukturen mit hoher Reinheit führt. Diese Arbeit wird weitergeführt durch EBID Experimente, mit dem Precursor  $\text{Co}(\text{CO})_3\text{NO}$ , auf dem dünnen MgO Film (Kapitel 9).

Nicht zuletzt wurden binäre Fe-Co Nanostrukturen auf  $\text{SiO}_x/\text{Si}(100)$  via EBID kombiniert mit AG in UHV produziert. Dabei wurde eine Gasmischung aus  $\text{Fe}(\text{CO})_5$  und  $\text{Co}(\text{CO})_3\text{NO}$  verwendet. Zum ersten Mal konnte aufgezeigt werden, dass kohlenstofffreie binäre Fe-Co Legierungen mit hohem Metallgehalt ( $> \sim 70$  at.%) hergestellt werden können. Verschiedene Wege zur Beeinflussung der chemischen Zusammensetzung der Abscheidungen wurden erforscht. Während des EBID Prozesses kann die chemische Zusammensetzung, z.B. das Fe/Co Verhältnis, durch einfaches Ändern der Partialdrücke der Precursoren in der Gasmischung eingestellt werden. Zusätzlich ändert sich das Fe/Co Verhältnis mit anschließender AG Zeit. Dies ist auf die unterschiedlichen autokatalytischen Zersetzungsraten des Eisen und Cobalt Precursors zurückzuführen. Daraus folgt, dass die Fe/Co Zusammensetzung der entsprechenden Abscheidungen auch durch die zu einer AG Zeit beeinflusst werden kann. Außerdem ist es auch möglich, das Fe/Co Verhältnis durch Änderung der Partialdrücke während des AG zu kontrollieren (Kapitel 10). Binäre Fe/Co Nanostrukturen, welche in dieser Arbeit hergestellt wurden, sind aufgrund ihrer magnetischen und katalytischen Eigenschaften interessant. Weitere Untersuchungen, um die magnetischen Eigenschaften zu bestimmen, können mit STXM durchgeführt werden. CNTs können ebenso auf diesen binären Nanostrukturen wachsen.

## 13 Appendix

### 13.1 Chapter 4.4.3 Characterization and nanofabrication with STXM

#### Self-made gas supply system

In order to providing metal-organic molecules as precursor in FXBID, a self-made gas supply system was connected to the gas cell setup of the PolLux-STXM at the Swiss Light Source. A schematic drawing of the gas supply system is depicted in Figure 12-1.

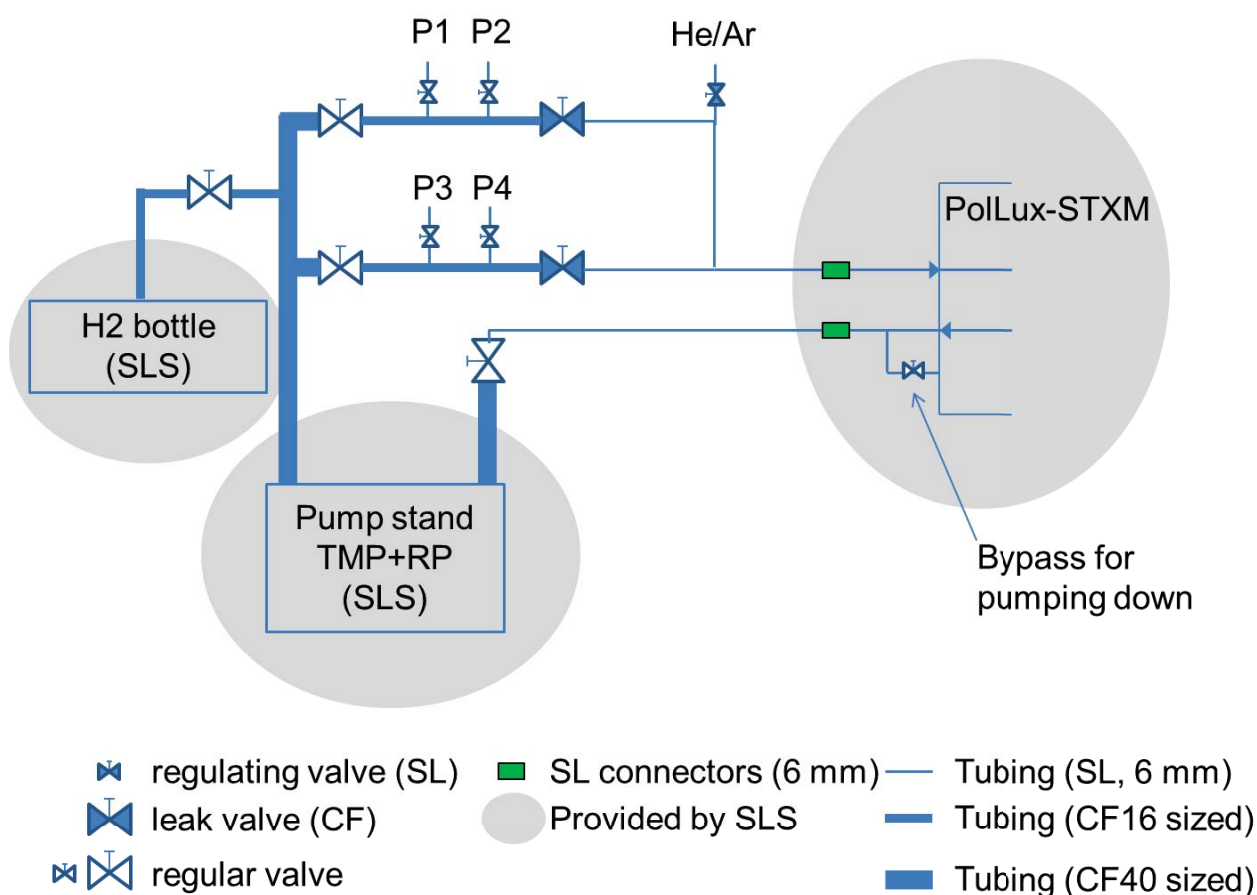


**Figure 13-1:** Scheme of the gas supply system connected to PolLux-STXM for FXBID experiments. The components covered by grey are supplied by Swiss Light Source. P1~P4 refer to the connection of independent precursor container. After setting up the system, careful leak checking was performed using He and mobile QMS station (MOBY 11).

## 13.2 Chapter 7.2.2 Optimization of Fe deposits fabrication

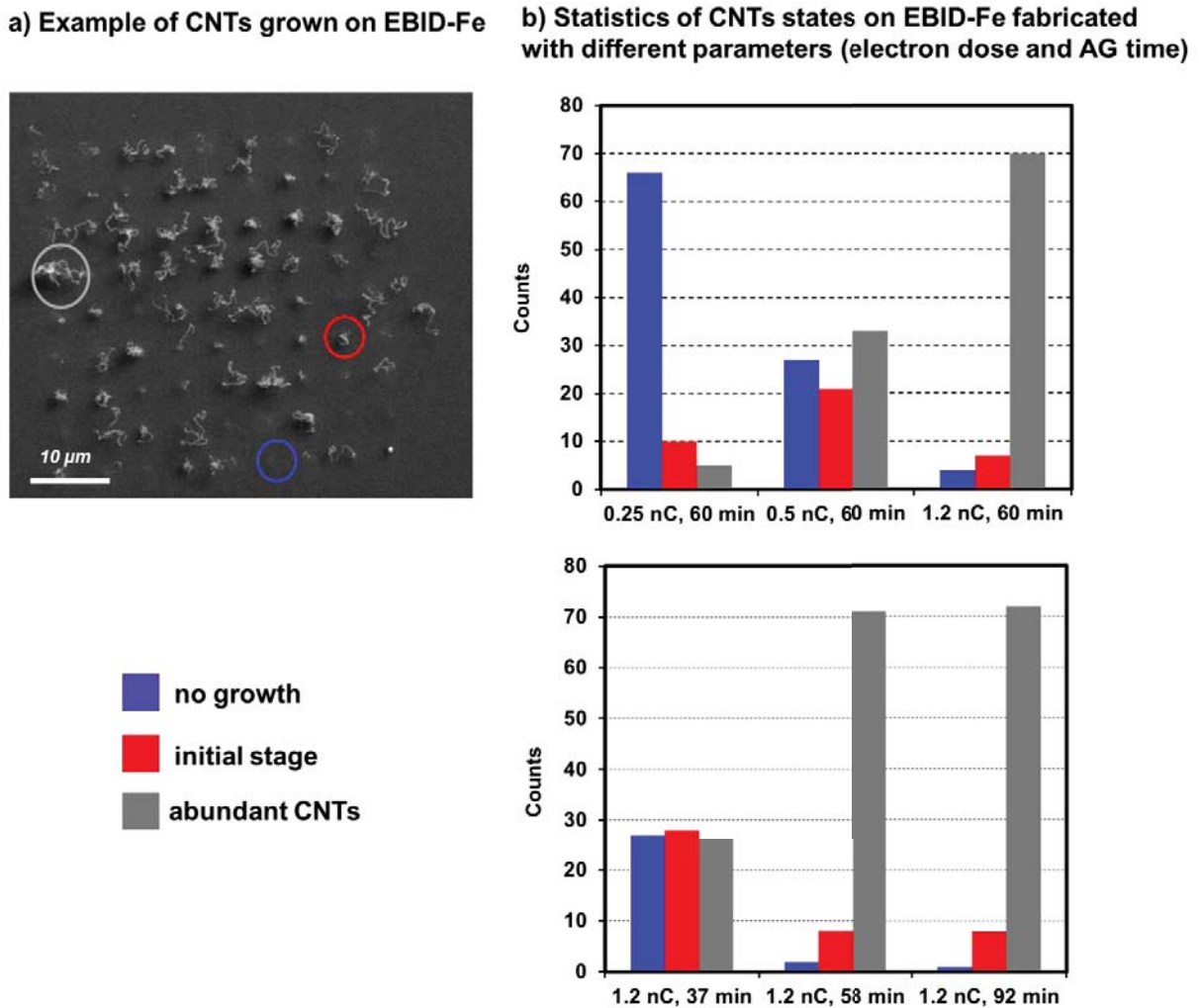


**Figure 13-2:** Statistics of CNT growth on EBID + AG deposits fabricated with different parameters (electron dose and AG time). (a) An example of CNTs grown on a 9 x 9 EBID-Fe point-matrix (1.2 nC and 37 min AG time). Different CNTs growth states were defined as indicated. (b) Statistics of CNT growth states using Fe deposits as catalysts which were fabricated via different AG time but the same electron dose. It can be observed that the yield of CNTs increases by using Fe deposits fabricated with increasing AG time and electron dose.

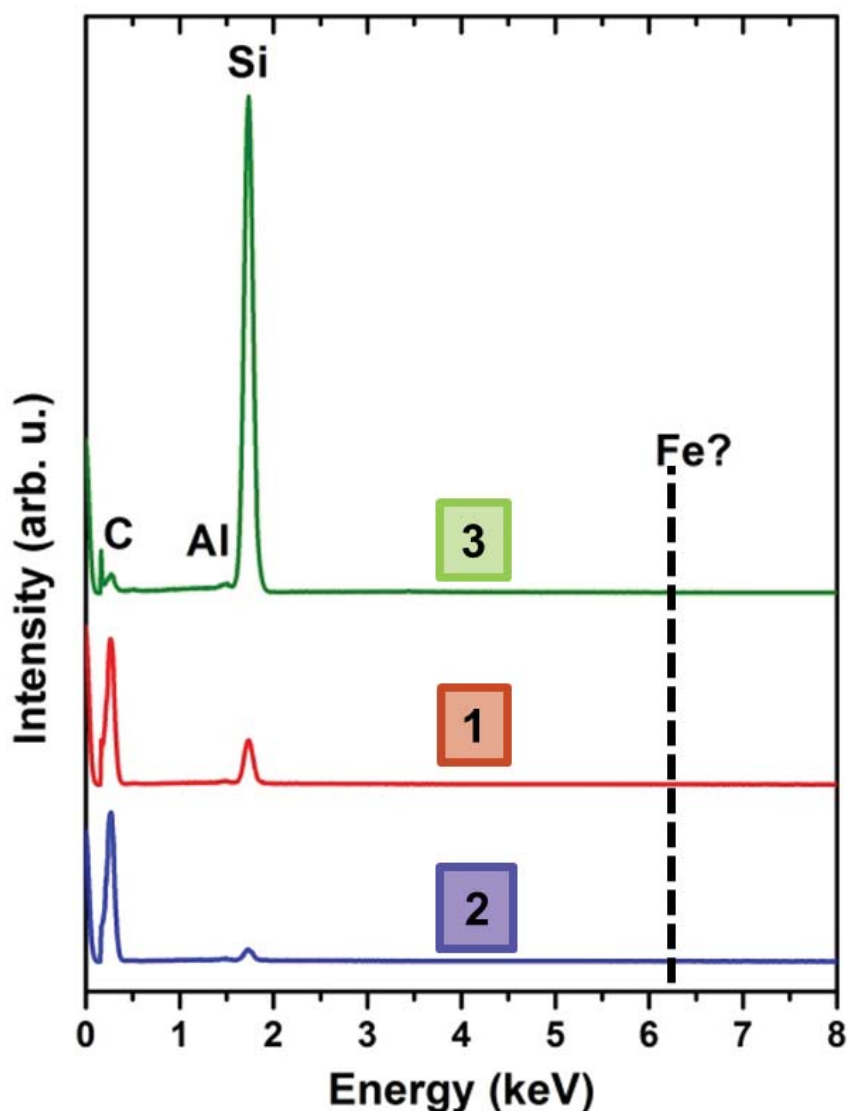


**Figure 13-3:** EDX spectra of the lifted-up nanostructures in Figure 7-6b. A large carbon signal can be observed at positions 1 and 2, indicating the growth of CNTs. Signals of Si are detected at the position 2, originating from the underlying substrate. At the surface (position 3), a large Si signal is observed along with minor carbon and aluminum signals. The carbon signal might derive from the corresponding surface contamination while the origin of the aluminum signal is certainly from the  $\text{Al}_2\text{O}_3$  layer. It is important to emphasize that no Fe signal is detectable at this instance, which has been explained in Chapter 7.2.3.

### 13.3 Chapter 10.2.1 Precursors

#### QMS of $\text{Fe}(\text{CO})_5$ and $\text{Co}(\text{CO})_3\text{NO}$

Precursor was dosed to the gas analysis chamber and mass spectra were recorded at a pressure of  $3 \times 10^{-7}$  mbar. Most likely fragments are indicated for the most prominent  $m/z$  features. Figure 12-4 and Figure 12-5 depict the QMS spectra of  $\text{Fe}(\text{CO})_5$  and  $\text{Co}(\text{CO})_3\text{NO}$  respectively. Figure 12-6 and Figure 12-7 present the QMS spectra of gas mixture of  $\text{Fe}(\text{CO})_5$  and  $\text{Co}(\text{CO})_3\text{NO}$  with different dosing strategies.

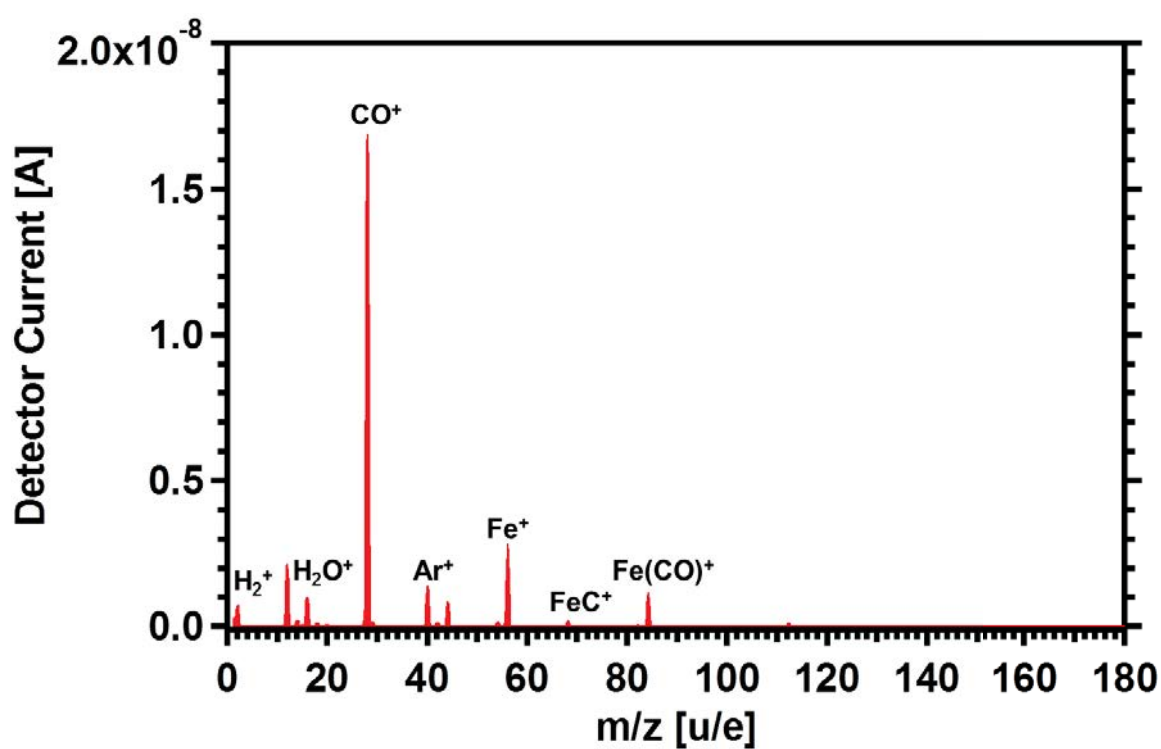


*Figure 13-4: Mass spectrum of  $\text{Fe}(\text{CO})_5$  recorded in the gas dosing chamber at a pressure of  $3 \times 10^{-7}$  mbar. The ratio between  $\text{Fe}^+$  ( $m/z = 56$ ) and  $\text{CO}$  ( $m/z = 28$ ) peak intensity is  $\sim 0.17$ .*

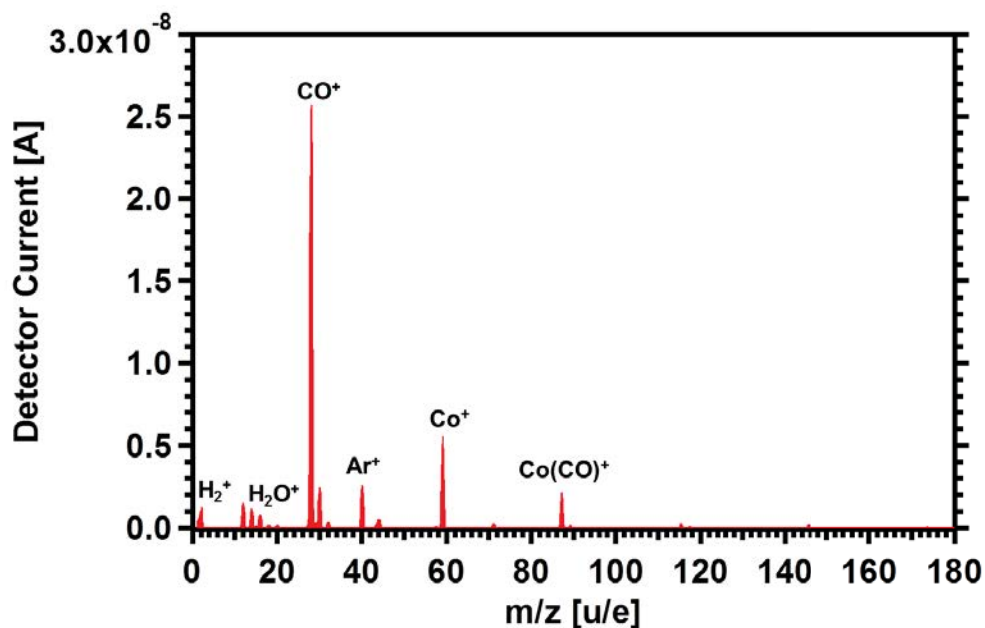


*Figure 13-5: Mass spectrum of  $\text{Co}(\text{CO})_3\text{NO}$  recorded in the gas dosing chamber at a pressure of  $3 \times 10^{-7}$  mbar. The ratio between  $\text{Co}^+$  ( $m/z = 58$ ) and  $\text{CO}$  ( $m/z = 28$ ) is  $\sim 0.22$ .*

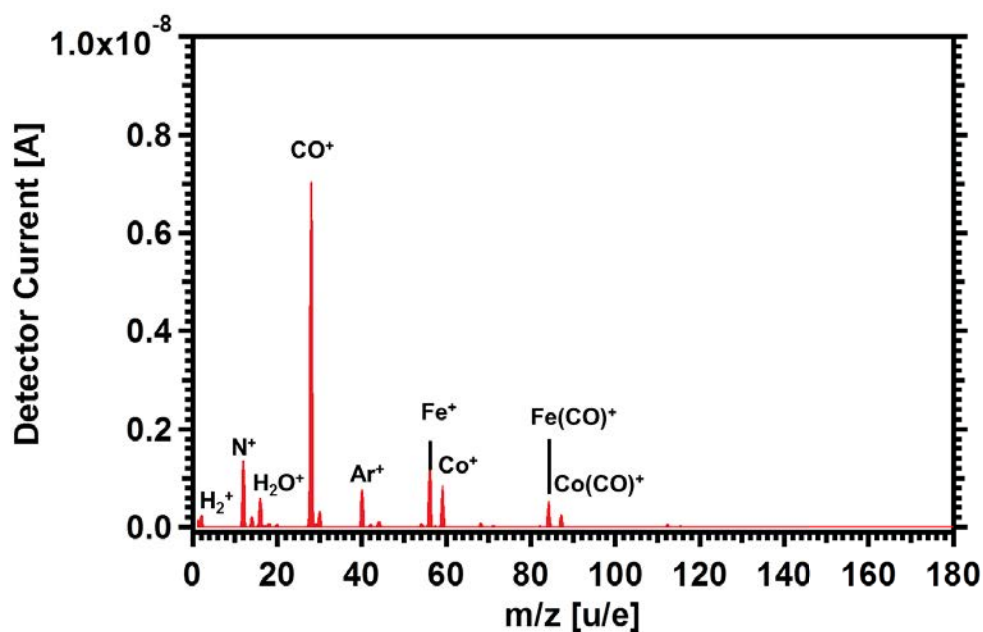


*Figure 13-6: Mass spectrum of gas mixture of  $\text{Fe}(\text{CO})_5$  and  $\text{Co}(\text{CO})_3\text{NO}$ .  $\text{Fe}(\text{CO})_5$  was firstly dosed until the background pressure arrived  $2 \times 10^{-7}$  mbar. Then  $\text{Co}(\text{CO})_3\text{NO}$  was exposed to the gas dosing chamber until the pressure went to  $3 \times 10^{-7}$  mbar. The ratio between  $\text{Fe}^+$  and  $\text{Co}^+$  peak intensity is 1.56. Likely fragments are indicated for the most prominent  $m/z$  features.*

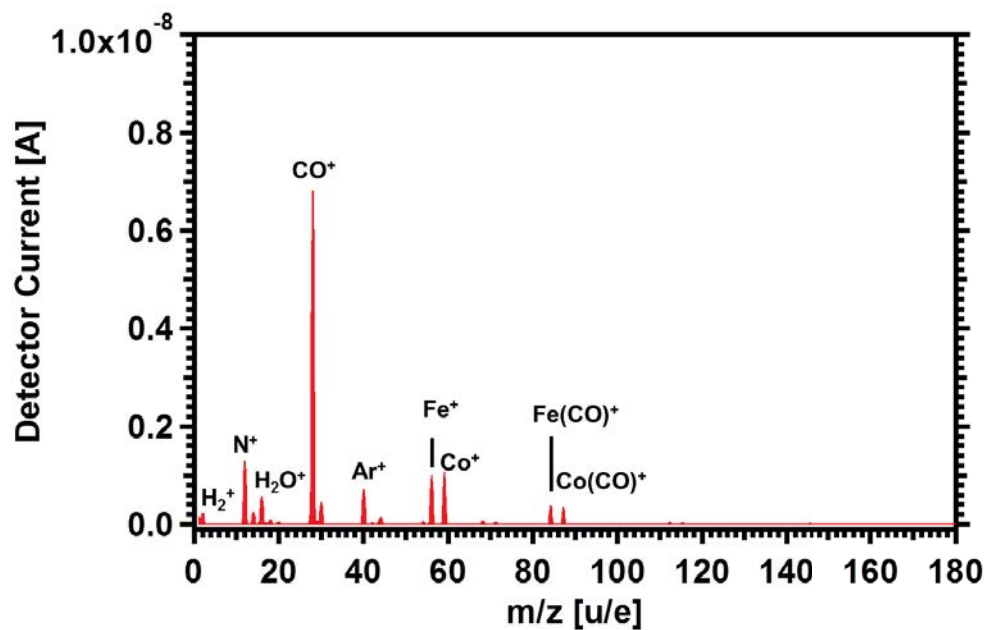


*Figure 13-7: Mass spectrum of gas mixture of  $\text{Fe}(\text{CO})_5$  and  $\text{Co}(\text{CO})_3\text{NO}$ .  $\text{Co}(\text{CO})_3\text{NO}$  was firstly dosed until the background pressure arrived  $1.5 \times 10^{-7}$  mbar. Then  $\text{Fe}(\text{CO})_5$  was exposed to the gas dosing chamber until the pressure went to  $3 \times 10^{-7}$  mbar. The ratio between  $\text{Fe}^+$  and  $\text{Co}^+$  peak intensity is 0.94. Likely fragments are indicated for the most prominent m/z features.*

## 14 References

- [1] R.P. Feynman, There's plenty of room at the bottom, *Engineering and science*, **23** (1960) 22-36.
- [2] G.E. Moore, Cramming more components onto integrated circuits, *Electronics letters*, **38** (1965).
- [3] M.D. Levenson, N. Viswanathan, R.A. Simpson, Improving resolution in photolithography with a phase-shifting mask, *IEEE Transactions on electron devices*, **29** (1982) 1828-1836.
- [4] W. Van Dorp, C. Hagen, A critical literature review of focused electron beam induced deposition, *Journal of Applied Physics*, **104** (2008) 081301.
- [5] I. Utke, P. Hoffmann, J. Melngailis, Gas-assisted focused electron beam and ion beam processing and fabrication, *Journal of Vacuum Science & Technology B*, **26** (2008) 1197-1276.
- [6] S. Randolph, J. Fowlkes, P. Rack, Focused, nanoscale electron-beam-induced deposition and etching, *Critical Reviews in Solid State and Materials Sciences*, **31** (2006) 55-89.
- [7] J. Fowlkes, S. Randolph, P. Rack, Growth and simulation of high-aspect ratio nanopillars by primary and secondary electron-induced deposition, *Journal of Vacuum Science & Technology B*, **23** (2005) 2825-2832.
- [8] N. Silvis-Cividjian, C.W. Hagen, Electron-Beam-Induced Nanometer-Scale Deposition, *Advances in Imaging and Electron Physics*, **143** (2006) 1-235.
- [9] W.F. Van Dorp, B. Van Someren, C.W. Hagen, P. Kruit, P.A. Crozier, Approaching the resolution limit of nanometer-scale electron beam-induced deposition, *Nano letters*, **5** (2005) 1303-1307.
- [10] H. Marbach, Electron beam induced surface activation: a method for the lithographic fabrication of nanostructures via catalytic processes, *Applied Physics A*, **117** (2014) 987-995.
- [11] M.-M. Walz, F. Vollnhals, F. Rietzler, M. Schirmer, H.-P. Steinrück, H. Marbach, Investigation of proximity effects in electron microscopy and lithography, *Applied Physics Letters*, **100** (2012) 053118.
- [12] M.M. Walz, M. Schirmer, F. Vollnhals, T. Lukasczyk, H.P. Steinrück, H. Marbach, Electrons as “invisible ink”: fabrication of nanostructures by local electron beam induced activation of SiO<sub>x</sub>, *Angewandte Chemie International Edition*, **49** (2010) 4669-4673.

## 14 References

- [13] F. Tu, M. Drost, F. Vollnhals, A. Späth, E. Carrasco, R. Fink, H. Marbach, On the magnetic properties of iron nanostructures fabricated via focused electron beam induced deposition and autocatalytic growth processes, *Nanotechnology*, **27** (2016) 355302.
- [14] F. Vollnhals, M. Drost, F. Tu, E. Carrasco, A. Späth, R.H. Fink, H.-P. Steinrück, H. Marbach, Electron-beam induced deposition and autocatalytic decomposition of Co (CO) 3NO, *Beilstein journal of nanotechnology*, **5** (2014) 1175-1185.
- [15] F. Vollnhals, T. Woolcot, M.-M. Walz, S. Seiler, H.-P. Steinrück, G. Thornton, H. Marbach, Electron beam-induced writing of nanoscale iron wires on a functional metal oxide, *The Journal of Physical Chemistry C*, **117** (2013) 17674-17679.
- [16] M. Walz, F. Vollnhals, F. Rietzler, M. Schirmer, A. Kunzmann, H. Steinrück, H. Marbach, Thin membranes versus bulk substrates: investigation of proximity effects in focused electron beam-induced processing, *Journal of Physics D: Applied Physics*, **45** (2012) 225306.
- [17] M. Gavagnin, H.D. Wanzenboeck, S. Wachter, M.M. Shawrav, A. Persson, K. Gunnarsson, P. Svedlindh, M. Stöger-Pollach, E. Bertagnolli, Free-standing magnetic nanopillars for 3D nanomagnet logic, *ACS applied materials & interfaces*, **6** (2014) 20254-20260.
- [18] W. van Dorp, Sub-10 nm writing: focused electron beam-induced deposition in perspective, *Applied Physics A*, **117** (2014) 1615-1622.
- [19] C. Hagen, The future of focused electron beam-induced processing, *Applied Physics A*, **117** (2014) 1599-1605.
- [20] A. Botman, J. Mulders, C. Hagen, Creating pure nanostructures from electron-beam-induced deposition using purification techniques: a technology perspective, *Nanotechnology*, **20** (2009) 372001.
- [21] N. Silvis-Cividjian, C. Hagen, P. Kruit, Spatial resolution limits in electron-beam-induced deposition, *Journal of Applied Physics*, **98** (2005) 084905.
- [22] T. Lukaszcyk, M. Schirmer, H.-P. Steinrück, H. Marbach, Generation of clean iron structures by electron-beam-induced deposition and selective catalytic decomposition of iron pentacarbonyl on Rh (110), *Langmuir*, **25** (2009) 11930-11939.
- [23] M.-M. Walz, F. Vollnhals, M. Schirmer, H.-P. Steinrück, H. Marbach, Generation of clean iron nanocrystals on an ultra-thin SiO<sub>x</sub> film on Si (001), *Physical Chemistry Chemical Physics*, **13** (2011) 17333-17338.
- [24] J. Mäklin, N. Halonen, O. Pitkänen, G. Tóth, K. Kordás, Solder transfer of carbon nanotube microfin coolers to ceramic chips, *Applied Thermal Engineering*, **65** (2014) 539-543.

## 14 References

- [25] M. Xu, F. Zaera, Mechanistic studies of the thermal decomposition of metal carbonyls on Ni (100) surfaces in connection with chemical vapor deposition processes, *Journal of Vacuum Science & Technology A*, **14** (1996) 415-424.
- [26] M.F. De Volder, S.H. Tawfick, R.H. Baughman, A.J. Hart, Carbon nanotubes: present and future commercial applications, *science*, **339** (2013) 535-539.
- [27] P.J. Potts, Electron probe microanalysis, in: *A Handbook of Silicate Rock Analysis*, Springer Netherlands, Dordrecht, 1987, pp. 326-382.
- [28] I. Utke, T. Bret, D. Laub, P. Buffat, L. Scandella, P. Hoffmann, Thermal effects during focused electron beam induced deposition of nanocomposite magnetic-cobalt-containing tips, *Microelectronic engineering*, **73** (2004) 553-558.
- [29] J.H. Kindt, G.E. Fantner, J.B. Thompson, P.K. Hansma, Automated wafer-scale fabrication of electron beam deposited tips for atomic force microscopes using pattern recognition, *Nanotechnology*, **15** (2004) 1131.
- [30] A. Fernández-Pacheco, N.-J. Steinke, D. Mahendru, A. Welbourne, R. Mansell, S.L. Chin, D. Petit, J. Lee, R. Dalgliesh, S. Langridge, R.P. Cowburn, Magnetic State of Multilayered Synthetic Antiferromagnets during Soliton Nucleation and Propagation for Vertical Data Transfer, *Advanced Materials Interfaces*, **3** (2016) 1600097.
- [31] H. Koops, O. Hoinkis, M. Honsberg, R. Schmidt, R. Blum, G. Böttger, A. Kuligk, C. Liguda, M. Eich, Two-dimensional photonic crystals produced by additive nanolithography with electron beam-induced deposition act as filters in the infrared, *Microelectronic engineering*, **57** (2001) 995-1001.
- [32] S.W. Chee, R. Sharma, Controlling the size and the activity of Fe particles for synthesis of carbon nanotubes, *Micron*, **43** (2012) 1181-1187.
- [33] R. Sharma, E. Moore, P. Rez, M.M. Treacy, Site-specific fabrication of Fe particles for carbon nanotube growth, *Nano letters*, **9** (2009) 689-694.
- [34] M. Ervin, B. Nichols, Electron beam induced deposition of cobalt for use as single- and multiwalled carbon nanotube growth catalyst, *Journal of Vacuum Science & Technology B*, **27** (2009) 2982-2985.
- [35] K. Edinger, H. Becht, J. Bihl, V. Boegli, M. Budach, T. Hofmann, H.W. Koops, P. Kuschnerus, J. Oster, P. Spies, Electron-beam-based photomask repair, *Journal of Vacuum Science & Technology B*, **22** (2004) 2902-2906.
- [36] M. Schirmer, M. Walz, C. Papp, F. Kronast, A. Gray, B. Balke, S. Cramm, C. Fadley, H. Steinrück, H. Marbach, Fabrication of layered nanostructures by successive electron beam induced deposition with two precursors: protective capping of metallic iron structures, *Nanotechnology*, **22** (2011) 475304.

## 14 References

- [37] T. Bret, I. Utke, P. Hoffmann, M. Abourida, P. Doppelt, Electron range effects in focused electron beam induced deposition of 3D nanostructures, *Microelectronic engineering*, **83** (2006) 1482-1486.
- [38] H. Plank, D.A. Smith, T. Haber, P.D. Rack, F. Hofer, Fundamental proximity effects in focused electron beam induced deposition, *ACS nano*, **6** (2011) 286-294.
- [39] R. Winkler, J. Fowlkes, A. Szkudlarek, I. Utke, P.D. Rack, H. Plank, The nanoscale implications of a molecular gas beam during electron beam induced deposition, *ACS applied materials & interfaces*, **6** (2014) 2987-2995.
- [40] H. Plank, J.H. Noh, J.D. Fowlkes, K. Lester, B.B. Lewis, P.D. Rack, Electron-beam-assisted oxygen purification at low temperatures for electron-beam-induced Pt deposits: towards pure and high-fidelity nanostructures, *ACS applied materials & interfaces*, **6** (2014) 1018-1024.
- [41] H. Plank, C. Gspan, M. Dienstleder, G. Kothleitner, F. Hofer, The influence of beam defocus on volume growth rates for electron beam induced platinum deposition, *Nanotechnology*, **19** (2008) 485302.
- [42] S. Mehendale, J. Mulders, P. Trompenaars, Purification of Au EBID structures by electron beam post-irradiation under oxygen flux at room temperature, *Microelectronic Engineering*, **141** (2015) 207-210.
- [43] M.G. Stanford, B.B. Lewis, J.H. Noh, J.D. Fowlkes, N.A. Roberts, H. Plank, P.D. Rack, Purification of nanoscale electron-beam-induced platinum deposits via a pulsed laser-induced oxidation reaction, *ACS applied materials & interfaces*, **6** (2014) 21256-21263.
- [44] A.V. Riazanova, Y.G. Rikers, J.J. Mulders, L.M. Belova, Pattern shape control for heat treatment purification of electron-beam-induced deposition of gold from the Me<sub>2</sub>Au (acac) precursor, *Langmuir*, **28** (2012) 6185-6191.
- [45] A. Fernández-Pacheco, J. De Teresa, R. Córdoba, M.R. Ibarra, Magnetotransport properties of high-quality cobalt nanowires grown by focused-electron-beam-induced deposition, *Journal of Physics D: Applied Physics*, **42** (2009) 055005.
- [46] K.L. Klein, S.J. Randolph, J.D. Fowlkes, L. Allard, H.M. Meyer III, M.L. Simpson, P.D. Rack, Single-crystal nanowires grown via electron-beam-induced deposition, *Nanotechnology*, **19** (2008) 345705.
- [47] W.F. van Dorp, I. Lazić, A. Beyer, A. Gölzhäuser, J.B. Wagner, T.W. Hansen, C.W. Hagen, Ultrahigh resolution focused electron beam induced processing: the effect of substrate thickness, *Nanotechnology*, **22** (2011) 115303.
- [48] W. Zhang, M. Shimojo, M. Takeguchi, K. Furuya, Electron beam-induced formation of nanosized  $\alpha$ -Fe crystals, *Journal of materials science*, **41** (2006) 2577-2580.

## 14 References

- [49] W. Van Dorp, C. Hagen, P. Crozier, P. Kruit, Growth behavior near the ultimate resolution of nanometer-scale focused electron beam-induced deposition, *Nanotechnology*, **19** (2008) 225305.
- [50] C.T. Wirth, B.C. Bayer, A.D. Gamalski, S. Esconjauregui, R.S. Weatherup, C. Ducati, C. Baetz, J. Robertson, S. Hofmann, The phase of iron catalyst nanoparticles during carbon nanotube growth, *Chemistry of Materials*, **24** (2012) 4633-4640.
- [51] A.B. Cundy, L. Hopkinson, R.L. Whitby, Use of iron-based technologies in contaminated land and groundwater remediation: A review, *Science of the total environment*, **400** (2008) 42-51.
- [52] L. Gao, J. Zhuang, L. Nie, J. Zhang, Y. Zhang, N. Gu, T. Wang, J. Feng, D. Yang, S. Perrett, Intrinsic peroxidase-like activity of ferromagnetic nanoparticles, *Nature nanotechnology*, **2** (2007) 577-583.
- [53] P.M. Valencia, O.C. Farokhzad, R. Karnik, R. Langer, Microfluidic technologies for accelerating the clinical translation of nanoparticles, *Nature nanotechnology*, **7** (2012) 623-629.
- [54] A. Shavel, B. Rodríguez-González, M. Spasova, M. Farle, L.M. Liz-Marzán, Synthesis and characterization of iron/iron oxide core/shell nanocubes, *Advanced functional materials*, **17** (2007) 3870-3876.
- [55] T. Vystavel, G. Palasantzas, S. Koch, J.T.M. De Hosson, Nanosized iron clusters investigated with in situ transmission electron microscopy, *Applied physics letters*, **82** (2003) 197-199.
- [56] N. Cabrera, N. Mott, Theory of the oxidation of metals, *Reports on progress in physics*, **12** (1949) 163.
- [57] A. Pratt, L. Lari, O. Hovorka, A. Shah, C. Woffinden, S.P. Tear, C. Binns, R. Kröger, Enhanced oxidation of nanoparticles through strain-mediated ionic transport, *Nature materials*, **13** (2014) 26-30.
- [58] Y. Yin, R.M. Rioux, C.K. Erdonmez, S. Hughes, G.A. Somorjai, A.P. Alivisatos, Formation of hollow nanocrystals through the nanoscale Kirkendall effect, *Science*, **304** (2004) 711-714.
- [59] A. Cabot, V.F. Puentes, E. Shevchenko, Y. Yin, L. Balcells, M.A. Marcus, S.M. Hughes, A.P. Alivisatos, Vacancy coalescence during oxidation of iron nanoparticles, *Journal of the American Chemical Society*, **129** (2007) 10358-10360.
- [60] I. Utke, P. Hoffmann, R. Berger, L. Scandella, High-resolution magnetic Co supertips grown by a focused electron beam, *Applied physics letters*, **80** (2002) 4792-4794.

## 14 References

- [61] G. Gazzadi, J. Mulders, P. Trompenaars, A. Ghirri, A. Rota, M. Affronte, S. Frabboni, Characterization of a new cobalt precursor for focused beam deposition of magnetic nanostructures, *Microelectronic Engineering*, **88** (2011) 1955-1958.
- [62] J. De Teresa, A. Fernández-Pacheco, R. Córdoba, L. Serrano-Ramón, S. Sangiao, M. Ibarra, Review of magnetic nanostructures grown by focused electron beam induced deposition (FEBID), *Journal of Physics D: Applied Physics*, **49** (2016) 243003.
- [63] O.V. Dobrovolskiy, M. Kompaniets, R. Sachser, F. Porrati, C. Gspan, H. Plank, M. Huth, Tunable magnetism on the lateral mesoscale by post-processing of Co/Pt heterostructures, *Beilstein journal of nanotechnology*, **6** (2015) 1082-1090.
- [64] R. Córdoba Castillo, B. Barcones, E. Roelfsema, M. Verheijen, J. Mulders, P. Trompenaars, B. Koopmans, Functional nickel-based deposits synthesized by focused beam induced processing, (2016).
- [65] J. De Teresa, A. Fernández-Pacheco, Present and future applications of magnetic nanostructures grown by FEBID, *Applied Physics A*, **117** (2014) 1645-1658.
- [66] I. Utke, J. Michler, P. Gasser, C. Santschi, D. Laub, M. Cantoni, P.A. Buffat, C. Jiao, P. Hoffmann, Cross section investigations of compositions and sub-structures of tips obtained by focused electron beam induced deposition, *Advanced Engineering Materials*, **7** (2005) 323-331.
- [67] M. Takeguchi, M. Shimojo, K. Furuya, Fabrication of magnetic nanostructures using electron beam induced chemical vapour deposition, *Nanotechnology*, **16** (2005) 1321.
- [68] R. Lavrijsen, R. Córdoba, F. Schoenaker, T. Ellis, B. Barcones, J. Kohlhepp, H. Swagten, B. Koopmans, J. De Teresa, C. Magén, Fe: O: C grown by focused-electron-beam-induced deposition: magnetic and electric properties, *Nanotechnology*, **22** (2010) 025302.
- [69] F. Porrati, M. Pohlit, J. Müller, S. Barth, F. Biegger, C. Gspan, H. Plank, M. Huth, Direct writing of CoFe alloy nanostructures by focused electron beam induced deposition from a heteronuclear precursor, *Nanotechnology*, **26** (2015) 475701.
- [70] A. Fernández-Pacheco, J. De Teresa, A. Szkudlarek, R. Córdoba, M. Ibarra, D. Petit, L. O'Brien, H. Zeng, E. Lewis, D. Read, Magnetization reversal in individual cobalt micro- and nanowires grown by focused-electron-beam-induced-deposition, *Nanotechnology*, **20** (2009) 475704.
- [71] E. Nikulina, O. Idigoras, P. Vavassori, A. Chuvilin, A. Berger, Magneto-optical magnetometry of individual 30 nm cobalt nanowires grown by electron beam induced deposition, *Applied Physics Letters*, **100** (2012) 142401.
- [72] M. Gabureac, L. Bernau, I. Utke, G. Boero, Granular Co-C nano-Hall sensors by focused-beam-induced deposition, *Nanotechnology*, **21** (2010) 115503.

## 14 References

- [73] L.A. Rodríguez, L. Deen, R. Córdoba, C. Magén, E. Snoeck, B. Koopmans, J.M. De Teresa, Influence of the shape and surface oxidation in the magnetization reversal of thin iron nanowires grown by focused electron beam induced deposition, *Beilstein journal of nanotechnology*, **6** (2015) 1319-1331.
- [74] S.S. Parkin, M. Hayashi, L. Thomas, Magnetic domain-wall racetrack memory, *Science*, **320** (2008) 190-194.
- [75] R. Lavrijsen, J.-H. Lee, A. Fernández-Pacheco, D.C. Petit, R. Mansell, R.P. Cowburn, Magnetic ratchet for three-dimensional spintronic memory and logic, *Nature*, **493** (2013) 647-650.
- [76] J.D. Fowlkes, R. Winkler, B.B. Lewis, M.G. Stanford, H. Plank, P.D. Rack, Simulation Guided 3D Nanomanufacturing via Focused Electron Beam Induced Deposition, *ACS nano*, (2016).
- [77] A. Fernández-Pacheco, L. Serrano-Ramón, J.M. Michalik, M.R. Ibarra, J.M. De Teresa, L. O'Brien, D. Petit, J. Lee, R.P. Cowburn, Three dimensional magnetic nanowires grown by focused electron-beam induced deposition, *Scientific reports*, **3** (2013).
- [78] V. Jourdain, C. Bichara, Current understanding of the growth of carbon nanotubes in catalytic chemical vapour deposition, *Carbon*, **58** (2013) 2-39.
- [79] M. Zhang, J. Li, Carbon nanotube in different shapes, *Materials today*, **12** (2009) 12-18.
- [80] Y. Yan, J. Miao, Z. Yang, F.-X. Xiao, H.B. Yang, B. Liu, Y. Yang, Carbon nanotube catalysts: recent advances in synthesis, characterization and applications, *Chemical Society Reviews*, **44** (2015) 3295-3346.
- [81] A.-C. Dupuis, The catalyst in the CCVD of carbon nanotubes—a review, *Progress in Materials Science*, **50** (2005) 929-961.
- [82] A. Moisala, A.G. Nasibulin, E.I. Kauppinen, The role of metal nanoparticles in the catalytic production of single-walled carbon nanotubes—a review, *Journal of Physics: condensed matter*, **15** (2003) S3011.
- [83] M. Meyyappan, L. Delzeit, A. Cassell, D. Hash, Carbon nanotube growth by PECVD: a review, *Plasma Sources Science and Technology*, **12** (2003) 205.
- [84] J.-F. Colomer, C. Stephan, S. Lefrant, G. Van Tendeloo, I. Willems, Z. Konya, A. Fonseca, C. Laurent, J.B. Nagy, Large-scale synthesis of single-wall carbon nanotubes by catalytic chemical vapor deposition (CCVD) method, *Chemical Physics Letters*, **317** (2000) 83-89.
- [85] Z. Kónya, *Catalytic production, purification, characterization and application of single- and multiwall carbon nanotubes*, in: *Carbon Filaments and Nanotubes: Common Origins, Differing Applications?*, Springer, 2001, pp. 85-109.

## 14 References

- [86] J. Gavillet, A. Loiseau, C. Journet, F. Willaime, F. Ducastelle, J.-C. Charlier, Root-growth mechanism for single-wall carbon nanotubes, *Physical review letters*, **87** (2001) 275504.
- [87] C.J. Lee, J. Park, Growth model of bamboo-shaped carbon nanotubes by thermal chemical vapor deposition, *Applied Physics Letters*, **77** (2000) 3397-3399.
- [88] S. Sinnott, R. Andrews, D. Qian, A.M. Rao, Z. Mao, E. Dickey, F. Derbyshire, Model of carbon nanotube growth through chemical vapor deposition, *Chemical Physics Letters*, **315** (1999) 25-30.
- [89] K. Hata, D.N. Futaba, K. Mizuno, T. Namai, M. Yumura, S. Iijima, Water-assisted highly efficient synthesis of impurity-free single-walled carbon nanotubes, *Science*, **306** (2004) 1362-1364.
- [90] W. Zhou, L. Ding, J. Liu, Role of catalysts in the surface synthesis of single-walled carbon nanotubes, *Nano Research*, **2** (2009) 593-598.
- [91] A. Takashima, Y. Izumi, E. Ikenaga, T. Ohkochi, M. Kotsugi, T. Matsushita, T. Muro, A. Kawabata, T. Murakami, M. Nihei, Low-temperature catalyst activator: mechanism of dense carbon nanotube forest growth studied using synchrotron radiation, *IUCrJ*, **1** (2014) 221-227.
- [92] S.M. Kim, C.L. Pint, P.B. Amama, D.N. Zakharov, R.H. Hauge, B. Maruyama, E.A. Stach, Evolution in catalyst morphology leads to carbon nanotube growth termination, *The Journal of Physical Chemistry Letters*, **1** (2010) 918-922.
- [93] W. Chen, Z. Fan, X. Pan, X. Bao, Effect of confinement in carbon nanotubes on the activity of Fischer–Tropsch iron catalyst, *Journal of the American Chemical Society*, **130** (2008) 9414-9419.
- [94] C. Liu, Y. Chen, Y. Tzeng, Effects of carbon content in iron catalyst coatings on the growth of vertically aligned carbon nanotubes on smooth silicon surfaces by thermal chemical vapor deposition, *Diamond and related materials*, **13** (2004) 1274-1280.
- [95] M. Cantoro, S. Hofmann, S. Pisana, V. Scardaci, A. Parvez, C. Ducati, A.C. Ferrari, A.M. Blackburn, K.-Y. Wang, J. Robertson, Catalytic chemical vapor deposition of single-wall carbon nanotubes at low temperatures, *Nano Letters*, **6** (2006) 1107-1112.
- [96] T. de los Arcos, M.G. Garnier, J.W. Seo, P. Oelhafen, V. Thommen, D. Mathys, The influence of catalyst chemical state and morphology on carbon nanotube growth, *The Journal of Physical Chemistry B*, **108** (2004) 7728-7734.
- [97] M. Chhowalla, K. Teo, C. Ducati, N. Rupesinghe, G. Amaratunga, A. Ferrari, D. Roy, J. Robertson, W. Milne, Growth process conditions of vertically aligned carbon nanotubes using plasma enhanced chemical vapor deposition, *Journal of Applied Physics*, **90** (2001) 5308-5317.

## 14 References

- [98] H. Ago, T. Komatsu, S. Ohshima, Y. Kuriki, M. Yumura, Dispersion of metal nanoparticles for aligned carbon nanotube arrays, *Applied Physics Letters*, **77** (2000) 79-81.
- [99] K. Teo, M. Chhowalla, G. Amaratunga, W. Milne, D. Hasko, G. Pirio, P. Legagneux, F. Wyczisk, D. Pribat, Uniform patterned growth of carbon nanotubes without surface carbon, *Applied Physics Letters*, **79** (2001) 1534-1536.
- [100] M. Yudasaka, R. Kikuchi, Y. Ohki, E. Ota, S. Yoshimura, Behavior of Ni in carbon nanotube nucleation, *Applied physics letters*, **70** (1997) 1817-1818.
- [101] C. Mattevi, C.T. Wirth, S. Hofmann, R. Blume, M. Cantoro, C. Ducati, C. Cepek, A. Knop-Gericke, S. Milne, C. Castellarin-Cudia, In-situ X-ray photoelectron spectroscopy study of catalyst– support interactions and growth of carbon nanotube forests, *The Journal of Physical Chemistry C*, **112** (2008) 12207-12213.
- [102] V. Novotny, G. Itnyre, A. Homola, L. Franco, Corrosion of thin film cobalt based magnetic recording media, *IEEE Transactions on Magnetics*, **23** (1987) 3645-3647.
- [103] I. Flis-Kabulska, Oxide growth on evaporated thin film and bulk iron exposed to humid air and HCl or HNO<sub>3</sub> vapours, *Journal of Electroanalytical Chemistry*, **508** (2001) 89-96.
- [104] C.R. Henry, Surface studies of supported model catalysts, *Surface Science Reports*, **31** (1998) 231235-233325.
- [105] Q. Fu, T. Wagner, Interaction of nanostructured metal overlayers with oxide surfaces, *Surface Science Reports*, **62** (2007) 431-498.
- [106] S. Hofmann, G. Csanyi, A. Ferrari, M. Payne, J. Robertson, Surface diffusion: the low activation energy path for nanotube growth, *Physical review letters*, **95** (2005) 036101.
- [107] J. Nørskov, Covalent effects in the effective-medium theory of chemical binding: Hydrogen heats of solution in the 3 d metals, *Physical Review B*, **26** (1982) 2875.
- [108] J. Sinfelt, Catalytic hydrogenolysis on metals, *Catalysis Letters*, **9** (1991) 159-171.
- [109] C.L. Cheung, A. Kurtz, H. Park, C.M. Lieber, Diameter-controlled synthesis of carbon nanotubes, *The Journal of Physical Chemistry B*, **106** (2002) 2429-2433.
- [110] F. Schäffel, M. Rummeli, C. Kramberger, U. Queitsch, E. Mohn, R. Kaltofen, T. Pichler, B. Büchner, B. Rellinghaus, L. Schultz, Tailoring the diameter, density and number of walls of carbon nanotubes through predefined catalyst particles, *physica status solidi (a)*, **205** (2008) 1382-1385.
- [111] Y. Chen, J. Zhang, Diameter controlled growth of single-walled carbon nanotubes from SiO<sub>2</sub> nanoparticles, *Carbon*, **49** (2011) 3316-3324.

## 14 References

- [112] P. Harris, Growth and structure of supported metal catalyst particles, *International materials reviews*, **40** (1995) 97-115.
- [113] P.A. Thiel, M. Shen, D.-J. Liu, J.W. Evans, Coarsening of two-dimensional nanoclusters on metal surfaces, *The Journal of Physical Chemistry C*, **113** (2009) 5047-5067.
- [114] J.M. Simmons, B.M. Nichols, M.S. Marcus, O.M. Castellini, R.J. Hamers, M.A. Eriksson, Critical Oxide Thickness for Efficient Single-Walled Carbon Nanotube Growth on Silicon Using Thin SiO<sub>2</sub> Diffusion Barriers, *Small*, **2** (2006) 902-909.
- [115] T. De Los Arcos, F. Vonau, M. Garnier, V. Thommen, H.-G. Boyen, P. Oelhafen, M. Düggelin, D. Mathis, R. Guggenheim, Influence of iron–silicon interaction on the growth of carbon nanotubes produced by chemical vapor deposition, *Applied Physics Letters*, **80** (2002) 2383-2385.
- [116] R. Lamber, N. Jaeger, G. Schulz-Ekloff, On the metal-support interaction in the Ni-SiO<sub>2</sub> system, *Surface science*, **227** (1990) 268-272.
- [117] S. Penner, D. Wang, D.S. Su, G. Rupprechter, R. Podlucky, R. Schlögl, K. Hayek, Platinum nanocrystals supported by silica, alumina and ceria: metal–support interaction due to high-temperature reduction in hydrogen, *Surface science*, **532** (2003) 276-280.
- [118] R. Pretorius, J. Harris, M. Nicolet, Reaction of thin metal films with SiO<sub>2</sub> substrates, *Solid-State Electronics*, **21** (1978) 667-675.
- [119] D. Bratton, D. Yang, J. Dai, C.K. Ober, Recent progress in high resolution lithography, *Polymers for Advanced Technologies*, **17** (2006) 94-103.
- [120] J.R. Maldonado, M. Peckerar, X-ray lithography: Some history, current status and future prospects, *Microelectronic Engineering*, **161** (2016) 87-93.
- [121] R. Feder, E. Spiller, J. Topalian, X-ray lithography, *Polymer Engineering & Science*, **17** (1977) 385-389.
- [122] A.F. Leontowich, A.P. Hitchcock, B. Watts, J. Raabe, Sub-25nm direct write (maskless) X-ray nanolithography, *Microelectronic Engineering*, **108** (2013) 5-7.
- [123] A.F. Leontowich, A.P. Hitchcock, Zone plate focused soft X-ray lithography, *Applied Physics A: Materials Science & Processing*, **103** (2011) 1-11.
- [124] D.C. Mancini, P. Skytt, J. Nordgren, P. Tägtström, Chemical vapour deposition of Cr, Mo and W thin films induced by synchrotron radiation, *Vacuum*, **46** (1995) 1165-1169.
- [125] R. Zanoni, M. Piancastelli, X. Jin, F. Sirotti, G. Rossi, A soft-X-ray photoemission study of iron deposition on Si (111) 2× 1 by synchrotron radiation-excited photodecomposition of adsorbed Fe (CO) 5, *Applied surface science*, **56** (1992) 474-479.

## 14 References

- [126] D.C. Mancini, S. Varma, J.K. Simons, R.A. Rosenberg, P.A. Dowben, Synchrotron radiation induced chemical vapor deposition of thin films from metal hexacarbonyls, *Journal of Vacuum Science & Technology B: Microelectronics Processing and Phenomena*, **8** (1990) 1804-1807.
- [127] S. Werner, S. Rehbein, P. Guttman, G. Schneider, Three-dimensional structured on-chip stacked zone plates for nanoscale X-ray imaging with high efficiency, *Nano Research*, **7** (2014) 528-535.
- [128] I. Mohacsi, P. Karvinen, I. Vartiainen, V.A. Guzenko, A. Somogyi, C.M. Kewish, P. Mercere, C. David, High-efficiency zone-plate optics for multi-keV X-ray focusing, *Journal of synchrotron radiation*, **21** (2014) 497-501.
- [129] W. Chao, P. Fischer, T. Tyliczszak, S. Rekawa, E. Anderson, P. Naulleau, Real space soft x-ray imaging at 10 nm spatial resolution, *Optics express*, **20** (2012) 9777-9783.
- [130] J. Vila-Comamala, K. Jefimovs, J. Raabe, T. Pilvi, R.H. Fink, M. Senoner, A. Maaßdorf, M. Ritala, C. David, Advanced thin film technology for ultrahigh resolution X-ray microscopy, *Ultramicroscopy*, **109** (2009) 1360-1364.
- [131] L. Reimer, *Scanning Electron Microscopy*, 2nd ed., Springer - Verlag Berlin Heidelberg, New York, 1998.
- [132] J. Wolstenholme, *Auger electron spectroscopy*, Momentum Press, New York, 2015.
- [133] M.P.S. David Briggs, *Practical Surface Analysis. Vol. 1: Auger and X-ray Photoelectron Spectroscopy*, 2nd ed., John Wiley & Sons Ltd, Chichester (England), 1990.
- [134] P.J. Cumpson, M.P. Seah, Elastic scattering corrections in AES and XPS. II. Estimating attenuation lengths and conditions required for their valid use in overlayer/substrate experiments, *Surface and Interface Analysis*, **25** (1997) 430-446.
- [135] C.J. Chen, *Introduction to Scanning Tunneling Microscopy*, Oxford University Press, New York, 1993.
- [136] H.-J.G. R. Wiesendanger, *Scanning Tunneling Microscopy III*, Springer-Verlag Berlin Heidelberg, New York, 1991.
- [137] C. Bai, *Scanning Tunneling Microscopy and Its Application*, 2nd ed., Springer-Verlag Berlin Heidelberg, New York, 2000.
- [138] S. Ditze, M. Stark, M. Drost, F. Buchner, H.P. Steinrück, H. Marbach, Activation Energy for the Self-Metalation Reaction of 2H-Tetraphenylporphyrin on Cu (111), *Angewandte Chemie International Edition*, **51** (2012) 10898-10901.
- [139] F. Buchner, E. Zillner, M. Röckert, S. Gläbel, H.P. Steinrück, H. Marbach, Substrate-Mediated Phase Separation of Two Porphyrin Derivatives on Cu (111), *Chemistry–A European Journal*, **17** (2011) 10226-10229.

## 14 References

- [140] F. Buchner, V. Schwald, K. Comanici, H.P. Steinrück, H. Marbach, Microscopic Evidence of the Metalation of a Free-Base Porphyrin Monolayer with Iron, *ChemPhysChem*, **8** (2007) 241-243.
- [141] N. Tao, C. Li, H. He, Scanning tunneling microscopy applications in electrochemistry—beyond imaging, *Journal of Electroanalytical Chemistry*, **492** (2000) 81-93.
- [142] M. Soriaga, J. Schimpf, A. Carrasquillo, J. Abreu, W. Temesghen, R. Barriga, J.-J. Jeng, K. Sashikata, K. Itaya, Electrochemistry of the I-on-Pd single-crystal interface: studies by UHV-EC and in situ STM, *Surface science*, **335** (1995) 273-280.
- [143] K. Itaya, E. Tomita, Scanning tunneling microscope for electrochemistry—a new concept for the in situ scanning tunneling microscope in electrolyte solutions, *Surface science*, **201** (1988) L507-L512.
- [144] D.B. Williams, C.B. Carter, *Transmission Electron Microscopy*, Springer US, New York, 1996.
- [145] M. Wu, *Advanced Transmission Electron Microscopy Investigation of Nano-clustering in Gd-doped GaN*, Doctor, Mathematisch-Naturwissenschaftlichen Fakultät I, Humboldt-Universität zu Berlin, Berlin, (2014).
- [146] H.K. L. Reimer, *Transmission Electron Microscopy*, 5th ed., Springer-Verlag Berlin Heidelberg, New York, 2008.
- [147] K.W. Urban, Studying atomic structures by aberration-corrected transmission electron microscopy, *Science*, **321** (2008) 506-510.
- [148] M. Haider, S. Uhlemann, E. Schwan, H. Rose, B. Kabius, K. Urban, Electron microscopy image enhanced, *Nature*, **392** (1998) 768.
- [149] M. Haider, H. Rose, S. Uhlemann, E. Schwan, B. Kabius, K. Urban, A spherical-aberration-corrected 200kV transmission electron microscope, *Ultramicroscopy*, **75** (1998) 53-60.
- [150] Q.M. Ramasse, C.R. Seabourne, D.-M. Kepaptsoglou, R. Zan, U. Bangert, A.J. Scott, Probing the bonding and electronic structure of single atom dopants in graphene with electron energy loss spectroscopy, *Nano letters*, **13** (2013) 4989-4995.
- [151] H. Tan, S. Turner, E. Yücelen, J. Verbeeck, G. Van Tendeloo, 2D atomic mapping of oxidation states in transition metal oxides by scanning transmission electron microscopy and electron energy-loss spectroscopy, *Physical review letters*, **107** (2011) 107602.
- [152] R. Egerton, Electron energy-loss spectroscopy in the TEM, *Reports on Progress in Physics*, **72** (2008) 016502.

## 14 References

- [153] A. Boulineau, L. Croguennec, C. Delmas, F. Weill, Reinvestigation of Li<sub>2</sub>MnO<sub>3</sub> structure: electron diffraction and high resolution TEM, *Chemistry of Materials*, **21** (2009) 4216-4222.
- [154] H. Lee, R. Lowe-Webb, W. Yang, P.C. Sercel, Determination of the shape of self-organized InAs/GaAs quantum dots by reflection high energy electron diffraction, *Applied physics letters*, **72** (1998) 812-814.
- [155] K. Takayanagi, Y. Tanishiro, M. Takahashi, S. Takahashi, Structural analysis of Si (111)-7×7 by UHV-transmission electron diffraction and microscopy, *Journal of Vacuum Science & Technology A: Vacuum, Surfaces, and Films*, **3** (1985) 1502-1506.
- [156] J. Guo, *X-rays in Nanoscience*, John Wiley & Sons, Germany, 2010.
- [157] T. Warwick, K. Franck, J. Kortright, G. Meigs, M. Moronne, S. Myneni, E. Rotenberg, S. Seal, W. Steele, H. Ade, A scanning transmission x-ray microscope for materials science spectromicroscopy at the advanced light source, *Review of scientific instruments*, **69** (1998) 2964-2973.
- [158] J. Stöhr, *NEXAFS Spectroscopy*, Springer-Verlag Berlin Heidelberg, New York, 1992.
- [159] S.-B. Choe, Y. Acremann, A. Scholl, A. Bauer, A. Doran, J. Stöhr, H.A. Padmore, Vortex core-driven magnetization dynamics, *Science*, **304** (2004) 420-422.
- [160] J. Stöhr, S. Anders, X-ray spectro-microscopy of complex materials and surfaces, *IBM Journal of Research and Development*, **44** (2000) 535-551.
- [161] J. Stöhr, Exploring the microscopic origin of magnetic anisotropies with X-ray magnetic circular dichroism (XMCD) spectroscopy, *Journal of Magnetism and Magnetic Materials*, **200** (1999) 470-497.
- [162] P. Wohlhüter, M.T. Bryan, P. Warnicke, S. Gliga, S.E. Stevenson, G. Heldt, L. Saharan, A.K. Suszka, C. Moutafis, R.V. Chopdekar, Nanoscale switch for vortex polarization mediated by Bloch core formation in magnetic hybrid systems, *Nature communications*, **6** (2015).
- [163] S.Y.T. M. A. Van Hove, *Surface Crystallography by LEED*, Springer-Verlag Berlin Heidelberg, New York, 1979.
- [164] W.H.W. M. A. Van Hove, C.-M. Chan, *Low-Energy Electron Diffraction*, Springer-Verlag Berlin Heidelberg, New York, 1986.
- [165] J. Köbl, T. Wang, C. Wang, M. Drost, F. Tu, Q. Xu, H. Ju, D. Wechsler, M. Franke, H. Pan, Hungry Porphyrins: Protonation and Self-Metalation of Tetraphenylporphyrin on TiO<sub>2</sub> (110)-1×1, *ChemistrySelect*, **1** (2016) 6103-6105.

## 14 References

- [166] M. Schirmer, *Generation of titanium oxide nanostructures via electron beam induced deposition in UHV*, Doctoral thesis, Lehrstuhl für Physikalische Chemie II, Friedrich-Alexander-Universität Erlangen-Nürnberg, Erlangen, (2012).
- [167] T. Lukasczyk, *Generation of pure iron nanostructures via electron-beam induced deposition in UHV*, Doctoral thesis, Lehrstuhl für Physikalische Chemie II, Friedrich-Alexander-Universität Erlangen-Nürnberg, Erlangen, (2010).
- [168] P.H. Dawson, *Quadrupole mass spectrometry and its applications*, Elsevier Scientific Publishing Company, Amsterdam, 1976.
- [169] G. Sauerbrey, Use of quartz vibration for weighing thin films on a microbalance, *Z. phys.*, **155** (1959) 206-212.
- [170] F. Vollnhals, *Exploring electron beam induced surface activation for the fabrication of well-defined nanostructures*, Doctoral thesis, Lehrstuhl für Physikalische Chemie II, Friedrich-Alexander-Universität Erlangen-Nürnberg, Erlangen, (2014).
- [171] J. Ackermann, *Manual for the SUPRA (VP) and ULTRA Scanning Electron Microscopes*, Carl Zeiss SMT Ltd, (09.2015).
- [172] Scienta Omicron GmbH, *Schematic of the UHV Gemini column*, <http://www.scientaomicron.com/en/products/lt-nanoprobe/instrument-concept> (Accessed: 14.02.2017).
- [173] H. Watanabe, S. Fujita, S. Maruno, K. Fujita, M. Ichikawa, Selective thermal decomposition of ultrathin silicon oxide layers induced by electron-stimulated oxygen desorption, *Applied physics letters*, **71** (1997) 1038-1040.
- [174] V. Friedli, I. Utke, Optimized molecule supply from nozzle-based gas injection systems for focused electron-and ion-beam induced deposition and etching: simulation and experiment, *Journal of Physics D: Applied Physics*, **42** (2009) 125305.
- [175] Institute of Micro- and Nanostructure Research group, Friedrich-Alexander-Universität Erlangen-Nürnberg, Germany, *Description of the equipments*, <http://em.tf.fau.eu/equipment.shtml> (Accessed: 17.02.2017).
- [176] J. Raabe, G. Tzvetkov, U. Flechsig, M. Böge, A. Jaggi, B. Sarafimov, M. Vernooij, T. Huthwelker, H. Ade, D. Kilcoyne, PolLux: A new facility for soft x-ray spectromicroscopy at the Swiss Light Source, *Review of Scientific Instruments*, **79** (2008) 113704.
- [177] T. Huthwelker, V. Zelenay, M. Birrer, A. Krepelova, J. Raabe, G. Tzvetkov, M.G. Vernooij, M. Ammann, An in situ cell to study phase transitions in individual aerosol particles on a substrate using scanning transmission x-ray microspectroscopy, *Review of Scientific Instruments*, **81** (2010) 113706.

## 14 References

- [178] A. Späth, F. Tu, F. Vollnhals, M. Drost, S.K. Calderón, B. Watts, R.H. Fink, H. Marbach, Additive fabrication of nanostructures with focused soft X-rays, *RSC Advances*, **6** (2016) 98344-98349.
- [179] A. Ouvrard, J. Niebauer, A. Ghalgaoui, C. Barth, C.R. Henry, B. Bourguignon, Characterization of thin MgO films on Ag (001) by low-energy electron diffraction and scanning tunneling microscopy, *The Journal of Physical Chemistry C*, **115** (2011) 8034-8041.
- [180] T. Jaouen, S. Tricot, G. Delhaye, B. Lépine, D. Sébilleau, G. Jézéquel, P. Schieffer, Layer-resolved study of Mg atom incorporation at the MgO/Ag (001) buried interface, *Physical review letters*, **111** (2013) 027601.
- [181] J. Pal, M. Smerieri, E. Celasco, L. Savio, L. Vattuone, M. Rocca, Morphology of monolayer MgO films on Ag (100): switching from corrugated islands to extended flat terraces, *Physical review letters*, **112** (2014) 126102.
- [182] F. Ringleb, Y. Fujimori, M.A. Brown, W.E. Kaden, F. Calaza, H. Kuhlenbeck, M. Sterrer, H.-J. Freund, The role of exposed silver in CO oxidation over MgO (001)/Ag (001) thin films, *Catalysis Today*, **240** (2015) 206-213.
- [183] M. Huth, F. Porrati, C. Schwalb, M. Winhold, R. Sachser, M. Dukic, J. Adams, G. Fantner, Focused electron beam induced deposition: A perspective, *Beilstein journal of nanotechnology*, **3** (2012) 597-619.
- [184] K. Kuepper, S. Wintz, J. Raabe, M. Buess, C. Akhmadaliev, L. Bischoff, C. Quitmann, J. Fassbender, Magnetization dynamics of Landau structures: tuning the response of mesoscopic magnetic objects using defects, *Journal of Physics: Condensed Matter*, **21** (2009) 436003.
- [185] B. Van Waeyenberge, A. Puzic, H. Stoll, K. Chou, T. Tyliczszak, R. Hertel, M. Fähnle, H. Brückl, K. Rott, G. Reiss, Magnetic vortex core reversal by excitation with short bursts of an alternating field, *Nature*, **444** (2006) 461-464.
- [186] K.W. Chou, A. Puzic, H. Stoll, G. Schütz, B. Van Waeyenberge, T. Tyliczszak, K. Rott, G. Reiss, H. Brückl, I. Neudecker, Vortex dynamics in coupled ferromagnetic multilayer structures, *Journal of applied physics*, **99** (2006) 08F305.
- [187] C. Moreau-Luchaire, C. Moutafis, N. Reyren, J. Sampaio, C. Vaz, N. Van Horne, K. Bouzehouane, K. Garcia, C. Deranlot, P. Warnicke, Additive interfacial chiral interaction in multilayers for stabilization of small individual skyrmions at room temperature, *Nature nanotechnology*, **11** (2016) 444-448.
- [188] A. Vansteenkiste, K. Chou, M. Weigand, M. Curcic, V. Sackmann, H. Stoll, T. Tyliczszak, G. Woltersdorf, C. Back, G. Schütz, X-ray imaging of the dynamic magnetic vortex core deformation, *Nature physics*, **5** (2009) 332-334.

## 14 References

- [189] H. Stoll, A. Puzic, B. Van Waeyenberge, P. Fischer, J. Raabe, M. Buess, T. Haug, R. Höllinger, C. Back, D. Weiss, High-resolution imaging of fast magnetization dynamics in magnetic nanostructures, *Applied Physics Letters*, **84** (2004) 3328-3330.
- [190] P. Fischer, T. Eimüller, G. Schütz, M. Köhler, G. Bayreuther, G. Denbeaux, D. Attwood, Study of in-plane magnetic domains with magnetic transmission X-ray microscopy, *Journal of Applied Physics*, **89** (2001) 7159-7161.
- [191] C. Chen, Y. Idzerda, H.-J. Lin, N. Smith, G. Meigs, E. Chaban, G. Ho, E. Pellegrin, F. Sette, Experimental confirmation of the X-ray magnetic circular dichroism sum rules for iron and cobalt, *Physical review letters*, **75** (1995) 152.
- [192] J. Pablo-Navarro, C. Magén, J.M. de Teresa, Three-dimensional core-shell ferromagnetic nanowires grown by focused electron beam induced deposition, *Nanotechnology*, **27** (2016) 285302.
- [193] L. Reimer, Scanning Electron Microscopy: Physics of Image Formation and Microanalysis, Second Edition, *Measurement Science and Technology*, **11** (2000) 1826.
- [194] T.-J. Park, S. Sambasivan, D.A. Fischer, W.-S. Yoon, J.A. Misewich, S.S. Wong, Electronic structure and chemistry of iron-based metal oxide nanostructured materials: a NEXAFS investigation of BiFeO<sub>3</sub>, Bi<sub>2</sub>Fe<sub>4</sub>O<sub>9</sub>,  $\alpha$ -Fe<sub>2</sub>O<sub>3</sub>,  $\gamma$ -Fe<sub>2</sub>O<sub>3</sub>, and Fe/Fe<sub>3</sub>O<sub>4</sub>, *The Journal of Physical Chemistry C*, **112** (2008) 10359-10369.
- [195] R.K. Hocking, E.C. Wasinger, F.M. de Groot, K.O. Hodgson, B. Hedman, E.I. Solomon, Fe L-edge XAS studies of K4 [Fe (CN) 6] and K3 [Fe (CN) 6]: A direct probe of back-bonding, *Journal of the American Chemical Society*, **128** (2006) 10442-10451.
- [196] P. Kuiper, B. Searle, L.-C. Duda, R. Wolf, P. Van der Zaag, Fe L 2, 3 linear and circular magnetic dichroism of Fe<sub>3</sub>O<sub>4</sub>, *Journal of Electron Spectroscopy and Related Phenomena*, **86** (1997) 107-113.
- [197] G. Cressey, C. Henderson, G. Van der Laan, Use of L-edge X-ray absorption spectroscopy to characterize multiple valence states of 3d transition metals; a new probe for mineralogical and geochemical research, *Physics and chemistry of minerals*, **20** (1993) 111-119.
- [198] G.W. Simmons, D.J. Dwyer, A LEED-AES study of the initial stages of oxidation of Fe (001), *Surface Science*, **48** (1975) 373-392.
- [199] A. Fromhold Jr, E.L. Cook, Kinetics of oxide film growth on metal crystals: thermal electron emission and ionic diffusion, *Physical Review*, **163** (1967) 650.
- [200] K. Kuepper, L. Bischoff, C. Akhmadaliev, J. Fassbender, H. Stoll, K. Chou, A. Puzic, K. Fauth, D. Dolgos, G. Schütz, Vortex dynamics in Permalloy disks with artificial defects: Suppression of the gyrotropic mode, *Applied physics letters*, **90** (2007) 062506.

## 14 References

- [201] C.M. Wang, D.R. Baer, L.E. Thomas, J.E. Amonette, J. Antony, Y. Qiang, G. Duscher, Void formation during early stages of passivation: Initial oxidation of iron nanoparticles at room temperature, *Journal of Applied Physics*, **98** (2005) 094308.
- [202] S.W. Yuan, H.N. Bertram, J.F. Smyth, S. Schultz, Size effects of switching fields of thin permalloy particles, *IEEE transactions on magnetics*, **28** (1992) 3171-3173.
- [203] M. Drost, F. Tu, F. Vollnhals, I. Szenti, J. Kiss, H. Marbach, On the Principles of Tweaking Nanostructure Fabrication via Focused Electron Beam Induced Processing Combined with Catalytic Growth Processes, *Small Methods*, **1** (2017) 1700095.
- [204] W. Jozwiak, E. Kaczmarek, T. Maniecki, W. Ignaczak, W. Maniukiewicz, Reduction behavior of iron oxides in hydrogen and carbon monoxide atmospheres, *Applied Catalysis A: General*, **326** (2007) 17-27.
- [205] D.N. Futaba, K. Hata, T. Yamada, T. Hiraoka, Y. Hayamizu, Y. Kakudate, O. Tanaike, H. Hatori, M. Yumura, S. Iijima, Shape-engineerable and highly densely packed single-walled carbon nanotubes and their application as super-capacitor electrodes, *Nature materials*, **5** (2006) 987.
- [206] R.H. Baughman, A.A. Zakhidov, W.A. De Heer, Carbon nanotubes--the route toward applications, *science*, **297** (2002) 787-792.
- [207] S. Sakurai, H. Nishino, D.N. Futaba, S. Yasuda, T. Yamada, A. Maigne, Y. Matsuo, E. Nakamura, M. Yumura, K. Hata, Role of subsurface diffusion and Ostwald ripening in catalyst formation for single-walled carbon nanotube forest growth, *Journal of the American Chemical Society*, **134** (2012) 2148-2153.
- [208] Z.-Y. Zhan, Y.-N. Zhang, G.-Z. Sun, L.-X. Zheng, K. Liao, The effects of catalyst treatment on fast growth of millimeter-long multi-walled carbon nanotube arrays, *Applied Surface Science*, **257** (2011) 7704-7708.
- [209] P.B. Amama, C.L. Pint, L. McJilton, S.M. Kim, E.A. Stach, P.T. Murray, R.H. Hauge, B. Maruyama, Role of water in super growth of single-walled carbon nanotube carpets, *Nano letters*, **9** (2008) 44-49.
- [210] S.J.B. Reed, S.J.B. Reed, *Electron microprobe analysis*, 1st ed., Cambridge University Press, Cambridge, 1975.
- [211] Z.P. Huang, D.Z. Wang, J.G. Wen, M. Sennett, H. Gibson, Z.F. Ren, Effect of nickel, iron and cobalt on growth of aligned carbon nanotubes, *Applied Physics A*, **74** (2002) 387-391.
- [212] D.S. Bethune, C.H. Kiang, M.S. de Vries, G. Gorman, R. Savoy, J. Vazquez, R. Beyers, Cobalt-catalysed growth of carbon nanotubes with single-atomic-layer walls, *Nature*, **363** (1993) 605-607.

## 14 References

- [213] W.-H. Chiang, R.M. Sankaran, Linking catalyst composition to chirality distributions of as-grown single-walled carbon nanotubes by tuning  $\text{Ni}_x\text{Fe}_{1-x}$  nanoparticles, *Nature materials*, **8** (2009) 882-886.
- [214] J. Stöhr, *NEXAFS spectroscopy*, Springer Science & Business Media, 2013.
- [215] J. Cazaux, A physical approach to the radiation damage mechanisms induced by X-rays in X-ray microscopy and related techniques, *Journal of Microscopy*, **188** (1997) 106-124.
- [216] H. Ade, A.P. Hitchcock, NEXAFS microscopy and resonant scattering: composition and orientation probed in real and reciprocal space, *Polymer*, **49** (2008) 643-675.
- [217] I. Mohacsi, I. Vartiainen, M. Guizar-Sicairos, P. Karvinen, V.A. Guzenko, E. Müller, C.M. Kewish, A. Somogyi, C. David, Fabrication and characterization of high-efficiency double-sided blazed x-ray optics, *Optics letters*, **41** (2016) 281-284.
- [218] B.L. Henke, E.M. Gullikson, J.C. Davis, X-ray interactions: photoabsorption, scattering, transmission, and reflection at  $E= 50\text{-}30,000$  eV,  $Z= 1\text{-}92$ , *Atomic data and nuclear data tables*, **54** (1993) 181-342.
- [219] A.F. Leontowich, A.P. Hitchcock, T. Tyliczszak, M. Weigand, J. Wang, C. Karunakaran, Accurate dosimetry in scanning transmission X-ray microscopes via the cross-linking threshold dose of poly (methyl methacrylate), *Journal of synchrotron radiation*, **19** (2012) 976-987.
- [220] A. Späth, B. Watts, L.T. Wasserthal, R.H. Fink, Quantitative study of contrast enhancement in soft X-ray micrographs of insect eyes by tissue selective mass loss, *Journal of synchrotron radiation*, **21** (2014) 1153-1159.
- [221] C. Chantler, Theoretical form factor, attenuation, and scattering tabulation for  $Z= 1\text{-}92$  from  $E= 1\text{-}10$  eV to  $E= 0.4\text{-}1.0$  MeV, *Journal of Physical and Chemical Reference Data*, **24** (1995) 71-643.
- [222] A.F. Leontowich, A.P. Hitchcock, Secondary electron deposition mechanism of carbon contamination, *Journal of Vacuum Science & Technology B, Nanotechnology and Microelectronics: Materials, Processing, Measurement, and Phenomena*, **30** (2012) 030601.
- [223] A. Saywell, G. Magnano, C.J. Satterley, L.M. Perdigão, A.J. Britton, N. Taleb, M. del Carmen Giménez-López, N.R. Champness, J.N. O'shea, P.H. Beton, Self-assembled aggregates formed by single-molecule magnets on a gold surface, *Nature communications*, **1** (2010) 75.
- [224] S. Mehendale, J. Mulders, P. Trompenaars, A new sequential EBID process for the creation of pure Pt structures from  $\text{MeCpPtMe}_3$ , *Nanotechnology*, **24** (2013) 145303.
- [225] A. Botman, J. Mulders, R. Weemaes, S. Mentink, Purification of platinum and gold structures after electron-beam-induced deposition, *Nanotechnology*, **17** (2006) 3779.

## 14 References

- [226] P. Salén, V. Yatsyna, L. Schio, R. Feifel, R. Richter, M. Alagia, S. Stranges, V. Zhaunerchyk, NEXAFS spectroscopy and site-specific fragmentation of N-methylformamide, N, N-dimethylformamide, and N, N-dimethylacetamide, *The Journal of Chemical Physics*, **144** (2016) 244310.
- [227] S. Yuasa, T. Nagahama, A. Fukushima, Y. Suzuki, K. Ando, Giant room-temperature magnetoresistance in single-crystal Fe/MgO/Fe magnetic tunnel junctions, *Nature materials*, **3** (2004) 868-871.
- [228] B. Yoon, H. Häkkinen, U. Landman, A.S. Wörz, J.-M. Antonietti, S. Abbet, K. Judai, U. Heiz, Charging effects on bonding and catalyzed oxidation of CO on Au<sub>8</sub> clusters on MgO, *Science*, **307** (2005) 403-407.
- [229] M. Sterrer, E. Fischbach, T. Risse, H.-J. Freund, Geometric characterization of a singly charged oxygen vacancy on a single-crystalline MgO (001) film by electron paramagnetic resonance spectroscopy, *Physical review letters*, **94** (2005) 186101.
- [230] J. Kramer, W. Ernst, C. Tegenkamp, H. Pfnür, Mechanism and kinetics of color center formation on epitaxial thin films of MgO, *Surface science*, **517** (2002) 87-97.
- [231] F. Porrati, B. Kämpken, A. Terfort, M. Huth, Fabrication and electrical transport properties of binary Co-Si nanostructures prepared by focused electron beam-induced deposition, *Journal of Applied Physics*, **113** (2013) 053707.
- [232] F. Porrati, E. Begun, M. Winhold, C.H. Schwalb, R. Sachser, A. Frangakis, M. Huth, Room temperature L10 phase transformation in binary CoPt nanostructures prepared by focused-electron-beam-induced deposition, *Nanotechnology*, **23** (2012) 185702.
- [233] M. Winhold, C.H. Schwalb, F. Porrati, R. Sachser, A.S. Frangakis, B. Kämpken, A. Terfort, N. Auner, M. Huth, Binary Pt-Si nanostructures prepared by focused electron-beam-induced deposition, *ACS nano*, **5** (2011) 9675-9681.
- [234] R. Che, M. Takeguchi, M. Shimojo, W. Zhang, K. Furuya, Fabrication and electron holography characterization of FePt alloy nanorods, *Applied Physics Letters*, **87** (2005) 223109.

## Acknowledgement

After four and half years of my PhD, I'm on the final line of my doctoral journey. Firstly I would like to express my sincere gratitude to my supervisor PD. Dr. Hubertus Marbach for his invaluable support, guidance, inspiration, encouragement and confidence in me. I appreciate very much everything he has done in the course of this thesis formation. I was allowed a great freedom on my research and received good advices from him at the right moment. Especially, he has convinced me to carry on a PhD in a total new research area compared to my master research work. I will keep in mind his advices and comments for all along my later career.

I must express many thanks to Prof. Hans-Peter Steinrück for giving me the chance to start my PhD here and let me open my eyes and mind to the world of research in surface science.

I am grateful to Prof. Rainer Fink, not only for dedicating his precious time to evaluate this thesis, but also for his support of experiments in synchrotron based X-ray microscopy.

I acknowledge the generous support of Martin Drost during writing this thesis. Without him, my thesis would never have been same as it is.

I also thank Dr. Andreas Späth for his immense contribution to many papers we formed. His knowledge in fundamentals of X-ray microscope gives the chances for many projects.

Now my thanks are oriented to the people who shared one of the important parts of everyday laboratory life: Dr. Florian Vollnhals, Dr. Esther Carrasco, Martin Drost, Luisa Berger and Christian Preischl for creating the nice working atmosphere; Hans-Peter Bäumler and Bernd Kreß for your outstanding technical support; Friedhold Wölfel and his mechanical workshop for their unselfish reliable helps.

Furthermore, my appreciation goes to people in all cooperation projects:

- Imre Szentı , Prof. Zoltán Kónya, and Prof. János Kiss (Department of Applied and Environment Chemistry, University of Szeged, Hungary)
- Dr. Mingjian Wu, Dr. Benjamin Winter, Dr. Benjamin Butz, and Prof. Dr. Erdmann Spiecker (Institute of Micro- and Nanostructure Research, Friedrich-Alexander-Universität Erlangen-Nürnberg, Germany)

## Acknowledgement

Away from the laboratory, thanks to Dr. Hao Wu, Dr. Kai Zhen, Dr. Xiaoyan Du, Dr. Liang Zhang and Dr. Tao Xu, for sharing joyful moments in my daily life.

Last but not least, I would like to thank my family Mrs. Yueqing Xia and Mr. Xiangyi Tu and my wife Luying Huang for their encouragement and eternal support throughout my life. The most important, thanks to my daughter Xinran Tu, you are always the biggest achievement during my PhD and of course the sunshine in my whole life.

## Publication list

### Journal articles

1. **Fan Tu**, Martin Drost, Imre Szenti, Janos Kiss, Zoltan Konya, Hubertus Marbach, “*Localized growth of carbon nanotubes via lithographic fabrication of metallic deposits*”, Beilstein Journal of Nanotechnology, 8, 2017, 2592
2. **Fan Tu**, Andreas Späth, Martin Drost, Florian Vollnhals, Sandra Krick Calderon, Rainer H. Fink, Hubertus Marbach, “*Exploring the fabrication of Co and Mn nanostructures with focused X-ray beam induced deposition*”, JVSTB, 35 (3), 2017, 031601 (feature article on JVSTB website and reported as scientific highlight on Switzerland Paul Scherrer Institut website)
3. Andreas Späth\*, **Fan Tu\***, Florian Vollnhals, Martin Drost, Sandra Krick Calderon, Benjamin Watts, Rainer H. Fink, Hubertus Marbach, “*Additive Fabrication of Nanostructures with Focused soft X-rays*”, RSC Advances, 6, 2016, 98344 – 98349 (\* **these authors contributed equally to this work**)
4. **Fan Tu**, Martin Drost, Florian Vollnhals, Andreas Späth, Esther Carrasco, Rainer Fink, Hubertus Marbach, “*On the Magnetic Properties of Iron Nanostructures Fabricated via Focused Electron Beam Induced Deposition*”, Nanotechnology, 27(35), 2016, 355302-355313
5. Martin Drost, **Fan Tu**, Florian Vollnhals, Imre Szenti, Janos Kiss, Hubertus Marbach, “*On the principles of tweaking nanostructure fabrication via focused electron beam processing combined with catalytic growth processes*”, Small methods, 2017, accepted
6. Julia Köbl, Cici Wang, Tao Wang, Martin Drost, **Fan Tu**, Qian Xu, Huanxin Ju, Daniel Wechsler, Matthias Franke, Haibin Pan, Hubertus Marbach, Hans-Peter Steinrück, Junfa Zhu and Ole Lytken, “*Hungry Porphyrins: Protonation and Self-Metalation of Tetraphenylporphyrin on TiO<sub>2</sub>(110) - 1 × 1*”, ChemistrySelect, 1(19), 2016, 6103-6105
7. Sebastian H Etschel, Luis Portilla, Johannes Kirschner, Martin Drost, **Fan Tu**, Hubertus Marbach, Rik R Tykwinski, Marcus Halik, “*Region-Selective Deposition of Core-Shell Nanoparticles for 3 D Hierarchical Assemblies by the Huisgen 1,3-Dipolar Cycloaddition*”, Angewandte Chemie International Edition, 54(32), 2015, 9235-9238

## Publication list

8. Florian Vollnhals, Martin Drost, **Fan Tu**, Esther Carrasco, Andreas Späth, Rainer H. Fink, Hans-Peter Steinrück, Hubertus Marbach, “*Electron-beam induced deposition and autocatalytic decomposition of  $\text{Co}(\text{CO})_3\text{NO}$* ”, Beilstein Journal of Nanotechnology, 5(1), 2014, 1175-1185

### Papers in preparation

1. Florian Vollnhals, Francesc Salvat-Pujol, Martin Drost, **Fan Tu**, Roser Valenti, Hubertus Marbach, “*Electron beam induced surface activation as a means to study fundamental aspects of electron scattering processes*”

2. Martin Drost, **Fan Tu**, Luisa Berger, Hartmut Gliemann, Christof Wöll, Hubertus Marbach, “*Focused electron beam induced processing on surface-anchored metal-organic frameworks*”

### Conference presentations

1. “*On the autocatalytic growth and magnetic properties of Fe nanostructures fabricated via focused electron beam induced deposition*”, **Talk**, 81<sup>st</sup> annual conference of the DPG – the spring meeting of surface science section, Dresden, Germany, 19-24 March, 2017

2. “*On the autocatalytic growth of clean iron nanostructures via focused electron beam induced processing and their characterizations*”, **Talk**, 6<sup>th</sup> workshop on focused electron beam induced processing (FEBIP 2016), Vienna, Austria, 4-6 July, 2016

3. “*On the magnetic properties of clean iron nanostructures fabricated by focused electron beam induced processing*”, **Poster**, The 60<sup>th</sup> international conference on electron, ion, and photon beam technology and nanofabrication (EIPBN 2016), Pittsburgh, USA, 31 May-3 June, 2016

### Best poster prize awarded

4. “*Nanostructures fabricated via focused X-ray beam induced deposition (FXBID)*”, **Talk**, 80<sup>th</sup> annual conference of the DPG – the spring meeting of surface science section, Regensburg, Germany, 6-11 March, 2016

5. “*Lithographic nanostructuring of oxide surfaces and molecular layers via focused electron beam induced processing*”, **Poster**, 1<sup>st</sup> funCOS international workshop, Erlangen, Germany, 8-10 November, 2015

6. “*Focused electron beam induced processing on  $\text{MgO}/\text{Ag}(100)$  surface*”, **Talk**, funCOS-ICICP PhD seminar, Plech, Germany, July, 2015

## Publication list

7. “*Magnetic properties of iron nanostructures fabricated by focused electron beam induced processing*”, **Poster**, 5<sup>th</sup> workshop on focused electron beam induced processing (FEBIP 2014), Frankfurt, Germany, 22-24 July, 2014
8. “*Fabrication of nanostructures with different precursors via focused electron beam induced processing in UHV*”, **Poster**, 1<sup>st</sup> meeting of COST action CM1301-CELINA 2014, Erlangen, Germany, 19-22 March, 2014
9. “*FEBIP: a lithographic method for the controlled fabrication of well-defined nanostructures*”, **Poster**, 6<sup>th</sup> cluster of excellence engineering of advanced materials (EAM) symposium, Kloster Banz, Germany, 24-26 November, 2014
10. “*Fabrication of iron nanostructures on various surfaces via focused electron beam induced processing in UHV*”, **Poster**, 77<sup>th</sup> annual conference of the DPG – the spring meeting of surface science section, Regensburg, Germany, 13-15 March, 2013